

UNIVERSITÄT
BAYREUTH

Thermal Properties of Colloidal Structured Materials

Dissertation

Zur Erlangung des akademischen Grades eines
Doktors der Naturwissenschaften
Dr. rer. nat.

An der
Universität Bayreuth
Fakultät für Biologie, Chemie und Geowissenschaften

Vorgelegt von
Anna Magdalena Neuhöfer
geboren in Coburg

Bayreuth, 2022

Die vorliegende Arbeit wurde in der Zeit von Januar 2017 bis März 2022 in Bayreuth am Lehrstuhl Physikalische Chemie I unter Betreuung von Herrn Prof. Dr. Markus Retsch angefertigt.

Vollständiger Abdruck der von der Fakultät für Biologie, Chemie und Geowissenschaften der Universität Bayreuth genehmigten Dissertation zur Erlangung des akademischen Grades eines Doktors der Naturwissenschaften (Dr. rer. nat.).

Dissertation eingereicht am: 18.03.2022

Zulassung durch die Prüfungskommission: 06.04.2022

Wissenschaftliches Kolloquium: 25.07.2022

Amtierender Dekan: Prof. Dr. Benedikt Westermann

Prüfungsausschuss:

Prof. Dr. Markus Retsch (Gutachter)

Prof. Dr. Andreas Greiner (Gutachter)

Prof. Dr. Josef Breu (Vorsitz)

Prof. Dr. Peter Strohriegl

Diese Arbeit wurde kumulativ verfasst und umfasst die folgenden Publikationen und Manuskripte:

1. Scalable Synthesis of Smooth PS@TiO₂ Core-Shell and TiO₂ Hollow Spheres in the (Sub) Micron Size Range: Understanding Synthesis and Calcination Parameters, Anna M. Lechner (m. Neuhöfer), Tanja Feller, Qimeng Song, Bernd A. F. Kopera, Lukas Heindl, Markus Drechsler, Sabine Rosenfeldt, Markus Retsch, *Colloid and Polymer Science*, 298 (7), 867-878, 2020
2. High Temperature Thermal Transport in Porous Silica Materials: Direct Observation of a Switch from Conduction to Radiation, Anna M. Neuhöfer, Kai Herrmann, Flora Lebeda, Tobias Lauster, Christoph Kathmann, Svend-Age Biehs, Markus Retsch, *Advanced Functional Materials*, 2108370, 2021
3. Thermal Transport Binary Colloidal Glasses, Anna M. Neuhöfer and Markus Retsch, *in preparation*
4. Thermal Transport in Ampholytic Polymers: The Role of Hydrogen Bonding and Water Uptake, Patrick Hummel, Anna M. Lechner (m. Neuhöfer), Kai Herrmann, Philip Biehl, Carsten Rössel, Lisa Wiedenhöft, Felix H. Schacher, and Markus Retsch, *Macromolecules*, 53 (13), 5528-5537, 2020
5. Tunable thermoelastic anisotropy in hybrid Bragg stacks with extreme polymer confinement, Zuyuan Wang, Konrad Rolle, Theresa Schilling, Patrick Hummel, Alexandra Philipp, Bernd A.F. Kopera, Anna M. Lechner (m. Neuhöfer), Markus Retsch, Josef Breu, George Fytas, *Angewandte Chemie Int. Ed.*, 59 (3), 1286-1294, 2020
6. Anisotropic Thermal Transport in Spray-Coated Single-Phase Two-Dimensional Materials: Synthetic Clay Versus Graphene Oxide, Alexandra Philipp, Patrick Hummel, Theresa Schilling, Patrick Feicht, Sabine Rosenfeldt, Michael Ertl, Marius Schöttle, Anna M. Lechner (m. Neuhöfer), Zhen Xu, Chao Gao, Josef Breu, and Markus Retsch, *ACS Appl. Mater. Interfaces*, 12 (16), 18785-18791, 2020

Für meine Familie.

Contents

Summary	xi
Zusammenfassung	xv
List of Publications	xix
List of Contributions	xxi
List of Abbreviationsxxiii
1 Introduction	1
1.1 Motivation	1
1.2 Colloidal Particles & Assemblies	3
1.3 Thermal Transport	8
2 Materials	21
2.1 Emulsifierfree Emulsion Polymerization	22
2.2 Dispersion Polymerization	28
2.3 SiO ₂ Shell Synthesis and Hollow Spheres	29
2.4 TiO ₂ Shell Synthesis and Hollow Spheres	32
2.5 PS@TiO ₂ @Ag Core-Shell Particles	32
3 Methods	35
3.1 Scanning Electron Microscopy	36
3.2 Light Flash Analysis	38
3.3 Differential Scanning Calorimetry	41
4 References	45
5 Thesis Overview	61
5.1 Synopsis	61
5.2 My Contributions to Joint Publications	75
6 Synthesis of PS@TiO₂ Core-Shell and TiO₂ Hollow Spheres	79
7 High-Temperature Thermal Transport in Porous Silica Materials	107

8 Thermal Transport in Binary Colloidal Glasses	143
9 Thermal Transport in Ampholytic Polymers	161
10 Tunable Thermoelastic Anisotropy in Hybrid Bragg Stacks	193
11 Anisotropic Thermal Transport in 2D Materials	237
Danksagung	xxi
Eidesstattliche Versicherungen und Erklärungenxxiii

Summary

Thermal management plays a huge role in our everyday life. It is crucial in a wide range of applications, e.g., for developing insulating materials for buildings or aerospace components, thermally conducting materials for heat sinks, and more sophisticated materials that can direct the heat flow for energy storage technologies. The requirements for the materials are increasing steadily, and new materials have to be developed. An important parameter is the size range of the device. Since electronic devices are getting smaller, the thermal management material needs to be functional at nano- and microscales. Therefore, it is necessary to develop a detailed understanding of the structure-property relationships of the thermal management material.

In this thesis, the thermal properties of different nanoscopic materials and their superstructures have been examined. The main target was to understand and control the thermal transport of colloidal structures, focusing on their insulating properties. Solid and hollow silicon dioxide (silica) and hollow titanium dioxide (titania) particles have been used as colloidal building bricks.

The first achievement of this thesis was the synthesis of titania hollow particles in the sub-micrometer size range. Three necessary steps have been elaborated: synthesis and functionalization of polystyrene template particles (1), growth of the shells - including an aging step (2), and the calcination parameters (3). Following these steps, it was possible to fabricate titania hollow particles in a simple, scalable, and reproducible way.

Titania material is known for its optical properties since it strongly absorbs light in the wavelength region between 1-8 μm . Therefore, it is used in thermal insulation applications to suppress thermal radiation at elevated temperatures. In contrast, silica material is optically transparent in the region between 1-5 μm and consequently strongly affected by thermal radiation. Colloidal superstructures from solid and hollow silica particles in the sub-micrometer size range have been characterized using light-flash analysis. The transition from conduction-dominated to

radiation-dominated thermal transport mechanism was observed and described in the temperature range from 25 to 925 °C, using an extended existing analytical framework. The results provide a better understanding of the challenges of fabricating and analyzing efficient high-temperature insulation materials.

At room temperature, silica hollow particle materials are highly insulating. To extend pre-existing knowledge about the structure-property relationship, the thermal properties of binary colloidal assemblies of 500 and 900 nm of solid and hollow silica particles have been studied. It was found that especially for hollow particles, the influence of the particle size exceeds the effect of binary mixtures, and a thermal conductivity of 20 mW/mK in vacuum was achieved.

Thermal characterization often requires information about the material specific heat coefficient. Especially when new materials are thermally characterized, characterization via DSC is essential. With my knowledge about this technique, I contributed to several further projects. While the former projects were based on inorganic materials, also organic and organic-inorganic composite materials are characterized in the second part of this thesis.

The first project was on ampholytic polymers. This unique class of polymers exhibits a hydrogen bond donor and acceptor group per repetition unit and therefore has a high functional group density. Four different ampholytic polymers have been investigated using infrared spectroscopy and the photoacoustic method. It was proven that the thermal conductivity increased with increasing hydrogen bond strength in the polymer. Due to the functional groups, the properties of the polymers were affected by humidity. However, the resulting properties could be well explained by mixing models. I supported this project by applying modulated DSC measurements to determine the glass transition temperatures of the polymers in the humid state.

In the remaining two projects, the anisotropic thermal properties of two-dimensional Bragg stacks were investigated. Bragg stacks consist of aligned nanoplatelets with in-plane dimensions in the micrometer regime, while the thickness in cross-plane direction is only a few nanometers. As platelets, hectorite and graphene oxide have been used. The in-plane thermal conductivity was significantly higher than the cross-plane thermal conductivity for both materials. The in-plane thermal conductivity of the hectorite stacks was found to be higher as in the graphene oxide stacks. Consequently, the overall anisotropy ratio was 2- to 3-fold higher. In a more advanced study, hectorite platelets have been layered with polyvinylpyrrolidone (PVP) with extreme polymer confinement and perfect periodicity. Increasing PVP volume fractions led to basal spacing in the range from 1.9 to 3.8 nm. The dominating influence of the PVP-hectorite interfaces led to a drastic drop of the

cross-plane thermal conductivity of 0.09 W/mK compared to the pure materials 0.17 W/mK for PVP and 5.71 W/mK for hectorite. A classical parallel mixing model could describe the in-plane thermal properties, including density, specific heat, and thermal conductivity. Overall, the structural perfection of these samples led to an exceptionally high thermal conductivity anisotropy. I provided both projects with all necessary DSC measurements to determine the specific heat of all materials and composites.

This thesis shows the beauty of “playing” with colloidal building bricks, extending the number of accessible materials and structures. Understanding the thermal structure-property relationship helps create tailored thermal management materials. In the future, this research may help solve thermal challenges, such as insulation applications and heat sinks in electronic devices.

Zusammenfassung

Wärmemanagement spielt in unserem täglichen Leben eine große Rolle. Es ist für eine Vielzahl von Anwendungen von entscheidender Bedeutung, z. B. für die Entwicklung von Isoliermaterialien für Gebäude oder Bauteile in der Luft- und Raumfahrt, wärmeleitende Materialien für Wärmesenken und anspruchsvollere Materialien, die den Wärmestrom für Energiespeichertechnologien lenken können. Die Anforderungen an die Materialien steigen stetig, weshalb neue Materialien entwickelt werden müssen. Dabei ist ein wichtiger Parameter der Größenbereich der Geräte. Da die elektronischen Geräte immer kleiner werden, muss das Material für das Wärmemanagement auf Nano- und Mikroebene anwendbar sein. Daher ist es notwendig, ein detailliertes Verständnis der Struktur-Eigenschafts-Beziehungen des Wärmemanagementmaterials zu entwickeln.

In dieser Arbeit wurden die thermischen Eigenschaften verschiedener nanoskopischer Materialien und ihrer Überstrukturen untersucht. Das Hauptziel bestand darin, den Wärmetransport von kolloidalen Strukturen zu verstehen und zu kontrollieren, wobei der Schwerpunkt auf ihren isolierenden Eigenschaften lag. Siliziumdioxid Voll- und Hohlkugeln und Titandioxid Hohlkugeln wurden als kolloidale Bausteine verwendet.

Das erste Ergebnis dieser Arbeit war die Synthese von hohlen Titandioxid Hohlkugeln im Submikrometerbereich. Drei notwendige Schritte wurden ausgearbeitet: Synthese und Funktionalisierung von Polystyrol-Templatpartikeln (1), das Wachstum der Schalen - einschließlich eines Alterungsschritts (2) - und die Kalzinierungsparameter (3). Nach diesen Schritten war es möglich, Titandioxid-Hohlkugeln auf einfache, skalierbare und reproduzierbare Weise herzustellen.

Titandioxid ist für seine optischen Eigenschaften bekannt, da es Licht im Wellenlängenbereich zwischen 1 und 8 μm stark absorbiert. Daher wird es eingesetzt, um radiativen Wärmetransport in Dämmmaterialien bei hohen Temperaturen zu unterdrücken. Im Gegensatz dazu ist Siliziumdioxid im Wellenlängenbereich von 1 - 5 μm optisch transparent und daher stark von radiativem Wärmetransport betroffen. Kolloidale

Überstrukturen aus Siliziumdioxid Voll- und Hohlkugeln im Submikrometerbereich wurden mit Hilfe der Laser Flash Analyse charakterisiert. Der Übergang vom leitungsdominierten zum strahlungsdominierten Wärmetransportmechanismus wurde im Temperaturbereich von 25 bis 925 °C beobachtet und beschrieben, wobei eine erweiterte bestehende analytische Methode verwendet wurde. Die Ergebnisse ermöglichen ein besseres Verständnis der Herausforderungen bei der Herstellung und Analyse von effizienten Hochtemperaturisolationmaterialien.

Bei Raumtemperatur sind Siliziumdioxid-Hohlkörpermaterialien hoch isolierend. Um das bereits vorhandene Wissen über die Struktur-Eigenschafts-Beziehung zu erweitern, wurden die thermischen Eigenschaften von binären kolloidalen Anordnungen von 500 und 900 nm festen und hohlen Siliziumdioxidpartikeln untersucht. Es wurde festgestellt, dass insbesondere bei Hohlpartikel der Einfluss der Partikelgröße die Wirkung von binären Mischungen übertrifft und eine Wärmeleitfähigkeit von 20 mW/mK im Vakuum erreicht wurde.

Für die thermische Charakterisierung sind häufig Informationen über den spezifischen Wärmekoeffizienten erforderlich. Insbesondere wenn neue Materialien thermisch charakterisiert werden, ist die Charakterisierung mittels Dynamischer Differenzkalorimetrie (eng. *differential scanning calorimetry, DSC*) unerlässlich. Mit meinem Wissen über diese Technik habe ich zu mehreren weiteren Projekten beigetragen. Während sich die ersten Projekte auf anorganische Materialien bezogen, werden im zweiten Teil dieser Arbeit auch organische und organisch-anorganische Verbundmaterialien charakterisiert.

Das erste Projekt befasste sich mit ampholytischen Polymeren. Diese einzigartige Klasse von Polymeren weist eine Wasserstoffbrückenbindungs-Donor- und -Akzeptorgruppe pro Wiederholungseinheit auf und verfügt daher über eine hohe Dichte an funktionellen Gruppen. Vier verschiedene ampholytische Polymere wurden mittels Infrarotspektroskopie und der photoakustischen Methode untersucht. Es wurde nachgewiesen, dass die Wärmeleitfähigkeit mit zunehmender Stärke der Wasserstoffbrückenbindungen im Polymer zunimmt. Aufgrund der funktionellen Gruppen wurden die Eigenschaften der Polymere durch Feuchtigkeit beeinflusst. Die resultierenden Eigenschaften konnten durch Mischungsmodelle gut erklärt werden. Ich unterstützte dieses Projekt, indem ich modulierte DSC-Messungen durchführte, um die Glasübergangstemperaturen der Polymere im feuchten Zustand zu bestimmen.

In den beiden anderen Projekten wurden die anisotropen thermischen Eigenschaften von zweidimensionalen Bragg-Stapeln untersucht. Bragg-Stapel bestehen aus ausgerichteten Nanoplättchen, deren Abmessungen in der Ebene im Mikrometerbereich liegen, während die Dicke in Richtung der Querebene nur wenige Nanometer beträgt.

Als Plättchen wurden Hectorit und Graphenoxid verwendet. Die Wärmeleitfähigkeit in der Ebene war bei beiden Materialien deutlich höher als die Wärmeleitfähigkeit in der Querebene. Die Wärmeleitfähigkeit in der Ebene der Hektoritstapel war höher als die der Graphenoxidstapel. Folglich war das Gesamtanisotropieverhältnis um das 2- bis 3-fache höher. In einer weiterführenden Studie wurden Hektoritplättchen mit Polyvinylpyrrolidon (PVP) mit extremem Polymereinschluss und perfekter Periodizität geschichtet. Zunehmende PVP-Volumenanteile führten zu Basalabständen im Bereich von 1.9 bis 3.8 nm. Der dominierende Einfluss der PVP-Hektorit-Grenzflächen führte zu einem drastischen Rückgang der Wärmeleitfähigkeit über die Ebene von 0.09 W/mK im Vergleich zu den reinen Materialien 0.17 W/mK für PVP und 5.71 W/mK für Hectorit. Ein klassisches paralleles Mischmodell konnte die thermischen Eigenschaften in der Ebene beschreiben, einschließlich Dichte, spezifischer Wärme und Wärmeleitfähigkeit. Insgesamt führte die strukturelle Perfektion dieser Proben zu einer außergewöhnlich hohen Anisotropie der Wärmeleitfähigkeit. Für beide Projekte habe ich alle erforderlichen DSC-Messungen durchgeführt, um die spezifische Wärmekapazität aller Materialien und Verbundstoffe zu bestimmen.

Diese Arbeit zeigt, wie schön es ist, mit kolloidalen Bausteinen zu „spielen“ und so die Zahl der zugänglichen Materialien und Strukturen zu erweitern. Das Verständnis der thermischen Struktur-Eigenschafts-Beziehung hilft bei der Entwicklung maßgeschneiderter Materialien für das Wärmemanagement. In Zukunft könnte diese Forschung dazu beitragen, thermische Herausforderungen zu lösen, z. B. bei Isolationsanwendungen und Wärmesenken in elektronischen Geräten.

List of Publications

My thesis is based on the following publications in peer-reviewed journals:

1. *Scalable Synthesis of Smooth PS@TiO₂ Core-Shell and TiO₂ Hollow Spheres in the (Sub) Micron Size Range: Understanding Synthesis and Calcination Parameters*
Anna M. Lechner (m. Neuhöfer), Tanja Feller, Qimeng Song, Bernd A. F. Kopera, Lukas Heindl, Markus Drechsler, Sabine Rosenfeldt, Markus Retsch
Colloid and Polymer Science, 298 (7), 867-878, 2020
2. *High Temperature Thermal Transport in Porous Silica Materials: Direct Observation of a Switch from Conduction to Radiation*
Anna M. Neuhöfer, Kai Herrmann, Flora Lebeda, Tobias Lauster, Christoph Kathmann, Svend-Age Biehs, Markus Retsch
Advanced Functional Materials, 2108370, 2021
3. *Thermal Transport in Ampholytic Polymers: The Role of Hydrogen Bonding and Water Uptake*
Patrick Hummel, Anna M. Lechner (m. Neuhöfer), Kai Herrmann, Philip Biehl, Carsten Rössel, Lisa Wiedenhöft, Felix H. Schacher, and Markus Retsch
Macromolecules, 53 (13), 5528-5537, 2020
4. *Tunable thermoelastic anisotropy in hybrid Bragg stacks with extreme polymer confinement*
Zuyuan Wang, Konrad Rolle, Theresa Schilling, Patrick Hummel, Alexandra Philipp, Bernd A.F. Kopera, Anna M. Lechner (m. Neuhöfer), Markus Retsch, Josef Breu, George Fytas
Angewandte Chemie Int. Ed., 59 (3), 1286-1294, 2020
5. *Anisotropic Thermal Transport in Spray-Coated Single-Phase Two-Dimensional Materials: Synthetic Clay Versus Graphene Oxide*
Alexandra Philipp, Patrick Hummel, Theresa Schilling, Patrick Feicht, Sabine Rosenfeldt, Michael Ertl, Marius Schöttle, Anna M. Lechner (m. Neuhöfer), Zhen Xu, Chao Gao, Josef Breu, and Markus Retsch
ACS Appl. Mater. Interfaces, 12 (16), 18785-18791, 2020

My thesis also includes the following manuscript:

6. *Thermal Transport Binary Colloidal Glasses*

Anna M. Neuhöfer and Markus Retsch

in preparation

My results from the following, peer-reviewed publication are not included:

7. *Direct Measurement of the In-Plane Thermal Diffusivity of Semitransparent Thin Films by Lock-In Thermography: An Extension of the Slopes Method*

Alexandra Philipp, Nelson W. Pech-May, Bernd A. F. Kopera, Anna M. Lechner

(m. Neuhöfer), Sabine Rosenfeldt, and Markus Retsch

Analytical Chemistry, 91, 8476-8483, 2019

My results from the following manuscript are not included:

8. *Particle Properties of Ellipsoidal Polystyrene Nanoparticles*

Dominik Benke, Tanja Feller, Marcel Krüsmann, Anna M. Neuhöfer, Friederike

Ganster, Matthias Karg and Markus Retsch

in preparation

List of Contributions

During my PhD, I made the following contributions to scientific conferences:

1. Poster presentation: *Synthesis of Well-Controlled Titania Hollow Spheres*, **2019**, Particle Based Materials Symposium, Ulm (DE)
2. Poster presentation: *Synthesis of Well-Controlled Titania Hollow Spheres*, **2019**, DPG Spring Meeting of the Condensed Matter Section, Regensburg (DE)
3. Poster presentaion: *Synthesis of Particle Nested Inverse Structures*, **2017**, Particle Based Materials Symposium, Saarbrücken (DE)

List of Abbreviations

AA	Acrylic acid
AIBA	2,2'-Azobis(isobutyramidine)hydrochloride
AIBN	2,2'-Azobis(isobutyronitril)
BCC	Body-centered-cubic
BSE	Backscattered electrons
CLSM	Confocal laser scanning microscopy
DSC	Differential scanning calorimetry
EtOH	Ethanol
FCC	Face-centered-cubic
FSD	Fourier self-deconvolution
GO	Graphene oxide
HCP	Hexagonal-close-packaging
IR	Infrared
KPS	Potassium peroxydisulfate
LFA	Light flash analysis
MFP	Mean free path
MTC	2-Methacryloxyethyltrimethylammonium chloride
nBA	n Butyl acrylate
PAA	Poly(acrylic acid)
PAGA	Poly(2-acrylamido glycolic acid)
PDha	Polydehydroalanine
PDI	Polydispersity index
PImAA	Poly(2-(imidazol-1-yl)acrylic acid)
PMeImAA	Poly(2-(methyl imidazolium-1-yl)acrylic acid)
PMMA	Poly-methyl methacrylate
PS	Polystyrene
PVP	Polyvinylpyrrolidone
SAXS	Small angle x-ray scattering
SE	Secondary electrons
SEM	Scanning electron microscopy
STA	Scanning thermal analysis

TBT	Titanium (IV) butoxide
TEM	Transmission electron microscopy
TEOS	Tetraethyl orthosilicate
TG	Thermogravimetry
UV	Ultraviolet light
VIS	Visible light
XRD	X-ray diffraction

Introduction

1.1 Motivation

I don't know anyone who never enjoyed playing with interlocking bricks. They have a variety of shapes and colors. It is possible to stack the bricks from a jumbled bunch into an endless number of geometries. In the end, every object has different properties regarding the three-dimensional structure, mechanical stability, color pattern, or functionality.

In the last years, the size of my bricks has been a million times smaller. The shape changed from rectangular to mainly spherical, and instead of different colors, I worked with different materials, like organic polymers and inorganic silica, titania, graphite, and clay. However, the concept stayed the same: The combination of different shapes, sizes, materials, and superstructures, opens up new material properties for various applications.

This thesis focuses on the thermal properties of different nanoscopic materials and their superstructures. Fundamental knowledge about these systems is necessary to improve the thermal management in our everyday life:

- in insulating materials for buildings, automobiles, and aerospace components;

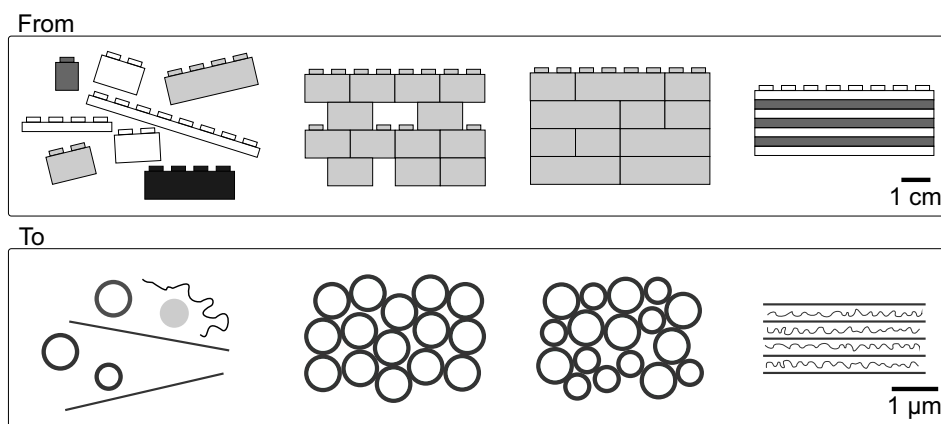


Fig. 1.1: From interlocking bricks in the size range of centimeters to (colloidal) superstructures in the nano- and micrometer size range.

- in thermally conducting materials, used in heat sinks to dissipate waste heat from electronic devices, in (flexible) electronics, and solar cells^[1];
- in materials that can direct the heat flow for more sophisticated applications in information, communication, and energy storage technologies^{[2],[3]}.

For all applications, it is important to find materials that are accessible in sufficient amounts and that have easy processability.

A standard example for highly insulating materials is silica aerogel.^[4] The drawback of this material is the need for a supercritical drying step. Easier manufacturing and the advantage of defined pore sizes is offered by assemblies of hollow silica particles. Since hollow silica particles are stable up to at least 950 °C^[5], the option in high-temperature applications is addressed in this thesis (Chapter 7). Furthermore, the thermal properties of binary assemblies of hollow silica particles are characterized (Chapter 8).

For the thermal management of electronic devices, materials with a high thermal, but low electric conductivity are required. This can be achieved by either adding filler materials to low conducting polymers or by polymer processing. Disadvantages of composite materials are increased material costs and a change in the electrical and optical properties. Polymer processing increases the chain orientation and crystallinity of the polymers and, therefore, the conductivity in one specific direction. For this purpose, special fabrication techniques, like electrospinning and mechanical stretching, are required.^[6] Amorphous polymers with improved interchain interactions have been designed and evaluated in the past years to circumvent these problems.^{[7],[8]} One contribution to this field of research is presented in this thesis. The humidity-dependent thermal conductivity and interchain interactions of several amorphous ampholytic polymers are examined in Chapter 9.

Even more advanced are materials that can direct the flow of heat in a specific direction. This property is provided by two-dimensional materials, like graphene and hexagonal boron nitride. Both materials additionally offer good mechanical flexibility.^[9] So far, synthetic clay was barely noticed in the field of thermal management, despite offering high aspect ratios, outstanding mechanical properties^[10], and a low cross-plane thermal conductivity^[11]. This gap was closed by two publications, shown in this thesis. The first publication examines the thermomechanical properties of hybrid Bragg stacks made of alternating synthetic hectorite and polymer layers (Chapter 10). The second publication compares synthetic hectorite to graphene oxide samples (Chapter 11). Both works reveal the outstanding anisotropy of the thermal conductivity of synthetic hectorite.

The above-mentioned projects show the variety of the interesting thermal properties that can be achieved when “playing” with different materials with dimensions in the nanoscale. This fundamental research may open ways for new materials for thermal management devices in the future.

As the last point, some words about the structure of this thesis. The following section gives a theoretical introduction to the two relevant scientific fields combined in this thesis. On the one hand, colloidal particles and their assemblies and, on the other hand, thermal transport. After the introduction, the synthesis of various organic polymer and inorganic hollow colloids is described in Chapter 2, representing my approach to nanoscale bricks. The three main characterization methods used in this work are discussed in the Methods part (Chapter 3). This is followed by an overview of the six publications included in this thesis and my specific contributions in Chapter 5. The individual publications can be read in Chapters 6 - 11.

1.2 Colloidal Particles & Assemblies

Thomas Graham was the first who used the term *colloid* in 1861 for substances that “are held in solution by a feeble power” and are not able to penetrate membranes.^[12] Today, *colloids* or *colloidal systems* are defined as two-phase systems, where one phase is in the order of 1 nm to 1 μ m and is dispersed in another phase. One has to distinguish between the dispersed (inner) phase and the dispersing (external) phase. Each phase can be gaseous, liquid, and solid, which results in eight possible combinations. Typical examples can be found in nature: clouds (liquid-gas), milk (liquid-liquid), and butter (liquid-solid). Furthermore, colloids are characterized by a large surface-to-volume ratio, which is why their behavior is mainly determined by the interfacial properties. In contrast, gravity and inertia play a subordinate role in colloidal science.^[13]

1.2.1 Materials and Shapes

Colloidal particles and their assemblies can be used for various applications in the fields of fundamental physics, materials science, energy transport, and (bio)sensing.^[14] In 1857, Michael Faraday synthesized the first gold nanoparticles in a scientific way.^[15] Since then, a countless number of different sizes, materials, and shapes have been developed. Figure 1.2 shows some examples of various nanoparticles to give an impression of their variety. The colloids are classified by their materials in inorganic, organic, and composite particles.

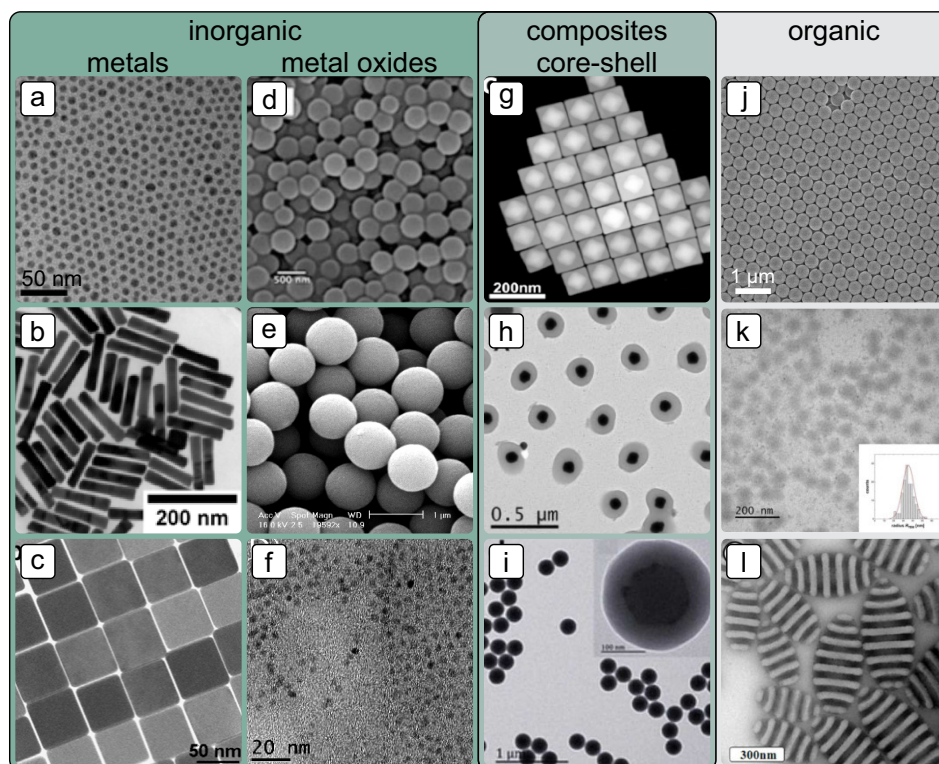


Fig. 1.2: Several nanoparticles exhibiting different materials, shapes, and sizes. a) TEM image of silver particles. Adapted with permission from Hummel *et al.*^[16] Copyright The Authors. b) TEM image of gold rods. Adapted with permission from Tebbe *et al.*^[17] Copyright 2014 American Chemical Society. c) TEM image of silver cubes. Adapted with permission from Yu *et al.*^[18] Copyright 2004 American Chemical Society. d) SEM image of silica particles. Adapted with permission from Gao *et al.*^[19] Copyright 2016 The Authors. e) SEM image of titania particles. Adapted with permission from Eiden-Assmann *et al.*^[20] Copyright 2004 American Chemical Society. f) TEM image of zinc oxide particles. Adapted with permission from Ehlert *et al.*^[21] Copyright 2013 Elsevier. g) SEM image of Au@Ag core-shell cubes. Adapted with permission from Gómez-Graña *et al.*^[22] Copyright 2013 American Chemical Society. h) TEM image of Au@PNIPAM core-shell particles. Adapted with permission from Liz-Marzán *et al.*^[23] Copyright 2008 WILEY-VCH Verlag GmbH & Co. KGaA. i) TEM image of PS@PNIPAM core-shell particles. Adapted with permission from Yuan *et al.*^[24] Copyright 2016 Springer Science Business Media New York. j) SEM image of PS particles. k) TEM image of PNIPAM hydrogel particles. Adapted with permission from Widmann *et al.*^[25] Copyright 2019 American Chemical Society. l) TEM image of Poly(styrene-*b*-2-vinylpyridine) diblock copolymers. Adapted with permission from Jang *et al.*^[26] Copyright 2013 American Chemical Society.

Gold^{[27],[28]} and silver^{[16],[29]} are often used materials for metal colloids. Because of their atomic structure, it is possible to synthesize these particles in different shapes, like rods^{[17],[30]}, wires^{[31],[32]}, and cubes^{[18],[33]}. Silica^{[19],[34]} and titania^{[20],[35]} are the most representative materials for metal-oxide colloids. More examples are copper oxide^[36], cerium oxide^[37], iron oxide, and zinc oxide^{[21],[38],[39]}. These particles are attractive because of their plasmonic and catalytic properties. Furthermore, they are used in the medical field for diagnostic and therapeutic interventions.^[40]

Organic colloids typically consist of polymers and can be divided into hard and soft colloidal particles. Typical hard spheres are made from poly(methyl methacrylate) or polystyrene and could be used for the assembly into colloidal crystals used for optical and thermal applications.^[14] More complex, conjugated polymer particles are used in colloidal crystal lasers.^{[41],[42]} In contrast to the hard particles, soft colloids are nano- or microgels. They are typically made from acrylamide monomers with poly(N-isopropyl acrylamide) (PNIPAM) being the most prominent one, shown in Figure 1.2k. One characteristic of soft colloids is their possibility to respond to external stimuli, like temperature, pressure, pH, and ionic strength. Because of their biocompatibility, the particles could be used for example in sensors, drug delivery applications, and cell and tissue engineering.^{[25],[43],[44]} Another class of organic colloids are association colloids that consist of self-assembled surfactant molecules or block copolymers. Due to microphase separation, lamellar morphologies are created from the different polymer blocks. With this concept, anisotropic particles can be synthesized, which is shown in Figure 1.2l.^{[26],[45]}

Inorganic and organic materials can be combined to tailor the optical, electrical, thermal, mechanical, magnetic, and catalytic properties.^[46] These composites often exhibit core-shell structures, as shown in Figure 1.2g,h,i. There are inorganic-inorganic combinations, such as metal@metal (Cu@Au^[47], Pt@Au^[47], Au@Ag^[22]), metal@metal-oxide (Ag@SiO₂ and Au@SiO₂^{[48]–[50]}), and metal-oxide@metal (SiO₂@Ag, SiO₂@Au, SiO₂@Cu^[51]). Examples for organic-organic combinations are polystyrene cores with PNIPAM^[24] and poly(ethyl acrylate)^[52] shells. To achieve inorganic-organic composites, metals and metal-oxides are coated with different hard and soft polymers.^{[16],[23],[38],[43],[53]–[55]} Organic-inorganic composites are the central material of this thesis. Often PS cores with different functionalities are coated with metal-oxides, like SiO₂^{[56],[57]} and TiO₂^{[58]–[60]}, or metals, like Ag and Au^{[61],[62]}. They can be converted into hollow inorganic particles through removal of the organic core. Classically, the organic core is dissolved or removed by calcination. For SiO₂ and TiO₂, the calcination step additionally promotes the condensation process and therefore increases the cross-linking, which makes the particles resistant to elevated temperatures.

1.2.2 Synthesis of Colloidal Particles

There are two possible ways to obtain colloidal systems: the top-down and the bottom-up approach. As the names imply, the matter is structured from larger to smaller length scales in the physical top-down approach. Typical top-down approaches are the more “crude” methods, like milling and grinding of bulk materials, who offer very little control over particle size, size distribution, and shape. More advanced approaches are the hard-template method, which is used to prepare nanowires, -tubes,

and -rods, the microfluidic particle fabrication, particle stretching, photolithographic or imprint lithography methods, and particle replication in nonwetting templates. By all these methods, a broad variety of different particle shapes, sizes, and surface properties is accessible.^[63] Within this thesis, the bottom-up approach is used. In this approach, particles are fabricated starting from building blocks at the molecular level.^[14]

There are various methods for the bottom-up synthesis of colloidal particles. As shown in Figure 1.2 it is possible to synthesize colloidal particles in different shapes. However, the spherical shape is preferred and driven by the minimization of the interfacial energy.^[46] To achieve different shapes, specific synthetic requirements, like microfluidics, or post-treatments, such as stretching, are needed.^{[64]–[67]} Furthermore, core-shell or hollow particles can be prepared by combining different synthesis methods.

Inorganic particles are typically synthesized by precipitation and sol-gel processing.^[68] The precipitation method involves an (electro-)chemical reduction step of metal cations and leads to metal nanoparticles. Metal-oxides are typically prepared by a sol-gel process, that requires a hydrolysis and condensation step of alkoxide-based precursors. The most prominent one is the Stöber process for the synthesis of silica nanoparticles from the precursor tetraethyl orthosilicate, which was first published in 1968.^[34]

Organic particles are typically synthesized by emulsion, suspension, and dispersion polymerization.^[14] These techniques mainly differ in the solubility of monomer and initiator in the solvent. Emulsion polymerizations can be divided in classical-, mini-, micro-, and emulsifierfree emulsion polymerizations. All have in common that the monomer is insoluble, while the initiator is soluble in the used solvent.^{[69]–[72]} In the suspension polymerization, the initiator is soluble in the monomer, while both – monomer and initiator – are insoluble in the solvent.^[73] Dispersion polymerization is characterized by a solubility of monomer and initiator in the solvent.^[74]

This thesis avails itself of dispersion and emulsifier-free emulsion polymerization for the synthesis of polymer particles in different size ranges and the sol-gel process for the synthesis of silica and titania shells. Therefore, details of the corresponding mechanisms can be found in the Materials section in Chapter 2.

The underlying concept for the synthesis of colloidal particles is a nucleation and growth mechanism. It was first described by LaMer in 1950 and is divided into three steps.^[75] (I) A rapid increase in the concentration of the free monomers in the solution until a certain degree of supersaturation is achieved. (II) Fast nucleation reduces the free monomer concentration in solution significantly, and therefore, stops the

nucleation process. (III) A growth step, that can be either described by the Ostwald ripening, digestive ripening, or coalescent attachment of several nuclei.^{[75]–[78]} The polydispersity index, $\text{PDI}=\sigma/d$, with σ being the standard deviation of the particle size, d , is a measure for the uniformity of the colloidal particles. The dispersity is strongly dependent on the degree of supersaturation in the nucleation phase and the nucleation time.^[76] In order to make colloidal crystals, monodisperse systems with a $\text{PDI}\leq 5\%$ are required.^[79]

1.2.3 Colloidal Assembly

Three-dimensional colloidal assemblies are typically prepared from particle dispersions by increasing the solid volume fraction, ϕ . Already in 1986, Pusey and Megan showed the influence of ϕ on the colloidal superstructure and developed an empiric phase diagram of colloidal dispersions.^[80] Later, more research and calculations have been performed on phase diagrams of the equilibrium liquid and crystalline states^{[79],[81],[82]}, and the non-equilibrium supercooled and glassy states^{[82]–[84]}. Figure 1.3 shows the different phases that a colloidal system can occupy, dependent on ϕ .

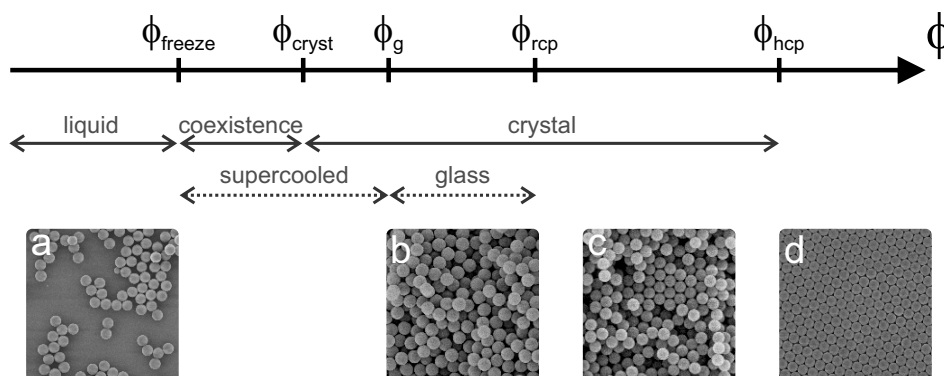


Fig. 1.3: Phase diagram of monodisperse hard spheres as a function of the volume fraction, ϕ , and exemplary SEM images. The solid arrows show the equilibrium stages and the dashed arrows the non-equilibrium states.^[85]

Below the freezing point, ϕ_{freeze} , the dispersion is liquid, above ϕ_{cryst} it is crystallized into stable face-centered-cubic (fcc) or body-centered-cubic (bcc) solids. In between the two phase boundaries a coexisting phase is found.^{[81],[85]} The exact phase boundary values depend strongly on several parameters, like the particle diameter, the repulsive Yukawa pair potential, and the Debye length, which is dependent on the salt concentration and temperature.^{[13],[81]} The upper limit of the solid volume fraction is $\phi_{\text{hcp}} = 0.74$ which is given by the hexagonal-close-packaging of monodisperse particles (Figure 1.3d).

The crystallization process of colloidal particles is not only influenced by ϕ , but it is also strongly influenced by a complex interplay of attractive (e.g. Van der Waals, capillary) and repulsive (e.g. steric, electrical double layer) forces.^[86] However, the nucleation-and-growth process changes with increasing ϕ . Near ϕ_{freeze} , the particle diffusion leads to formation and dissolving of nuclei. When a random nucleus overcomes the free energy barrier and exceeds a critical size, it further grows into a stable crystallite. At higher ϕ , the free energy barrier is reduced or non-existent, leading to the simultaneous nucleation and growth of multiple crystallites.^{[79],[82],[87]}

In order to get supercooled and glassy structures, ϕ has to be increased fast enough to avoid crystallization. The supercooled region lies between ϕ_{freeze} and $\phi_{\text{g}} \approx 0.58$, whereas the glassy region is limited by the random-close-packaging boundary, $\phi_{\text{rcp}} \approx 0.64$ (Figure 1.3b). Above ϕ_{rcp} , the structure must at least exhibit crystalline domains, or ideally be entirely crystallized (Figure 1.3c).

There are various methods for the three-dimensional colloidal assembly into crystalline and glassy structures^[14]:

- Colloidal crystals are achieved by (static) vertical lifting deposition^{[88],[89]}, multilayers^[90], evaporation induced self-assembly^{[91]–[93]}, centrifugation^[94] and doctor blading^{[95],[96]}.
- Colloidal glasses are achieved through mixing of different particle diameters to generate a certain degree of polydispersity ($> 6\%$).^{[85],[97],[98]}
- Both structures can be achieved, using electro deposition^{[99],[100]}, spray deposition^{[101],[102]}, and filtration^{[103]–[105]}. In the last case, especially the speed of the process and the particle density define the resulting structure.

The resulting structures can then be characterized concerning their optical, mechanical, and thermal properties.

1.3 Thermal Transport

Thermal properties is a collective term that describes all material's properties that are functions of temperature or heat. Examples are the thermal conductivity, thermal diffusivity, thermal expansion, heat resistance, specific heat, glass transition and melting temperature.

According to the zeroth law of thermodynamics, two systems that are in a thermal equilibrium state among each other, have one collective property - they have the same temperature. Whenever there is a temperature difference in a medium or between different systems, the systems aim to achieve an equilibrium state. Thereby, the heat is always transferred from the hot to the cold side, which is described by the second law of thermodynamics.^[106]

There are three different types of heat transfer processes: conduction, convection, and radiation. Figure 1.4 illustrates the different types. Conduction refers to heat transfer across a stationary medium, which can be a solid, fluid, or gas. Convection includes a surface and a moving fluid or gas that are at different temperatures. Radiation is the term for electromagnetic waves that are emitted from surfaces of temperatures >0 K. The heat flux q'' [W/m^2] is defined as the energy flow per unit area.^[107]

Hereinafter, conduction and radiation as thermal transport processes are discussed in more detail. Convection of the gas phase does not play a significant role in the thermal properties of colloidal systems, because it is negligible for pore sizes below 4 nm.^{[92],[93],[108]} Therefore, convection will not be discussed in this thesis.

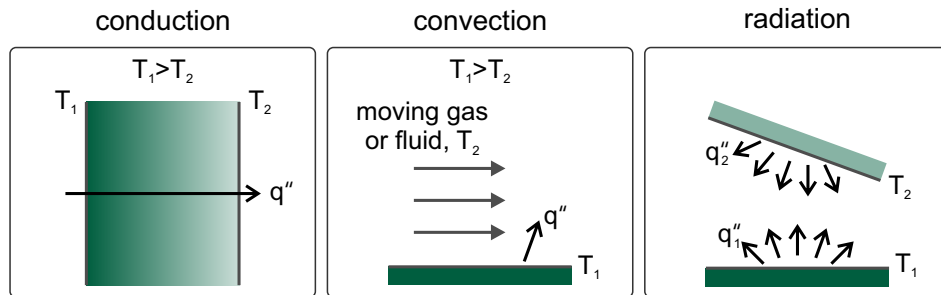


Fig. 1.4: Heat transfer processes: conduction, convection, radiation.^[107]

1.3.1 Physical Fundamentals of Thermal Transport

Conduction

For a conduction process the transfer rate of the heat flux is given by Fourier's law. The most simple case – the one-dimensional heat transport – is shown in Figure 1.4 and is expressed by Equation 1.1. A temperature difference causes a heat transfer in the x direction with the measurable heat rate q_x . The heat flux, q_x'' , is given by the heat transfer rate in the x direction per unit area, A . It is proportional to the temperature gradient dT/dx .

$$q_x'' = \frac{q_x}{A} = -\kappa \frac{dT}{dx}. \quad (1.1)$$

The parameter κ [W/m · K] is the thermal conductivity, a material-dependent transport property. According to Equation 1.1, the conduction heat flux increases with increasing thermal conductivity for a given temperature gradient.^[107]

An other important property in heat transfer analysis is the thermal diffusivity, α , which describes the ability of a material to conduct thermal energy relative to its ability to store thermal energy. The thermal energy storage capability is described by the volumetric heat capacity [J/m³ · K], being the product of density, ρ , and specific heat capacity, c_P . Therefore, the thermal diffusivity is expressed as:

$$\alpha = \frac{\kappa}{\rho \cdot c_P}. \quad (1.2)$$

The larger the thermal diffusivity, the faster is the response to a change in the thermal environment. The smaller the thermal diffusivity, the longer it takes for a material to reach a new equilibrium state.

How do the material properties influence the thermal conductivity? This may be explained by an atomic model. The solid may be described by a lattice of periodically bound atoms and free electrons. Consequently, the thermal energy may be transferred through transport of the electrons and lattice vibrational waves. Described in a quantum mechanical way, lattice vibrational waves are quasi-particles and termed as phonons. Therefore, the thermal conductivity can be expressed by the kinetic theory for both, electrons and phonons:

$$\kappa = \frac{1}{3} C_v \nu \Lambda_{\text{mfp}}, \quad (1.3)$$

where C_v is the electron or phonon specific heat per unit volume, ν is the mean electron or phonon sound velocity, and Λ_{mfp} is the electron or phonon mean free path. The mean free path is a measure for the average distance that is travelled by an electron or phonon between consecutive collisions. With increasing mean free path of the energy carrier, the thermal conductivity increases. Yet, it can be affected by scattering events, that redirect the direction of the energy carrier's propagation. This effect occurs when a particle impinges upon the other particles, imperfections, impurities, grain boundaries, dopants, and material boundaries.^[109] Boundary scattering becomes important when the dimension of the structure is in the size range of the mean free path, like in thin films, polycrystalline, and nanostructured materials.

The thermal conductivity of a solid is composed of the electron and phonon thermal conductivity:

$$\kappa_s = \kappa_e + \kappa_{\text{pho}}. \quad (1.4)$$

According to the Wiedemann-Franz law, κ_e is proportional to the electric conductivity of a material.^[106] In metals that have a high electric conductivity, κ_e is dominating the heat transfer.^[110] In contrast, dielectric materials with high electric resistivities have low contributions of κ_e . In that case, the thermal conductivity is primarily dominated by κ_{pho} , which is dependent on the regularity of the atomic lattice. Therefore, the thermal conductivity of crystalline non-metals is higher than that of amorphous materials, which could be described as crystals with extremely high defect density.^[111]

Figure 1.5 shows the temperature dependence of the thermal conductivities of silver, silicon, and fused silica as exemplary materials for metals, crystalline dielectrics, and amorphous dielectrics, respectively. The thermal conductivity of metals, being κ_e -dominated materials, decreases with increasing temperature. The higher temperature leads to a stronger movement of the core atoms, which increases the number of collisions and therefore decreases the mean free path. In the case of κ_{pho} -dominated materials, one has to distinguish between crystalline and amorphous structures. The temperature-dependent behavior of crystalline, dielectric materials is split into two regimes, with a maximum at $T \approx \Theta_D/10$, with Θ_D being the Debye temperature. Below $\Theta_D/10$, only a few phonon modes are thermally excited. Therefore, scattering events happen rarely, and the mean free path is long. Consequently, the thermal conductivity is dominated by the specific heat of the material. According to Debye's temperature law, the specific heat, and therefore the thermal conductivity, in crystalline materials increases with a scaling law of T^3 for $T < \Theta_D/10$. Above $\Theta_D/10$, the phonon density increases, leading to more phonon-phonon scattering events. As a result, the phonon mean free path gets smaller, and its influence outweighs the impact of the increasing heat capacity, and therefore, the thermal conductivity decreases.^{[112],[113]} The phonon mean free path of amorphous, dielectric structures is very short because of the lack of atomic order. In an extreme case, the mean free path is only limited by the disordered nature of the structure and could be seen as independent of phonon wavelength and density above 270 K. Consequently, the thermal conductivity is proportional to the heat capacity of the material that increases with increasing temperature.^[114]

So far, the focus has been on the thermal properties of solid matter. The following paragraph will discuss the thermal properties of fluids, focusing on the gaseous state. In this case, the intermolecular spacing is larger, leading to a random molecule motion. Therefore, the gaseous thermal conductivity is expressed by the kinetic gas theory:

$$\kappa_g = \frac{1}{3} c_v \rho \nu \Lambda_{\text{mfp}} \quad (1.5)$$

In this case, ν is the mean molecular speed, that is direct proportional to the temperature and indirect proportional to the molecular weight. ρ is the gas density,

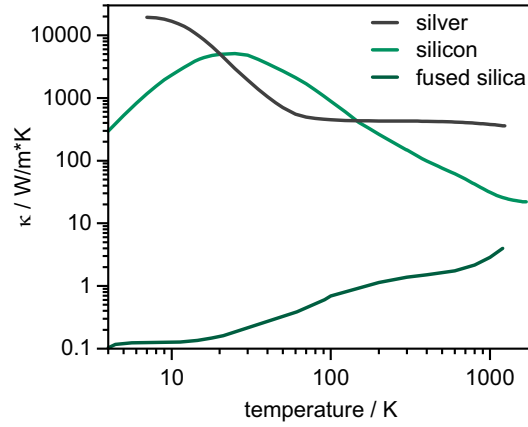


Fig. 1.5: Temperature-dependent thermal conductivities of silver^[115], silicon^[115], and fused silica^{[107],[116]} as examples for metals, crystalline dielectrics, and amorphous dielectrics.

and Λ_{mfp} is the mean free path of the gas molecules. It can be calculated by the Maxwell Equation:

$$\Lambda_{\text{mfp}} = \frac{kT}{\sqrt{2}\pi p d_{\text{gas}}}, \quad (1.6)$$

with the Boltzmann constant, k , and the gas molecule diameter, d_{gas} . In Figure 1.6, the temperature and pressure-dependent mean free paths of nitrogen, helium, and carbon dioxide, as three exemplary gasses, have been calculated. The data illustrates, as follows from Equation 1.6, that Λ_{mfp} is directly proportional to the temperature and indirect proportional to the pressure of the system.^[106]

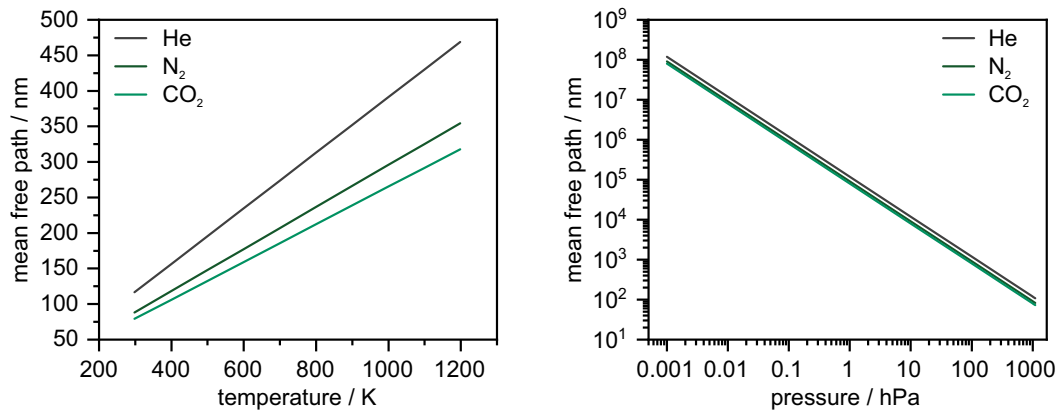


Fig. 1.6: Temperature (@1013 hPa) and pressure (@298.15 K) dependent mean free path of nitrogen, helium, and carbon dioxide.

Λ_{mfp} strongly affects the gaseous thermal conductivity, especially when the dimensions of the system get smaller. The Knudsen number, K_n , is a dimensionless number used to predict the thermal behavior of the gas phase. It is defined as the ratio of the mean free path of the gas and the dimension, d , of the enclosure:

$$K_n = \frac{\Lambda_{\text{mfp}}}{d} \quad (1.7)$$

When $K_n \ll 1$, the thermal conductivity is dominated by molecule-molecule collisions and thus it can be calculated using Equation 1.5. In contrast, when $K_n \gg 1$, the mean free path of the gas molecules is much larger than the dimension of the enclosure. In this case, the thermal conductivity is dominated by molecule-interface collisions. Due to the partial elastic reflection of the gas molecule, less thermal energy is transferred to the interface. Consequently, the thermal conductivity decreases with decreasing enclosure dimensions.^[117]

Radiation

In contrast to heat transfer by conduction, radiation takes place without a temperature gradient and matter transporting the heat. Invariably, it is emitted by all forms of matter that have temperatures above 0 K. It can be described either as propagating particles, termed photons, or as propagating electromagnetic waves. These are generated by oscillations due to the internal energy of matter, which are emitted from the surface. The emissive power, E [W/m²], describes the rate at which energy is released per unit area. It is calculated by the Stefan-Boltzmann law:

$$E = \varepsilon \sigma T^4, \quad (1.8)$$

with T being the surface temperature, σ being the Stefan-Boltzmann constant, and ε being the emissivity. It is the ratio between the radiation emitted by a real surface and the radiation emitted by an ideal blackbody at the same temperature. Consequently, it can have values between $0 \leq \varepsilon \leq 1$. The smaller ε gets, the less efficient is the energy emitted.^[118]

The emitted radiation intensity varies continuously with the wavelength, λ , and is described by the Planck distribution in the case of an ideal blackbody, expressed by

$$I_{\lambda,b}(\lambda, T) = \frac{2hc_0^2}{\lambda^5 [\exp(hc_0/\lambda kT) - 1]}. \quad (1.9)$$

h , and k are the universal Planck and Boltzmann constants, respectively, c_0 is the speed of light in vacuum, and T the surface temperature. Figure 1.7 shows the Planck distributions for several temperatures. Generally, thermal radiation is emitted in the ultraviolet, visible, and infrared region of the wavelength spectrum, more precisely between 0.1 and 100 μm . With increasing surface temperature, the magnitude of the emitted radiation increases and the maximum intensity shifts to shorter wavelengths. The temperature-dependent wavelength of the maximum of the radiative emission can be calculated by

$$\lambda_{\max} = \frac{C}{T} = \frac{2898 \mu\text{mK}}{T}, \quad (1.10)$$

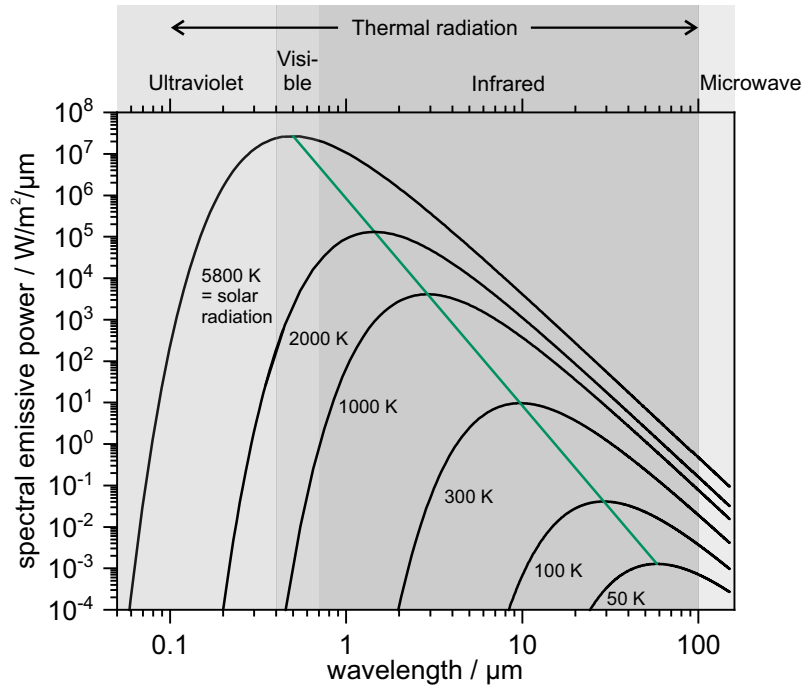


Fig. 1.7: Spectral blackbody emissive power at several temperatures. The shift of λ_{\max} according to the Wien's displacement law is denoted by the green line.^[107]

which is called the Wien's displacement law and denoted by the green line in Figure 1.7. At 5800 K, the surface temperature of the sun, the maximum of the emitted radiation is predominantly in the visible region of the electromagnetic spectrum, whereas at room temperature it is solely in the infrared region.

Besides the spectral effects, the emitted radiation also exhibits a directional distribution. All together, the radiative emission is strongly dependent on the surface material, finish, shape, and temperature.

In the following, the radiative exchange between two surfaces is considered. All surfaces with temperatures above 0 K exchange heat by radiation. For two parallel and ideal blackbody surfaces, the net heat exchange, q , from body 1 to body 2 is given by

$$q = \sigma A_1 (T_1^4 - T_2^4). \quad (1.11)$$

For non-ideal systems, Equation 1.11 has to be extended to

$$q = \sigma A_1 \mathcal{F}_{1-2} (T_1^4 - T_2^4), \quad (1.12)$$

with \mathcal{F}_{1-2} being a factor that is effected by the view factor and the emissivity of the surfaces. Hereby, the view factor takes into account that only a fraction of energy leaving body 1 intercepts with body 2.^[112] This shows that the radiative heat

transfer between two or more surfaces is a complex interplay between the radiative properties of the individual surfaces and their geometries and orientations.

Mixing Models for Hybrid Structures

The effective thermal conductivity of nanostructured materials depends on the composition, the involved interfaces and the mutual orientation of the components. Mixing models have been widely used to estimate the effective thermal conductivity. Up to now, several mixing models have been proposed for different heterogeneous or composite materials. The five basic binary mixing models are shown in Figure 1.8. The parallel and series models take no interfacial thermal resistances into account

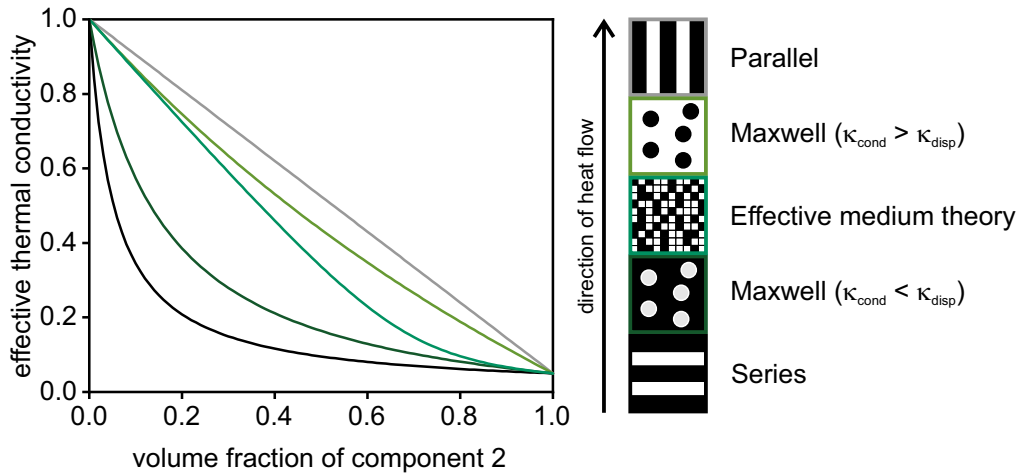


Fig. 1.8: Relative effective thermal conductivities for five basic binary mixing models.^{[119],[120]}

and give the upper and lower bounds for the effective thermal conductivity with regard to the direction of the heat flow. Knowing the thermal conductivities of the single components, $\kappa_{1,2}$, and the volume fraction of component 2, v_2 , the boundary values are provided by:

$$\text{Parallel model: } \kappa_e = (1 - v_2)\kappa_1 + v_2\kappa_2 \quad (1.13)$$

$$\text{Series model: } \kappa_e = \frac{1}{(1 - v_2)/\kappa_1 + v_2/\kappa_2} \quad (1.14)$$

For materials that are macroscopically homogeneous, isotropic and consist of two phases, the Maxwell-Eucken models are applied. In this case, one has to distinguish two cases. When the thermal conductivity of the continuous phase is higher than

that for the dispersed phase, the effective thermal conductivity is close to the parallel model and described by

$$\text{Maxwell-Eucken 1: } \kappa_e = \kappa_1 \cdot \frac{2\kappa_1 + \kappa_2 - 2(\kappa_1 - \kappa_2)v_2}{2\kappa_1 + \kappa_2 + (\kappa_1 - \kappa_2)v_2}. \quad (1.15)$$

When the thermal conductivity of the continuous phase is smaller than that of the dispersed phase, the effective thermal conductivity is expressed by

$$\text{Maxwell-Eucken 2: } \kappa_e = \kappa_2 \cdot \frac{2\kappa_2 + \kappa_1 - 2(\kappa_2 - \kappa_1)(1 - v_2)}{2\kappa_2 + \kappa_1 + (\kappa_2 - \kappa_1)(1 - v_2)}. \quad (1.16)$$

In the case, the two components of a heterogeneous material are randomly distributed, the Effective Medium Theory is applied. It describes a system where no phase is necessarily continuous or dispersed. Depending on the relative amounts, either component may form continuous thermal transport paths.^{[119],[120]}

$$\text{EMT: } \kappa_e = \frac{1}{4} \left((3v_2 - 1)\kappa_2 + (3(1 - v_2) - 1)\kappa_1 + \sqrt{[(3v_2 - 1)\kappa_2 + (3(1 - v_2) - 1)\kappa_1]^2 + 8\kappa_1\kappa_2} \right) \quad (1.17)$$

1.3.2 Thermal Insulation

Thermal insulation is still a big challenge in everyday life, for example in buildings, automobiles, and aerospace components. Since 1931, aerogels have been researched and optimized for thermal applications.^[121] According to the IUPAC definition, aerogel is a “gel comprised of a microporous solid in which the dispersed phase is a gas.”^[122] Typical backbone materials are carbon and silica. Its low thermal conductivity, high melting temperature, and chemical inertness make silica suitable for thermal insulation applications. A further advantage of silica is the natural abundance and the possibility to recycle it after usage. These properties make aerogels superior to conventional insulation materials, like mineral wool and expanded polystyrene. Furthermore, aerogels with thermal conductivities down to 12 mW/mK are more efficient than conventional insulation materials, with thermal conductivities in the range of 30-40 mW/mK. Consequently, less material is needed and the insulation layers get thinner.^[123] However, the fabrication of aerogels needs a supercritical drying step, resulting in high production costs. Furthermore, the material is very fragile and may lead to puncturing.^[124]

Therefore, an emerging field of study is the research on insulation materials based on hollow silica spheres in the sub-micrometer region. Due to the controllability of pore sizes, shell thickness, and superstructures, the determination of structure-property relationships is simplified, compared to aerogel materials. A further advantage is

the easier fabrication that only needs a calcination process to achieve the hollow structure, compared to a supercritical drying step for aerogel fabrication. In 2011, Liao *et al.* determined the thermal conductivity of hollow sphere powders by the 3ω -technique.^[125] Since then, much research has been done by the groups of Tao Gao and Markus Retsch.^{[5],[57],[124],[126],[127]} Both groups published consistent results with thermal conductivities down to 20 mW/mK. The main difference of both groups was the shell structure: while the group of Gao had raspberry-like shells, the group of Retsch worked with smooth, and therefore structurally more well-defined, shells.

In the following, more details of the thermal properties at ambient and high temperatures are discussed for both - aerogel and hollow particle materials. According to Du *et al.*, aerogels have densities between 1 and 1000 kg/m³.^[4] Hollow particle assemblies have densities between 180 and 883 kg/m³.^[57] Therefore, the hollow particle materials can be categorised as high-density aerogels and it can be assumed that the main trends are valid for both materials.

Thermal Transport in Porous Matter and Particulate Systems

Nano-structured, particulate systems and porous matter can be classified as composite materials because they consist of a solid and a gaseous phase. In that case, the total thermal conductivity is determined by the solid and gaseous conduction, and radiation processes.

$$\kappa_{\text{tot}} = \kappa_{\text{solid}} + \kappa_{\text{gas}} + \kappa_{\text{radiation}} \quad (1.18)$$

As mentioned above, convection processes do not play a significant role in pore sizes below 4 mm.^[108] The contribution of radiative heat transfer can also be neglected for temperatures below 50 °C. This was shown experimentally and theoretically by different studies. Herrmann *et al.* compared the thermal conductivities of pure and opacified silica aerogels and did not see a significant difference between the samples at ambient temperatures.^{[128]–[130]} Indeed, a decreasing influence of radiative thermal transport with increasing material density was found.^[131]

At ambient temperatures, solid and gaseous conduction dominate the heat transport.^[132] With decreasing amount of solids in a sample, the thermal conductivity decreases, because the propagation of heat is restricted to the chains in the tenuous structure. Density-dependent thermal conductivity measurements on aerogels with densities between 50 and 250 kg/m³ showed that the solid conduction is proportional to $\rho^{1.6}$.^[133] Furthermore, the solid conduction is determined by the contact points of the nanoparticles that build up the material. In the case of an aerogel, the solid backbone is made of interconnected silica particles with diameters below

10 nm.^{[127],[134],[135]} In contrast, particulate systems consist of particles having 100 times larger diameters. In both cases, the area and amount of the contact points strongly influence the thermal transport. The contact area of particles can be calculated using the Hertz theory. An increase of the thermal conductivity with increasing contact area was shown experimentally in different ways. Ban experimentally compressed particle beds with increasing loading pressures and determined the resulting thermal conductivities.^{[136],[137]} A different approach was applied by Nutz *et al.*, who heated polymer particles above the glass transition temperature to increase the contact area without increasing the number of contact points.^[138] The influence of the number of contact points was shown by Nutz *et al.* A switch from crystalline to disordered structures through binary particle mixtures leads to a decreasing number of next neighbors of a single particle and increasing relative streamline length. Therefore, the thermal conductivity drops with a reduced number of contact points.^[97]

Gaseous conduction takes place in the aerogels' pores or in and between hollow particles. Various groups researched the influence of gas pressure on the thermal transport of these materials. Collectively, increasing thermal conductivities with increasing gas pressures have been found.^{[57],[127],[129],[133],[139]} This is in good agreement with the theory explained in the previous section. With increasing gas pressure, the mean free path decreases, which opens additional diffusion pathways through the gaseous phase (Figure 1.6). Furthermore, the gaseous conductivity is dependent on the gas species and pore size, which has been described in Chapter 1.3.1. The larger the pore size and the smaller the Knudsen number, the more heat is transported via the gaseous phase. This was shown experimentally by Nutz *et al.* who determined the pressure-dependent thermal conductivity of colloidal crystals in air and helium atmosphere. The colloidal structure exhibited pore sizes of 57-151 nm, the mean free path of air and helium are ~ 66 nm and ~ 179 nm. Since the Knudsen number of air was ≤ 1 , the thermal conductivity of air within the pores was almost unaffected by the pore structure. In contrast, for helium the Knudsen number was > 1 and, therefore, the thermal conductivity was reduced by 50 % of its bulk value.^[138] The decreasing thermal conductivity with increasing Knudsen number was also experimentally and theoretically studied by Raed and Gross on ceramic insulation materials with varying pore sizes.^[140]

High Temperature Thermal Insulation

Thermal insulation materials for power plants, manufacturers, and aerospace must be applicable at high operating temperatures. In this case two main influences have to be considered: the gaseous conductivity and thermal radiation.

As follows from Equation 1.5, the gaseous thermal conductivity strongly depends on the temperature since the specific heat, mean molecular speed, and mean free path are temperature-dependent parameters. The temperature-dependent increase of the bulk thermal conductivities of the three gases helium, nitrogen, and carbon dioxide are shown in Figure 1.9. As shown in Figure 1.6, the mean free path strongly increases with increasing temperature. Therefore, the gaseous thermal transport in confined spaces may change from a molecule-molecule-dominated to a molecule-interface-dominated process, leading to a drop in thermal conductivity.

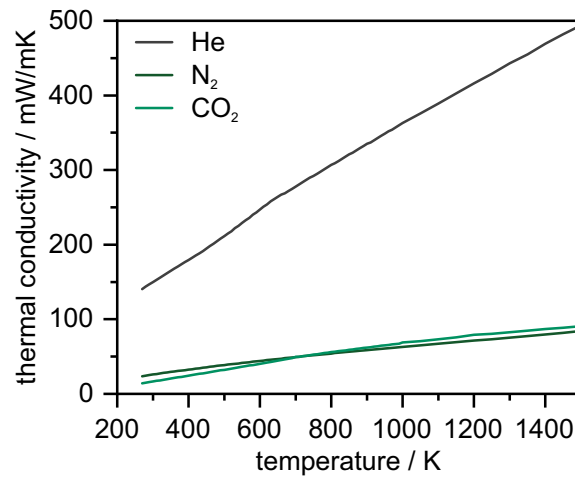


Fig. 1.9: Temperature-dependent thermal conductivities of helium, nitrogen, and carbon dioxide.^[141]

Additionally, increasing temperatures increase the efficiency of heat transport via thermal radiation.^[107] The effect of the temperature on the thermal radiation was shown by Xie *et al.*^[142] While the influence of thermal radiation can be neglected at room-temperature, it becomes the main transport path at temperatures higher than 325 °C. In Figure 1.10 the transmission of bulk borosilicate and quartz glass is shown in comparison to black body irradiance at 25, 325, 525, 725, and 925 °C. It can be clearly seen that the transparent window of the silica glass in the range

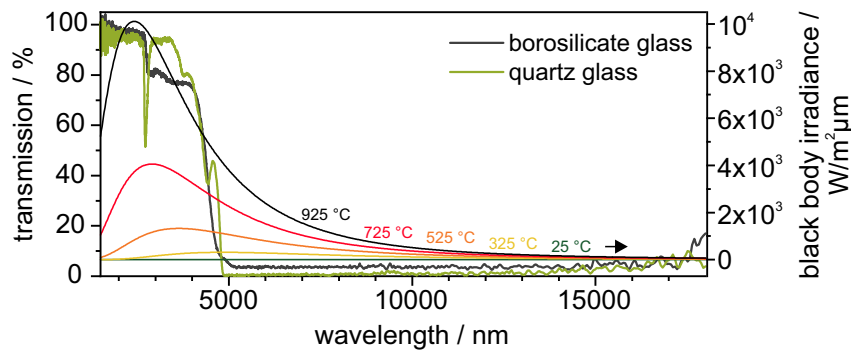
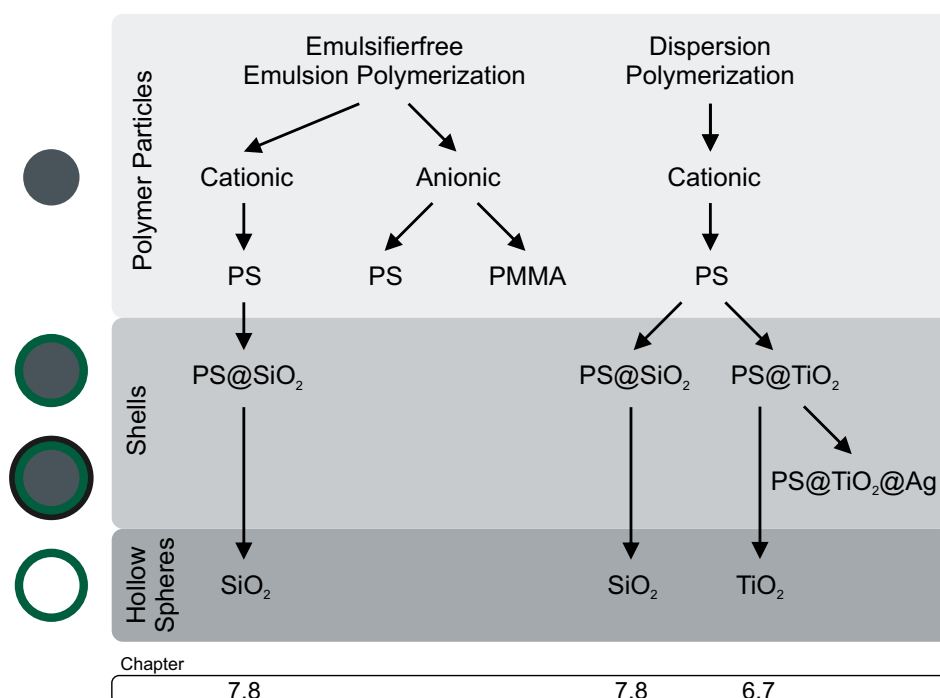


Fig. 1.10: IR transmission data of bulk borosilicate and quartz glass in comparison to black body irradiance. Adapted with permission from Neuhöfer *et al.*^[143] Copyright 2021 The Authors.

of 1-5 μm coincides with the maximum radiation intensity for temperatures above 325 $^{\circ}\text{C}$. The contribution of thermal radiation should be suppressed as much as possible to improve the aerogel's high-temperature insulating performance. This is achieved by the addition of opacifiers, like carbon or mineral dust, such as TiO_2 , SiC , Al_2O_3 , and Fe_3O_4 .^{[133],[142],[144]-[146]}

Materials

In this work, colloidal structures from silica (SiO_2) and titania (TiO_2) hollow particles have been characterized. For the synthesis, polymer template particles have been used. An overview of all different synthesis methods for colloidal particles used in this thesis is shown in Scheme 2.1. Additional materials such as the ampholytic polymers (Chapter 9) and hybrid Bragg stacks (Chapters 10 and 11) have been synthesized by cooperation partners and are not dealt with in detail in this section.



Scheme 2.1: Schematic overview of the the different synthesis methods discussed in the materials part.

For the synthesis of polymer template particles, emulsifier-free emulsion polymerization was used for particle diameters smaller than 600 nm and dispersion polymerization has been used for particle diameters larger than 600 nm up to 2000 nm. Cationic polymer particles have been used for the synthesis of PS@SiO_2 and PS@TiO_2 core-shell and the corresponding hollow spheres. Furthermore, some first attempts have been made to obtain $\text{PS@TiO}_2\text{@Ag}$ structures. In this case, the TiO_2 surface has been utilized to attract the silver to the particle surface. Only a fraction of these synthetic achievements has been included in the publications of this cumulative

thesis. For reasons of completeness, the key synthetic procedures and main results are summarized in the following sub-chapters.

Reagents and Solvents

The following reagents and solvents were used as received: 2,2'-Azobis(isobutyramidine)-hydrochloride (AIBA, Sigma-Aldrich GmbH, 97 %), 2-Methacryloxyethyltrimethylammoniumchloride (MTC, Polyscience, 70 % soln. in water), Acrylic acid (AA, Sigma-Aldrich GmbH, 99 %), Ethanol (Sigma-Aldrich GmbH, ≥ 99.8 %), Polyvinylpyrrolidone K30 (PVP, Alfa Aesar, 55 000 g/mol), Polyvinylpyrrolidone (PVP, Sigma-Aldrich GmbH, 40 000 g/mol), Potassium peroxydisulfate (KPS, ≤ 99 %), Styrene (Sigma-Aldrich GmbH, >99 %), Tetraethyl orthosilicate (TEOS, Sigma-Aldrich GmbH, 98 %), Titanium(IV) butoxide (Sigma-Aldrich GmbH, 97 %), Ammonium hydroxide (Fluka, 30-33 %).

Millipore water was taken from a Millipore Direct Q3UV unit (Merck Millipore) for synthesis and purification.

Methyl methacrylate (MMA, Sigma-Aldrich GmbH, 99 %), and n Butyl acrylate (nBA, Sigma-Aldrich GmbH, ≥ 99 %) were purified by filtration over an alumina column (activated, basic, Brockmann I)

2,2'-Azobis(isobutyronitril) (AIBN, Sigma-Aldrich GmbH) has to be recrystallized before use: ≥ 80 g of AIBN is dissolved in 600 ml of pure methanol at 45 °C. The solution is slowly cooled to room temperature and the resulting crystals were filtrated through a Büchner funnel and washed with methanol. It is dried under vacuum at room temperature.

2.1 Emulsifierfree Emulsion Polymerization

Emulsifierfree emulsion polymerization was used to prepare polystyrene (PS) and poly(methyl methacrylate) (PMMA) particles in the range of 180 nm to 600 nm. The original method was published by Goodwin *et al.*^[72] and advanced by Pia Ruckdeschel for cationic PS particles and Fabian Nutz for anionic PS particles.^{[57],[105],[138]} The synthesis of anionic PMMA and P(MMA-co-nBA) particles has been described by Still *et al.* and Nutz *et al.*^{[147],[148]}

The particles are synthesized by emulsifier-free emulsion polymerization of styrene or MMA in water using the initiator 2,2'-azobis(isobutyramidine)hydrochloride (AIBA)

for cationic particles or potassium persulfate (KPS) for anionic particles. The synthesis consists of several steps that are exemplary shown in Figure 2.1 for cationic particles.

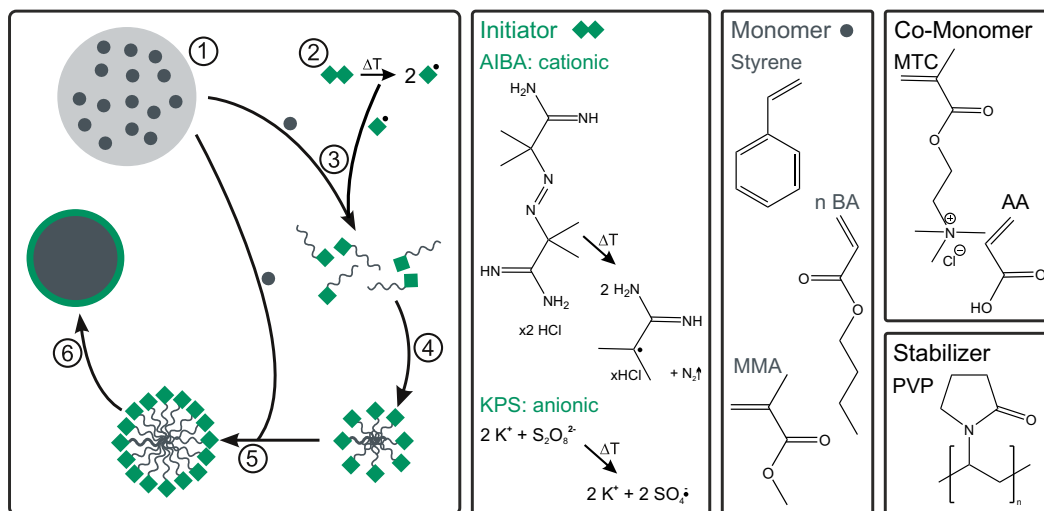


Fig. 2.1: Scheme for the synthesis of cationic polystyrene particles via emulsifier-free emulsion polymerization.^[149]

Monomer droplets emerge through vigorous stirring of the water-insoluble monomer in the water (1). Radicals are generated through homolytic fission of the water-soluble initiator (2). The radicals induce the polymerization with monomer molecules in the aqueous phase (3). When the oligomer chains exceed a certain molecular weight, they become insoluble in water and coagulate into small micelles (4). As polymerization proceeds further, more positively charged initiator radicals are incorporated on the particle surface increasing the electrostatic repulsive forces. Furthermore, the polymer chains in the particles grow by diffusion of the monomer from the droplets in the micelles (5). Finally, stable PS particles are formed (6).^{[150],[151]}

To increase the steric stability of the cationic dispersion, the polymer polyvinylpyrrolidone (PVP) and the positively charged comonomer 2-methacryloxyethyltrimethylammoniumchloride (MTC) is added (Chapter 2.1.1). For anionic particles, the comonomer acrylic acid (AA) or 4-styrenesulfonic acid sodium salt hydrate (PSS) can be added (Chapter 2.1.2). It is also possible to vary the glass transition temperature of PMMA particles by co-polymerization of methyl methacrylate (MMA) with n-butyl acrylate (nBA), which is discussed in Chapter 2.1.3.

2.1.1 Cationic Polystyrene Particles

Experimental Procedure

For the synthesis, 1.8 g PVP (55 000 g/mol) was dissolved in 10 ml water and added to a 500 ml three-neck flask equipped with a gas inlet and reflux condenser. 225 ml water, 26 ml styrene and 50 μ l MTC was added. The emulsion was stirred at a stirring speed of 850 rpm using a large egg-shaped magnetic stirrer bar and heated to 70 °C under a slight argon flow. After 60 min 0.6 g AIBA, dissolved in 5 ml water, was added to initiate the polymerization. After the nucleation, when the color in the flask turned from turbid white to white, the stirring speed was reduced to 450 rpm and the reaction was allowed to continue over night. The polymerization was stopped by exposing the dispersion to ambient air and filtrated using a 125 μ m nylon filter sieve.

Results and Discussion

The size can be adjusted by the amount of MTC that is added, which is shown in Figure 2.2. The particles diameters were plotted against the amount of MTC that was added to the synthesis. Basically, the particle size was supposed to increase with decreasing amount of MTC. Overall this trend was confirmed.

However, it was seen clearly that the size did not only depend on that parameter. For example, particles that are tagged with a * in Figure 2.2.A were in the same size range, but they were produced with different amounts between 0 μ l and 200 μ l of the comonomer. This result might be explained by the fact that the polymerizations depend not only on the inserted amounts of the single components. Instead, external parameters, like the heating and stirring plate and the combination of stirring bar and flask, have an important influence on the nucleation and growth of the particles, too.

2.1.2 Anionic Polystyrene Particles

Experimental Procedure

250 ml water and 30 ml styrene were added to a 500 ml three-neck flask equipped with a gas inlet and reflux condenser. The mixture was stirred at a stirring speed of 850 rpm using a large egg-shaped magnetic stirrer bar and heated to 70 °C or 80 °C

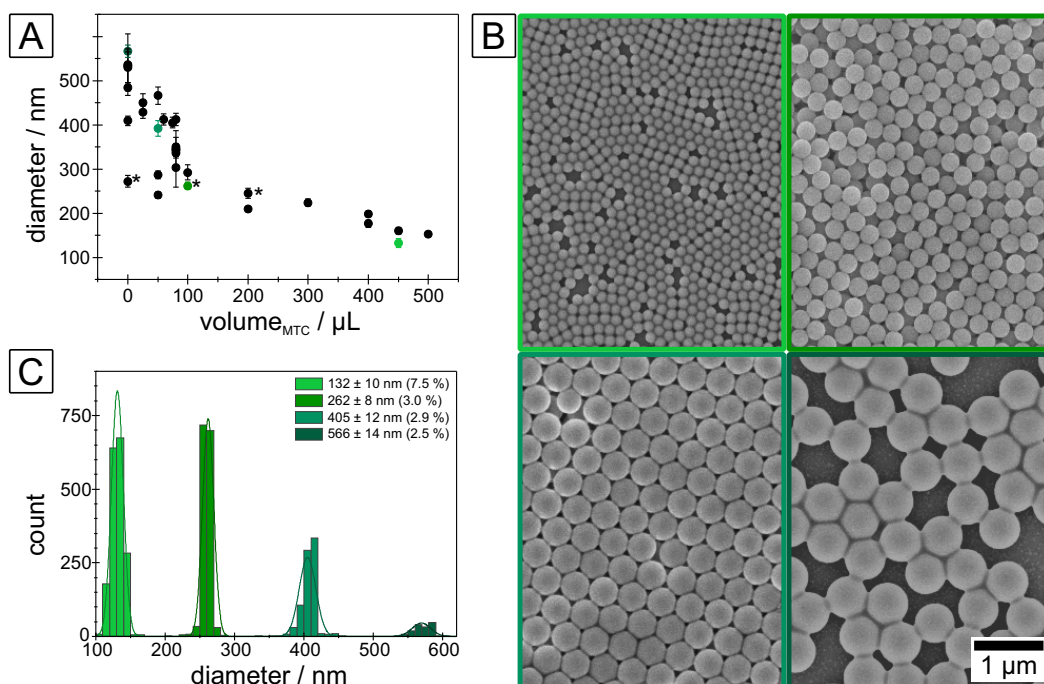


Fig. 2.2: Particle sizes plotted vs. the amount of MTC used for the synthesis (A). The points tagged with a * highlight particles in the same size range but produced with different amounts of MTC. SEM images of four samples with different sizes, adjusted by the amount of MTC (B). Corresponding size-histograms to show the dispersity of the samples (C).

under a slight argon flow. After 60 min 1 ml up to 3.5 ml acrylic acid was added and the emulsion was allowed to stir for another 60 min. 100 mg KPS was dissolved in 5 ml water using the Vortex mixer and added to the mixture. After nucleation, when the color in the flask turned from turbid white to white, the stirring speed was reduced to 450 rpm and the reaction was allowed to continue over night. The polymerization was stopped by exposing the dispersion to ambient air and filtrated using a 125 μm nylon filter sieve.

Results and Discussion

Anionic PS particles that have been synthesized in this thesis are shown in Figure 2.3. To adjust the size of the particles, the amount of acrylic acid, NaCl, and the temperature have been varied, which is shown in table 2.1. Samples A-D show that with an increasing amount of acrylic acid, the particles get smaller. However, shown by samples B and C, the particle size depends also on external parameters, like the heating and stirring plate, the flask, and stirring bar. Both samples had the same ingredients, but the diameter deviates by around 100 nm.

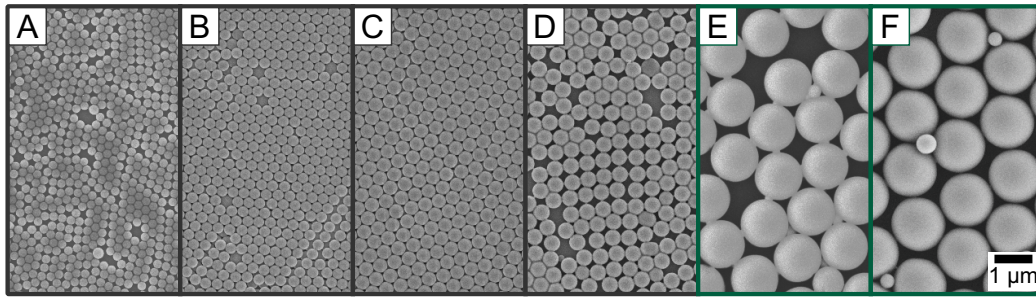


Fig. 2.3: SEM images of anionic PS particles that have been synthesized. The green labelled particles have been synthesized with additional 0.04 mol/l NaCl.

Tab. 2.1: Amount of acrylic acid, V_{AA} , concentration of sodium chloride, c_{NaCl} , and temperature, T , used for the synthesis, and the diameter, d , of the anionic PS particles shown in Figure 2.3.

	V_{AA} / ml	c_{NaCl} / mol/l	T / °C	d / nm
A	3.5	-	80	221 ± 7
B	2	-	70	294 ± 16
C	2	-	70	384 ± 8
D	1	-	70	432 ± 20
E	0	0.04	80	$1306 \pm 31^*$
F	1	0.04	70	$1432 \pm 28^*$

* Without secondary nucleated particles

To increase the particle size above 1 μm , NaCl was added to the reaction, according to Goodwin *et al.*^[72]. Samples E and F with 1.3 and 1.4 μm have been achieved. Sample F, synthesized with acrylic acid is larger than sample E, which contrasts with the particles without NaCl. In this case, the reaction temperature may play a role. The higher the temperature, the smaller get the particles, because of higher decomposition rate of the initiator, which leads to more nuclei. This is also in agreement with Goodwin *et al.*^[72] However, both samples E and F show secondary nucleated particles, that had to be removed by centrifugation before further processing.

2.1.3 Anionic PMMA-nBA Particles

Experimental Procedure

The synthesis of 400 nm particles is described by Nutz *et al.*^[148] In detail, 225 ml water was added to a 500 ml three-neck flask equipped with a gas inlet and reflux condenser. It was heated to 75 °C under a slight argon flow and stirred at a stirring rate of 650 rpm using an egg-shaped magnetic stirrer bar for 15 min. 25 ml of MMA

or a mixture of MMA and n-BA (which was pre-mixed using the Vortex mixer) was added to the water. After another 15 min 2 ml of AA was added. The emulsion was allowed to stir for 5 min. 150 mg KPS was dissolved in 5 ml of water and added to the mixture. Quickly, the beaker was rinsed with water once and the water was also added. The reaction was allowed to continue over night and stopped by exposing the dispersion to ambient air. The dispersion was filtrated using a 125 μm nylon filter sieve. For purification, the particle dispersion was dialyzed against ultrapure water for 5 days, changing the water twice a day.

Results and Discussion

Still *et al.* and Nutz *et al.* already showed that it is possible to tune the glass transition (T_g) of PMMA-nBA particles through the nBA content.^{[147],[148]} Random copolymerization of MMA and nBA in specific ratios leads to T_g between the pure polymers PMMA (125 $^{\circ}\text{C}$) and PnBA (-49°C). Both groups varied the MMA content to be 70, 80, 90, and 100 % and achieved T_g between 54 and 127 $^{\circ}\text{C}$ with differences of around 20 $^{\circ}\text{C}$. I varied the MMA content between 80 and 92.5 % in 2.5 % steps, to get smaller T_g -steps. The result is shown in Figure 2.4. For comparison, the data from Nutz *et al.* was plotted in the graph. It can be seen that my results of the 80 and 90 % MMA-content are in good agreement with the already published data. The T_g of the other MMA-ratios also show a linear dependence. Overall, the T_g was tuned in the range of 75 to 100 $^{\circ}\text{C}$. The results show how finely the T_g can be tuned by adjusting the ratio of MMA and nBA.

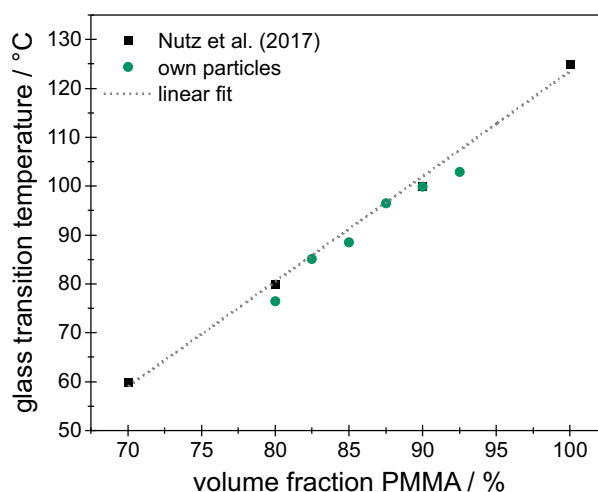


Fig. 2.4: Glass transition temperature of 400 nm particles plotted against the volume percentage of MMA that was used during the synthesis. The black data points have been published by Nutz *et al.*^[148]

2.2 Dispersion Polymerization

The mechanism of dispersion polymerization has been discussed by Barrett and Arshady.^{[152],[153]} Size control in dispersion polymerization is achieved by solvent^{[152],[154],[155]}, and stabilizer selection^{[153]–[155]}, respectively. Cheng *et al.*^[60] used an ethanol/water mixture as solvent and polyvinylpyrrolidone as stabilizer. The dispersion polymerization consists of several steps that are shown in Figure 2.5. Initially, all components (monomer, styrene, and initiator) are soluble in the solvent mixture (1). This is the main difference to an emulsion polymerization, where the monomer is not soluble in the solvent. The second difference is the initiator, which is water-soluble in the case of emulsion polymerization and oil-soluble / non-polar in the dispersion polymerization. The initiator is thermally activated (2) and induces the polymerization of monomer molecules into oligomers (3). The most important step is the formation of particle nuclei, which needs to happen homogenously within the reaction mixture. The increase in molecular weight of the growing polymer chain renders them insoluble in the solvent mixture. The precipitating polymers coagulate into nuclei that become sterically stabilized by the presence of PVP (4). Further addition of monomer can be used to adjust the particle size. The comonomer can be used to introduce a specific surface charge (5). Further polymerization and coagulation happen only in the already formed nuclei that grow to the final particle size, once all monomer and co-monomer are consumed (6).

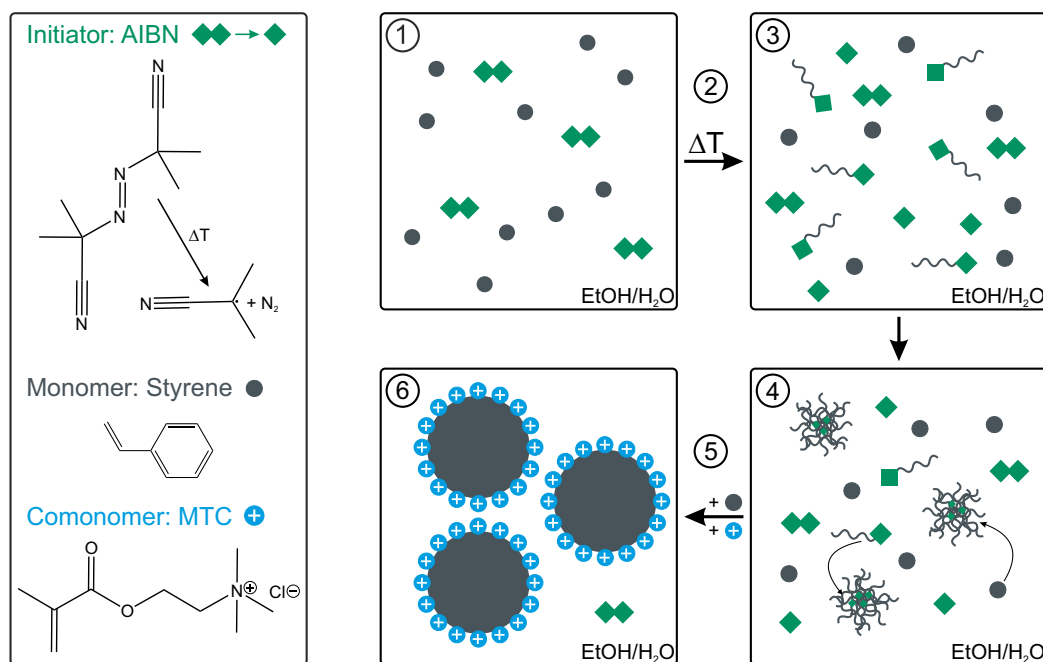


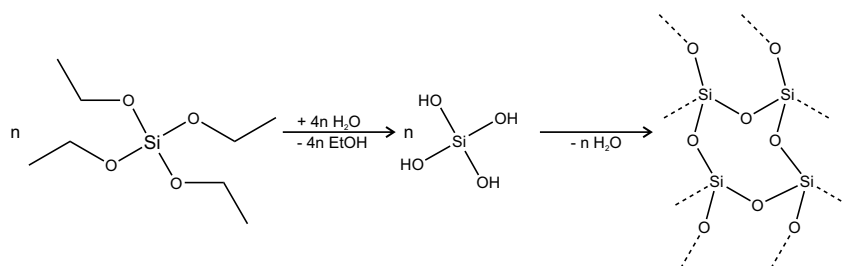
Fig. 2.5: Scheme of the synthesis of cationic polystyrene particles by dispersion polymerization. The stabilizer PVP is not included in the Scheme.

Experimental Procedure, Results and Discussion

The experimental procedure and a detailed discussion of the effect of the individual components on the size and shape of the PS particles can be found in the publication "Scalable synthesis of smooth PS@TiO₂ core-shell and TiO₂ hollow spheres in the (sub) micron size range: understanding synthesis and calcination parameters"^[156] (Chapter 6).

2.3 SiO₂ Shell Synthesis and Hollow Spheres

The cationic PS particles can be used as template for producing PS@SiO₂ core-shell or SiO₂ hollow particles. A modified Stöber process was used for this synthesis.^{[34],[157]} This reaction is based on an ammonia-catalyzed hydrolysis of tetraethylorthosilicate (TEOS) and condensation to SiO₂, which is shown in scheme 2.2. Electrostatic attraction between the positively charged PS particles and TEOS in a basic environment and the steric stabilizer PVP on the PS particle surface result in the growth of the silica directly on the PS surface.^[92] Smooth silica shells on the PS particles' surfaces are obtained.



Scheme 2.2: Scheme of hydrolysis and condensation reaction of TEOS to a silica network

Experimental Procedure

2.5 ml PS particle dispersion was diluted with 17.5 ml ethanol, and 1/10 of TEOS and stirred at 400 rpm at room temperature. After 20 min equilibration time, 1.3 ml NH₃ solution was added. The remaining TEOS was added in nine more steps in time intervals bigger than 15 min and the reaction was stirred at room temperature over night. The particles were centrifuged and washed once with ethanol and three times with Millipore water for purification. For larger yields, the volume could be scaled up to the 100-fold amount.

Hollow SiO₂ particles were fabricated through calcination in air at 500 °C for 12 h.

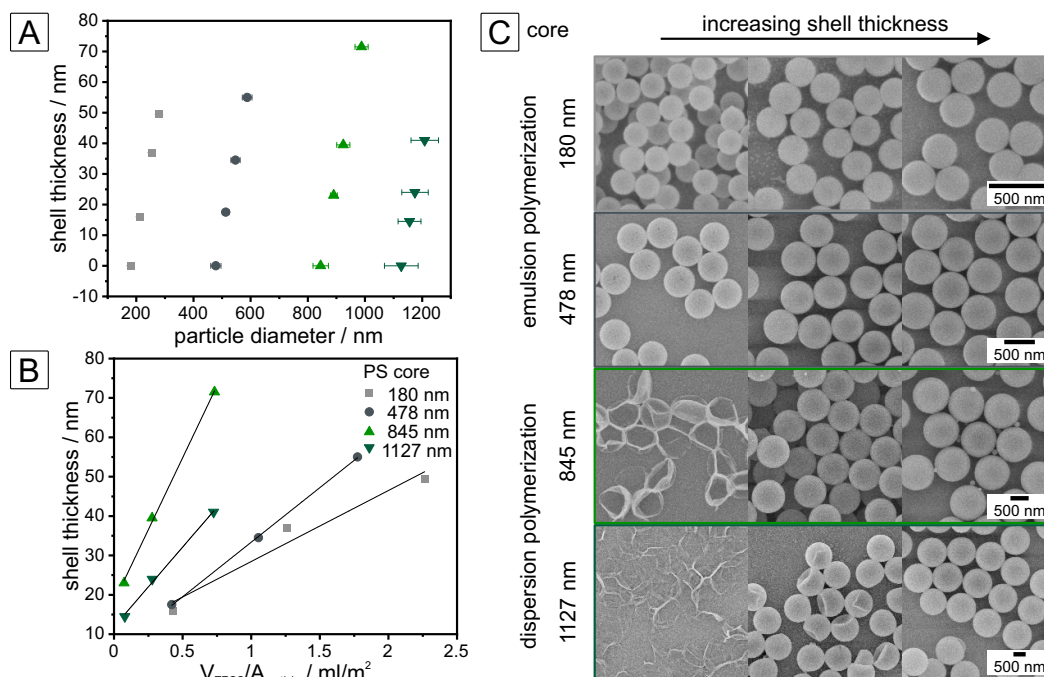


Fig. 2.6: SiO₂ shell thickness series for four different PS template particles with diameters of 180, 478, 845, and 1127 nm. Shell thickness versus particle diameter (A) and versus amount of TEOS per particle surface area (B). SEM images of corresponding hollow particles (C).

Results and Discussion

The Stöber process could be applied to get shell thicknesses from 15 nm up to 70 nm to all sizes of PS template particles, which is shown in Figure 2.6.A. The amount of TEOS, V_{TEOS} , for a certain shell thickness, r_{shell} , had to be calculated previous to the synthesis. Two different approaches were applied, depending on the synthesis of the PS particles. For particles smaller than 600 nm, synthesized via emulsifierfree emulsion polymerization (EP), the shell thickness was approximated with the amount of SiO₂ per particle. Therefore, Equations 2.1 and 2.2 were used.

$$r_{\text{shell},1} = \sqrt[3]{\frac{3}{4\pi} V_{\text{SiO}_2/\text{particle}} + r_{\text{PS}}^3} - r_{\text{PS}} \quad (2.1)$$

$$V_{\text{SiO}_2} = V_{\text{TEOS}} \cdot \frac{\rho_{\text{TEOS}}}{M_{\text{TEOS}}} \frac{M_{\text{SiO}_2}}{\rho_{\text{SiO}_2}} \quad (2.2)$$

With the radius of the core particle, r_{PS} , the volume of silica per particle, $V_{\text{SiO}_2/\text{particle}}$, and density, ρ , and molecular weight, M , of TEOS and silica. The number of particles is calculated from the concentration of the PS dispersion, r_{PS} , and the PS density. For particles larger than 600 nm, synthesized via dispersion polymerization (DP),

an approximation with V_{TEOS} led to better results. Therefore, Equation 2.3 was used.

$$r_{\text{shell},2} = \sqrt[3]{\frac{3}{4\pi} V_{\text{TEOS}/\text{particle}} + r_{\text{PS}}^3} - r_{\text{PS}} \quad (2.3)$$

A comparison of both approaches to the actual shell thickness is shown in table 2.2. For small particles, equation 2.1 led to results closer to the experiment, while for

Tab. 2.2: Shell thickness, r_{shell} , calculated with Equations 2.1 and 2.3, comparison and deviations to experimental results.

Experiment		Theory			
$d_{\text{PS}} / \text{nm}$	$r_{\text{shell}} / \text{nm}$	$r_{\text{shell},1}$	dev1 / %	$r_{\text{shell},2}$	dev2 / %
180	16	10	38	51	219
180	37	25	32	100	170
180	50	39	21	137	177
478	18	11	40	65	271
478	35	25	28	129	273
478	55	39	28	182	230
845	23	2	92	14	38
845	40	7	82	50	26
845	72	18	74	113	59
1127	15	2	86	15	5
1127	24	7	70	51	113
1127	41	18	55	119	189

the 845 nm particles, equation 2.3 led to better results. For the 1127 nm particles, both equations could be applied. In Figure 2.6.B the experimental shell thickness is plotted against the amount of TEOS per particle. Pia Ruckdeschel was able to deduce a correlation between V_{TEOS} and the resulting shell thickness for a narrow PS diameter range between 220 and 414 nm.^[92] For a broad PS diameter range this is not possible anymore. A potential reason for this result is the amount of PVP used for the PS particles synthesis, which is more than three times higher for the dispersion polymerization. Consequently, more PVP may cover the particle surface leading to a decreased SiO_2 density of 1.9 g/cm^3 , compared to 2.1 g/cm^3 for core particles synthesized via emulsifierfree emulsion polymerization. Therefore, less TEOS is needed for particles synthesized via dispersion polymerization to get the same shell thickness as those synthesized via emulsifierfree emulsion polymerization. These results also show that it is always necessary to do pre-experiments to find the right amount of TEOS for the individual PS particles.

Figure 2.6.C shows SEM images of the calcined particles from Figure 2.6.A. All particles have a smooth SiO_2 surface. It can be seen that for bigger particles, thin shells are unstable and collapse during the calcination process. However, with increasing shell thickness it is possible to get stable hollow SiO_2 particles with sizes

up to 1200 nm. Therefore, hollow SiO₂ particles in the broad size range from 180 to 1127 nm were obtained.

2.4 TiO₂ Shell Synthesis and Hollow Spheres

The experimental procedure and a detailed discussion of the structure and stability of the TiO₂ shells and hollow spheres can be found in the publication "Scalable synthesis of smooth PS@TiO₂ core-shell and TiO₂ hollow spheres in the (sub) micron size range: understanding synthesis and calcination parameters" (Chapter 6).

2.5 PS@TiO₂@Ag Core-Shell Particles

Titania-metal nanocomposites are interesting because of two reasons. First, they maximize the efficiency of photocatalytic reactions.^{[158],[159]} Second, they have an increased thermal conductivity compared to polymer nanoparticles. With a sufficient amount of particles, colloidal alloys could be prepared from pure PS and PS@TiO₂@Ag particles and the thermal behaviour could be studied. Furthermore, the TiO₂ surface attracts the metal-salts and less secondary nucleation takes place. Thus, less surface modification of the PS particles is needed. In this thesis, first promising experiments have been performed to get a defined core-shell-shell particle structure.

2.5.1 Experimental Procedure

A modified silver plating method of Mann *et al.* was used for the synthesis of PS@TiO₂@Ag particles.^[61] For the reducing agent, 60 mg glucose, 6 mg tartaric acid, 150 µl ethanol, and 30 ml water were stirred under a slight argon flow at 100 °C in a 50 ml three-neck flask equipped with a gas inlet and reflux condenser. After 2 h, the solution was cooled to room temperature.

For PS@TiO₂@Ag-1 10 mg sodium hydroxide, and 500 µl PS@TiO₂ (10 wt%) were added to 100 ml water in a round-bottom flask. 7 ml of the reducing agent was added, the dispersion was degassed with argon, and stirred at 0 °C in an ice bath. After 15 min, 5 ml of a [Ag(NH₃)₂]⁺ solution, made from 100 mg silver nitrate and ammonium hydroxide (25 %), was added. The dispersion was stirred for 1 h and centrifuged once for purification.

For PS@TiO₂@Ag-2 5 ml of a [Ag(NH₃)₂]⁺ solution, made from 50 mg silver nitrate and ammonium hydroxide (25 %), 10 mg sodium hydroxide, and 500 μl PS@TiO₂ (10 wt%) were added to 100 ml water in a round-bottom flask. The dispersion was degassed, and stirred at 0 °C in an ice bath. After 15 min, 7 ml reducing agent was added. The dispersion was stirred for 1 h and centrifuged once for purification.

2.5.2 Results and Discussion

Two different ways have been chosen for the silver plating. For PS@TiO₂@Ag-1, the [Ag(NH₃)₂]⁺ solution was added to the PS@TiO₂ particle + reducing agent dispersion. For PS@TiO₂@Ag-2, the reducing agent was added to the PS@TiO₂ particle + [Ag(NH₃)₂]⁺ dispersion. Figure 2.7 shows SEM images of the resulting particles. All PS@TiO₂ particles are covered homogeneously with silver nanoparticles and there is no remarkable difference between both synthesis routes. However, no closed shells could be achieved. This may be improved by either adding a second amount of [Ag(NH₃)₂]⁺ solution to the reaction mixture, or doing a second plating step with the cleaned particles. Overall, this method is promising for preparing PS@TiO₂@Ag particles with closed silver shells in the future.

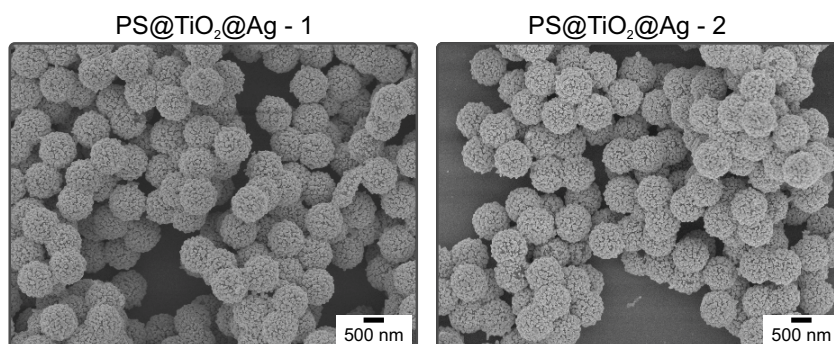


Fig. 2.7: SEM images of PS@TiO₂@Ag core-shell particles.

Methods

Several different characterization methods have been used for this thesis. An overview is shown in Figure 3.1.

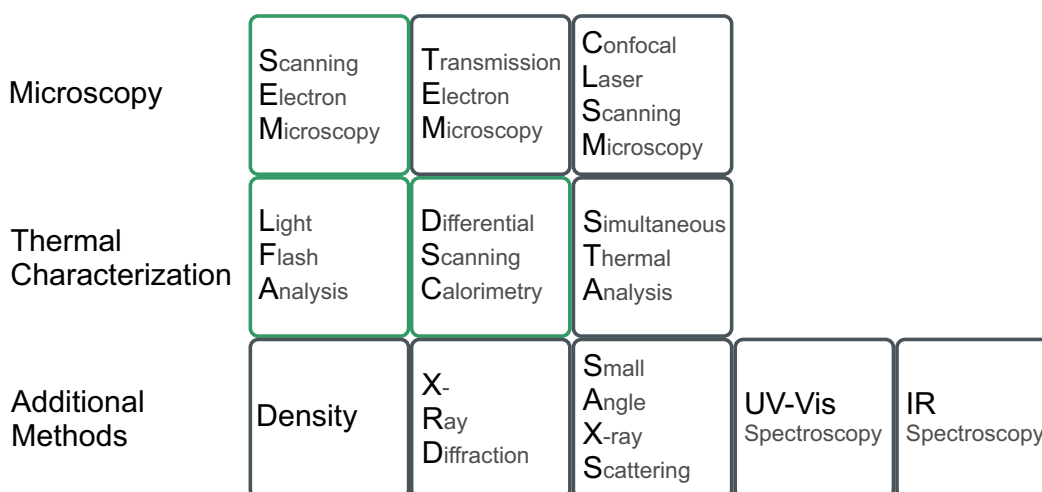


Fig. 3.1: Overview of the different experimental methods that were used for characterization in this thesis. The green highlighted ones SEM, LFA, and DSC are discussed in detail in the methods part.

Microscopy techniques have been used for sample characterization at different preparation steps. Particles (size, shape, dispersity, shell thickness) and particle assemblies were characterized by scanning and transmission electron microscopy (SEM, TEM). Confocal laser scanning microscopy (CLSM) was used for the determination of thickness and volume of disc-shaped colloidal glasses with a diameter of around 10 mm and a thickness of around 1 mm.

Thermal properties have been characterized by light flash analysis (LFA), differential scanning calorimetry (DSC), and simultaneous thermal analysis (STA). The LFA technique was used for the determination of the thermal diffusivity of the samples. DSC was used to evaluate the glass transition and melting temperatures, and the specific heat capacity of different materials. STA was used for measuring combined temperature-dependent thermogravimetry, differential scanning calorimetry, and IR-spectroscopy. This technique was beneficial for high-temperature measurements up to 1000 °C.

Several other methods have been used to complete the sample characterization. The materials density was determined by pycnometry. The specimen density was calculated from the sample mass and volume. X-ray powder diffraction (XRD) was used to characterize the phases of TiO₂ samples. Small-angle X-ray scattering (SAXS) results contributed to structural characterization. UV-Vis and IR-spectroscopy have been used to determine the optical properties of the samples.

Simulations completed the experimental methods to gain further insight into the respective properties. The reconstruction of TEM tomography data provided information about the surface structure and granularity of titania hollow particles. The structure of particle assemblies was calculated by MD simulations, and the mean interparticle distance was determined using the 3D radial distribution function. In collaboration with Age Biehs (Institut für Physik, Carl von Ossietzky Universität, Oldenburg), simulations of transmission spectra and transmission coefficients, heating dynamics, and the influence of coupling surface modes have been made to gain a deeper understanding of the radiative transport through bulk and particulate silica materials.

The three methods SEM, LFA, and DSC, are discussed in detail because of their special relevance for the following chapters. Since SEM was the primary technique for determining the success and quality of all syntheses and assemblies, it is explained in more detail in Chapter 3.1. Understanding the thermal diffusivity and conductivity of colloidal assemblies, especially at high temperatures, was my work's main focus. That is why LFA is outlined as a key technique in Chapter 3.2. With DSC measurements, I contributed to several collaborative research projects. The specific use of this technique is explained in Chapter 3.3.

3.1 Scanning Electron Microscopy

SEM was used to get a visual impression of the nano- and microparticles and their assemblies. Especially for the determination of particle sizes and dispersities, SEM was frequently utilized. As its name implies, it works with electrons instead of light, increasing the microscope's resolution. The resolution of an optical system is defined as the smallest distance, d , between two points that can be distinguished as two separate entities. The resolution is calculated by the Abbe Equation

$$d = \frac{\lambda}{2 \cdot \text{NA}} = \frac{\lambda}{2 \cdot n \cdot \sin(\alpha)} \quad (3.1)$$

with the wavelength of the light, λ and the numerical aperture, NA, that is calculated by the refractive index, n , between the objective and the object, and the half of

the opening angle of the objective, α .^[160] The wavelength of the electrons can be calculated by the De Broglie Equation

$$\lambda = \frac{h}{mv} = \frac{h}{\sqrt{2 \cdot m \cdot e \cdot U}} \quad (3.2)$$

with the Planck constant, h , the mass, m , the speed, v , elementary charge, e , and electric potential, U , of the electron.^{[106],[161]} Thus, the theoretical resolution of an electron microscope at a voltage of 1 kV is 0.019 nm according to Abbe, assuming NA=1. However, the actual resolution is about 1.7 nm, because of three limiting factors: the size of the electron spot, size of interaction volume and lens aberrations.

The SEM works with electrons generated by a field emission cathode and attracted and accelerated by an anode. The electrons pass through a hole in the anode and are focused through condenser lenses. The objective lens focuses the electron beam at a small point of the sample surface. Scan coils affect the electron beam to scan the sample surface.^[162]

There are different ways how the electron beam interacts with the sample. An overview gives Figure 3.2 (left). A SEM is able to detect backscattered electrons (BSE), secondary electrons (SE), Auger electrons and X-rays. A scanning transmission electron detector (STEM) enables additionally the measurement of transmitted electrons. The interaction volume is called electron diffusion cloud (3.2 (right)). Important for the generation of an image are the BSE and SE. The BSE arise from elastic scattering of the electrons at the atomic nucleus. They are emitted from up to 100 nm below the sample surface and are scattered one or more times inside the specimen. The energy of a BSE is comparable to that of a primary electron. SE are generated by an inelastic scattering of the primary electrons at the outer atomic shells. They are separated in three groups: SE1 are generated by the collision of the primary electrons on the sample. SE2 are generated by BSE and SE3 are electrons that are generated by the interaction of BSE with parts of the microscope. All SE electrons have a penetration depth of 10 nm. Electrons that are generated deeper in the sample do not reach the detector anymore.^{[162]–[165]}

Mainly two detectors are used in this thesis. Both attract the electrons with a positive voltage and accelerate them. The electrons produce photons that are amplified in a photomultiplier and converted to a current of electrons. The Everhart-Thornley (SE) detector is mounted laterally on the specimen chamber side and attracts mainly SE, but BSE that randomly reach the detector can also be detected. The Everhart-Thornley detector produces more plastic images than the Inlens detector that is positioned above the optical lens, which leads to a more topographic image.^{[162],[165],[166]}

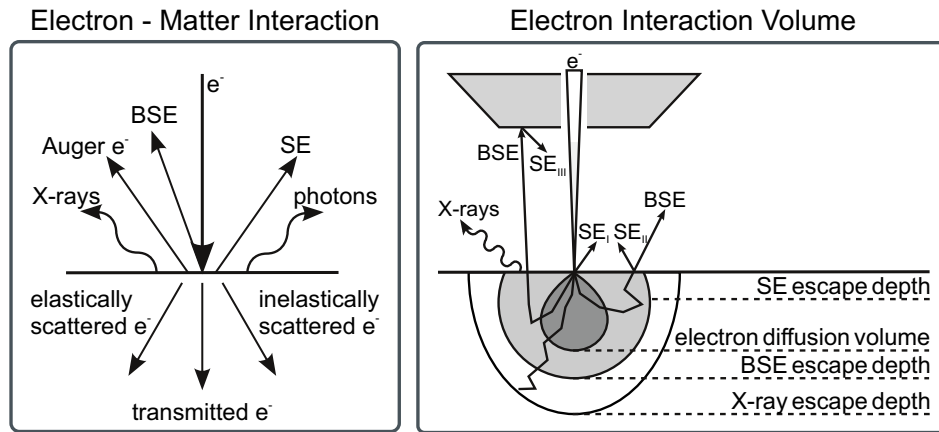


Fig. 3.2: Electron - Matter interaction (left) and electron interaction volume (right) in a SEM.

The measurements were taken on a Zeiss Ultraplus with acceleration voltages between 1 and 3 kV. The particle suspensions were dried on silicon wafers. Colloidal assemblies have been broken into small pieces and clamped into sideview holders. Before measuring, a 1.3 nm platinum layer was sputtered on all samples. To make STEM images, the core-shell particles were dried on SiO₂ TEM grids and calcined at 500 °C before the measurement.

To evaluate the diameter and dispersity of the particles, a Matlab circle detection function was used. For an easier utilization, a graphical user interface, the *Particle Sizer*, was programmed by Bernd Kopera.^[167]

3.2 Light Flash Analysis

LFA measurements were used to determine the thermal diffusivity, α , of the silica and titania hollow and solid samples. The thermal diffusivity is defined as the ability to conduct thermal energy relative to its ability to store thermal energy.^[168] It can be expressed by

$$\alpha = \frac{\kappa}{\rho \cdot c_P} \quad (3.3)$$

with the thermal conductivity, κ , density, ρ , and specific heat capacity, c_P , of a material. This Equation is also used to calculate the thermal conductivity from the LFA measurement results.

The LFA has four main components: a furnace, a flash lamp, a sample, and an IR detector. As systematic setup is shown in Figure 3.3A The sample is positioned in the middle of the furnace that ensures a defined temperature and gas environment. An energy impulse from the flashbulb or laser is absorbed at the sample's bottom and heats up this surface. The heat diffuses through the sample, and the temperature

rise at the top is detected by the IR detector. The thermal diffusivity can be deduced from the time-dependent temperature increase on the top surface (Figure 3.3B).

The method possesses a lot of advantages, like a short measurement time (< 10 sec) and therefore a high throughput, small sample size compared to steady-state methods (e.g., diameters up to 20 cm and several centimeter thicknesses for hot plate method vs. 1 cm diameter and 1 mm thickness for LFA), assessment of temperature-, pressure-, gas composition-dependence, and the option for high-temperature measurements (up to 2800 °C).^[169] It is conspicuous that the advantages are on the experimental side of the method. The challenges arise with the data evaluation.

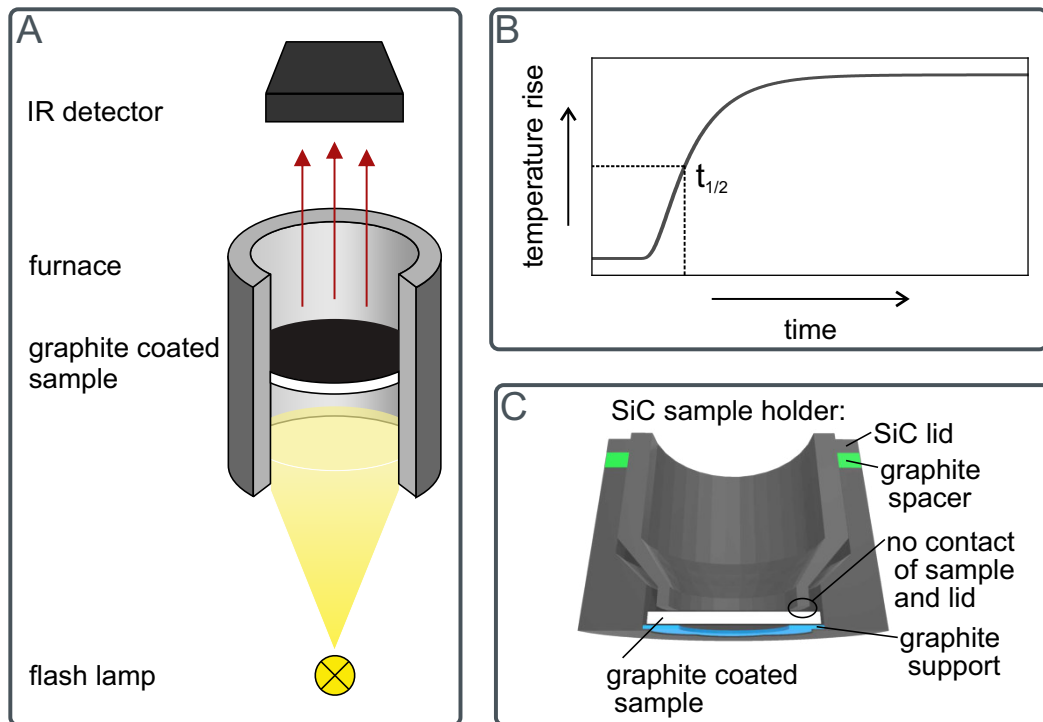


Fig. 3.3: Schematic setup of a LFA instrument (A). Theoretical signal shape LFA measurement of an ideal sample (B). Adapted sample holder for LFA 476 HyperFlash apparatus (Netzsch) (C). Adapted with permission from Neuhöfer et al.^[143] Copyright 2021 The Authors.

Parker *et al.* was the first who developed a model to calculate α from the half rise time, $t_{1/2}$, and the sample thickness, d , of an ideal measurement:

$$\alpha = 1.38 \cdot \frac{d^2}{\pi^2 \cdot t_{1/2}}. \quad (3.4)$$

The preconditions for the applicability of this Equation are a negligibly short and uniform heat pulse, that is uniformly irradiated as well as uniformly absorbed by the full bottom of the sample. Additionally, the sample must be uniform in thickness,

isotropic, and be optically and thermally opaque to block the light flash and prevent radiative heat transfer.^{[169],[170]}

However, LFA samples and measurements take place extreme rarely under ideal conditions. A sketch of heat transfer processes in a (semi-)transparent, colloidal sample is shown in Figure 3.4A. The influence on the corresponding measurement signal is shown in Figure 3.4B. Consequently, Parker's Equation has been enhanced in the last decades. Heat losses arise in almost all non-adiabatic measurements. For an ideal measurement, the temperature increases with time until a plateau is reached (Figure 3.3B). Due to heat losses, the temperature decreases after reaching a maximum. Furthermore, the half-time shifts to shorter times. Cape and Lehman developed a model, that covers these losses due to radiation and convection.^[171] Philipp *et al.* showed, that this model covers also radial losses that happen, when the sample is incompletely excited at the bottom, and facial losses into the sample holder.^[169] Radiation occurs, if the sample is (semi-)transparent to the excitation source or exhibits a porous structure, like (colloidal) silica structures. Furthermore, this effect gets more prominent with increasing temperatures. In this case, the light energy is transmitted directly to the detector. In the measurement signal, this results in a sharp temperature peak at $t \approx 0$ ms and a shift of the half-time to shorter times. Blumm *et al.* extended Parker's model and incorporated these radiation effects.^[172] Another parameter that has to be taken into account is the length and shape of the energy pulse. In the ideal measurement, this pulse would be negligibly short and uniform. Experimental, the pulse has a duration of few milliseconds, and different shapes, like triangular, exponential, and linear-exponential. A correction term for this finite pulse effect was developed by Douza.^{[169],[173]}

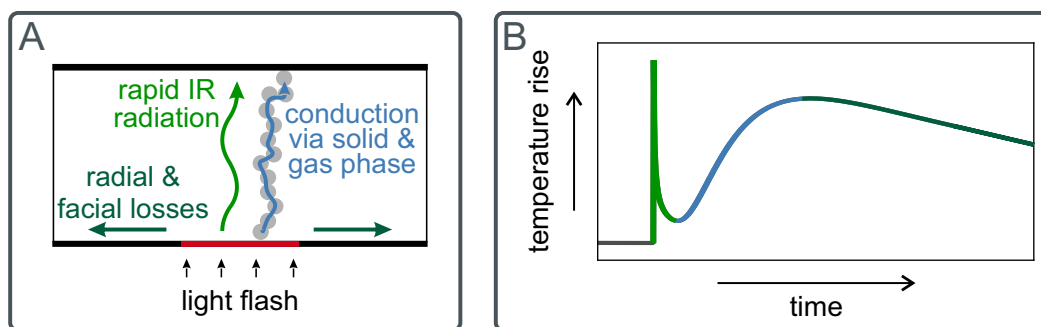


Fig. 3.4: Sketch of heat transfer processes in a (semi-)transparent, coated LFA sample (A) with the corresponding measurement signal in a LFA measurement (B).

The measurements were performed on a LFA 467 HT HyperFlasch apparatus (Netzsch) with a cooled InSb infrared detector and a ZoomOptics system for an optimized detection area of 1.8 mm. This instrument can measure up to 1250 °C in a vacuum and inert gas atmosphere. The samples have to be 10 mm in diameter and a thickness of around 1 mm. For better absorption and emission of the light pulse,

the samples are coated with a thin graphite layer on top and bottom. The sample holder was equipped with a self-made graphite support and spacer (Figure 3.3C) to enable the measurement of not perfectly shaped and fragile colloidal samples.

The thermal conductivity was calculated with Equation 3.3. The sample's thickness and volume have been determined using the Confocal Laser Scanning Microscope LEXT OLS5000-SAF microscope (Olympus). For density determination, the weight of the samples was measured with the micro scales Sartorius Cubis MSE3.6P-000-DM (Sartorius). Specific heat capacity determination is explained in detail in Chapter 3.3.1.

3.3 Differential Scanning Calorimetry

DSC has been widely used in this thesis to determine thermal transitions and the specific heat capacity of many polymeric and inorganic samples. The heart of a DSC is a furnace that is flushed with inert gas during the measurement. In the furnace there is a thermoelectric disk with two integrated heat flux sensors for the sample and reference pans.^[174] During the temperature scan, the heat is transferred from the oven to the pans through the thermoelectric disk. When sample and reference have the same thermal properties the heat flux at both pans are identical and there is no temperature difference. The heat flux from the sample changes, when a chemical reaction or a physical transition, like melting, takes place. This results in a temperature difference between sample and reference pans, which is actually measured. Once the thermal resistance, R , of the thermoelectric disc is known, the heat flux, q , is calculated by:

$$q = \frac{\Delta T}{R} \quad (3.5)$$

The temperature-dependent change of the heat flux contains the information about the chemical or physical changes that happen in the sample.

Up to 450 °C DSC was measured on a Discovery 2500 DSC (TA Instruments). 8 - 20 mg of the sample was weighed in a standard aluminum pan. For samples with lower masses, low mass pans were used. The pan was closed with a non-hermetic lid with a small hole in the middle that allowed evaporation of solvents during the first heating cycle. High temperature measurements up to 1000 °C have been performed on a STA 449 F3 Jupiter (Netzsch), equipped with a DSC/TG OctoS sample holder. As pans PtRh20 crucibles with lids were used. For the determination of glass transition and melting temperatures, typically, a heating rate of 10 K/min has been used. For more advanced techniques, like the specific heat capacity determination

and modulated DSC, different heating rates had to be applied. These techniques are described in more detail in the following two sections.

3.3.1 Specific Heat Capacity

The DSC can be used to determine the specific heat capacity, c_P , that is needed to calculate the thermal conductivity, as described in Chapter 3.2. In general, the specific heat capacity describes how much heat is needed to raise the temperature of 1 g of the sample by one Kelvin.^{[106],[161]} The c_P -determination is standardized by the ASTM E1269 standard.^[175] The heat flow of the sample, H_S , an empty pan, H_e , and a sapphire standard, H_{St} , are measured in the same temperature range with a heating rate $b=20$ K/min. From these measurements, and the literature c_P values of sapphire, $c_P(St)$, and pan, $c_P(c)$, first the calorimetric sensitivity, E , of the DSC machine is calculated:

$$E = \left[\frac{b}{60 \cdot (H_{St} - H_e)} \right] [W_{St} \cdot c_P(St) + \Delta W \cdot c_P(c)] \quad (3.6)$$

With the mass of the sapphire, W_{St} , and the difference in mass between sapphire specimen holder and empty specimen holder, ΔW . The calorimetric sensitivity is now used to calculate the samples' heat capacity, $c_P(S)$.

$$c_P(S) = \frac{60 \cdot E \cdot (H_S - H_e)}{W_S \cdot b} - \frac{\Delta W_S \cdot c_P(c)}{W_S} \quad (3.7)$$

With the mass of the sample, W_S , and the difference in mass between sample pan and empty pan, ΔW_S .

The determination of the specific heat capacity is a quantitative measurement of energy as a function of temperature and therefore requires proper preparation, including the instrument and the samples. The instrument's heat flow and temperature modes must be calibrated before a measurement. Especially the heat flow information is critical because its absolute values are an integral part of the specific heat capacity determination. Ideally, the same specimen holder is used for three required measurements of the empty pan, sapphire standard, and sample. However, this is time-consuming and rarely applicable in everyday life. Therefore, three different specimen holders are used. To minimize measurement inaccuracies, using specimen holders with equal weights is recommended, requiring properly weighed and sorted specimen holder pans and lids.

3.3.2 Modulated Differential Scanning Calorimetry

The standard DSC technique is very powerful for material characterization. However, it has some limitations concerning separation of overlapping processes, and characterization of polymer blends with several different polymers. Furthermore, it is impossible to improve the sensitivity for low energy transitions without decreasing the resolution of a measurement. These disadvantages are eliminated when using modulated DSC (MDSC).

A heat flow signal can be described by the following Equation^{[176],[177]}:

$$\frac{dH}{dt} = C_P \frac{dT}{dt} + f(T, t) \quad (3.8)$$

$\frac{dH}{dt}$ is the total heat flow, which is equivalent to a standard DSC measurement with a linear heating rate. $\frac{dT}{dt}$ is the measured heating rate that has a linear and a modulated component. $C_P \frac{dT}{dt}$ is the reversing heat flow component, while $f(T, t)$ is the non-reversing or kinetic component of the data.

The MDSC technique uses two superimposed heating rates, a linear and a sinusoidal or modulated rate, to split up the measurement signal in the reversing and non-reversing component. Details about the data evaluation are shown in Figure 3.5. The reversing signal carries information about the specific heat capacity and heating rate dependent transitions, like the glass transition and melting temperature. The non-reversing signal carries information about absolute temperature-dependent transitions, like crystallization, relaxation, curing, evaporation, and decomposition processes.

The technique is helpful when overlaying processes take place in one sample. One example is enthalpy relaxation processes that distort the exact glass transition temperature evaluation of a polymer. However, the measurement needs more preliminary tests and knowledge about the sample to choose the right heating rate, temperature amplitude, and modulation period.^[178] Furthermore, the measurements take much longer, since typically heating rates between 0.1 and 5 K/min are applied. For each set of heating rate, temperature amplitude, and modulation period, a calibration measurement with a sapphire standard has to be performed.^[177]

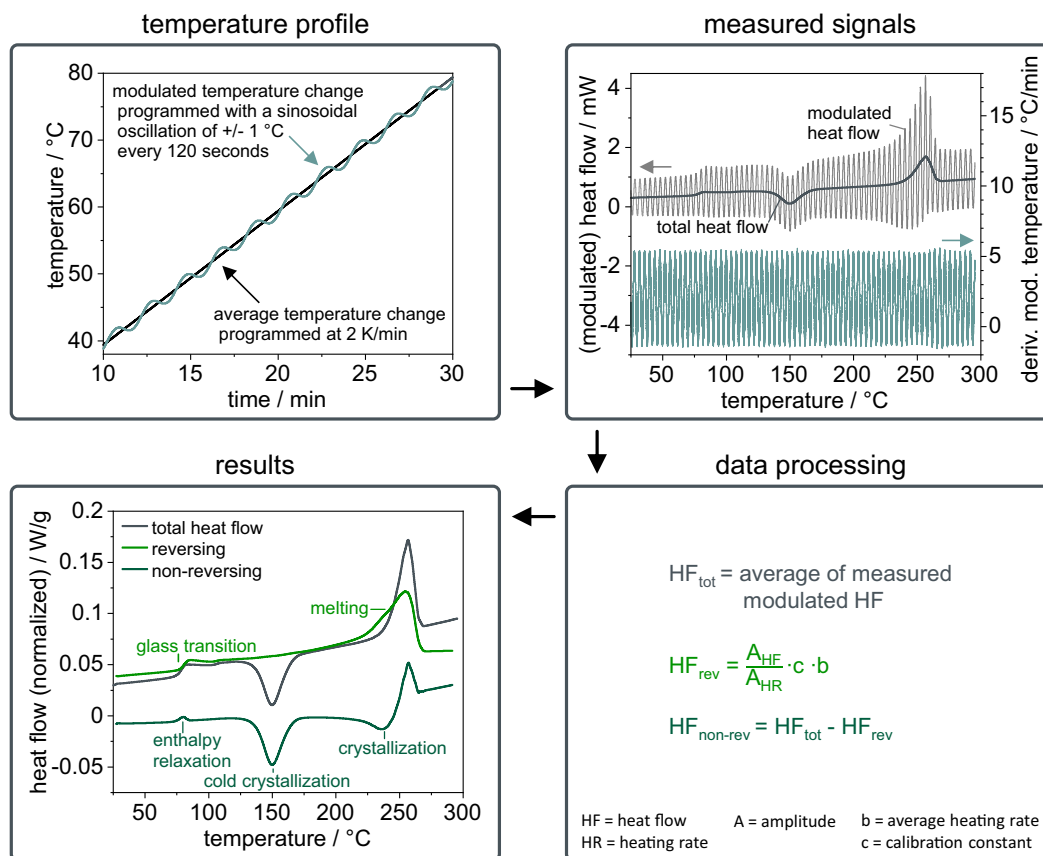


Fig. 3.5: MDSC data evaluation of a PET polymer sample. The temperature profile leads to the modulated heat flow data, which is used for the calculation of the total and reversing heat flow. The difference between both heat flows is the non-reversing part of the data.^[177]

References

- [1] X. Xu, J. Chen, J. Zhou, and B. Li, „Thermal conductivity of polymers and their nanocomposites“, *Advanced Materials*, vol. 30, no. 17, p. 1705544, Mar. 2018.
- [2] M. C. K. Swamy and Satyanarayan, „A review of the performance and characterization of conventional and promising thermal interface materials for electronic package applications“, *Journal of Electronic Materials*, vol. 48, no. 12, pp. 7623–7634, Sep. 2019.
- [3] K. M. F. Shahil and A. A. Balandin, „Graphene–multilayer graphene nanocomposites as highly efficient thermal interface materials“, *Nano Letters*, vol. 12, no. 2, pp. 861–867, Jan. 2012.
- [4] A. Du, B. Zhou, Z. Zhang, and J. Shen, „A special material or a new state of matter: A review and reconsideration of the aerogel“, *Materials*, vol. 6, no. 3, pp. 941–968, Mar. 2013.
- [5] P. Ruckdeschel, T. W. Kemnitzer, F. A. Nutz, J. Senker, and M. Retsch, „Hollow silica sphere colloidal crystals: Insights into calcination dependent thermal transport“, *Nanoscale*, vol. 7, no. 22, pp. 10059–10070, 2015.
- [6] D. R. Anderson, „Thermal conductivity of polymers“, *Chemical Reviews*, vol. 66, no. 6, pp. 677–690, Oct. 1966.
- [7] G.-H. Kim, D. Lee, A. Shanker, *et al.*, „High thermal conductivity in amorphous polymer blends by engineered interchain interactions“, *Nature Materials*, vol. 14, no. 3, pp. 295–300, Nov. 2014.
- [8] X. Xie, D. Li, T.-H. Tsai, *et al.*, „Thermal conductivity, heat capacity, and elastic constants of water-soluble polymers and polymer blends“, *Macromolecules*, vol. 49, no. 3, pp. 972–978, Jan. 2016.
- [9] H. Song, J. Liu, B. Liu, *et al.*, „Two-dimensional materials for thermal management applications“, *Joule*, vol. 2, no. 3, pp. 442–463, Mar. 2018.
- [10] B. Fischer, M. Ziadeh, A. Pfaff, J. Breu, and V. Altstädt, „Impact of large aspect ratio, shear-stiff, mica-like clay on mechanical behaviour of PMMA/clay nanocomposites“, *Polymer*, vol. 53, no. 15, pp. 3230–3237, Jul. 2012.
- [11] M. D. Losego, I. P. Blitz, R. A. Vaia, D. G. Cahill, and P. V. Braun, „Ultralow thermal conductivity in organoclay nanolaminates synthesized via simple self-assembly“, *Nano Letters*, vol. 13, no. 5, pp. 2215–2219, Apr. 2013.

- [12] T. Graham, „X. liquid diffusion applied to analysis“, *Philosophical Transactions of the Royal Society of London*, vol. 151, pp. 183–224, Dec. 1861.
- [13] H.-J. Butt, K. Graf, and M. Kappl, *Physics and Chemistry of Interfaces*. Wiley, Sep. 2003.
- [14] N. Vogel, M. Retsch, C.-A. Fustin, A. del Campo, and U. Jonas, „Advances in colloidal assembly: The design of structure and hierarchy in two and three dimensions“, *Chemical Reviews*, vol. 115, no. 13, pp. 6265–6311, Jun. 2015.
- [15] V. Reddy, „Gold nanoparticles: Synthesis and applications“, *Synlett*, vol. 2006, no. 11, pp. 1791–1792, Jul. 2006.
- [16] P. Hummel, A. Lerch, S. Goller, M. Karg, and M. Retsch, „Simple and high yield synthesis of metal-polymer nanocomposites: The role of theta-centrifugation as an essential purification step“, *Polymers*, vol. 9, no. 12, p. 659, Nov. 2017.
- [17] M. Tebbe, M. Maennel, A. Fery, N. Pazos-Perez, and R. A. Alvarez-Puebla, „Organized solid thin films of gold nanorods with different sizes for surface-enhanced raman scattering applications“, *The Journal of Physical Chemistry C*, vol. 118, no. 48, pp. 28 095–28 100, Nov. 2014.
- [18] D. Yu and V. W.-W. Yam, „Controlled synthesis of monodisperse silver nanocubes in water“, *Journal of the American Chemical Society*, vol. 126, no. 41, pp. 13 200–13 201, Oct. 2004.
- [19] W. Gao, M. Rigout, and H. Owens, „Facile control of silica nanoparticles using a novel solvent varying method for the fabrication of artificial opal photonic crystals“, *Journal of Nanoparticle Research*, vol. 18, no. 12, Dec. 2016.
- [20] S. Eiden-Assmann, J. Widoniak, and G. Maret, „Synthesis and characterization of porous and nonporous monodisperse colloidal TiO₂ particles“, *Chemistry of Materials*, vol. 16, no. 1, pp. 6–11, Dec. 2003.
- [21] S. Ehlert, T. Lunkenbein, J. Brey, and S. Förster, „Facile large-scale synthetic route to monodisperse ZnO nanocrystals“, *Colloids and Surfaces A: Physicochemical and Engineering Aspects*, vol. 444, pp. 76–80, Mar. 2014.
- [22] S. Gómez-Graña, B. Goris, T. Altantzis, *et al.*, „Au@Ag nanoparticles: Halides stabilize {100} facets“, *The Journal of Physical Chemistry Letters*, vol. 4, no. 13, pp. 2209–2216, Jun. 2013.
- [23] R. Contreras-Cáceres, A. Sánchez-Iglesias, M. Karg, *et al.*, „Encapsulation and growth of gold nanoparticles in thermoresponsive microgels“, *Advanced Materials*, vol. 20, no. 9, pp. 1666–1670, May 2008.

- [24] S. Yuan, F. Ge, X. Yang, and S. Guang, „Self-assembly of colloidal photonic crystals of PS@PNIPAM nanoparticles and temperature-responsive tunable fluorescence“, *Journal of Fluorescence*, vol. 26, no. 6, pp. 2303–2310, Oct. 2016.
- [25] T. Widmann, L. P. Kreuzer, N. Hohn, *et al.*, „Hydration and solvent exchange induced swelling and deswelling of homogeneous poly(n-isopropylacrylamide) microgel thin films“, *Langmuir*, vol. 35, no. 49, pp. 16 341–16 352, Nov. 2019.
- [26] S. G. Jang, D. J. Audus, D. Klinger, *et al.*, „Striped, ellipsoidal particles by controlled assembly of diblock copolymers“, *Journal of the American Chemical Society*, vol. 135, no. 17, pp. 6649–6657, Apr. 2013.
- [27] C. D. D. Souza, B. R. Nogueira, and M. E. C. Rostelato, „Review of the methodologies used in the synthesis gold nanoparticles by chemical reduction“, *Journal of Alloys and Compounds*, vol. 798, pp. 714–740, Aug. 2019.
- [28] P. Edwards and J. Thomas, „Gold in a metallic divided state - from faraday to present-day nanoscience“, *Angewandte Chemie International Edition*, vol. 46, no. 29, pp. 5480–5486, Jul. 2007.
- [29] M. Yamamoto, Y. Kashiwagi, and M. Nakamoto, „Size-controlled synthesis of monodispersed silver nanoparticles capped by long-chain alkyl carboxylates from silver carboxylate and tertiary amine“, *Langmuir*, vol. 22, no. 20, pp. 8581–8586, Sep. 2006.
- [30] M. Tebbe, C. Kuttner, M. Männel, A. Fery, and M. Chanana, „Colloidally stable and surfactant-free protein-coated gold nanorods in biological media“, *ACS Applied Materials & Interfaces*, vol. 7, no. 10, pp. 5984–5991, Mar. 2015.
- [31] J.-Q. Hu, Q. Chen, Z.-X. Xie, *et al.*, „A simple and effective route for the synthesis of crystalline silver nanorods and nanowires“, *Advanced Functional Materials*, vol. 14, no. 2, pp. 183–189, Feb. 2004.
- [32] N. R. Jana, L. Gearheart, and C. J. Murphy, „Wet chemical synthesis of silver nanorods and nanowires of controllable aspect ratio“, *Chemical Communications*, no. 7, pp. 617–618, 2001.
- [33] W. Niu, Z.-Y. Li, L. Shi, *et al.*, „Seed-mediated growth of nearly monodisperse palladium nanocubes with controllable sizes“, *Crystal Growth & Design*, vol. 8, no. 12, pp. 4440–4444, Sep. 2008.
- [34] W. Stöber, A. Fink, and E. Bohn, „Controlled growth of monodisperse silica spheres in the micron size range“, *Journal of Colloid and Interface Science*, vol. 26, no. 1, pp. 62–69, Jan. 1968.
- [35] C. Han, R. Luque, and D. D. Dionysiou, „Facile preparation of controllable size monodisperse anatase titania nanoparticles“, *Chem. Commun.*, vol. 48, no. 13, pp. 1860–1862, 2012.

- [36] L. Gou and C. J. Murphy, „Solution-phase synthesis of Cu₂O nanocubes“, *Nano Letters*, vol. 3, no. 2, pp. 231–234, Feb. 2003.
- [37] S. Yang and L. Gao, „Controlled synthesis and self-assembly of CeO₂ nanocubes“, *Journal of the American Chemical Society*, vol. 128, no. 29, pp. 9330–9331, Jul. 2006.
- [38] V. B. Leffler, L. Mayr, P. Paciok, *et al.*, „Controlled assembly of block copolymer coated nanoparticles in 2D arrays“, *Angewandte Chemie*, May 2019.
- [39] K. Shen, Y. Wang, and Y. Li, „One-pot synthesis of shape-controlled Fe₃O₄ nanocrystals with alkylsulfonylacetic acid“, *Chemistry Letters*, vol. 42, no. 5, pp. 479–480, May 2013.
- [40] R. Augustine, A. P. Mathew, and A. Sosnik, „Metal oxide nanoparticles as versatile therapeutic agents modulating cell signaling pathways: Linking nanotechnology with molecular medicine“, *Applied Materials Today*, vol. 7, pp. 91–103, 2017.
- [41] A. Mikosch, S. Ciftci, and A. J. C. Kuehne, „Colloidal crystal lasers from monodisperse conjugated polymer particles via bottom-up coassembly in a sol–gel matrix“, *ACS Nano*, vol. 10, no. 11, pp. 10 195–10 201, Oct. 2016.
- [42] A. J. Kuehne, M. C. Gather, and J. Sprakel, „Monodisperse conjugated polymer particles by suzuki–miyaura dispersion polymerization“, *Nature Communications*, vol. 3, no. 1, Jan. 2012.
- [43] M. Karg, A. Pich, T. Hellweg, *et al.*, „Nanogels and microgels: From model colloids to applications, recent developments, and future trends“, *Langmuir*, vol. 35, no. 19, pp. 6231–6255, Apr. 2019.
- [44] F. A. Plamper and W. Richtering, „Functional microgels and microgel systems“, *Accounts of Chemical Research*, vol. 50, no. 2, pp. 131–140, Feb. 2017.
- [45] C. K. Wong, X. Qiang, A. H. Müller, and A. H. Gröschel, „Self-assembly of block copolymers into internally ordered microparticles“, *Progress in Polymer Science*, vol. 102, p. 101 211, Mar. 2020.
- [46] Y. Xia, H. Fudouzi, Y. Lu, and Y. Yin, „Colloidal crystals: Recent developments and niche applications“, in *Colloids and Colloid Assemblies*, Wiley-VCH Verlag GmbH & Co. KGaA, pp. 284–316.
- [47] L. Chen, A. Leonardi, J. Chen, *et al.*, „Imaging the kinetics of anisotropic dissolution of bimetallic core–shell nanocubes using graphene liquid cells“, *Nature Communications*, vol. 11, no. 1, Jun. 2020.
- [48] H. Baida, P. Billaud, S. Marhaba, *et al.*, „Quantitative determination of the size dependence of surface plasmon resonance damping in single Ag@SiO₂ nanoparticles“, *Nano Letters*, vol. 9, no. 10, pp. 3463–3469, Aug. 2009.

- [49] J. L. Montaña-Priede, O. Peña-Rodríguez, and U. Pal, „Near-electric-field tuned plasmonic Au@SiO₂ and Ag@SiO₂ nanoparticles for efficient utilization in luminescence enhancement and surface-enhanced spectroscopy“, *The Journal of Physical Chemistry C*, vol. 121, no. 41, pp. 23 062–23 071, Oct. 2017.
- [50] J. Montaña-Priede, J. P. Coelho, A. Guerrero-Martínez, O. Peña-Rodríguez, and U. Pal, „Fabrication of monodispersed Au@SiO₂ nanoparticles with highly stable silica layers by ultrasound-assisted Stöber method“, *The Journal of Physical Chemistry C*, vol. 121, no. 17, pp. 9543–9551, Apr. 2017.
- [51] B. Jankiewicz, D. Jamiola, J. Choma, and M. Jaroniec, „Silica–metal core–shell nanostructures“, *Advances in Colloid and Interface Science*, vol. 170, no. 1-2, pp. 28–47, Jan. 2012.
- [52] M. Gallei, „Functional polymer opals and porous materials by shear-induced assembly of tailor-made particles“, *Macromolecular Rapid Communications*, vol. 39, no. 4, p. 1 700 648, Dec. 2017.
- [53] M. Karg and T. Hellweg, „New “smart” poly(NIPAM) microgels and nanoparticle microgel hybrids: Properties and advances in characterisation“, *Current Opinion in Colloid & Interface Science*, vol. 14, no. 6, pp. 438–450, Dec. 2009.
- [54] K. Volk, J. P. S. Fitzgerald, M. Retsch, and M. Karg, „Time-controlled colloidal superstructures: Long-range plasmon resonance coupling in particle monolayers“, *Advanced Materials*, vol. 27, no. 45, pp. 7332–7337, Oct. 2015.
- [55] C. G. Schäfer, T. Winter, S. Heidt, *et al.*, „Smart polymer inverse-opal photonic crystal films by melt-shear organization for hybrid core–shell architectures“, *Journal of Materials Chemistry C*, vol. 3, no. 10, pp. 2204–2214, 2015.
- [56] C. Graf, D. L. J. Vossen, A. Imhof, and A. van Blaaderen, „A general method to coat colloidal particles with silica“, *Langmuir*, vol. 19, no. 17, pp. 6693–6700, Aug. 2003.
- [57] P. Ruckdeschel and M. Retsch, „Interface and morphology control of the thermal conductivity in core-shell particle colloidal crystals“, *Advanced Materials Interfaces*, vol. 4, no. 24, p. 1 700 963, Nov. 2017.
- [58] A. Imhof, „Preparation and characterization of titania-coated polystyrene spheres and hollow titania shells“, *Langmuir*, vol. 17, no. 12, pp. 3579–3585, Jun. 2001.
- [59] P. Wang, D. Chen, and F.-Q. Tang, „Preparation of titania-coated polystyrene particles in mixed solvents by ammonia catalysis“, *Langmuir*, vol. 22, no. 10, pp. 4832–4835, May 2006.

- [60] X. Cheng, M. Chen, L. Wu, and G. Gu, „Novel and facile method for the preparation of monodispersed titania hollow spheres“, *Langmuir*, vol. 22, no. 8, pp. 3858–3863, Mar. 2006.
- [61] D. Mann, D. Nascimento-Duplat, H. Keul, *et al.*, „The influence of particle size distribution and shell imperfections on the plasmon resonance of Au and Ag nanoshells“, *Plasmonics*, vol. 12, no. 3, pp. 929–945, Aug. 2016.
- [62] D. Mann, S. Chattopadhyay, S. Pargen, *et al.*, „Glucose-functionalized polystyrene particles designed for selective deposition of silver on the surface“, *RSC Adv.*, vol. 4, no. 108, pp. 62 878–62 881, Nov. 2014.
- [63] T. J. Merkel, K. P. Herlihy, J. Nunes, *et al.*, „Scalable, shape-specific, top-down fabrication methods for the synthesis of engineered colloidal particles“, *Langmuir*, vol. 26, no. 16, pp. 13 086–13 096, Aug. 2010.
- [64] E. Matijevic, „Preparation and properties of uniform size colloids“, *Chemistry of Materials*, vol. 5, no. 4, pp. 412–426, Apr. 1993.
- [65] S. Guha and A. B. Jindal, „An insight into obtaining of non-spherical particles by mechanical stretching of micro- and nanospheres“, *Journal of Drug Delivery Science and Technology*, vol. 59, p. 101 860, Oct. 2020.
- [66] Y.-C. Lo, Y.-J. Chiu, H.-F. Tseng, and J.-T. Chen, „Thermal-annealing-induced self-stretching: Fabrication of anisotropic polymer particles on polymer films“, *Langmuir*, vol. 33, no. 43, pp. 12 300–12 305, Oct. 2017.
- [67] S. Xu, Z. Nie, M. Seo, *et al.*, „Generation of monodisperse particles by using microfluidics: Control over size, shape, and composition“, *Angewandte Chemie*, vol. 117, no. 5, pp. 734–738, Jan. 2005.
- [68] B. L. Cushing, V. L. Kolesnichenko, and C. J. O’Connor, „Recent advances in the liquid-phase syntheses of inorganic nanoparticles“, *Chemical Reviews*, vol. 104, no. 9, pp. 3893–3946, Aug. 2004.
- [69] W. D. Harkins, „A general theory of the mechanism of emulsion polymerization“, *Journal of the American Chemical Society*, vol. 69, no. 6, pp. 1428–1444, Jun. 1947.
- [70] K. Landfester, N. Bechthold, F. Tiarks, and M. Antonietti, „Formulation and stability mechanisms of polymerizable miniemulsions“, *Macromolecules*, vol. 32, no. 16, pp. 5222–5228, 1999.
- [71] J. S. Guo, M. S. El-Aasser, and J. W. Vanderhoff, „Microemulsion polymerization of styrene“, *Journal of Polymer Science Part A: Polymer Chemistry*, vol. 27, no. 2, pp. 691–710, Jan. 1989.
- [72] J. W. Goodwin, J. Hearn, C. C. Ho, and R. H. Ottewill, „Studies on the preparation and characterisation of monodisperse polystyrene latices“, *Colloid and Polymer Science*, vol. 252, no. 6, pp. 464–471, Jun. 1974.

- [73] W. P. Hohenstein and H. Mark, „Polymerization of olefins and diolefins in suspension and emulsion. Part I.“, *Journal of Polymer Science*, vol. 1, no. 2, pp. 127–145, Mar. 1946.
- [74] C. M. Tseng, Y. Y. Lu, M. S. El-Aasser, and J. W. Vanderhoff, „Uniform polymer particles by dispersion polymerization in alcohol“, *Journal of Polymer Science Part A: Polymer Chemistry*, vol. 24, no. 11, pp. 2995–3007, Nov. 1986.
- [75] V. K. LaMer and R. H. Dinegar, „Theory, production and mechanism of formation of monodispersed hydrosols“, *Journal of the American Chemical Society*, vol. 72, no. 11, pp. 4847–4854, Nov. 1950.
- [76] N. T. K. Thanh, N. Maclean, and S. Mahiddine, „Mechanisms of nucleation and growth of nanoparticles in solution“, *Chemical Reviews*, vol. 114, no. 15, pp. 7610–7630, Jul. 2014.
- [77] W. Ostwald, „Über die vermeintliche Isomerie des roten und gelben Quecksilberoxyds und die Oberflächenspannung fester Körper“, *Zeitschrift für Physikalische Chemie*, vol. 34U, no. 1, pp. 495–503, Jul. 1900.
- [78] W.-r. Lee, M. G. Kim, J.-r. Choi, *et al.*, „Redox-transmetalation process as a generalized synthetic strategy for core-shell magnetic nanoparticles“, *Journal of the American Chemical Society*, vol. 127, no. 46, pp. 16 090–16 097, Nov. 2005.
- [79] E. Zaccarelli, C. Valeriani, E. Sanz, *et al.*, „Crystallization of hard-sphere glasses“, *Physical Review Letters*, vol. 103, no. 13, Sep. 2009.
- [80] P. N. Pusey and W. van Megen, „Phase behaviour of concentrated suspensions of nearly hard colloidal spheres“, *Nature*, vol. 320, no. 6060, pp. 340–342, Mar. 1986.
- [81] A.-P. Hynninen and M. Dijkstra, „Phase diagrams of hard-core repulsive yukawa particles“, *Physical Review E*, vol. 68, no. 2, Aug. 2003.
- [82] P. N. Pusey, E. Zaccarelli, C. Valeriani, *et al.*, „Hard spheres: Crystallization and glass formation“, *Philosophical Transactions of the Royal Society A: Mathematical, Physical and Engineering Sciences*, vol. 367, no. 1909, pp. 4993–5011, Dec. 2009.
- [83] S. Auer and D. Frenkel, „Suppression of crystal nucleation in polydisperse colloids due to increase of the surface free energy“, *Nature*, vol. 413, no. 6857, pp. 711–713, Oct. 2001.
- [84] H. J. Schöpe, G. Bryant, and W. van Megen, „Effect of polydispersity on the crystallization kinetics of suspensions of colloidal hard spheres when approaching the glass transition“, *The Journal of Chemical Physics*, vol. 127, no. 8, p. 084 505, Aug. 2007.

- [85] G. L. Hunter and E. R. Weeks, „The physics of the colloidal glass transition“, *Reports on Progress in Physics*, vol. 75, no. 6, p. 066 501, May 2012.
- [86] Q. Li, U. Jonas, X. S. Zhao, and M. Kappl, „The forces at work in colloidal self-assembly: A review on fundamental interactions between colloidal particles“, *Asia-Pacific Journal of Chemical Engineering*, vol. 3, no. 3, pp. 255–268, May 2008.
- [87] C. Valeriani, E. Sanz, E. Zaccarelli, *et al.*, „Crystallization and aging in hard-sphere glasses“, *Journal of Physics: Condensed Matter*, vol. 23, no. 19, p. 194 117, Apr. 2011.
- [88] M. H. Kim, S. H. Im, and O. O. Park, „Rapid fabrication of two- and three-dimensional colloidal crystal films via confined convective assembly“, *Advanced Functional Materials*, vol. 15, no. 8, pp. 1329–1335, Aug. 2005.
- [89] M. Retsch and U. Jonas, „Hierarchically structured, double-periodic inverse composite opals“, *Advanced Functional Materials*, vol. 23, no. 43, pp. 5381–5389, May 2013.
- [90] S. Reculosa and S. Ravaine, „Synthesis of colloidal crystals of controllable thickness through the langmuir-blodgett technique“, *Chemistry of Materials*, vol. 15, no. 2, pp. 598–605, Jan. 2003.
- [91] S. Im, Y. Lim, D. Suh, and O. O. Park, „Three-dimensional self-assembly of colloids at a water–air interface: A novel technique for the fabrication of photonic bandgap crystals“, *Advanced Materials*, vol. 14, no. 19, pp. 1367–1369, Oct. 2002.
- [92] P. Ruckdeschel, „Transport phenomena in silica hollow spheres and hybrid materials“, dissertation, University of Bayreuth, 2018.
- [93] F. A. Nutz, „Thermal transport in polymer colloidal assemblies.“, dissertation, University of Bayreuth, 2018.
- [94] W. L. Vos, M. Megens, C. M. van Kats, and P. Bösecke, „X-ray diffraction of photonic colloidal single crystals“, *Langmuir*, vol. 13, no. 23, pp. 6004–6008, Nov. 1997.
- [95] B. G. Prevo and O. D. Velev, „Controlled, rapid deposition of structured coatings from micro- and nanoparticle suspensions“, *Langmuir*, vol. 20, no. 6, pp. 2099–2107, Mar. 2004.
- [96] H. Yang and P. Jiang, „Large-scale colloidal self-assembly by doctor blade coating“, *Langmuir*, vol. 26, no. 16, pp. 13 173–13 182, Aug. 2010.
- [97] F. A. Nutz, A. Philipp, B. A. F. Kopera, M. Dulle, and M. Retsch, „Low thermal conductivity through dense particle packings with optimum disorder“, *Advanced Materials*, vol. 30, no. 14, p. 1 704 910, Feb. 2018.
- [98] P. G. Bolhuis and D. A. Kofke, „Monte carlo study of freezing of polydisperse hard spheres“, *Physical Review E*, vol. 54, no. 1, pp. 634–643, Jul. 1996.

- [99] M. Trau, D. A. Saville, and I. A. Aksay, „Field-induced layering of colloidal crystals“, *Science*, vol. 272, no. 5262, pp. 706–709, May 1996.
- [100] K. Katagiri, Y. Tanaka, K. Uemura, *et al.*, „Structural color coating films composed of an amorphous array of colloidal particles via electrophoretic deposition“, *NPG Asia Materials*, vol. 9, no. 3, e355, Mar. 2017.
- [101] L. Cui, Y. Zhang, J. Wang, *et al.*, „Ultra-fast fabrication of colloidal photonic crystals by spray coating“, *Macromolecular Rapid Communications*, vol. 30, no. 8, pp. 598–603, Apr. 2009.
- [102] S. Yoshioka and Y. Takeoka, „Production of colourful pigments consisting of amorphous arrays of silica particles“, *ChemPhysChem*, vol. 15, no. 11, pp. 2209–2215, Jun. 2014.
- [103] O. D. Velev, T. A. Jede, R. F. Lobo, and A. M. Lenhoff, „Porous silica via colloidal crystallization“, *Nature*, vol. 389, no. 6650, pp. 447–448, Oct. 1997.
- [104] B. T. Holland, „Synthesis of macroporous minerals with highly ordered three-dimensional arrays of spheroidal voids“, *Science*, vol. 281, no. 5376, pp. 538–540, Jul. 1998.
- [105] P. Ruckdeschel, A. Philipp, B. A. F. Kopera, *et al.*, „Thermal transport in binary colloidal glasses: Composition dependence and percolation assessment“, *Physical Review E*, vol. 97, no. 2, Feb. 2018.
- [106] G. Wedler and H. Freund, *Lehrbuch der Physikalischen Chemie*, ser. Wiley VCH Lehrbuchkollektion 1. Wiley-VCH, 2012.
- [107] F. Incropera, D. DeWitt, T. Bergman, and A. Lavine, *Fundamentals of Heat and Mass Transfer*. Wiley, 2007.
- [108] L. W. Hrubesh and R. W. Pekala, „Thermal properties of organic and inorganic aerogels“, *Journal of Materials Research*, vol. 9, no. 3, pp. 731–738, Mar. 1994.
- [109] M. Ashghi, K. Kurabayashi, R. Kasnavi, and K. E. Goodson, „Thermal conduction in doped single-crystal silicon films“, *Journal of Applied Physics*, vol. 91, no. 8, pp. 5079–5088, Apr. 2002.
- [110] Z. Tong, S. Li, X. Ruan, and H. Bao, „Comprehensive first-principles analysis of phonon thermal conductivity and electron-phonon coupling in different metals“, *Physical Review B*, vol. 100, no. 14, Oct. 2019.
- [111] K. Behnia, „Conductivity, thermal“, in *Encyclopedia of Condensed Matter Physics*, Elsevier, 2005, pp. 225–229.
- [112] W. Rohsenow, J. Hartnett, Y. Cho, and Y. Cho, *Handbook of Heat Transfer*, ser. McGraw-Hill handbooks. McGraw-Hill Education, 1998.

- [113] A. M. Marconnet, M. Asheghi, and K. E. Goodson, „From the casimir limit to phononic crystals: 20 years of phonon transport studies using silicon-on-insulator technology“, *Journal of Heat Transfer*, vol. 135, no. 6, May 2013.
- [114] C. Kittel, „Interpretation of the thermal conductivity of glasses“, *Physical Review*, vol. 75, no. 6, pp. 972–974, Mar. 1949.
- [115] C. Y. Ho, R. W. Powell, and P. E. Liley, „Thermal conductivity of the elements“, *Journal of Physical and Chemical Reference Data*, vol. 1, no. 2, pp. 279–421, Apr. 1972.
- [116] R. Berman, „The thermal conductivities of some dielectric solids at low temperatures (experimental)“, *Proceedings of the Royal Society of London. Series A. Mathematical and Physical Sciences*, vol. 208, no. 1092, pp. 90–108, Aug. 1951.
- [117] M. Knudsen, „Die Gesetze der Molekularströmung und der inneren Reibungsströmung der Gase durch Röhren“, *Annalen der Physik*, vol. 333, no. 1, pp. 75–130, 1909.
- [118] J. H. Lienhard IV and J. H. Lienhard V, *A Heat Transfer Textbook*, 5th. Cambridge, MA: Phlogiston Press, 2020, 784 pp., Version 5.10.
- [119] J. K. Carson, S. J. Lovatt, D. J. Tanner, and A. C. Cleland, „Thermal conductivity bounds for isotropic, porous materials“, *International Journal of Heat and Mass Transfer*, vol. 48, no. 11, pp. 2150–2158, May 2005.
- [120] J. Wang, J. K. Carson, M. F. North, and D. J. Cleland, „A new structural model of effective thermal conductivity for heterogeneous materials with co-continuous phases“, *International Journal of Heat and Mass Transfer*, vol. 51, no. 9-10, pp. 2389–2397, May 2008.
- [121] S. S. Kistler, „Coherent expanded aerogels and jellies“, *Nature*, vol. 127, no. 3211, pp. 741–741, May 1931.
- [122] J. V. Alemán, A. V. Chadwick, J. He, *et al.*, „Definitions of terms relating to the structure and processing of sols, gels, networks, and inorganic-organic hybrid materials (IUPAC recommendations 2007)“, *Pure and Applied Chemistry*, vol. 79, no. 10, pp. 1801–1829, Jan. 2007.
- [123] E. Cuce, P. M. Cuce, C. J. Wood, and S. B. Riffat, „Toward aerogel based thermal superinsulation in buildings: A comprehensive review“, *Renewable and Sustainable Energy Reviews*, vol. 34, pp. 273–299, Jun. 2014.
- [124] L. I. C. Sandberg, T. Gao, B. P. Jelle, and A. Gustavsen, „Synthesis of hollow silica nanospheres by sacrificial polystyrene templates for thermal insulation applications“, *Advances in Materials Science and Engineering*, vol. 2013, pp. 1–6, 2013.

- [125] Y. Liao, X. Wu, H. Liu, and Y. Chen, „Thermal conductivity of powder silica hollow spheres“, *Thermochimica Acta*, vol. 526, no. 1-2, pp. 178–184, Nov. 2011.
- [126] S. A. Mofid, B. P. Jelle, X. Zhao, *et al.*, „Utilization of size-tunable hollow silica nanospheres for building thermal insulation applications“, *Journal of Building Engineering*, vol. 31, p. 101 336, Sep. 2020.
- [127] G. Tang, C. Bi, Y. Zhao, and W. Tao, „Thermal transport in nano-porous insulation of aerogel: Factors, models and outlook“, *Energy*, vol. 90, pp. 701–721, Oct. 2015.
- [128] G. Herrmann, R. Iden, M. Mielke, F. Teich, and B. Ziegler, „On the way to commercial production of silica aerogel“, *Journal of Non-Crystalline Solids*, vol. 186, pp. 380–387, Jun. 1995.
- [129] M. Reim, G. Reichenauer, W. Körner, *et al.*, „Silica-aerogel granulate – structural, optical and thermal properties“, *Journal of Non-Crystalline Solids*, vol. 350, pp. 358–363, Dec. 2004.
- [130] W.-Z. Fang, H. Zhang, L. Chen, and W.-Q. Tao, „Numerical predictions of thermal conductivities for the silica aerogel and its composites“, *Applied Thermal Engineering*, vol. 115, pp. 1277–1286, Mar. 2017.
- [131] Y.-J. Dai, Y.-Q. Tang, W.-Z. Fang, H. Zhang, and W.-Q. Tao, „A theoretical model for the effective thermal conductivity of silica aerogel composites“, *Applied Thermal Engineering*, vol. 128, pp. 1634–1645, Jan. 2018.
- [132] X. Lu, R. Caps, J. Fricke, C. Alviso, and R. Pekala, „Correlation between structure and thermal conductivity of organic aerogels“, *Journal of Non-Crystalline Solids*, vol. 188, no. 3, pp. 226–234, Aug. 1995.
- [133] J. Fricke and T. Tillotson, „Aerogels: Production, characterization, and applications“, *Thin Solid Films*, vol. 297, no. 1-2, pp. 212–223, Apr. 1997.
- [134] D. Dan, H. Zhang, and W.-Q. Tao, „Effective structure of aerogels and decomposed contributions of its thermal conductivity“, *Applied Thermal Engineering*, vol. 72, no. 1, pp. 2–9, Nov. 2014.
- [135] B. Himmel, T. Gerber, H. Bürger, G. Holzhüter, and A. Olbertz, „Structural characterization of SiO₂@Al₂O₃ aerogels“, *Journal of Non-Crystalline Solids*, vol. 186, pp. 149–158, Jun. 1995.
- [136] J. Mo and H. Ban, „Measurements and theoretical modeling of effective thermal conductivity of particle beds under compression in air and vacuum“, *Case Studies in Thermal Engineering*, vol. 10, pp. 423–433, Sep. 2017.
- [137] D. Garrett and H. Ban, „Compressive pressure dependent anisotropic effective thermal conductivity of granular beds“, *Granular Matter*, vol. 13, no. 5, pp. 685–696, Jun. 2011.

- [138] F. A. Nutz, P. Ruckdeschel, and M. Retsch, „Polystyrene colloidal crystals: Interface controlled thermal conductivity in an open-porous mesoparticle superstructure“, *Journal of Colloid and Interface Science*, vol. 457, pp. 96–101, Nov. 2015.
- [139] K. Swimm, G. Reichenauer, S. Vidi, and H.-P. Ebert, „Gas pressure dependence of the heat transport in porous solids with pores smaller than 10“, *International Journal of Thermophysics*, vol. 30, no. 4, pp. 1329–1342, Jul. 2009.
- [140] K. Raed and U. Gross, „Modeling of influence of gas atmosphere and pore-size distribution on the effective thermal conductivity of knudsen and non-knudsen porous materials“, *International Journal of Thermophysics*, vol. 30, no. 4, pp. 1343–1356, Jun. 2009.
- [141] S. C. S. Y. S. Touloukian P. E. Liley, *Thermophysical Properties of Matter - The TPRC Data Series. Volume 3. Thermal Conductivity - Nonmetallic Liquids and Gases*. IFL Plenum, 1970.
- [142] T. Xie, Y.-L. He, and Z.-J. Hu, „Theoretical study on thermal conductivities of silica aerogel composite insulating material“, *International Journal of Heat and Mass Transfer*, vol. 58, no. 1-2, pp. 540–552, Mar. 2013.
- [143] A. M. Neuhöfer, K. Herrmann, F. Lebeda, *et al.*, „High-temperature thermal transport in porous silica materials: Direct observation of a switch from conduction to radiation“, *Advanced Functional Materials*, vol. 32, no. 8, p. 2108370, Nov. 2021.
- [144] S. Zeng, A. Hunt, and R. Greif, „Theoretical modeling of carbon content to minimize heat transfer in silica aerogel“, *Journal of Non-Crystalline Solids*, vol. 186, pp. 271–277, Jun. 1995.
- [145] H. Liu, T. Li, Y. Shi, and X. Zhao, „Thermal insulation composite prepared from carbon foam and silica aerogel under ambient pressure“, *Journal of Materials Engineering and Performance*, vol. 24, no. 10, pp. 4054–4059, Sep. 2015.
- [146] U. Heinemann, R. Caps, and J. Fricke, „Radiation-conduction interaction: An investigation on silica aerogels“, *International Journal of Heat and Mass Transfer*, vol. 39, no. 10, pp. 2115–2130, Jul. 1996.
- [147] T. Still, M. Retsch, U. Jonas, *et al.*, „Vibrational eigenfrequencies and mechanical properties of mesoscopic copolymer latex particles“, *Macromolecules*, vol. 43, no. 7, pp. 3422–3428, Apr. 2010.
- [148] F. A. Nutz and M. Retsch, „Tailor-made temperature-dependent thermal conductivity via interparticle constriction“, *Science Advances*, vol. 3, no. 11, eaao5238, Nov. 2017.

- [149] B. Vollmert, „Synthesis and reactions of macromolecular compounds“, in *Polymer Chemistry*, Springer Berlin Heidelberg, 1973, pp. 33–321.
- [150] P. J. Feeney, D. H. Napper, and R. G. Gilbert, „Surfactant-free emulsion polymerizations: Predictions of the coagulative nucleation theory“, *Macromolecules*, vol. 20, no. 11, pp. 2922–2930, Nov. 1987.
- [151] M. S.-D. Juang and I. M. Krieger, „Emulsifier-free emulsion polymerization with ionic comonomer“, *Journal of Polymer Science: Polymer Chemistry Edition*, vol. 14, no. 9, pp. 2089–2107, Sep. 1976.
- [152] R. Arshady, „Suspension, emulsion, and dispersion polymerization: A methodological survey“, *Colloid & Polymer Science*, vol. 270, no. 8, pp. 717–732, Aug. 1992.
- [153] K. E. J. Barrett, „Dispersion polymerisation in organic media“, *British Polymer Journal*, vol. 5, no. 4, pp. 259–271, Jul. 1973.
- [154] S. Kawaguchi and K. Ito, „Dispersion polymerization“, in *Polymer Particles*, Springer Berlin Heidelberg, Feb. 2005, pp. 299–328.
- [155] A. J. Paine, W. Luymes, and J. McNulty, „Dispersion polymerization of styrene in polar solvents. 6. Influence of reaction parameters on particle size and molecular weight in poly(n-vinylpyrrolidone)-stabilized reactions“, *Macromolecules*, vol. 23, no. 12, pp. 3104–3109, Jun. 1990.
- [156] A. M. Lechner, T. Feller, Q. Song, *et al.*, „Scalable synthesis of smooth PS@TiO₂ core-shell and TiO₂ hollow spheres in the (sub) micron size range: Understanding synthesis and calcination parameters“, *Colloid and Polymer Science*, vol. 298, no. 7, pp. 867–878, Mar. 2020.
- [157] I. Tissot, J. P. Reymond, F. Lefebvre, and E. Bourgeat-Lami, „SiOH Functionalized polystyrene latexes. A step toward the synthesis of hollow silica nanoparticles“, *Chemistry of Materials*, vol. 14, no. 3, pp. 1325–1331, Mar. 2002.
- [158] A. Dawson and P. V. Kamat, „Semiconductor-metal nanocomposites. photoinduced fusion and photocatalysis of gold-capped TiO₂(TiO₂/gold) nanoparticles“, *The Journal of Physical Chemistry B*, vol. 105, no. 5, pp. 960–966, Feb. 2001.
- [159] L. Zhang, J. C. Yu, H. Y. Yip, *et al.*, „Ambient light reduction strategy to synthesize silver nanoparticles and silver-coated TiO₂ with enhanced photocatalytic and bactericidal activities“, *Langmuir*, vol. 19, no. 24, pp. 10 372–10 380, Nov. 2003.
- [160] E. Abbe, „Beiträge zur Theorie des Mikroskops und der mikroskopischen Wahrnehmung“, *Archiv für Mikroskopische Anatomie*, vol. 9, no. 1, pp. 413–468, Dec. 1873.

- [161] P. Atkins, J. de Paula, M. Bär, A. Schleitzer, and C. Heinisch, *Physikalische Chemie*, Bd. 1. Wiley, 2006.
- [162] G. Dehm, J. Howe, and J. Zweck, *In-situ Electron Microscopy: Applications in Physics, Chemistry and Materials Science*. Wiley, 2012.
- [163] D. C. Bell and N. Erdman, Eds., *Low Voltage Electron Microscopy*. John Wiley & Sons, Ltd, Dec. 2012.
- [164] L. Sawyer, D. Grubb, and G. Meyers, *Polymer Microscopy*, ser. Springer ebook collection / Chemistry and Materials Science 2005-2008. Springer New York, 2008.
- [165] J. Ackermann, *Handbuch für die Rasterelektronenmikroskope SUPRA(VP) und ULTRA*. 2004.
- [166] R. Egerton, *Physical Principles of Electron Microscopy*. Springer International Publishing, 2016.
- [167] B. Kopera, „Building scientific tools: From heat transport to particulate systems“, dissertation, University of Bayreuth, 2020.
- [168] T. Bergman, F. Incropera, D. DeWitt, and A. Lavine, *Fundamentals of Heat and Mass Transfer*, 6th ed. Wiley, 2007.
- [169] A. Philipp, J. F. Eichinger, R. C. Aydin, *et al.*, „The accuracy of laser flash analysis explored by finite element method and numerical fitting“, *Heat and Mass Transfer*, vol. 56, no. 3, pp. 811–823, Oct. 2019.
- [170] W. J. Parker, R. J. Jenkins, C. P. Butler, and G. L. Abbott, „Flash method of determining thermal diffusivity, heat capacity, and thermal conductivity“, *Journal of Applied Physics*, vol. 32, no. 9, pp. 1679–1684, Sep. 1961.
- [171] J. A. Cape and G. W. Lehman, „Temperature and finite pulse-time effects in the flash method for measuring thermal diffusivity“, *Journal of Applied Physics*, vol. 34, no. 7, pp. 1909–1913, Jul. 1963.
- [172] J. Blumm, J. Henderson, O. Nilsson, and J. Fricke, „Laser flash measurement of the phononic thermal diffusivity of glasses in the presence of ballistic radiative transfer“, *High Temperatures-High Pressures*, vol. 29, no. 5, pp. 555–560, 1997.
- [173] L. Dusza, „Combined solution of the simultaneous heat loss and finite pulse corrections with the laser flash method“, *High Temperatures-High Pressures*, vol. 27/28, no. 5, pp. 467–473, 1995.
- [174] A. Frick and C. Stern, *Dynamische Differenzkalorimetrie (DSC)*, ser. DSC-Prüfung in der Anwendung. Carl Hanser Verlag GmbH & Co. KG, 2006, pp. 17–50.
- [175] *Standard test method for determining specific heat capacity by differential scanning calorimetry*, ASTM, West Conshohocken, ASTM International, 2011.

- [176] P. S. Gill, S. R. Sauerbrunn, and M. Reading, „Modulated differential scanning calorimetry“, *Journal of Thermal Analysis*, vol. 40, no. 3, pp. 931–939, 1993.
- [177] L. C. Thomas, „Modulated DSC Paper # 2 Modulated DSC Basics; Calculation and Calibration of MDSC Signals“, 2005.
- [178] —, „Modulated DSC Paper # 3 Modulated DSC Basics; Optimization of MDSC Experimental Conditions“, 2005.
- [179] R. C. Schroden, M. Al-Daous, C. F. Blanford, and A. Stein, „Optical properties of inverse opal photonic crystals“, *Chemistry of Materials*, vol. 14, no. 8, pp. 3305–3315, 2002.

Thesis Overview

5.1 Synopsis

A graphical overview of this thesis is shown in Figure 5.1. In this thesis, the thermal properties of different nanoscopic materials and their superstructures have been examined. The main target was to understand and control the thermal transport of colloidal structures, focusing on their insulating properties. Chapters 6-8 present the core publications of this cumulative thesis, where I was leading the material synthesis and characterization. Solid and hollow silicon dioxide (silica) and hollow titanium dioxide (titania) particles have been used as colloidal building bricks. A closer focus on the synthesis of PS particles with diameters larger than 600 nm and their usage as templates for hollow titanium dioxide (titania) particles are described in Chapter 6. Furthermore, I prepared hollow silica particles of different sizes assembled into colloidal glasses and binary colloidal glasses in Chapters 7 and 8. Additionally, I contributed to many research projects – that are not included in this thesis – with cationic and anionic polystyrene (PS), polymethylmethacrylate (PMMA), and silicon dioxide (silica) hollow particles. Therefore, the synthesis of my particle library was already described in Chapter 2. The materials have been characterized using scanning electron microscopy (SEM), (high-temperature) light flash analysis (LFA), and differential scanning calorimetry (DSC). These have

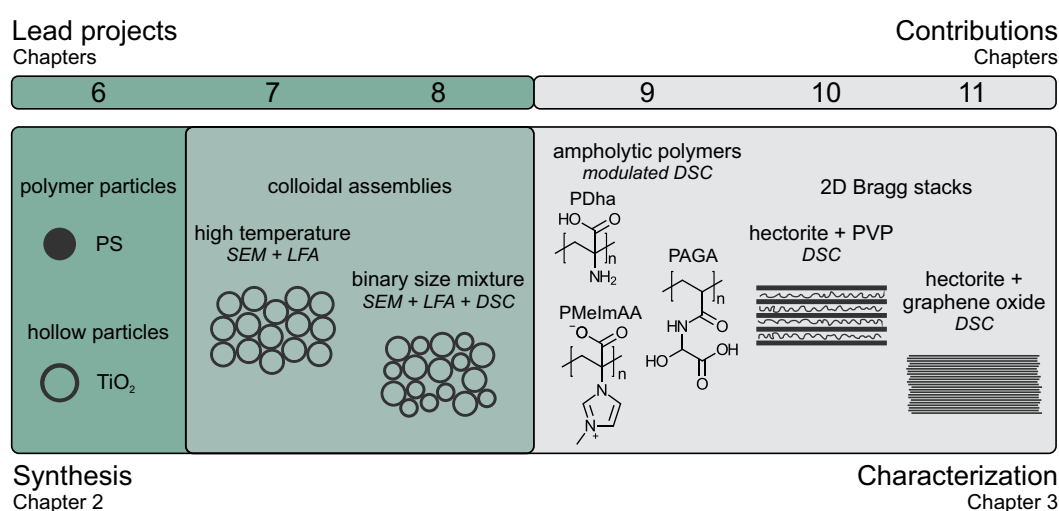


Fig. 5.1: Graphical overview of this thesis.

been my main characterization methods and have been described in the previous Chapter 3.

With my knowledge about DSC measurements, I contributed to three further projects in the field of thermal characterization. For Chapter 9, I used the more complex method of modulated DSC to determine the specific heat capacity, c_P , of several ampholytic polymers, stored under various relative humidity conditions, to determine the influence of the hydration level. In Chapters 10 and 11, I contributed with DSC measurements to two projects in the field of two-dimensional Bragg stacks.

For the target of this thesis – understanding the thermal transport properties of colloidal superstructures – colloidal building bricks had to be synthesized. There had been some requirements, like a spherical shape, size control, reproducibility, up-scalable to large amounts. The aim was to find materials with low density and with thermal conductivities larger than those of silica. Considering these parameters, I opted for a synthesis route towards hollow particles with titania as shell material.

Titania, with its different polymorphs, like rutile, brookite, and anatase, is an interesting material because of its optical and semiconducting properties. It can be incorporated in insulating silica materials to suppress thermal radiation and can be used as thermoelectric material. Besides, it can be used for various applications in the fields of photovoltaic, photoconversion, hydrogen storage, and structural coloration or efficient scattering. In Chapter 6, a controlled synthesis route to produce hollow titania particles is presented. These are beneficial because they combine a high surface area with low density. The particles have been made using a three-step template-based approach. First, PS particles have been synthesized via dispersion polymerization with a cationic comonomer. Second, the shell growth was controlled by slow addition of the titania precursor. Third, the template particles have been removed by a calcination process in an inert atmosphere.

The PS particles have been synthesized by dispersion polymerization of styrene, with the cationic comonomer 2-methacryloxyethyltrimethylammoniumchloride (MTC). The particle diameter was linearly dependent on the amount of styrene and increased from 673 to 1353 nm (Figure 5.2b). A constant ratio between monomer and comonomer of 0.8 mol% resulted in a zeta potential of about +40 mV. It was also tested to change the monomer-comonomer ratio. Without MTC, the zeta potential was around 0 mV, but the particle dispersion was still stable because of the steric stabilizer PVP. When increasing the MTC content, the particles aggregated and deformed (Figure 5.2a). A decrease of the particle diameter by 200 nm with increasing MTC content was observed due to the increased stability of PS oligomers during the synthesis. Overall, highly monodisperse PS particles with standard deviations that are less or equal 5 % of the diameter have been achieved.

These particles were used as seed templates without further purification to allow for a simple scale-up. The amount of MTC on the particle surface influenced the resulting titania shells. With an increasing amount of MTC, the particle surface got more compact and less granular. The shell structure was also preserved after the calcination process, which is shown in Figure 5.2.

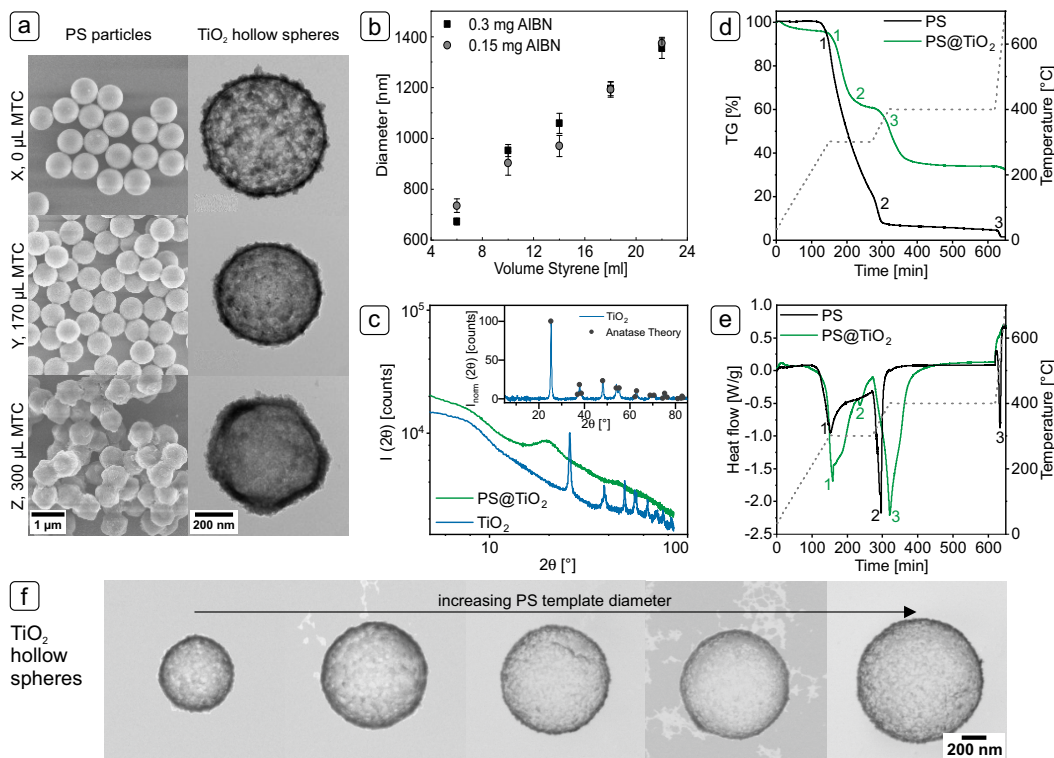


Fig. 5.2: SEM and TEM images of PS particles, synthesized with different amount of MTC, and corresponding hollow titania particles (a) Diameter of particles from dispersion polymerization dependent on the amount of styrene and the amount of initiator AIBN (b). XRD measurements of the PS@TiO₂ and hollow titania spheres (c). Combined STA (d) and DSC (e) measurements to investigate the calcination process of pure PS particles and PS@TiO₂ particles. STEM images of single titania hollow spheres made from PS template particles with increasing diameter (f). Adapted with permission from Lechner *et al.*, Colloid Polym Sci 298, 867–878 (2020). Copyright 2020 The Authors.

The crucial step of the synthesis was the aging step of 24 h before the calcination. This aging was necessary to improve the formation of a pre-condensed titania network and covalent connectivity among the granular nuclei in the shell. The temperature profile of the calcination process itself was also critical. A process with two isothermal steps was developed, based on the profile of Schrodén *et al.*^[179]. The isothermal steps were chosen to be at 300 °C, the onset temperature of the PS degradation, and 400 °C to achieve full degradation of the organic material. To obtain a better understanding of the calcination process itself, combined TGA, DSC, and IR measurements have been performed in air and nitrogen atmosphere. The results of the air calcination reveal the differences between the neat PS and core-shell particles. The TG curves (Figure 5.2d) show that the decomposition of the neat

PS particles was significantly faster than the core-shell particles' decomposition. This can be explained by the mass transport that is limited by the titania shell. Furthermore, a condensation process of the titania network was observed in the DSC measurement (Figure 5.2e). The phase change from amorphous to anatase titania, which was verified by X-ray powder diffraction (Figure 5.2c), was not visible in the DSC measurements because it was superimposed by the exothermic degradation peak of the PS. During calcination, the shell thickness shrunk from around 30-40 nm before calcination to 24 nm after calcination.

Finally, PS particles with increasing diameters from 673 to 1353 nm have been coated with titania. An isotropic shrinkage up to 20 % was observed during calcination in air. For particles larger than 700 nm, the shrinkage was not systematic anymore. It resulted in hollow titania particles with diameters of around 900 nm, independent of the core-shell particle size (Figure 5.2f). The ratio between shell thickness, and particle diameter, decreased from 4 % for the smallest hollow particles to 2 % for the largest hollow particles. Consequently, the particles got unstable, and an increased portion of fractured or buckled hollow particles were observed.

Overall, a facile, reproducible, and scalable method towards well-defined titania hollow particles was presented. The particles can be used for various applications, where the properties of titania are beneficial. Due to its optical properties, titania is applied in silica aerogels to suppress thermal radiation at elevated temperatures. Silica itself is optically transparent in the region of 1-8 μm and consequently strongly affected by thermal radiation. This is a challenge when fabricating efficient thermal insulation materials for high-temperature applications. In Chapter 7, the suitability of particular silica matter was tested for high-temperature applications using LFA measurements. A transition from conduction to radiation-dominated heat transfer has been found and discussed.

Five samples have been measured by LFA in the range of 25-925 $^{\circ}\text{C}$ in inert gas atmosphere: two silica hollow particle samples with particle diameters of 278 and 882 nm and a shell thickness of about 30 nm and three silica solid particle samples with particle diameters of 353, 889, and 8000 nm. The measurements were completed by reference measurements on bulk borosilicate and quartz glass, a pyroceram standard, a titania hollow particle sample, and inert calcined hollow particle samples that comprise carbon residues. Figure 5.3a shows the normalized measurement data for the small silica hollow and solid samples. Below 450 $^{\circ}\text{C}$, the heat transport is dominated by a slow process due to conduction. With increasing temperature, a second much faster contribution gets more and more dominant. This contribution is referred to thermal radiation occurring in the samples.

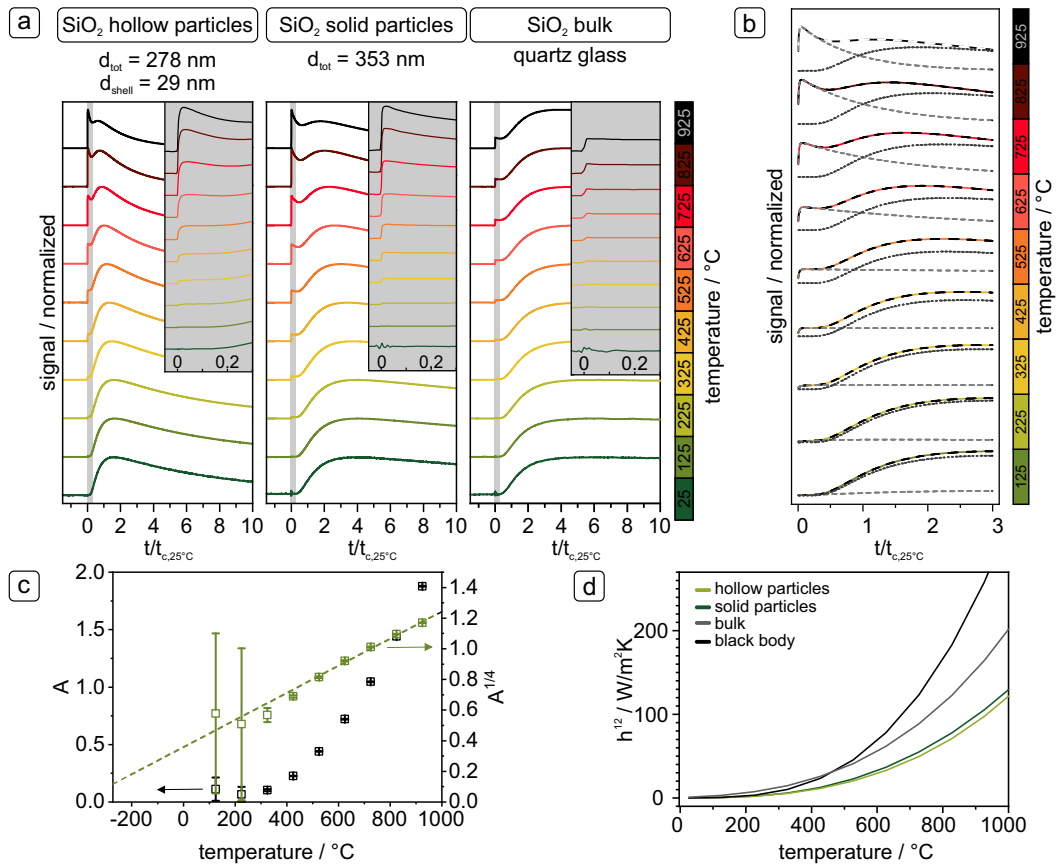


Fig. 5.3: Temperature dependent LFA measurement signal of the small silica hollow, and solid particles, and bulk quartz glass. The grey insets show details of the radiation peak. The time data is normalized by the characteristic thermal response time t_c (a) Double-diffusive model applied on 278 nm hollow particle measurements (b). Resulting ratio, A , of first and second diffusive process (c). Integrated heat transfer coefficient h^{12} for hollow and solid silica particles, and bulk quartz glass, in comparison with black body radiation (d). Adapted with permission from Neuhöfer *et al.*, *Adv. Funct. Mater.* 2022, 32, 2108370. Copyright 2021 The Authors.

The increasing influence of radiative heat transfer is also occurring in the reference glass measurements (Figure 5.3a). However, a major difference in the peak shape was found. While the granular samples demonstrate a marked loss in surface temperature after the initial increase, the bulk samples reach a plateau. In the case of the hollow particle samples, the temperature increase from the radiative peak is significantly slower than for the other samples. Due to this slow dynamic and the high peak intensity, established models are not capable of fitting the process accurately anymore for temperatures above 525 °C.

In a simple approximation, the measurement was treated as a superposition of two diffusive transport processes. It was fitted by a simplified model that used the same diffusive thermal transport formalism for the radiative and conductive transport. This model is robust for a wide temperature range, which is shown in

Figure 5.3b. Furthermore, it allows separating the contributions of the separate individual processes. The temperature-dependent ratio of these contributions is non-linear and scales with T^4 , due to the radiative nature obeying Stefan-Boltzmann's law (Figure 5.3c).

The optical properties of the samples control the radiative thermal transport. Silica, in its bulk and particulate form, is optically transparent in the wavelength region between 1-5 μm . In combination with good thermal emitters in the form of graphite layers at the boundaries, the radiative heat transport pathway is opened. In contrast, titania is opaque in the wavelength region between 1-8 μm , and no radiative transport process was observed in the LFA measurements.

To gain a deeper understanding on the radiative transport mechanism, the optical properties of the bulk, solid, and hollow samples have been modeled using an effective multilayer approach and a boundary element method. The results revealed that surface wave modes do not play a significant role in the high-temperature transport through particulate silica materials because the Reststrahlen band is too far red-shifted. Furthermore, the optical density of the particle ensemble determines which wavelengths can be transported through the structures by evanescent waves. In the case of the hollow silica samples, the large porosity suppresses the evanescent waves. Nevertheless, the integrated heat transfer coefficients of the solid and hollow samples are comparable because the hollow samples are stronger transmitting between 5-8 μm and therefore have higher wavelength modes (Figure 5.3d). Thus, the contributions of evanescent waves and wavelength modes compensate each other when comparing the hollow and solid particulate samples.

This work helped to gain a deeper understanding of the high-temperature thermal transport mechanisms in particle-based silica materials. At room temperature, conduction through the silica backbone dominates. With increasing temperature, the influence of thermal radiation increases until it dominates the overall heat transfer. Therefore, the materials have high insulating properties at room temperature and transform to better thermal conductors at elevated temperatures. To maintain the strong insulation behaviour of the material, the optical properties in the mid-IR range have to be controlled by changing the composition, the structure, or by adding additives.

Having discussed the high-temperature properties of particular silica materials and unveiled their insulation advantages, particularly at room temperature, the next challenge was to further decrease the effective thermal conductivity of these materials. In Chapter 8, the influence of the material density, disorder, and particle size on the thermal properties of particle-based silica materials have been discussed with the aim to find the right parameters for an effective reduction of the thermal conductivity.

Two strategies have been followed: reduction of the density by a switch from solid to hollow particles and enhancing the degree of disorder by using binary particle mixtures and fast assembly through the filtration method. For this purpose, binary colloidal samples of solid and hollow silica particles in the size range of 500 and 900 nm, with 0, 20, 40, 60, 80, and 100 vol% of the large particles have been prepared (Figure 5.4a).

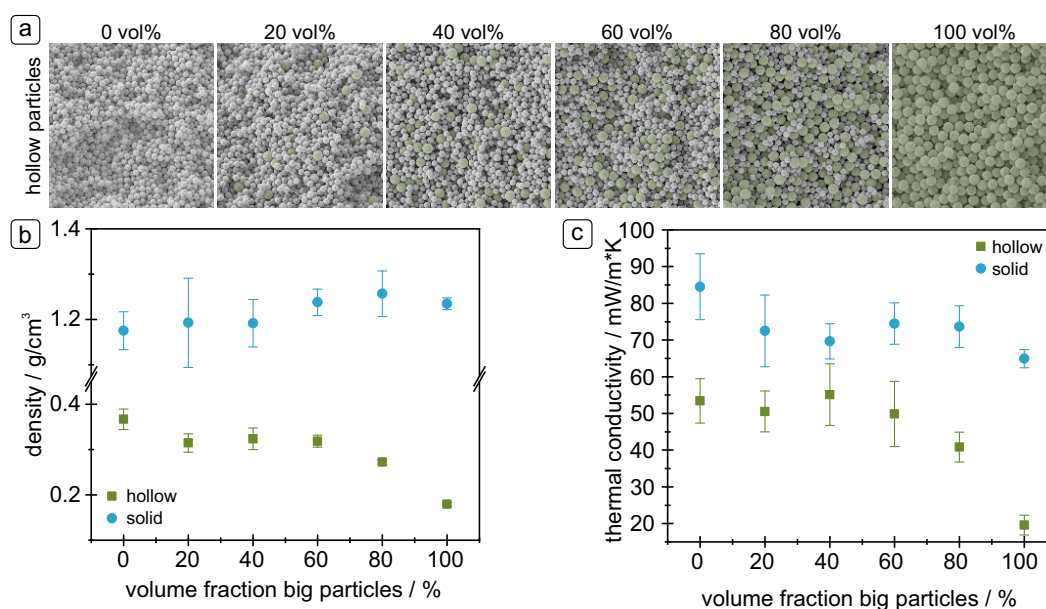


Fig. 5.4: SEM sideview images of colloidal glasses with increasing amount of big particles. Top row: hollow binary mixtures (a). Density of samples made from hollow and solid binary mixtures (b). Thermal conductivity of hollow and solid binary mixtures (c).

The sample densities are shown in Figure 5.4b. While the densities of the solid particle samples stayed constant at $\sim 1.2 \text{ g/cm}^3$, the hollow particle samples densities decreased from 0.4 g/cm^3 for the 0 vol% to 0.2 g/cm^3 for the 100 vol% large particle assemblies. Therefore, a reduction of the density of up to 85% compared to the solid particle sample has been achieved. From the material densities, the packing densities of the samples were calculated. While the packing densities of the solid samples were more comparable in the random-close-packing state, the packing densities of the hollow samples had strong fluctuations between 0.5-0.7, with the 100% large particle sample having the lowest packing density and therefore the highest degree of disorder. This already indicated the strong influence of the particle size on the material properties in the case of the hollow particle samples.

The thermal conductivity data of the hollow and solid particle ensembles, shown in Figure 5.4c, affirmed the strong influence of the particle size and sample density. Both effects dominate over the influence of the degree of disorder of the sample. Increasing the particle size from 500 to 900 nm reduced the thermal conductivity by about 20%. This effect is caused by the smaller relative contact areas between

the individual particles, which is deduced from the solid particle data. Additionally, the decrease of the density from the solid to the hollow particle samples led to a systematic drop in the thermal conductivity of 60 % from the small to the large particles in the case of the hollow particle ensembles.

This project showed that it is possible to tune the thermal conductivity of colloidal assemblies by adjusting the particle size and density of colloidal glasses. Thermal conductivities down to 20 mW/mK have been achieved for the 900 nm hollow silica samples. Therefore, these colloidal glasses offer an interesting alternative to insulation materials based on silica aerogels, with the advantage of a high structural control over the particle geometry and a more facile preparation without supercritical drying steps.

In addition to my lead projects, I contributed to further projects in the field of thermal characterization with my knowledge about DSC measurements (Chapters 9-11). For all projects, I determined the specific heat capacity, which was essential to calculate the thermal conductivities from thermal diffusivity data. Especially in the project in Chapter 9, the sample preparation was crucial due to the fact that it was challenging to achieve a uniform distribution of the samples in the sample pan, and the specific heat capacity was dependent on the sample humidity. In the same project, I also applied the more complex method of modulated DSC. Here, several pre-tests for the determination of the right measurement parameters were necessary. However, without this method, it would not have been possible to determine the glass transition temperatures of ampholytic polymers because they were superimposed with broad water-evaporation signals.

Water processable polymers have attracted interest in current thermal transport research, owing to the possibility to introduce hydrogen bonds as a motif to increase the thermal conductivity even in amorphous specimen. Ampholytic functional groups that exhibit donor and acceptor groups for the formation of hydrogen bonds in one polymer chain have the advantage of preventing demixing as typically observed in polymer blends. Up to now, the role and influence of the hydrogen bonds on the thermal conductivity was still unclear. This is why the thermal transport of four ampholytic polymers is discussed in Chapter 9 concerning their thermal transport properties and how the polymer microstructure affects these.

Figure 5.5a shows an overview of the examined polymers PMMA, poly(acrylic acid) (PAA), polydehydroalanine (PDha), poly(2-acrylamido glycolic acid) (PAGA), poly(2-(imidazole-1-yl)acrylic acid) (PImAA), and its methylated derivative poly(2-(3-methylimidazolium-1-yl)-acrylic acid) (PMeImAA). PMMA can not form hydrogen bonds and was therefore used as reference material. PAA has only one

functional group per repetition unit. The other polymers provide at least two different functional groups.

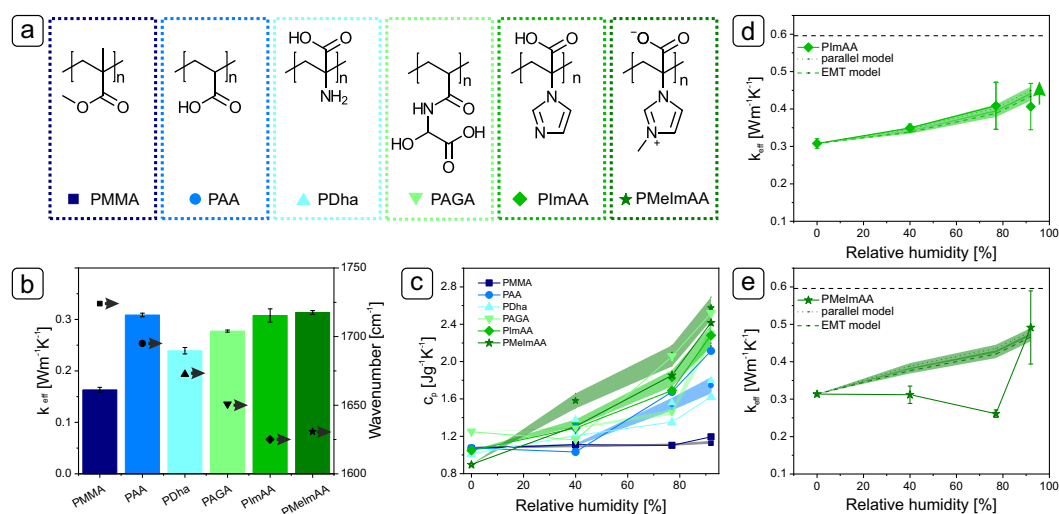


Fig. 5.5: Structure of the ampholytic polymers and the reference polymers PAA and PMMA (a). The ampholytic polymers have at least two functional groups per repetition unit. Measured effective thermal conductivity of all samples (solid bars) and peak position (black symbols) of the carbonyl band measured by IR spectroscopy (b). Specific heat, measured by MDSC, increases with humidity (solid lines and symbols). Shaded areas rationalize the expected trend of the cp based on the water uptake (c). Effective thermal conductivity vs relative humidity for PImAA (d) and PMeImAA (e). The solid symbols depict the experimental data, while the dashed and dotted lines are calculated values using the parallel and the EMT mixing model, respectively. The shaded areas consider the variability because of the deviation of the moisture content determination. The dashed black line represents the thermal conductivity of water. Adapted with permission from Hummel *et al.*, *Macromolecules* 2020, 53, 5528-5537. Copyright 2020 American Chemical Society.

The position of the carbonyl peak at 1700 cm^{-1} of IR spectra is directly connected to the strength of the hydrogen bond. The strength of the carboxylic hydrogen bonds systematically increased from PAA to PMeImAA, as the peak shifted to lower frequencies. The effective thermal conductivity of the polymers was determined using the photoacoustic method. As expected, the thermal conductivity increased with increasing hydrogen bond strength in the dry state, as shown in Figure 5.5b.

Fourier self-deconvolution (FSD) showed that PAA mainly formed strongly coordinated hydrogen bonds and even covalently condensed anhydrides. From PDha, over PAGA and PImAA to PMeImAA, the number of classes of hydrogen bonds that are not formed between two carboxylic acid groups increased and followed the trend of increased hydrogen bond strength.

Ampholytic polymers and PAA are strongly influenced by humidity. Therefore, all samples have been stored at 45, 77, and 92 % relative humidity, and the moisture content, specific heat, and IR measurements have been performed. Except for PMMA,

all samples exhibited a significant water uptake, accompanied by an increasing specific heat, which is shown in Figure 5.5c. There were two possibilities for how the water was absorbed. IR measurements showed that in PAA the water molecules were bound directly to the carboxylic acid groups and intercalated between the polymer chains without affecting the conformation and, therefore, the interchain thermal transport. PDha did also show this effect, but less pronounced. In PAGA, PImAA, and PMeImAA, water was adsorbed in a less bound state. Therefore, the effective thermal conductivity could be rationalized by a volume-weighted parallel mixing model and an effective medium model. The exemplary results for PImAA are shown in Figure 5.5d. The deviations from PMeImAA (Figure 5.5e) to the mixing models could be explained by the stronger ionic interactions interrupted by the water molecules.

This work helped to get a better understanding of the role of hydrogen bonds for thermal transport in polymer materials. It was proven that the thermal conductivity increased with increasing hydrogen bond strength in the polymer. The absorption of water was different for all polymers and individually influenced the hydrogen bond motifs. However, the effective thermal conductivity of ampholytic polymers could be well explained by mixing models.

The effective medium and parallel mixing model also have been applied to describe the thermal and mechanical properties of hybrid Bragg stacks with extreme polymer confinement, as discussed in Chapter 10. Spray coating of dilute nematic mixtures of delaminated, high-aspect-ratio clay and PVP led to self-supported, highly coherent Bragg stacks with lateral extensions of several square centimeters. X-ray diffraction and transmission electron microscopy measurements showed that the layers were strictly alternating and exhibited a long-range periodicity, which is shown in Figure 5.6a. Because the PVP layer thickness was ranging from 9 to 28 Å, which is smaller than the polymer chain's radius of gyration, even in the order of an individual polymer chain, strong polymer confinement was implied. This was a result of the PVP layer thickness that could only be varied in discrete steps. Therefore, just discrete polymer volume fractions led to defect-free Bragg stacks, as shown for a 31 % hectorite sample in Figure 5.6a in contrast to 51 % hectorite sample in Figure 5.6b.

The in- and cross-plane thermal conductivity and mechanical properties of six samples, varying from 0, 23, 31, 40, 51, and 100 vol% hectorite, have been examined. The in- and cross-plane thermal conductivities of all samples were measured with lock-in thermography and photoacoustic methods. It was found that the in-plane thermal conductivity followed a parallel mixing model with the lower limit of 0.17 W/mK of pure PVP, and the higher limit of 5.71 W/mK of pure hectorite sample, as shown in Figure 5.6c. Therefore, the polymer confinement in the stacked samples did

not influence the thermal conductivity compared to the bulk components. This is also indicated by the specific heat data, shown in Figure 5.6e. The specific heat decreases from 1190 to 890 J/kgK with increasing hectorite content, which follows the prediction of an effective medium model. In contrast, the cross-plane thermal conductivity was around 0.09 W/mK for all mixed samples (Figure 5.6d). It deviated strongly from an effective medium behavior due to the dominating influence of the PVP-hectorite interface resistance. Overall, the structural perfection of the samples led to an exceptionally high thermal conductivity anisotropy, with a maximum of 38 for the 51 vol% hectorite sample.

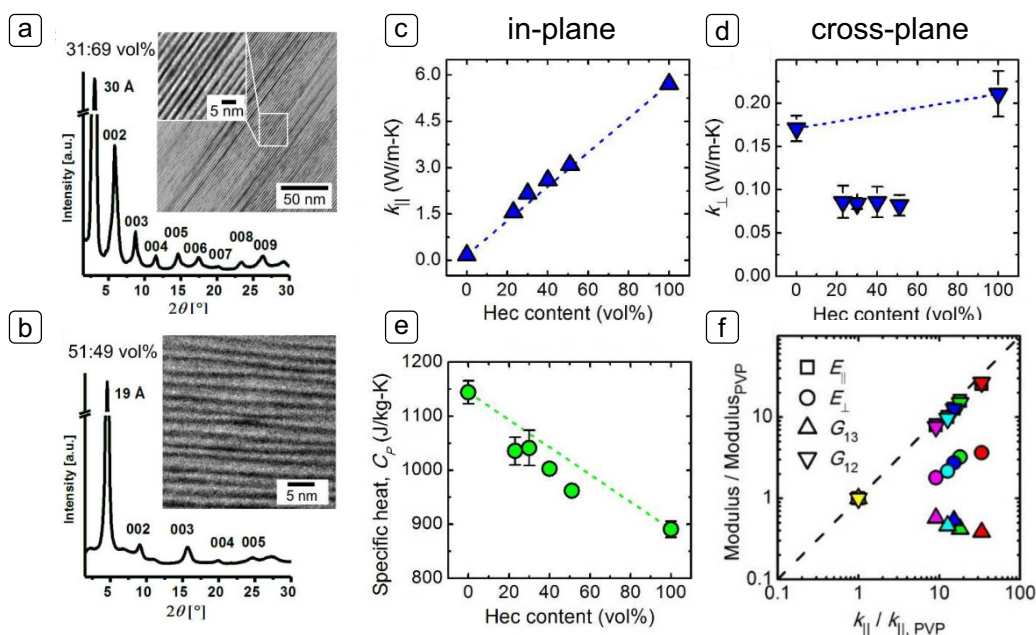


Fig. 5.6: XRD patterns of Hec31/PVP69 (defect-free material) showing intense 001-reflections and a rational series of basal reflections up to the ninth order (a). The cross-sectional TEM images show exceptionally periodic homogeneity of these hybrid films over large length scales. XRD patterns and cross-sectional TEM image of Hec51/PVP49 displaying a random stacking of two gallery heights (b). In-plane (c) and cross-plane (d) thermal conductivities of Hec/PVP hybrid Bragg stacks, as a function of the hectorite volume fraction. Specific heat of Hec/PVP hybrid Bragg stacks, as a function of the hectorite volume fraction (e). Normalized mechanical moduli vs. normalized effective in-plane (f) thermal conductivity. The dashed line shows a direct correlation between the two axes with a power of one. Adapted with permission from Wang *et al.*, *Angew. Chem. Int. Ed.*, 2020, 59, 1286- 1294. Copyright 2019 The Authors.

In combination with Brillouin light spectroscopy measurements, a detailed analysis of the anisotropic mechanical and thermal properties was possible. In the in-plane direction, the phonon mean free path was dependent on the hybrid composition and increased from 2 Å for the pure PVP sample to 14 Å for the pure hectorite sample. Since these values were much smaller than the lateral size of the hectorite nanosheets, the high in-plane thermal conductivities of the samples were governed by the intrinsic material properties, not by the grain boundaries. Furthermore, a direct

relation of the in- and cross-plane Young's moduli and the torsional shear modulus to the in-plane thermal conductivity was found, which is shown in Figure 5.6f. The thermal transport in the cross-plane direction did not correlate with the mechanical moduli but was dominated by interfacial effects, as verified using a series resistance model. A reduction of the interfacial conductance for a hectorite-PVP interface ($89 \text{ MW/m}^2\text{K}$) in contrast to hectorite-hectorite ($219 \text{ MW/m}^2\text{K}$) was determined.

While the last two Chapters focused on polymer-water and polymer-hectorite composite materials, Chapter 11 highlights the anisotropic thermal properties of pure hectorite Bragg stacks and compares them to graphene oxide Bragg stacks. The stacks consisted of aligned hectorite and GO nanosheets featuring high aspect ratios due to their large lateral size compared to their low thickness. These samples have also been produced by spray coating dilute nematic mixtures of hectorite and GO. Cross-sectional TEM and SEM images are shown in Figure 5.7a and 5.7b for hectorite and graphene oxide. For each material, two samples with small and large platelets have been examined.

The results of the thermal conductivities are presented in Figure 5.7c. All values were in reasonable agreement with literature data. The thermal conductivity anisotropy was found to be 2- to 3-fold higher for the hectorite samples due to a higher in-plane thermal conductivity.

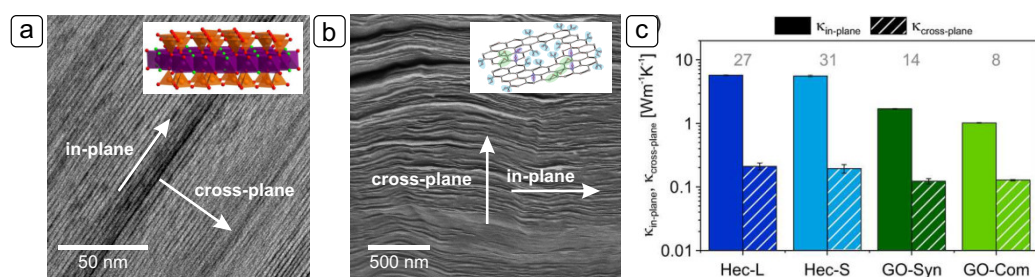


Fig. 5.7: A cross-sectional TEM image of an aligned smectic hectorite film (a). White arrows illustrate the in-plane and cross-plane directions. The inset shows the structure of a sodium fluorohectorite platelet. Sodium counter ions are located between two Hec platelets. SEM image of an aligned GO film (b). White arrows illustrate the in-plane and cross-plane directions. The inset shows an exemplary structure of graphene oxide. Thermal properties: in-plane ($\kappa_{\text{in-plane}}$) and cross-plane ($\kappa_{\text{cross-plane}}$) thermal conductivity (c). The numbers in the graph represent the anisotropy ratio of the thermal conductivity ($\kappa_{\text{in-plane}}/\kappa_{\text{cross-plane}}$). Adapted with permission from Philipp *et al.*, ACS Appl. Mater. Interfaces 2020, 12, 16, 18785–18791. Copyright 2020 American Chemical Society.

The small hectorite nanosheets ($A < 0.4 \mu\text{m}$) were fabricated via ultrasonication of the large sheets ($A < 800 \mu\text{m}$). The treatment and reduced surface area did not affect the basal spacing, order, and chemical composition of the samples. As discussed before in Chapter 10, the in-plane mean free path was still smaller than

the small platelet sizes. Consequently, boundary effects were negligible, which was in agreement with the comparable in-plane thermal conductivity values.

Comparable to the hectorite samples, the sheet size did not affect the structure of the GO samples. However, the stacking was less well-defined, having varied layer separation and randomly interstratified structures. The main influence on the thermal conductivity was found to be the degree of oxidation in both GO samples. An increased amount of defects in the structure with an increasing degree of oxidation is responsible for a decreased thermal conductivity of a sample.

Overall, the hectorite samples were superior to the GO samples concerning the structural order, chemical composition, processability, and thermal anisotropy. Therefore, synthetic hectorite represents a promising material for thermal interface materials or heat management applications.

In conclusion, this thesis explored the thermal properties of different nanoscopic materials and their superstructures with a focus on the structure-property relationship. Thereby, a broad range of materials has been covered: colloidal hollow silica and titania particles, ampholytic polymers, and two-dimensional Bragg stacks made from hectorite polyvinylpyrrolidone, and graphene oxide. The combination of different materials and the assembly into superstructures resulted in thermal properties ranging from high-temperature insulation materials to highly anisotropic materials.

This thesis shows that it is worth “playing” with interlocking bricks in the nanoscale, extending the number of accessible materials and structures. Understanding the thermal structure-property relationship helps create new thermal management materials with tailored properties. In the future, this basic research may help solve thermal challenges, such as insulation applications and heat sinks in electronic devices.

5.2 My Contributions to Joint Publications

Scalable Synthesis of Smooth PS@TiO₂ Core-Shell and TiO₂ Hollow Spheres in the (Sub) Micron Size Range: Understanding Synthesis and Calcination Parameters

by **Anna M. Lechner** (m. Neuhöfer), Tanja Feller, Qimeng Song, Bernd A. F. Kopera, Lukas Heindl, Markus Drechsler, Sabine Rosenfeldt, Markus Retsch

We published this article in *Colloid and Polymer Science*, 2020, 298, 7, 867-878.

I synthesized and prepared the samples, performed the scanning electron and scanning transmission electron microscopy measurements, evaluated the data, created the figures, and worked on the manuscript. Tanja Feller conducted the simultaneous thermal analysis measurements. Qimeng Song performed the reconstruction of the transmission electron microscopy tilt-series data. Bernd Kopera helped with the evaluation of the particle diameters and simultaneous thermal analysis data. Lukas Heindl performed the Zeta potential measurements. Markus Drechsler performed the transmission electron microscopy measurements. Sabine Rosenfeldt performed and analyzed the small-angle X-ray scattering and X-ray powder diffraction experiments. Markus Retsch supervised the work and corrected the manuscript.

High Temperature Thermal Transport in Porous Silica Materials: Direct Observation of a Switch from Conduction to Radiation

by **Anna M. Neuhöfer**, Kai Herrmann, Flora Lebeda, Tobias Lauster, Christoph Kathmann, Svend-Age Biehs, Markus Retsch

We published this article in *Advanced Functional Materials*, 2021, 2108370.

I prepared the samples, performed the high-temperature laser-flash analysis experiments, UV-Vis and IR spectroscopy, scanning electron microscopy, evaluated the data, created the figures, and worked on the manuscript. Kai Herrmann evaluated the data with the double-diffusive model and contributed to the manuscript. Flora Lebeda performed the Comsol simulations. Tobias Lauster helped with the UV-Vis and IR measurements and performed additional measurements. Christoph Kathmann performed the SCUFF-EM calculations. Svend-Age Biehs performed the calculations of the transmission coefficients and heat transfer coefficients, was involved in the scientific discussion, and contributed to the manuscript. Markus Retsch supervised the work, was involved in the scientific discussion, and corrected the manuscript.

Thermal Transport in Binary Colloidal Glasses

by **Anna M. Neuhöfer**, Markus Retsch

in preparation

I prepared the samples, and performed all measurements: scanning electron microscopy, differential scanning calorimetry, density, and light flash analysis. I evaluated the data, created the figures, and wrote the manuscript. Markus Retsch supervised the work, was involved in the scientific discussion, and corrected the manuscript.

Thermal Transport in Ampholytic Polymers: The Role of Hydrogen Bonding and Water Uptake

by Patrick Hummel, **Anna M. Lechner** (m. Neuhöfer), Kai Herrmann, Philip Biehl, Carsten Rössel, Lisa Wiedenhöft, Felix H. Schacher, and Markus Retsch

We published this article in *Macromolecules*, 2020, 53, 13, 5528-5537.

Patrick Hummel prepared the samples, performed the photoacoustic measurements, the density determination, the IR measurements, the humidity experiments, and worked on the manuscript. I performed standard and modulated differential scanning calorimetry measurements. Kai Herrmann conducted additional photoacoustic and density measurements. Philip Biehl, Carsten Rössel and Lisa Wiedenhöft synthesized and characterized the ampholytic polymers PDha, PAGA, PImAA and PMeImAA. Felix H. Schacher supervised to the polymer synthesis and contributed to the manuscript. Markus Retsch supervised the project and worked on the manuscript.

Tunable thermoelastic anisotropy in hybrid Bragg stacks with extreme polymer confinement

by Zuyuan Wang, Konrad Rolle, Theresa Schilling, Patrick Hummel, Alexandra Philipp, Bernd A.F. Kopera, **Anna M. Lechner** (m. Neuhöfer), Markus Retsch, Josef Breu, George Fytas

We published this article in *Angewandte Chemie Int. Ed.*, 2020, 59, 3, 1286-1294.

Zuyuan Wang and Konrad Rolle performed the mechanical characterization with Brillouin light scattering. Theresa Schilling prepared the composite hectorite samples. Patrick Hummel measured the through plane thermal diffusivity with the photoacoustic method. Alexandra Philipp and Bernd Kopera built and implemented the lock-in thermography setup. Alexandra Philipp measured the in-plane thermal diffusivity with lock-in thermography. I measured differential scanning calorimetry to obtain the specific heat capacity. Markus Retsch, Josef Breu, and George Fytas supervised the work and corrected the manuscript.

Anisotropic Thermal Transport in Spray-Coated Single-Phase Two-Dimensional Materials: Synthetic Clay Versus Graphene Oxide

by Alexandra Philipp, Patrick Hummel, Theresa Schilling, Patrick Feicht, Sabine Rosenfeldt, Michael Ertl, Marius Schöttle, **Anna M. Lechner** (m. Neuhöfer), Zhen Xu, Chao Gao, Josef Breu, and Markus Retsch

We published this article in ACS Appl. Mater. Interfaces, 2020, 12, 16, 18785-18791.

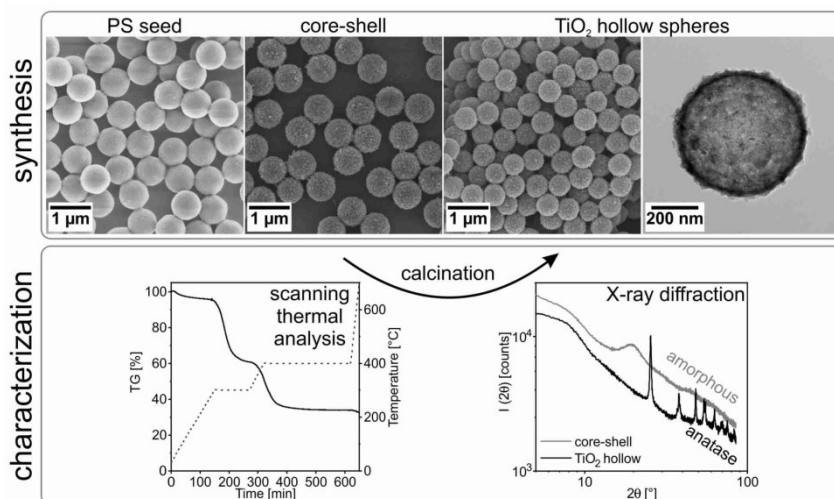
Alexandra Philipp measured the in-plane thermal diffusivity with lock-in thermography and contributed to the manuscript. Patrick Hummel measured the cross-plane thermal conductivity with the photoacoustic method and contributed to the manuscript. Theresa Schilling prepared hectorite and graphene oxide samples and contributed to the manuscript. Patrick Feicht synthesized the graphene oxide (GO-syn) sample. Sabine Rosenfeldt performed the small-angle X-ray scattering measurements. Michael Ertl performed the X-ray photoelectron spectroscopy experiments. Marius Schöttle conducted the Raman measurements. I measured differential scanning calorimetry to obtain the specific heat capacity. Zhen Xu provided the commercial GO material. Chao Gao proofread the manuscript. Josef Breu was involved in scientific discussion, supervised the project and corrected the manuscript. Markus Retsch was involved in scientific discussion, supervised the project and corrected the manuscript.

Scalable Synthesis of Smooth PS@TiO₂ Core-Shell and TiO₂ Hollow Spheres in the (Sub) Micron Size Range: Understanding Synthesis and Calcination Parameters

Anna M. Lechner¹, Tanja Feller¹, Qimeng Song¹, Bernd A. F. Kopera¹, Lukas Heindl¹, Markus Drechsler², Sabine Rosenfeldt^{1,2}, and Markus Retsch^{1,2}

¹ Physical Chemistry I, University of Bayreuth, Universitätsstraße 30, 95440 Bayreuth, Germany

² Bavarian Polymer Institute (BPI), University of Bayreuth, Universitätsstraße 30, 95440 Bayreuth, Germany



Published in *Colloid and Polymer Science*, 2020, DOI: 10.1007/s00396-020-04626-3

Reprinted with permission from Lechner *et al.*, *Colloid Polym Sci* 298, 867–878

(2020). Copyright 2020 The Authors.

6.1 Abstract

Hollow spheres made from titanium dioxide (TiO_2) are interesting structures because of their high surface area and low density, combined with semiconducting properties of the TiO_2 . However, the synthesis is still challenging because of the high reactivity of the titania precursors. Here, we present a simple, reproducible, and scalable way to synthesize TiO_2 hollow spheres in the micrometer/sub-micrometer size range comprising three steps: synthesis of polystyrene template particles, growth of TiO_2 shells, and calcination to hollow spheres. We investigate the importance of adjusting the seed particle surface functionalization via the appropriate choice of comonomer during the dispersion polymerization. An aging step and a calcination process at low temperatures are mandatory to retain the particle integrity during the seed particle removal. We provide a detailed characterization of each step of this process including electron microscopy, small angle X-ray scattering, and simultaneous thermal analysis.

6.2 Introduction

Environmental pollution is a worldwide pressing issue, which needs to be addressed by society, politicians, and researchers. Whereas “chemistry” certainly contributes in various ways to environmental pollution, it also offers solutions toward a more sustainable future. The awareness of this fact led to the field of “green chemistry”. It was introduced in 1998 by Paul Anastas and John Warner and is based on twelve principles to design chemical products and processes in an environmental friendly way^{[1]–[3]}. It includes less hazardous chemical synthesis and solvents, design for energy efficiency, and catalysis. One particular materials class that is regularly discussed in the context of green chemistry is titanium dioxide. Titanium dioxide (TiO_2) can be classified as a green chemical or material because of its photocatalytic activity^{[4],[5]}, usage in solar cells^{[6]–[8]} and batteries^{[9]–[11]}, low toxicity, and high chemical stability.

TiO_2 exists in many different polymorphs, with rutile, brookite, and anatase being the most prominent ones. The main difference of the three polymorphs is their thermodynamic stability. Rutile is the most stable phase in bulk materials and at high temperatures^{[12],[13]}. However, anatase and brookite phases are preferentially formed in small structures in nature as well as during solution-based synthesis^{[13]–[15]}. An amorphous TiO_2 phase is also known and typically used as the starting material for transformations into phase pure anatase particles at high temperatures $> 100\text{ }^\circ\text{C}$ ^{[13],[16],[17]}.

In addition to the microscopic structure, the mesoscopic shape of the TiO_2 material is important for photovoltaic, or photonic applications. Different shapes have been tested as electrodes for photovoltaic applications: thin films, nanoparticle assemblies, inverse opals, and nanotube arrays^{[18]–[23]}. Nanotube arrays achieved photoconversion efficiencies up to 4.9% in solar cells^[22] and can also be used for hydrogen storage applications^[24]. For optical and photonic applications, typically inverse opal structures are used^{[12],[25]–[27]}. Here, the high refractive index of the different polymorphs of TiO_2 is used in the context of structural coloration or efficient scattering.

The different shapes can be achieved via a wide range of synthesis routes^{[12],[28]}. The most common and easy one is the sol-gel method, where a precursor is first hydrolyzed in an acidic or basic environment, followed by polymerization into TiO_2 . Organic metal compounds or inorganic metal salts are used as precursors. The sol-gel synthesis method leads to a wide variety of structures, from nanoparticles in different sizes and shapes to rod- and tube-like structures. Further methods are hydrothermal or solvothermal synthesis, where the reaction takes place at temperatures above the boiling point of the solvent up to 240 °C in an autoclave, and thus at high pressures^{[12],[13],[29]}. Using this method, it is possible to generate phase pure nanoparticles or nanorods. Chemical or physical vapor deposition processes are further synthesis methods that lead to oriented nanowire arrays^{[12],[28]}.

It is also possible to build TiO_2 structures in a templated approach. This leads to inverse opals or hollow spheres after removal of the template. To prepare inverse opals, usually, a template structure from assembled polymer particles is infiltrated either with a precursor mixture that undergoes a sol-gel reaction in the pores or with pre-synthesized TiO_2 nanoparticles^[30]. A different approach was used by Lu *et al.* who first prepared polymer- TiO_2 core-shell particles that were assembled and calcined to get macroporous structures. They were able to prepare phase pure anatase particles at room temperature by using polystyrene particles with grafted poly(styrene sodium sulfonate) chains as template particles. The TiO_2 particles were synthesized by a sol-gel process in between the grafted polymer chains by slowly adding a precursor solution. The core-shell particles were assembled by drying the dispersion and calcined in argon to remain the three-dimensional structure^[4]. This synthesis is located between an inverse opal and a hollow sphere synthesis. Hollow sphere objects have evolved over the past years as a particularly interesting shape, owing to the material structuring on multiple length scales: shell, particle diameter, and particle ensemble^{[31]–[33]}. The particles have a low density but are large enough to be easily filtered and recycled after a catalysis process. Furthermore, the surface area is large and freely accessible from both sides which may be interesting for solar cells or battery devices.

A wide-spread and general approach toward hollow sphere structures is based on shell growth on top of polymeric seed particles. Three steps need to be controlled for this process: (1) template particle formation, (2) shell growth, and (3) template removal (see Fig. 6.1).

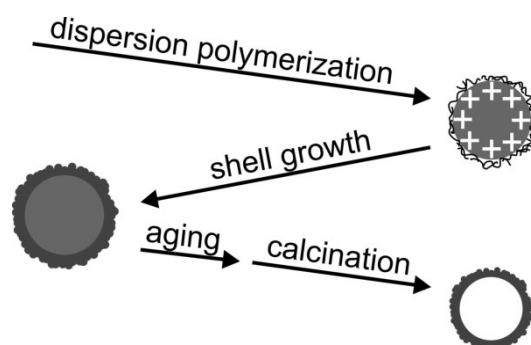
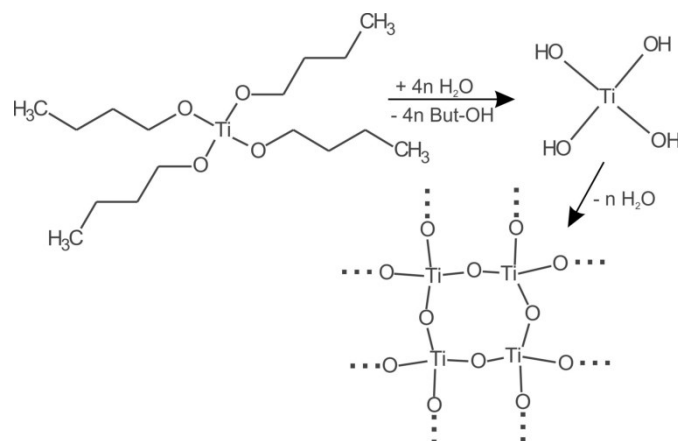


Fig. 6.1: Overview on the three steps that are needed to prepare TiO_2 hollow spheres. First, cationic polystyrene particles are synthesized via dispersion polymerization, using Polyvinylpyrrolidone (PVP) as stabilizer and 2-Methacryloxyethyltrimethylammoniumchloride (MTC) as comonomer. The TiO_2 shells are fabricated by a condensation reaction of titanium butoxide (TBT). After an aging step of 24 h, the particles were calcined at 400°C in air

We briefly outline these steps:

1. The template particles are typically synthesized via emulsifier-free emulsion polymerization or dispersion polymerization. The mechanism of dispersion polymerization has been discussed by Barrett and Arshady and is well known^{[34],[35]}. Generally, size control in dispersion polymerization is achieved by the amount of monomer^[36], solvent^{[35],[37],[38]}, and stabilizer selection^{[34],[37],[38]}, respectively. Cheng *et al.*^[36] used an ethanol/water mixture as solvent and polyvinylpyrrolidone (PVP) as stabilizer. Furthermore, a co-monomer can be used to introduce a specific surface charge.
2. Shell growth: One major issue of the TiO_2 shell growth – in contrast to a silica coating – is the high reactivity of the TiO_2 precursors. Barlier *et al.* examined the condensation reaction in detail^[39]. The reaction happens in two steps: the hydrolysis of the titanium precursor and the condensation to the TiO_2 network (Scheme 6.1). Imhof was the first who coated polystyrene (PS) particles with a thin TiO_2 layer in a one-step sol-gel approach^[40]. Up to now, several more methods have been published based on sol-gel synthesis: varying precursors, solvents, and template particles^{[36],[41]–[43]} Wang *et al.* controlled the diffusion of the TiO_2 precursor by synthesizing in an ethanol/acetonitrile mixture. With this approach, they were able to get defined shell thicknesses between 8 and 65 nm on 300 nm anionic PS particles^[43]. Taniguchi *et al.* used

grafted poly[2-(N,Ndimethylamino)ethyl] methacrylate chains on PS template particles that catalyzed the hydrolysis and condensation of the TiO_2 precursor and were able to coat template particles in a size range of 90– 450 nm^[42]. Cheng *et al.* were the only ones who controlled the reaction speed by adding the TiO_2 precursor dropwise within 30 min instead of one quick addition step. Similar to Imhof *et al.*, they used cationic PS template particles that attracted the TiO_2 precursor and lead to shell growth^[36].



Scheme 6.1: Condensation reaction of titanium butoxide in water

- There are two options to remove the template particles: dissolution and calcination. Toluene^[40] or THF^[41] are commonly used to dissolve non-crosslinked polymer cores via repeated centrifugation and redispersion. This requires a certain degree of porosity and pore sizes in the coated shell to allow for sufficient mass transport. Cheng *et al.* removed the core directly after the synthesis while heating the core-shell particles in an ethanol-ammonia mixture^[36]. Calcination, however, is the more widespread strategy to remove the template^{[40]–[44]}. An inherent side-effect of the thermal decomposition is the concomitant phase transition of the amorphous TiO_2 shell into its anatase form. Therefore, the selection of the right temperature profile and calcination atmosphere is of main importance for the stability of the final hollow particles. It is common to simply heat the samples in air between 500 and 600 °C, followed by an isothermal step of 2 to 3 h^{[40],[42],[43]}. Lu *et al.* found that their structures collapsed when using this simple approach. That is why they first pyrolysed their structures in an inert atmosphere at 500 °C, followed by a calcination step in air to remove the carbon that stabilized the structure^[4]. Schroden *et al.* solved the stability problem by applying a more complex heating ramp. Generally, they used very slow heating rates of 2 K/min and heated the sample first to 300 °C for 2 h, followed by a second heating step to 400 °C for 2 h. With this profile, they were able to get stable inverse opal structures without using an inert atmosphere during the thermal treatment^[25].

We build upon these existing methods and provide an approach toward highly uniform TiO₂ hollow spheres with a scalable and simple synthesis route. We used dispersion polymerization to prepare monodisperse polystyrene particles in a size range of 700 nm to 1.3 μm. Our method extends the range of accessible particle sizes known from emulsifier-free emulsion polymerization considerably, where an upper limit of 600–800 nm is known^[45]. Furthermore, few purification steps are needed in our protocol, which improves the efficiency and yield of the synthesis. Using a combined mass loss – differential scanning calorimetry – infrared analysis, we also provide a better understanding of the calcination mechanism.

6.3 Materials and methods

6.3.1 Materials

2-Methacryloxyethyltrimethylammoniumchloride (MTC, Sigma-Aldrich GmbH, 75 % soln. in water), ethanol abs. (Sigma-Aldrich GmbH, ≥ 99.8 %), polyvinylpyrrolidone (PVP, Sigma-Aldrich GmbH, 40.000 g/mol), styrene (Sigma-Aldrich GmbH, > 99 %), titanium butoxide (TBT, Sigma Aldrich GmbH, 97 %) were used as received. Millipore water was taken from a Millipore Direct Q3UV unit (Merck Millipore). 2,2'-Azobis(2-methylpropionitril) (AIBN, Sigma-Aldrich GmbH) was recrystallized from ethanol before use.

6.3.2 Synthesis of PS particles

3 g PVP (40.000 g/mol) were dissolved in 10 mL ethanol via ultrasonication. The PVP solution, 46 mL of ethanol, 10 mL ultrapure water, half of the styrene (see Table 6.1), and 300 mg AIBN were added to a 250 mL three-necked flask equipped with a reflux condenser and a gas inlet. The solution was degassed while stirring with an egg-shaped stirring bar with a speed of 150 rpm. After 30 min, the mixture was slowly heated to the reaction temperature of 70 °C by turning the hot plate on. Fifty-six milliliters of ethanol, the second half of the styrene, and the MTC were premixed in an Erlenmeyer flask and added after 90 min. The reaction was carried out overnight stirring continuously with a speed of 150 rpm under a slight argon flow. The polymerization was stopped by exposing the dispersion to ambient air and filtrated using a 125 μm nylon filter sieve. The concentration of the particles was determined gravimetrically. For the calculation of the conversion of the particles, the concentration was divided by the theoretical concentration at 100 % conversion.

Tab. 6.1: Amount of styrene, comonomer 2-methacryloxyethyltrimethylammoniumchloride, and initiator 2,2'-Azobis(2-methylpropionitril) (AIBN) that was used for the dispersion polymerization with 112 mL ethanol and 10 mL water. Concentration^a, conversion^a, diameter^b, d , standard deviation^b, σ , and zeta potential, ζ , of the resulting particles

Sample	V (Styrene) [ml]	V (MTC) [μ L]	m (AIBN) [g]	Conc. [mg/mL] ^a	Conv. [%] ^a	d (SEM) [nm] ^b	σ [%] ^b	ζ [mV] ^d
A	6	109	0.3	65	90	673	1.9	34
B	10	180	0.3	90	87	952	2.4	40
C	14	254	0.3	110	83	1059	3.6	34
D	18	327	0.3	134	82	1196	2.3	39
E	22	400	0.3	158	81	1353	2.8	36
F	6	109	0.15	65	87	735	3.6	38
G	10	180	0.15	89	88	902	5.0	37
H	14	254	0.15	106	80	970	4.2	39
I	18	327	0.15	131	81	1191	2.5	37
J	22	400	0.15	178	92	1374	1.7	38
X	6	0	0.3	65	92	802	2.3	1
Y	6	170	0.3	62	86	621	3.6	34
Z ^c	6	300	0.3	51	69			34

^a Determined gravimetrically,

^b measured by SEM image analysis of at least 100 particles,

^c no values are provided for diameter and standard deviation because of an unspherical shape and clustering of the particles, and

^d the zeta potential was determined in an ethanolic dispersion

6.3.3 Synthesis of TiO₂ shells

The synthesis was performed at room temperature. 6.3 mL PS dispersion and 37 mL ethanol were added to an Erlenmeyer flask equipped with a septum. The dispersion was stirred at 350 rpm using a magnetic stirrer bar during the degassing and TBT addition steps. The dispersion was degassed for 10 min with argon. 0.8 mL TBT was mixed with 3.2 mL ethanol and added within 30 min using a syringe pump. After the addition, the dispersion was allowed to age for 24 h without stirring. This aging step is essential to obtain core-shell particles of sufficient mechanical robustness to allow for the final calcination procedure. Particles were washed three times with ethanol for purification.

6.3.4 Synthesis of hollow TiO₂ particles

The particles were freeze-dried in an 80:20 vol% ethanol-water mixture. The PS core was removed by calcination in air. A modified temperature profile of Schroden *et al.*^[25] was used. The samples were heated to 300 °C with a heating rate of 2 K/min, followed by an isothermal step of 2 h. The samples were then heated to 400 °C with a heating rate of 2 K/min, followed by an isothermal step of 12 h. Finally, the samples were cooled down to room temperature for 5 h.

6.3.5 Characterization methods

Scanning electron microscopy (SEM) and scanning transmission electron microscopy (STEM) were performed using a Zeiss Ultraplus instrument using acceleration voltages of 3 kV or 10 kV. InLens, Everhard-Thornley, and STEM detector were used. Core-shell particles were calcined directly on a silicon wafer or SiO₂ TEM grid (Plano GmbH).

The diameter of the PS template particles was evaluated using the MATLAB circle detection function (see S1). The search parameters were optimized manually.

Zeta potential was measured using Zetasizer Nano-ZS (Malvern Panalytical). Three measurements consisting of 10–100 runs were performed. The particles were diluted in ethanol without further purification. No additional substances were added to adjust the pH and background salt concentration.

Transmission electron microscopy (TEM) measurements were performed with a JEOL JEM-2200FS field emission energy filtering transmission electron microscope (FEFTEM) operated at an acceleration voltage of 200 kV. Zero-loss filtered micrographs ($\Delta E \sim 0$ eV) were recorded with a bottom-mounted CMOS camera system (OneView, Gatan) and processed with DM 3.3 image processing software (Gatan). Tilt series and tomography reconstructions were performed with SerialEM and IMOD software packages, supporting the entire tomography workflow, from data acquisition to image processing and modeling. The software was developed by David Mastrorade at the Boulder Laboratory for 3D Electron Microscopy (Boulder, Colorado, USA). Videos of the tilt-series of hollow TiO₂ particles were exported from ImageJ distribution Fiji^[46].

Small-angle X-ray scattering (SAXS) measurements were performed on freeze-dried samples in 1 mm glass capillaries (Hilgenberg, code 4007610, Germany) at room temperature. The measurements were performed in a transmission geometry using a Double Ganesha AIR system (SAXSLAB). A rotating copper anode (MicroMax

007HF, Rigaku Corporation) is the X-ray source of this system. Data was recorded using a position-sensitive detector (PILATUS 300 K, Dectris). Different detector positions were used to cover scattering vectors q between 0.0024 and 0.2 \AA^{-1} . The radially averaged data were normalized to the incident beam and sample thickness. Calculations were done using the software SASFIT (version 0.94.1, Kohlbrecher and Bressler)^[47] or SasView (version 4.2)^[48] or Scatter (version 2.5)^[49].

X-ray powder diffraction patterns for the core-shell and hollow spheres were recorded in Bragg-Brentano-geometry on an Empyrean diffractometer (PANalytical B.V.; the Netherlands) using Cu-K $_{\alpha}$ radiation ($\lambda = 1.54187 \text{ \AA}$)

Simultaneous thermal analysis (STA) measurements were performed on a STA 449 F3 Jupiter (Netzsch) equipped with a Bruker Alpha II IR spectrometer using the same temperature ramp that was used for calcination. A DSC/TG OctoS sample holder and PtRh20 crucibles with lids were used. An airflow of 50 mL/min was adjusted for the measurement. Differential scanning calorimetry (DSC) measurements show an increase in the baseline at the heating step from 400 to 700 °C, which is caused by the baseline calibration. IR measurements were divided by a reference measurement that was taken before the sample measurement started. Due to fluctuations of the baseline over the measurement time, this led to transmission values above 100 % for water bands (3750 cm^{-1} and 1500 cm^{-1}) and CO $_2$ bands (2250 cm^{-1}). Furthermore, a rubber band baseline correction was performed to cancel out an overall intensity shift that was caused by the increasing temperature of the measured gas.

6.4 Results and discussion

6.4.1 Synthesis of polystyrene template particles

An overview on the explicit particle recipes is shown in Table 6.1. To control the particle size, the amount of styrene was increased from 6 to 22 mL. As can be seen in Fig. 6.2a, the particle diameter can be adjusted linearly with the amount of added styrene. The amount of initiator 2,2'-Azobis(2-methylpropionitril) (AIBN) does not influence the final particle size. This can be inferred from particles A–E with 0.3 g of AIBN, and particles F–J with 0.15 g AIBN. Further, we find no influence of the initiator concentration on the conversion of the synthesis within this range. The overall conversion was determined to be 80 to 90 % for all syntheses (see Table 6.1).

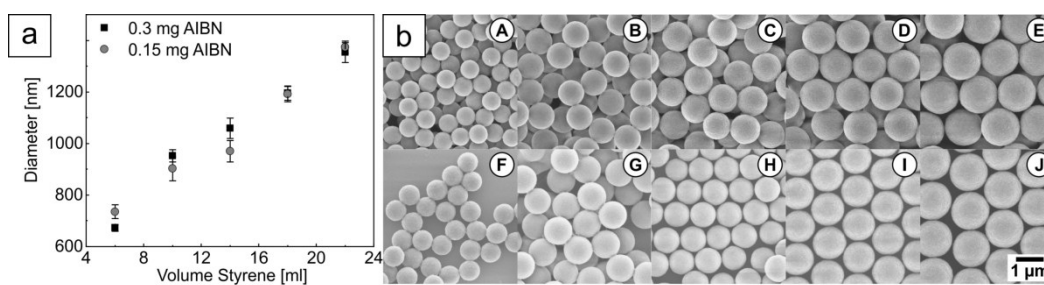


Fig. 6.2: Diameter of particles from dispersion polymerization dependent on the amount of styrene and the amount of initiator AIBN (a). Corresponding SEM images of the PS particles (b) top row with a high and bottom row with a low initiator concentration. The styrene volume increases from left to right

Electrostatic stabilization is introduced by the addition of the comonomer 2-Methacryloxyethyltrimethylammoniumchloride (MTC). This introduces a positive charge to the particle surface. For particles A–J, we kept the molar ratio between monomer and comonomer constant with a ratio of 0.8 mol%. This ratio results in a zeta potential of about +40 mV for all particles. A ratio between monomer and comonomer in the range of 0.8 mol% (particles A–J) up to 1.2 mol% (particles Y) leads to well-functionalized, stable colloids. This is demonstrated by the synthesis of particles X–Z with different amounts of MTC, while styrene and AIBN concentration were kept constant (Fig. 6.3). Particle X was fabricated without MTC, resulting in a zeta potential ~ 0 mV. Nevertheless, owing to the use of PVP as a steric stabilizer, the dispersion is still stable. Without MTC, the particles exhibit a very smooth surface. Increasing the amount of MTC to 170 μ l lead to a rougher surface, while the particle shape remained spherical. Further increasing the amount of MTC to 300 μ l lead to aggregated and deformed particles. The particle aggregation is accompanied by a reduction in the overall conversion. The particle diameter decreased by 200 nm from particles X to Y. A potential reason for this deviation from the expected particle diameter is the better solubility of the PS oligomers due to the copolymerization with MTC. This can reduce the tendency for newly formed oligomers to precipitate onto the existing nuclei. As a consequence, the particle growth is less compared to the comonomer free synthesis. Furthermore, newly formed, small nuclei may aggregate on larger particles, resulting in an increasing particle roughness. Overall, using dispersion polymerization, it is possible to prepare polymer particles with standard deviations that are less or equal 5% of the diameter and are, therefore, highly monodisperse (see SI Fig. 2). It provides access to a complementary size range with particle sizes around 1 μ m. We want to stress the simplicity of these recipes, where all chemicals, except for AIBN were used without any additional purification.

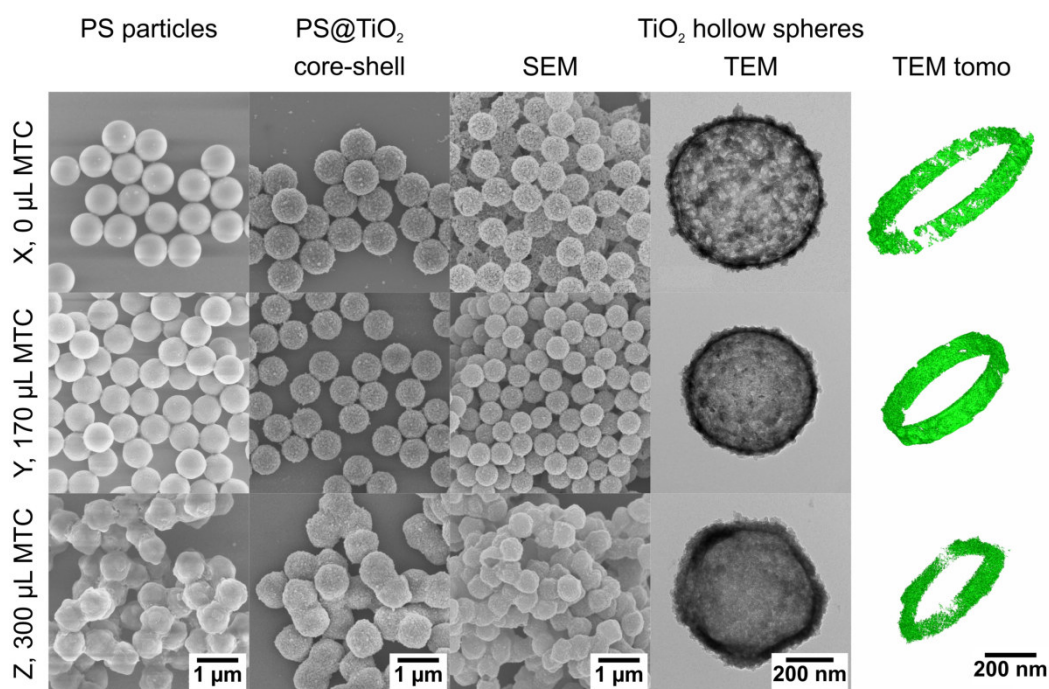


Fig. 6.3: SEM and TEM images of particles X–Z, the corresponding PS@TiO₂ core-shell particles, and hollow TiO₂ particles, as well as TEM tomography reconstructions of parts of a slice of the hollow particles

6.4.2 Synthesis of TiO₂ shells

The PS particles were used as seed templates without purification – not even centrifugation after the dispersion polymerization was employed. This procedure is similar to the scalable synthesis of PS@SiO₂ core-shell and SiO₂ hollow spheres^[50], which provided access to gram-scale amounts of hollow silica spheres. An ethanolic solution ($V = 4 \text{ mL}$) of the precursor titanium butoxide (TBT) was added with a concentration of 0.6 molL^{-1} to the ethanolic particle dispersion using a syringe pump within 30 min. We first investigated the influence of the template particle surface functionalization on the TiO₂ immobilization and shell formation.

Figure 6.3 demonstrates the necessity to adjust the cationic surface functionalization. Without the addition of MTC granular TiO₂ nuclei are immobilized on the polymer surface. For both cases of added MTC (particles Y and Z, respectively) an increasingly smooth shell was observed. The granular appearance of the TiO₂ shell is already apparent in the amorphous shell directly after the TiO₂ condensation. This can be inferred from the SEM images of the core-shell structures (Fig. 6.3, second column), where white speckles cover the previously smooth surface. The presence of MTC at the particle surface apparently influences the nucleation and growth mechanism, which we assign to the altered electrostatic environment. Removing the template core by calcination preserves this granularity, which is shown in TEM

and TEM tomography images (Fig. 6.3 right panels). The spherical shape of the hollow sphere is also preserved, which is apparent from the TEM tilt series (see SI gif files). The highest amount of MTC resulted in the most compact and least granular shells. Nevertheless, the TiO₂ coated structures were clustered due to the already clustered particles in the PS seed dispersion. Consequently, a balanced adjustment of the particle surface functionality via MTC is crucial for the colloidal stability and successful coating step.

6.4.3 Calcination process

Calcination is the final step to obtain hollow TiO₂ particles (Fig. 6.3 right panel). We want to stress that the core-shell particles can only be transformed into hollow spheres successfully after aging the core-shell dispersion for 24 h prior to purification. This aging process apparently improves the formation of a pre-condensed TiO₂ network and proper covalent connectivity among the granular nuclei in the shell. The shell resilience to the thermal decomposition process is improved.

Furthermore, the calcination process itself is very important. We used an adapted temperature profile of Schrodin *et al.*^[25], where the template removal is achieved in a two-step process. The first calcination step is undertaken just at the onset of PS decomposition at a relatively low temperature (300 °C). The complete degradation of the PS is then achieved by a second step at 400 °C. To gain a deeper understanding of the calcination process, combined TGA, DSC, and IR measurements have been performed in air and nitrogen (see Fig. 6.4 a–d and Fig. 6.9).

The pure template particles (polystyrene) show three prominent steps. These are directly related to the applied temperature profile. The degradation starts at the end of the first heating ramp (2 K/min) (1). Already 80 % of polystyrene decompose in the form of CO₂ during the isothermal conditions (300 °C), which took 2 h. The PS decomposition is strongly accelerated during the second heat ramp (2 K/min) to 400 °C (2). Within 300 mins another 13 % of PS are decomposed to CO₂, whereas the residues remain stable in air during the 5 h isothermal heating step at 400 °C. The last 5 % of material is fully decomposed during the last heating ramp up to 700 °C (3). The IR spectra (Fig. 6.4c) only indicated CO₂ as the decomposition product. Single IR spectra of the three steps can be found in the supporting information. Each of the decomposition steps was accompanied by an exothermal event in the DSC signal. This indicates the oxidative decomposition of the polystyrene backbone^{[51],[52]}.

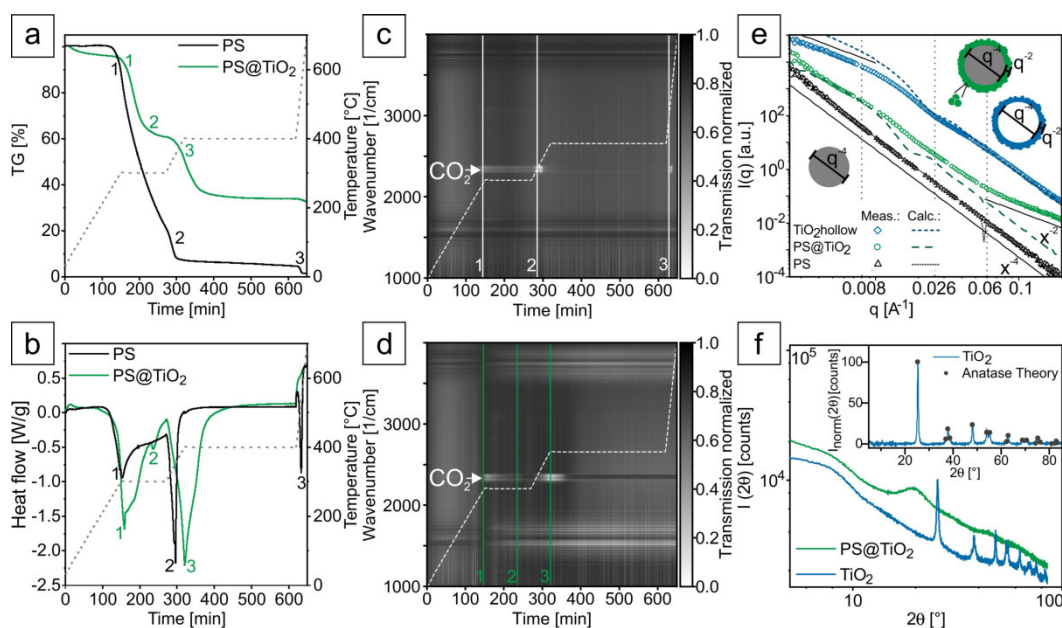


Fig. 6.4: Combined STA (a), DSC (b), and IR measurements to investigate the calcination process of pure PS particles (c) and PS@TiO₂ particles (d). Results of SAXS measurements of PS, PS@TiO₂, and TiO₂ hollow spheres (e) and XRD measurements of the PS@TiO₂ and hollow TiO₂ spheres (f). For all measurements, particles Y have been used

The calcination of the core-shell particles shows a couple of interesting deviations from the pure PS decomposition. The degradation starts at the same time/temperature as the pure polystyrene particles (1). Since the IR spectra show exclusively CO₂ bands (see Fig. 6.4d), it is reasonable to assume that only the polymer decomposed at this point. The PS decomposition, however, is significantly slower compared to the neat seed particles. This could be caused by the limited mass transport to the PS core owing to the presence of the TiO₂ shell. Only 40 % mass has been lost by the end of the first isothermal annealing step at 300 °C. The DSC signal reveals a second event occurring during the isothermal part at 300 °C (2). Xie *et al.* saw a similar exothermic peak in their differential thermal analysis measurements on TiO₂ particles from different phases at 280 °C^[53]. They found that this peak is due to the loss of water absorbed at the TiO₂ particle surface. Therefore, the peak could be linked to a condensation process in the TiO₂ shell and the release of the enclosed water molecules. However, we cannot unambiguously determine the onset of water loss in the IR spectra because the amount of released water is very low and cannot be separated from the background water bands at 3750 cm⁻¹ and 1500 cm⁻¹. The second heating ramp lead to a third prominent step at 400 °C (3). In this case, the degradation product is also CO₂. In contrast to the pure PS particles, the last heating step to 700 °C results in a very small mass loss of only 2%. Since the corresponding IR data show no trace of CO₂, all PS must already be decomposed at the end of the second isothermal step, and a further condensation reaction of the

TiO₂ is assumed. Calculations show that 34 % material should be left over, which agrees well with the experimental data of 33 %.

We conclude that the TiO₂ shell aids the decomposition reaction of the polymer even though the mass transfer is reduced. In our case, it is not possible to see the transformation of the amorphous to the anatase phase in the DSC curves. Xi *et al.* and Li *et al.* saw this event happening at temperatures above 400 °C^{[53],[54]}. Therefore, the effect is likely to be superimposed by the exothermic degradation peak of PS.

These results show the importance of the right temperature profile for the calcination process. The overall particle shrinkage can be estimated by the mass loss of the PS particle at the first heating step. The mass loss translates into a volume shrinkage of the template particle. Assuming an isotropic shrinkage of the template particle, the diameter of the shrunk particle can be recalculated. The shrunk particle size then corresponds to the final hollow-core diameter. Starting with an initial particle with a diameter of 621 nm and considering a mass loss of 40 %, this would result in a shrunk particle diameter of 520 nm. This is in reasonable agreement with the experimental data, where the hollow core has a size of ~ 500 nm. Calcinations in inert atmosphere, where the template particle is intact much longer, show less shrinkage of the hollow spheres (see SI Fig. 6.9). This observation strengthens the interpretation that the second peak in the DSC measurements is connected to the formation of the final and stable TiO₂ structure, and therefore to the shell condensation process. Calcination profiles, which omit the mild calcination at 300 °C or which feature too fast heating ramps, sacrifice the shell integrity and result in collapsed structures (see SI Fig. 6.10).

The structures of the polystyrene, core-shell, and hollow particles Y (see Fig. 6.4e) were further characterized by SAXS and SEM/TEM. The measured SAXS data exhibit only weak features, which prevent a thorough fitting analysis. Furthermore, PS seed particles are too large to identify the radius in the experimentally reachable q range. Thus, based on the TEM result, we calculated the form factor of homogeneous spheres with a diameter of 621 nm and compared it to our experimental data - both agree well. The model has a Gaussian size distribution with a standard deviation of 10 %, which is slightly higher compared to the SEM images due to instrumental smearing effects. The measurement of the PS@TiO₂ core-shell particles is shown in Fig. 6.4e (green symbols). The scattering of PS@SiO₂ can be described by the model of a homogeneous core-homogeneous shell^[50]. The sharp and well defined boundary between core and (monodisperse) shell leads to significant oscillations in the scattering data. In contrast to PS@SiO₂ the shell of PS@TiO₂ is less dense and highly particulate (see Fig. 6.3). As consequence of such a fractal-like shell morphology, the corresponding form factor scattering miss such pronounced oscillations. The

main features are a q^{-4} scaling at intermediate q (ca. $0.008\text{--}0.05 \text{ \AA}^{-1}$) and a q^{-2} power law for $q > 0.057 \text{ \AA}^{-1}$. A very weak oscillation around 0.017 \AA^{-1} hints toward the expected dimension of the shell thickness of about 30–40 nm before calcination. The q^{-2} power law for $q > 0.057 \text{ \AA}^{-1}$ is indicative of strong scatters with a mainly 2D structure. This is in contrast to scattering patterns of similar (silica-based) core-shell systems^{[55],[56]}. These systems exhibit a pronounced form factor and no q^{-2} scaling law at high q .

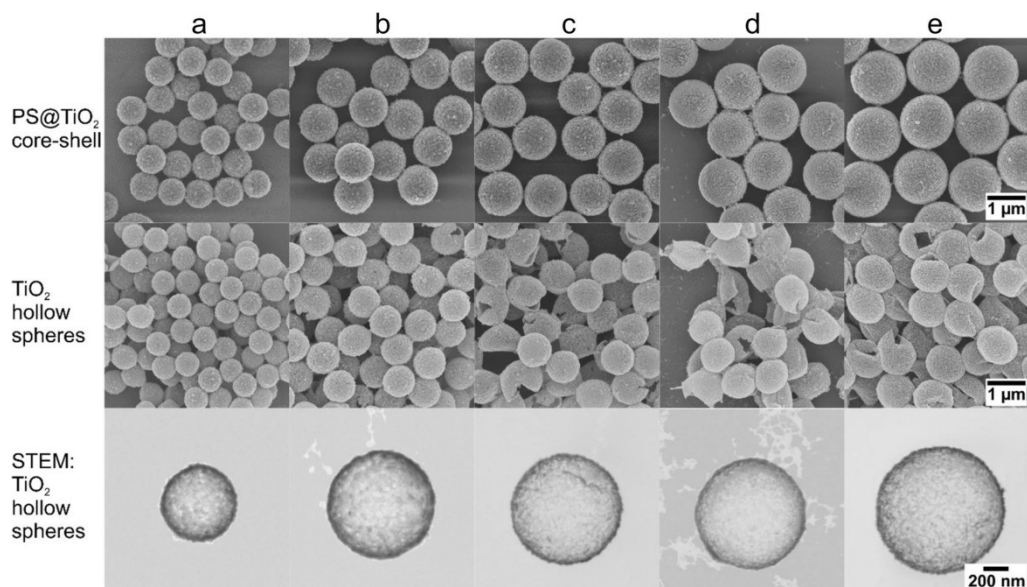


Fig. 6.5: SEM images of PS@TiO₂ core-shell particles of different sizes (A–E) and corresponding TiO₂ hollow spheres. The last row shows STEM images of single TiO₂ hollow spheres

The deviation of our system from these findings can be understood by the scattering contrast situation ($\text{PS} \approx 9.51 \times 10^{-6} \text{ \AA}^{-2}$, $\text{TiO}_2 \approx 31.8 \times 10^{-6} \text{ \AA}^{-2}$, no solvent) and the lower bending curvature due to the large template particle diameter. At high q , the q^{-2} term seems to simply add up to the scattering of a pure PS sphere (q^{-4}) underlining the fact that the shell is particulate. For comparison, the scattering of homogeneous core-homogeneous shell spheres is given ($d = 621 \text{ nm}$, 10% Gaussian distribution and $d_{\text{shell}} = 35 \text{ nm}$, 20% Gaussian distribution; green dotted line PS@TiO₂). During the calcination process, the amorphous TiO₂ shells undergo a transformation into anatase phase (Fig. 6.4f). During this process the overall size of the particle shrinks. The experimental SAXS scattering pattern of these hollow spheres exhibits a minimum at $q \approx 0.026 \text{ \AA}^{-1}$. The corresponding correlation length of about 24 nm agrees well with the thickness of the TiO₂ shell obtained from TEM analysis. The q^{-4} behavior at intermediate and high q reflects the contrast situation for hollow spheres. This is corroborated by the calculation of homogenous hollow spheres (blue dotted line; $d_{\text{inner}} = 621 \text{ nm}$, 10% Gaussian with zero contrast, $d_{\text{shell}} = 24 \text{ nm}$, 25% Gaussian with contrast $31.8 \times 10^{-6} \text{ \AA}^{-2}$). The

q^{-2} power law at low q is attributed to the particulate shell, since rough surfaces can be considered as fractals.

As stated above, the TiO_2 shell undergoes a phase transition during the calcination procedure. This can be seen in X-ray diffraction measurements in Fig. 6.4f. The core-shell particles (green line) do not show any features except for an amorphous halo. This pattern is caused by the TiO_2 and the amorphous polymer core. After calcination, distinct peaks are visible (blue line). The inset shows the normalized data that agree very well with the expected diffraction pattern of anatase.

6.4.4 Size series of TiO_2 hollow particles

We now want to highlight the robustness of our synthetic protocol. Therefore, TiO_2 shells have been synthesized on PS particles A–E. Setting the MTC/Styrene ratio to 0.8 mol% during the seed synthesis and the amount of TBT to 5.5×10^{-4} to 6.5×10^{-4} mol/m² particle surface during the coating step, it is possible to fabricate TiO_2 core-shell particles without secondary nucleation or particle clustering (Fig. 6.5). When using 800 μL of TBT, shell thicknesses between 45 and 60 nm could be achieved. Stable and smooth TiO_2 shells could be immobilized on the PS seed particles. Also, the template particles themselves remain colloidally stable and are coated as individual objects. One may expect that the shell thickness decreases with increasing template particle diameter when employing the same amount of TBT precursor. This, however, would only be true, if the same particle concentration was used. Owing to our scalable process, we directly use the as-synthesized polymer dispersion, where both, particle diameter and particle concentration vary with the initial monomer concentration. Both parameters cancel each other out leading to comparable shell thicknesses for each batch.

Calcination of the particles in air leads to an isotropic shrinkage up to 20 % compared to the core-shell size (see STEM, Fig. 6.5). For particles > 700 nm we find no systematic variation of the degree of shrinkage to the particle size. As a consequence, the TiO_2 hollow spheres B, C, and D all have the same particle diameter of ~ 900 nm; particle E is slightly larger with 1025 nm. Yet, despite the considerable shrinkage, the particles retain their spherical shape and shrink in an isotropic fashion. This is even more remarkable as the ratio t/D between shell thickness (t) and particle diameter (D) is very small. t/D ranges from 4 % for the smallest hollow spheres to 2 % for the largest one. With decreasing t/R ratio the mechanical stability of the TiO_2 hollow spheres decreases, which is also known for their silica shell counterparts^[57]. We, consequently, observed an increased portion of fractured or buckled hollow spheres from particles C to E.

6.5 Conclusion

Our contribution addresses several important aspects in the field of templated hollow sphere synthesis. We firstly introduced dispersion polymerization as a suitable alternative to established emulsion polymerization techniques for synthesizing template particles in the 500 to 1300 nm size regime. The template particles can be functionalized with comonomers to control the particle surface charge. These template beads can be used without additional purification steps for the synthesis of homogeneous TiO₂ shells. This strategy allows for a scalable synthesis of well-coated TiO₂ core-shell particles. However, it is important to control the amount of comonomer used during the dispersion polymerization. This affects the stability of the colloidal particles and the granularity of the TiO₂ shell. We thoroughly investigated the calcination procedure yielding the hollow particles. The usage of an isothermal step at the onset of polystyrene decomposition is crucial for retaining the hollow particle shape. Our presented method could be applied to a range of template particles with different sizes. Overall, this facile, reproducible and scalable method, creates well-defined TiO₂ core-shell or hollow particles that can be used in applications, where the properties of TiO₂ are beneficial.

Acknowledgements

We thank Stefan Rettinger for the help with STA experiments and the Bavarian Polymer Institute, especially Martina Heider, for helping with SEM and STEM measurements. Prof. André Gröschel is acknowledged for the help regarding the TEM reconstruction.

Funding information

Open Access funding provided by Projekt DEAL. This project was funded by the German Research Foundation (DFG Colloid Polym SciRE3550/2-1). Additional support was provided by ERC Starting Grant VISIRday under Grant No. 714968. This work benefited from the use of the SasView application, originally developed under NSF Award DMR- 0520547. SasView also contains code developed with funding from EU Horizon 2020 programme under the SINE2020 project Grant No. 654000.

6.6 References

- [1] P. Anastas and N. Eghbali, „Green chemistry: Principles and practice“, *Chem. Soc. Rev.*, vol. 39, no. 1, pp. 301–312, 2010.
- [2] R. A. Sheldon, I. W. C. E. Arends, and U. Hanefeld, *Green Chemistry and Catalysis*. Wiley, Feb. 2007.
- [3] P. T. Anastas, „Introduction: green chemistry“, *Chemical Reviews*, vol. 107, no. 6, pp. 2167–2168, Jun. 2007.
- [4] Y. Lu, M. Hoffmann, R. S. Yelamanchili, *et al.*, „Well-defined crystalline TiO₂ nanoparticles generated and immobilized on a colloidal nanoreactor“, *Macromolecular Chemistry and Physics*, vol. 210, no. 5, pp. 377–386, Mar. 2009.
- [5] H. Kisch, Ed., *Semiconductor Photocatalysis*. Wiley-VCH Verlag GmbH & Co. KGaA, Dec. 2014.
- [6] B. O'Regan and M. Grätzel, „A low-cost, high-efficiency solar cell based on dye-sensitized colloidal TiO₂ films“, *Nature*, vol. 353, no. 6346, pp. 737–740, Oct. 1991.
- [7] O. K. Varghese, M. Paulose, and C. A. Grimes, „Long vertically aligned titania nanotubes on transparent conducting oxide for highly efficient solar cells“, *Nature Nanotechnology*, vol. 4, no. 9, pp. 592–597, Aug. 2009.
- [8] G. Phani, G. Tulloch, D. Vittorio, and I. Skryabin, „Titania solar cells: New photovoltaic technology“, *Renewable Energy*, vol. 22, no. 1-3, pp. 303–309, Jan. 2001.
- [9] L. Fu, T. Zhang, Q. Cao, H. Zhang, and Y. Wu, „Preparation and characterization of three-dimensionally ordered mesoporous titania microparticles as anode material for lithium ion battery“, *Electrochemistry Communications*, vol. 9, no. 8, pp. 2140–2144, Aug. 2007.
- [10] G. F. Ortiz, I. Hanzu, T. Djenizian, *et al.*, „Alternative li-ion battery electrode based on self-organized titania nanotubes“, *Chemistry of Materials*, vol. 21, no. 1, pp. 63–67, Jan. 2009.
- [11] K.-T. Kim, G. Ali, K. Y. Chung, *et al.*, „Anatase titania nanorods as an intercalation anode material for rechargeable sodium batteries“, *Nano Letters*, vol. 14, no. 2, pp. 416–422, Jan. 2014.
- [12] X. Chen and S. S. Mao, „Titanium dioxide nanomaterials: synthesis, properties, modifications, and applications“, *Chemical Reviews*, vol. 107, no. 7, pp. 2891–2959, Jul. 2007.

- [13] D. Reyes-Coronado, G. Rodriguez-Gattorno, M. E. Espinosa-Pesqueira, *et al.*, „Phase-pure TiO₂nanoparticles: Anatase, brookite and rutile“, *Nanotechnology*, vol. 19, no. 14, p. 145 605, Mar. 2008.
- [14] A. Zaban, S. T. Aruna, S. Tirosh, B. A. Gregg, and Y. Mastai, „The effect of the preparation condition of tio₂ colloids on their surface structures“, *The Journal of Physical Chemistry B*, vol. 104, no. 17, pp. 4130–4133, May 2000.
- [15] J. F. Banfield, B. L. Bischoff, and M. A. Anderson, „TiO₂ accessory minerals: Coarsening, and transformation kinetics in pure and doped synthetic nanocrystalline materials“, *Chemical Geology*, vol. 110, no. 1-3, pp. 211–231, Nov. 1993.
- [16] K. Yanagisawa and J. Ovenstone, „Crystallization of anatase from amorphous titania using the hydrothermal technique: Effects of starting material and temperature“, *The Journal of Physical Chemistry B*, vol. 103, no. 37, pp. 7781–7787, Sep. 1999.
- [17] H. Yin, Y. Wada, T. Kitamura, *et al.*, „Hydrothermal synthesis of nanosized anatase and rutile TiO₂ using amorphous phase TiO₂“, *Journal of Materials Chemistry*, vol. 11, no. 6, pp. 1694–1703, 2001.
- [18] K. Shankar, J. Bandara, M. Paulose, *et al.*, „Highly efficient solar cells using TiO₂nanotube arrays sensitized with a donor-antenna dye“, *Nano Letters*, vol. 8, no. 6, pp. 1654–1659, Jun. 2008.
- [19] M. Paulose, K. Shankar, O. K. Varghese, *et al.*, „Backside illuminated dye-sensitized solar cells based on titania nanotube array electrodes“, *Nanotechnology*, vol. 17, no. 5, pp. 1446–1448, Feb. 2006.
- [20] M. Zukalova, A. Zukal, L. Kavan, *et al.*, „Organized mesoporous TiO₂films exhibiting greatly enhanced performance in dye-sensitized solar cells“, *Nano Letters*, vol. 5, no. 9, pp. 1789–1792, Sep. 2005.
- [21] P. Somani, C. Dionigi, M. Murgia, *et al.*, „Solid-state dye PV cells using inverse opal TiO₂ films“, *Solar Energy Materials and Solar Cells*, vol. 87, no. 1-4, pp. 513–519, May 2005.
- [22] M. Adachi, Y. Murata, I. Okada, and S. Yoshikawa, „Formation of titania nanotubes and applications for dye-sensitized solar cells“, *Journal of The Electrochemical Society*, vol. 150, no. 8, G488, 2003.
- [23] Y. Ohsaki, N. Masaki, T. Kitamura, *et al.*, „Dye-sensitized TiO₂ nanotube solar cells: Fabrication and electronic characterization“, *Physical Chemistry Chemical Physics*, vol. 7, no. 24, p. 4157, 2005.
- [24] S. H. Lim, J. Luo, Z. Zhong, W. Ji, and J. Lin, „Room-temperature hydrogen uptake by TiO₂nanotubes“, *Inorganic Chemistry*, vol. 44, no. 12, pp. 4124–4126, Jun. 2005.

- [25] R. C. Schroden, M. Al-Daous, C. F. Blanford, and A. Stein, „Optical properties of inverse opal photonic crystals“, *Chemistry of Materials*, vol. 14, no. 8, pp. 3305–3315, Aug. 2002.
- [26] M. Retsch and U. Jonas, „Hierarchically structured, double-periodic inverse composite opals“, *Advanced Functional Materials*, vol. 23, no. 43, pp. 5381–5389, May 2013.
- [27] A. Stein, B. E. Wilson, and S. G. Rudisill, „Design and functionality of colloidal-crystal-templated materials chemical applications of inverse opals“, *Chem. Soc. Rev.*, vol. 42, no. 7, pp. 2763–2803, 2013.
- [28] M. T. Noman, M. A. Ashraf, and A. Ali, „Synthesis and applications of nano-TiO₂: A review“, *Environmental Science and Pollution Research*, vol. 26, no. 4, pp. 3262–3291, Dec. 2018.
- [29] A. Rabenau, „The role of hydrothermal synthesis in preparative chemistry“, *Angewandte Chemie International Edition in English*, vol. 24, no. 12, pp. 1026–1040, Dec. 1985.
- [30] C.-Y. Cho and J. H. Moon, „Hierarchical twin-scale inverse opal TiO₂ electrodes for dye-sensitized solar cells“, *Langmuir*, vol. 28, no. 25, pp. 9372–9377, Jun. 2012.
- [31] X. Wang, J. Feng, Y. Bai, Q. Zhang, and Y. Yin, „Synthesis, properties, and applications of hollow micro-/nanostructures“, *Chemical Reviews*, vol. 116, no. 18, pp. 10983–11060, May 2016.
- [32] M. Chen, C. Ye, S. Zhou, and L. Wu, „Recent advances in applications and performance of inorganic hollow spheres in devices“, *Advanced Materials*, vol. 25, no. 37, pp. 5343–5351, Jun. 2013.
- [33] L. Zhou, Z. Zhuang, H. Zhao, *et al.*, „Intricate hollow structures: Controlled synthesis and applications in energy storage and conversion“, *Advanced Materials*, vol. 29, no. 20, p. 1602914, Feb. 2017.
- [34] R. Arshady, „Suspension, emulsion, and dispersion polymerization: A methodological survey“, *Colloid & Polymer Science*, vol. 270, no. 8, pp. 717–732, Aug. 1992.
- [35] K. E. J. Barrett, „Dispersion polymerisation in organic media“, *British Polymer Journal*, vol. 5, no. 4, pp. 259–271, Jul. 1973.
- [36] X. Cheng, M. Chen, L. Wu, and G. Gu, „Novel and facile method for the preparation of monodispersed titania hollow spheres“, *Langmuir*, vol. 22, no. 8, pp. 3858–3863, Apr. 2006.
- [37] S. Kawaguchi and K. Ito, „Dispersion polymerization“, in *Polymer Particles*, Springer Berlin Heidelberg, Feb. 2005, pp. 299–328.

- [38] A. J. Paine, W. Luymes, and J. McNulty, „Dispersion polymerization of styrene in polar solvents. 6. influence of reaction parameters on particle size and molecular weight in poly(n-vinylpyrrolidone)-stabilized reactions“, *Macromolecules*, vol. 23, no. 12, pp. 3104–3109, Jun. 1990.
- [39] V. Barlier, V. Bounor-Legare, G. Boiteux, J. Davenas, and D. Leonard, „Hydrolysis–condensation reactions of titanium alkoxides in thin films: A study of the steric hindrance effect by x-ray photoelectron spectroscopy“, *Applied Surface Science*, vol. 254, no. 17, pp. 5408–5412, Jun. 2008.
- [40] A. Imhof, „Preparation and characterization of titania-coated polystyrene spheres and hollow titania shells“, *Langmuir*, vol. 17, no. 12, pp. 3579–3585, Jun. 2001.
- [41] M. Agrawal, A. Pich, N. E. Zafeiropoulos, and M. Stamm, „Fabrication of hollow titania microspheres with tailored shell thickness“, *Colloid and Polymer Science*, vol. 286, no. 5, pp. 593–601, Jan. 2008.
- [42] T. Taniguchi, F. Murakami, M. Kasuya, *et al.*, „Preparation of titania hollow particles with independently controlled void size and shell thickness by catalytic templating core–shell polymer particles“, *Colloid and Polymer Science*, vol. 291, no. 1, pp. 215–222, May 2012.
- [43] P. Wang, D. Chen, and F.-Q. Tang, „Preparation of titania-coated polystyrene particles in mixed solvents by ammonia catalysis“, *Langmuir*, vol. 22, no. 10, pp. 4832–4835, May 2006.
- [44] R. S. Yelamanchili, Y. Lu, T. Lunkenbein, *et al.*, „Shaping colloidal rutile into thermally stable and porous mesoscopic titania balls“, *Small*, vol. 5, no. 11, pp. 1326–1333, Jun. 2009.
- [45] P. Ruckdeschel, „Transport phenomena in silica hollow spheres and hybrid materials“, PhD thesis, University of Bayreuth, 2018.
- [46] J. Schindelin, I. Arganda-Carreras, E. Frise, *et al.*, „Fiji: An open-source platform for biological-image analysis“, *Nature Methods*, vol. 9, no. 7, pp. 676–682, Jun. 2012.
- [47] I. Breßler, J. Kohlbrecher, and A. F. Thünemann, „SASfit: A tool for small-angle scattering data analysis using a library of analytical expressions“, *Journal of Applied Crystallography*, vol. 48, no. 5, pp. 1587–1598, Sep. 2015.
- [48] M. Doucet, J. H. Cho, G. Alina, *et al.*, *Sasview version 4.2*, 2018.
- [49] S. Förster, S. Fischer, K. Zielske, *et al.*, „Calculation of scattering-patterns of ordered nano- and mesoscale materials“, *Advances in Colloid and Interface Science*, vol. 163, no. 1, pp. 53–83, Mar. 2011.
- [50] P. Ruckdeschel, M. Dulle, T. Honold, *et al.*, „Monodisperse hollow silica spheres: An in-depth scattering analysis“, *Nano Research*, vol. 9, no. 5, pp. 1366–1376, May 2016.

- [51] P. Kannan, J. J. Biernacki, D. P. Visco, and W. Lambert, „Kinetics of thermal decomposition of expandable polystyrene in different gaseous environments“, *Journal of Analytical and Applied Pyrolysis*, vol. 84, no. 2, pp. 139–144, Mar. 2009.
- [52] S. Malhotra, „Thermal decomposition of polystyrene“, *Polymer*, vol. 16, no. 2, pp. 81–93, Feb. 1975.
- [53] H. Xie, Q. Zhang, T. Xi, J. Wang, and Y. Liu, „Thermal analysis on nanosized TiO₂ prepared by hydrolysis“, *Thermochimica Acta*, vol. 381, no. 1, pp. 45–48, Jan. 2002.
- [54] D. Li, S. Chen, D. Wang, *et al.*, „Thermo-analysis of nanocrystalline TiO₂ ceramics during the whole sintering process using differential scanning calorimetry“, *Ceramics International*, vol. 36, no. 2, pp. 827–829, Mar. 2010.
- [55] J. A. Balmer, O. O. Mykhaylyk, A. Schmid, *et al.*, „Characterization of polymer-silica nanocomposite particles with core-shell morphologies using monte carlo simulations and small angle x-ray scattering“, *Langmuir*, vol. 27, no. 13, pp. 8075–8089, Jul. 2011.
- [56] L. A. Fielding, O. O. Mykhaylyk, A. Schmid, *et al.*, „Visible mie scattering from hollow silica particles with particulate shells“, *Chemistry of Materials*, vol. 26, no. 2, pp. 1270–1277, Jan. 2014.
- [57] J. Yin, M. Retsch, J.-H. Lee, E. L. Thomas, and M. C. Boyce, „Mechanics of nanoindentation on a monolayer of colloidal hollow nanoparticles“, *Langmuir*, vol. 27, no. 17, pp. 10 492–10 500, Sep. 2011.

6.7 Supporting Information

6.7.1 Particle diameter evaluation

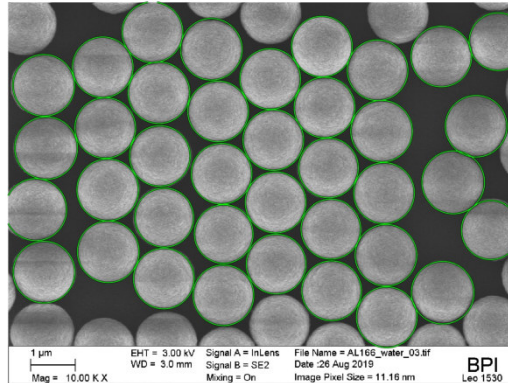


Fig. 6.6: Output of SEM image after MATLAB circle detection method. The green circles indicate the particles that were included in the evaluation

6.7.2 PS particle histograms

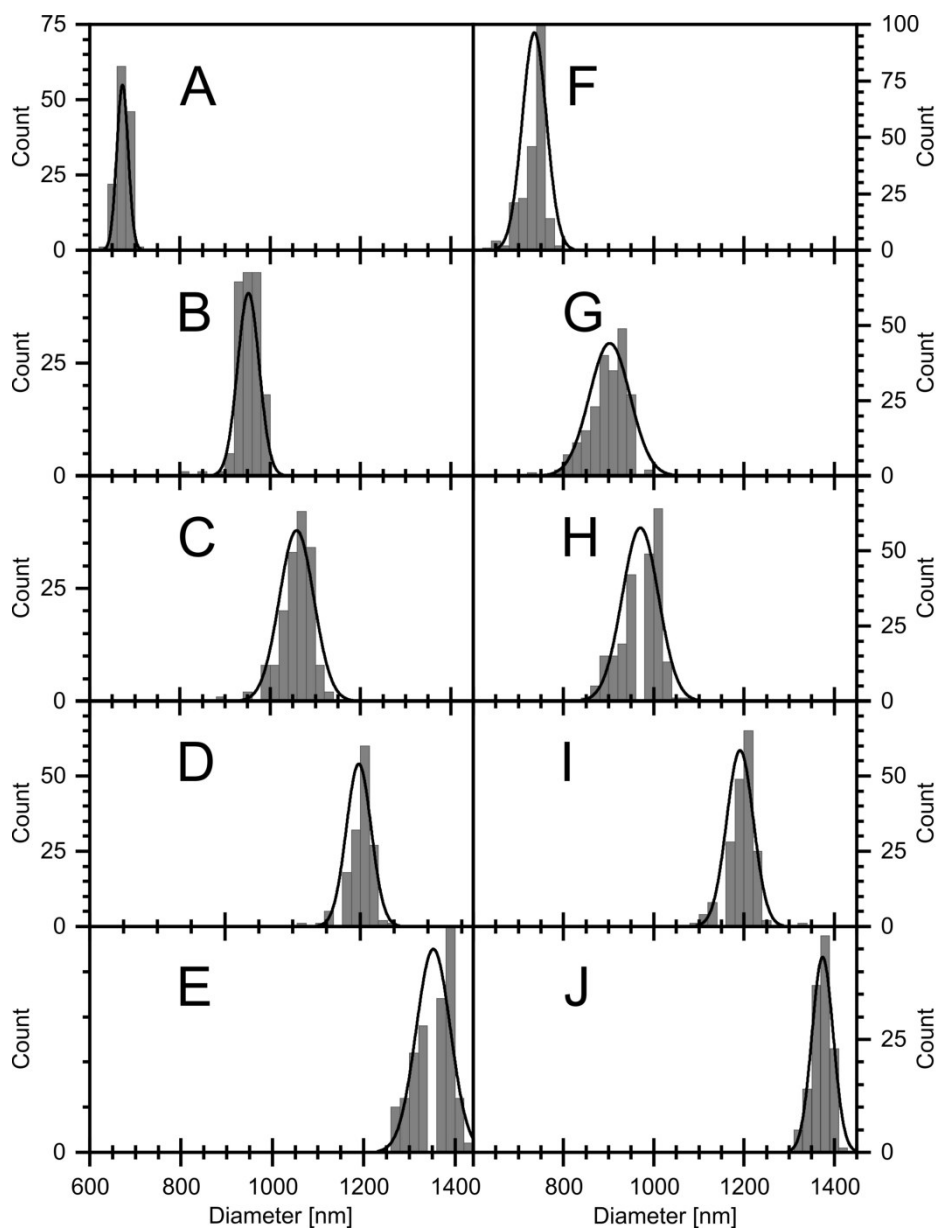


Fig. 6.7: Histograms of the polystyrene particles A-J

6.7.3 PS particle surface area per mL dispersion

Tab. 6.2: Calculation of total surface area (A_{tot}) per ml PS particle dispersion, assuming the density of PS being 1040 kg/m^3 . First, the number (n) of particles is calculated from the mass (m) of a single particle and the concentration (c) of the dispersion. A_{tot} is determined by multiplying n with the surface area of one particle. The total surface area per ml does not change significantly.

	d (SEM) [nm]	m (particle) [mg]	c [mg/ml]	n (particle) per ml	A (particle) [m^2]	A_{tot} per ml
A	673	1.66E-10	6.50E+01	3.92E+11	1.42E-12	5.57E-01
B	952	4.70E-10	9.00E+01	1.92E+11	2.85E-12	5.45E-01
C	1059	6.47E-10	1.10E+02	1.70E+11	3.52E-12	5.99E-01
D	1196	9.32E-10	1.34E+02	1.44E+11	4.49E-12	6.46E-01
E	1353	1.35E-09	1.58E+02	1.17E+11	5.75E-12	6.74E-01

6.7.4 Single IR spectra

Fig. 6.8 shows the single IR spectra of the STA measurements of pure PS and PS@TiO₂ particles shown in Fig. 6.4. The spectra were exported after the first baseline correction. At the first baseline correction, the measured signal is divided by a baseline measurement that is taken before the sample measurement starts. Since the baseline varies with increasing temperature, this can lead to transmittance values larger than 1. This effect was visible in the PS sample. Furthermore, an intensity shift is visible with increasing temperature. The effect is larger for the PS@TiO₂ sample and is caused by the increasing temperature of the measured gas, which is not considered in the first baseline correction. The OPUS software tries to cancel this effect out by the rubberband baseline correction.

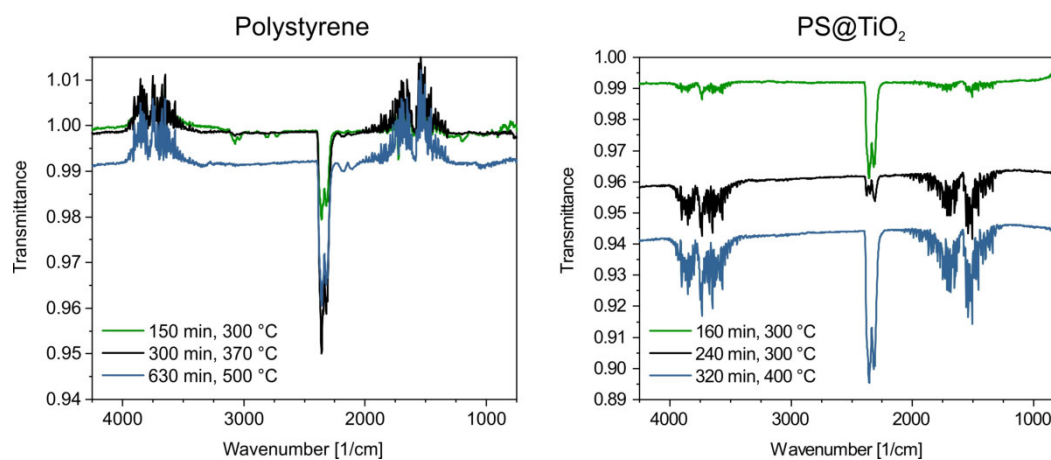


Fig. 6.8: Single IR Spectra of STA measurements at positions 1, 2 and 3 of Fig. 6.4. The spectra were taken before the rubberband baseline correction.

6.7.5 Particle shrinkage inert calcination

The left column of figure 6.9 shows the STA data from inert calcination of PS@TiO₂ particles A. In the TG (a) and DSC (b) curves three events are visible. The first step happens during the first heating ramp to 300 °C and may be due to loss of adsorbed water and loss of low molecular weight residues. The DSC signal reveals a jump at the onset of the isothermal step (2). In contrast to calcination in air, we observe only a minimum mass loss during this isothermal step. The last step (3) happens at the second heating ramp to 400 °C. During this heating ramp a rapid mass loss to the expected value of about 35 % happens. Owing to the inert atmosphere the IR signal shows only spectra of aromatic hydrocarbons and no CO₂ in this range. The decomposition occurs in this case via an endothermic decomposition in contrast to the exothermic combustion in air.

From the SEM images on the right column (d-f) it can be seen that the particle shrinkage in inert calcination atmosphere is less than in air calcination. In the case of inert calcination, the mass loss is 10 % until the precondensation starts. In the case of core-shell particles A, the diameter shrinkage is 12 % in the case of inert calcination and 18 % in the case of air calcination. This underlines our observation that the first degradation and size reduction of the PS template particle strongly affects the size of the final TiO₂ hollow particles.

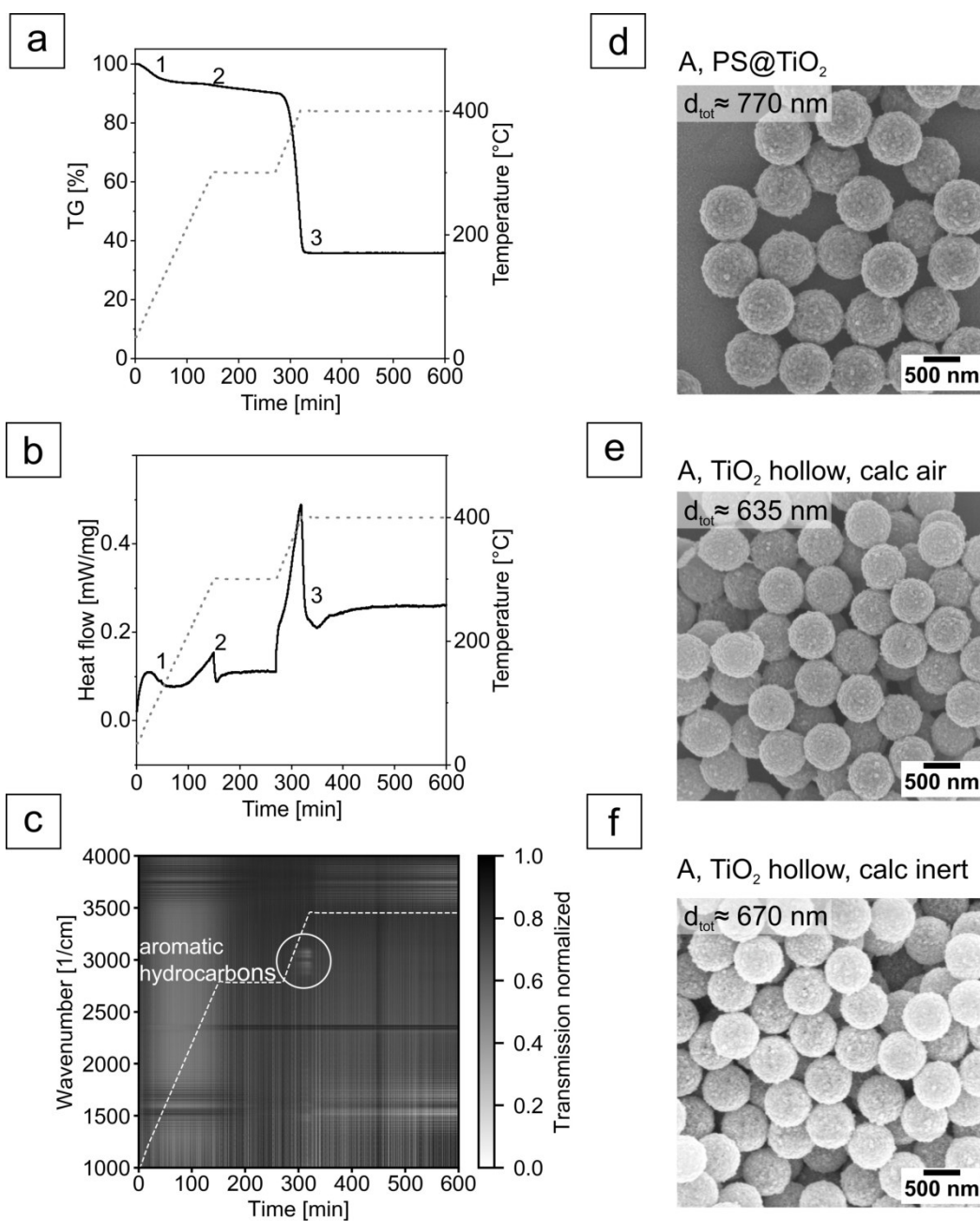


Fig. 6.9: TG (a), DSC (b), and IR (c) measurements of inert calcination of PS@TiO₂ particles A. The right column shows SEM images of the core-shell (d) particles, hollow TiO₂ particles calcined in air (e) and hollow particles calcined in inert atmosphere (f)

6.7.6 Influence of calcination ramp on particle stability

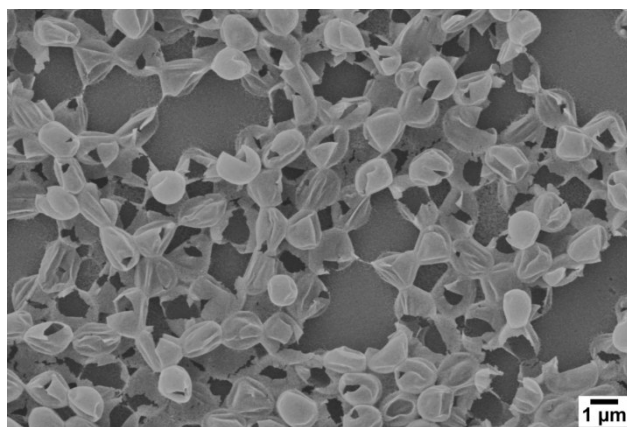


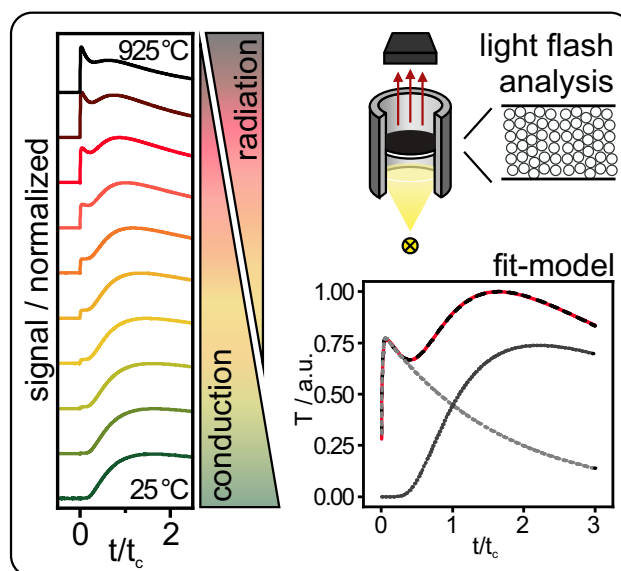
Fig. 6.10: Particles that collapsed during calcination to 500 °C with 2 K/min without isothermal steps

High-Temperature Thermal Transport in Porous Silica Materials: Direct Observation of a Switch from Conduction to Radiation

Anna M. Neuhöfer¹, Kai Herrmann¹, Flora Lebeda¹, Tobias Lauster¹, Christoph Kathmann², Svend-Age Biehs², Markus Retsch¹

¹ Physical Chemistry I, University of Bayreuth, Universitätsstraße 30, 95440 Bayreuth, Germany

² Institut für Physik, Carl von Ossietzky Universität, 26111 Oldenburg, Germany



Published in *Advanced Functional Materials*, **2020**, DOI: 10.1002/adfm.202108370

Reprinted with permission from Neuhöfer *et al.*, *Adv. Funct. Mater.* 2022, 32, 2108370. Copyright 2021 The Authors.

7.1 Abstract

Efficient thermal insulation at high temperatures poses stringent requirements on suitable materials. Low density, porous inorganic structures with pore sizes in the sub-micrometer range are of particular interest for such materials to control heat conduction. Simultaneously, thermal radiation has to be suppressed, which depends on the optical properties of the constituents. Here, the authors demonstrate a direct observation of the transition from a conduction dominated to a radiation dominated thermal transport mechanism for the case of particulate silica materials at temperatures reaching up to 925 °C. A detailed analysis of the radiative transport through bulk silica as well as solid and hollow silica particles is provided. Optical transparency at high temperatures is the driving force, whereas surface wave modes barely contribute, particularly in case of the insulating particle packings. The existing analytical framework of laser flash analysis is extended to qualitatively describe the radiative and conductive heat transport by two independent diffusive transport models. The analysis provides a better understanding of the challenges to fabricate and analyze efficient thermal insulation materials at high operating temperatures, where multiple heat transport mechanisms need to be controlled.

7.2 Introduction

Thermal insulation plays an enormous role in various applications in everyday life, like buildings, automobiles, the oil and gas industry, and aerospace components. Aerogels—typically made from carbon or silica—are compelling materials for thermal insulation. Especially, silica is suitable for thermal applications owing to its low thermal conductivity, high melting temperature, and chemical inertness. Furthermore, silica is naturally abundant and can be recycled after usage.

Colloidal structures based on hollow silica spheres can be regarded as high-density aerogels with a hierarchical pore structure. Aerogels have densities between 1 and 1000 kg/m³^[1], while the density of hollow silica particle assemblies is in the range of 180 to 883 kg/m³^[2]. Colloidal assemblies have the advantage of easier fabrication due to the absence of a supercritical drying procedure. Furthermore, their well-defined pore sizes simplify the determination of structure–property relationships.

Most of the thermal insulation applications of aerogel materials have been considered at ambient temperatures. However, heat insulation at high operating temperatures is of great relevance for power plants, manufacturers, and aerospace. The thermal properties of insulating samples at high temperatures have been typically determined by the hot wire or hot plate techniques.^{[3]–[8]} One drawback of these techniques is

that relatively large samples with diameters up to 20 cm and several centimeter thicknesses are needed for the measurements. In case of the transient hot disc method, even two identical specimens are required. Therefore, high-temperature (HT) laser flash analysis (LFA) would be an interesting alternative, because just one sample with a diameter of 1 cm and a few mm thickness is needed. The LFA method has been well-established for room temperature (RT) measurements on a wide range of samples, including composites, monoliths, polymers, to name a few. Ruckdeschel *et al.* performed LFA on colloidal crystals from hollow silica nanoparticles and examined the thermal transport mechanisms.^{[2],[9]} While Ruckdeschel *et al.* examined the size range of 250 – 500 nm, Mofid *et al.* examined the thermal properties of the sub 100 nm region.^[10] There are few cases where LFA was used for aerogel samples up to 1500 °C. They have been performed by Wiener *et al.*^[11] and Feng *et al.*^[12] However, the groups used carbon aerogels, which render them opaque across a wide spectral range.

The overall thermal conductivity of porous materials, like aerogels and colloidal structures, can be described by three contributions: solid and gaseous conduction and radiation. Solid conduction takes place in the amorphous silica matrix material. The microstructure of the materials dictates the thermal conductivity in the solid conduction case. Amorphous structures, inclusions of defects, or micropores reduce the thermal conductivity through the skeleton of the porous material.^[13]

Gaseous conduction takes place in the pores in the aerogel or between and in the (hollow) nanoparticles. It is strongly influenced by the Knudsen effect when the mean free path of the gas equals or exceeds the pore size of the surrounding system.^[14] For nitrogen gas, the mean free path is between 88 nm at 25 °C and 354 nm at 925 °C^[15], precisely in the region of colloidal crystals under investigation here. Therefore, the Knudsen effect plays a significant role in gaseous conduction and is strongly reduced due to the strong confinement in pores smaller than 100 nm.

Radiation describes the effect that a surface emits electromagnetic waves due to its temperature. This energy is absorbed by another surface and reemitted, and so forth.^[16] Every matter with temperatures above 0 K emits thermal radiation. An idealized object that absorbs all incident radiation and emits with an emissivity of unity is called a black body radiator. The emissive power of other surfaces is compared to this maximum performance and is a fraction of 1. For highly insulating applications, the contribution of thermal radiation shall be suppressed as much as possible. This is achieved for polymer foams and aerogels by the addition of opacifiers^[17], like carbon^{[4],[6],[18],[19]}, or doping with materials such as Y₂O₃^[20]. The group of Prof. Fricke has developed a thorough understanding of heat transport in aerogels.^{[4],[6],[7]} They found that for high-density aerogels the solid conduction is the main transport path. Gaseous conduction and radiation become more critical with

lower density. Heinemann *et al.* were able to show that there is a complex interaction of radiation and conduction inside the sample, while conduction predominates at the boundaries.^{[4],[6]} In the last ten years, the theoretical description of radiative heat transfer in many-body systems, including the contribution of near-field effects, has made great progress.^[21] In particular, heat radiation in nanoparticle assemblies has been studied in a large number of works within the dipole approximation.^[22] Within this approximation the radiative heat conductivity can be calculated in systems composed of several thousand or ten thousand nanoparticles.^{[23],[24]} However, this method is strictly speaking not applicable in dense colloids because higher multipole moments need to be included in this case^[25] which makes the theoretical evaluation of the heat conductivity in many-body systems difficult. Since our samples are relatively large and dense we chose for the optical modelling an effective multilayer approach similar to Sakatani *et al.*^[26] to calculate the radiative heat conductivity in powdered materials, but with the extension that we include near-field effects, i.e. the contribution of evanescent waves.

Our investigation uses the time resolution of high-temperature LFA measurements to unravel the gradual transition from solid conduction to radiative heat transport. We apply this unique advantage, which is not accessible by steady-state characterization methods, to colloidal glasses made from SiO₂ and TiO₂ solid and hollow particles. We work out the existence of these two transport processes in such porous materials and relate them to their optical properties.

7.3 Results and Discussion

We base our analysis on two types of porous silica materials, one comprising solid, the other comprising hollow spheres, owing to their high thermal insulation capability. We investigated for each type two samples of comparable size ($d_{\text{tot}} \sim 300$ nm and 800 nm) and complement this data set with one batch of large $d_{\text{tot}} \sim 8$ μm sized solid silica beads. Owing to the filtration fabrication process, these particle assemblies can be considered to be colloidal glasses (Figure 7.9). The key geometries and resulting density data are summarized in Table 1. We measured LFA on these SiO₂ hollow and solid particles in a temperature range from 25 – 925 °C (Figure 7.1).

Tab. 7.1: Density, δ , thermal diffusivity, α , and thermal conductivity, κ , at 25 °C of the colloidal glasses from particles with diameter, d_{tot} , and shell thickness, d_S .

Sample	d_{tot} [nm]	d_S [nm]	δ [g/cm ³]	α [mm ² /s]	κ [W/mK]
SiO ₂ hollow small	278	29	0.594	0.251	0.111
SiO ₂ hollow big	882	31	0.219	0.226	0.037
SiO ₂ solid small	353		1.362	0.164	0.166
SiO ₂ solid big	889		1.347	0.113	0.113
SiO ₂ solid huge	8000		1.150	0.181	0.155

We represent the raw data of the time-dependent temperature evolution on the top surface of the samples in a normalized fashion. Precisely, we normalized the intensity data by the maximum peak intensity since only the relative temperature change is relevant for our evaluation. We also normalized the timescale to better work out the two distinct transport mechanisms. Radiative and conductive heat transport occur at different characteristic time scales. By normalizing the time at 25 °C, $t_{c,25^\circ\text{C}} = L^2/\pi^2\alpha$, with the sample thickness, L , and the thermal diffusivity at 25 °C, α , according to Cape and Lehmann, we remove any influence from the individual sample thickness.^[27] This way of time-normalization, consequently, renders the time-dependent measurements more comparable to one another. At room temperature, we observe only the conductive heat transport contribution. This is represented by the broad maximum, which slowly decays due to thermal losses to the sample holder and environment. This shape of the time-dependent temperature evolution is the classical case of an LFA experiment with solely conductive transport occurring through the sample. It can be well fitted for all cases based on established models, which include the one-dimensional heat diffusion equation in combination with certain loss mechanisms. For a detailed discussion and evaluation of the data fitting procedure in LFA experiments, we refer the reader to recent literature.^[28] The results for thermal diffusivity and thermal conductivity at 25 °C are summarized in Table 7.1 and confirm the thermal insulation properties of such particle packings. In particular the hollow sphere structures are strongly insulating. With increasing temperature, a second, much faster contribution starts to become more and more prominent in case of the sub- μm sized silica samples. Only the case of the 8 μm beads is still dominated by the slow process. All other samples have two maxima – one sharp at $t_{c,25^\circ\text{C}} < 0.2$, and one broad maximum at $1 < t/t_{c,25^\circ\text{C}} < 4$, which we interpret as radiative and conductive transport as outlined below, respectively. The evolution of this fast heat transport is most pronounced for the 882 nm hollow particles, where at 925 °C, no conduction peak is visible anymore. The time-dependent temperature profiles that we consistently observed in our sub- μm granular samples are highly unusual in the case of LFA experiments and cannot be described by the established models. Quite frankly, such data are typically “bad” measurements and are not considered any

further. To prove the correctness of our measurements, we performed additional tests to exclude any other sources that could lead to this unique time-dependent temperature evolution at the sample surface (Figure 7.2). We, therefore, measured reference materials with known thermal diffusivities and ruled out a potential influence from our tailor-made sample holder (Figure 7.2c). This sample holder was equipped with a graphite support, which was necessary to carry the samples, which were smaller than the contact face of the original holder. Furthermore, a spacer between the holder and the lid was required to reduce the mechanical load of the lid onto the sample, which would have led to a breakage of the sample.

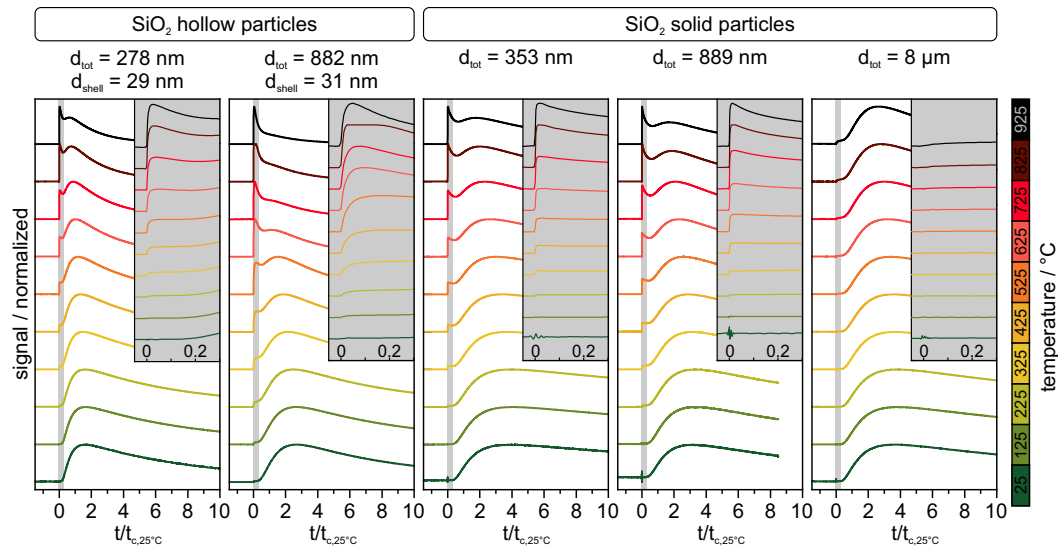


Fig. 7.1: Temperature-dependent LFA measurement signal of SiO₂ hollow and solid particles. The grey insets show details of the radiation peak. The time data is normalized by the characteristic thermal response time t_c .

Figure 7.2a shows the normalized measurement data, at 25 °C, 525 °C, and 925 °C for the original sample holder, with our graphite support, and with the graphite spacer in combination with pyroceram as standard material. The measurement data show an identical time-temperature evolution regardless of the sample holder configuration. There is no evolution of a second peak discernible. Fitting of the thermal diffusivity for this standard material provided slightly varying thermal diffusivity data, which we attribute to changes of thermal losses into the holder. Overall a good agreement between the measured and literature data was observed for this opaque standard material (Figure 7.2d). As a second class of reference material, we measured the properties of optically transparent bulk borosilicate and quartz glass (Figure 7.2b). The corresponding thermal diffusivities and literature values are shown in Figure 7.2e. Literature values for quartz glass have been calculated according to Sergeev *et al.*^[29] and match well with our measured data. Literature values for borosilicate glass were taken from Johnson *et al.*^[30] and are systematically higher compared to our data. We note, however, that borosilicate glass may differ depending on the supplier, which can explain the deviations to our data. The thermal diffusivity of

borosilicate glass above 625 °C decreased, because the glass softened and changed its shape.

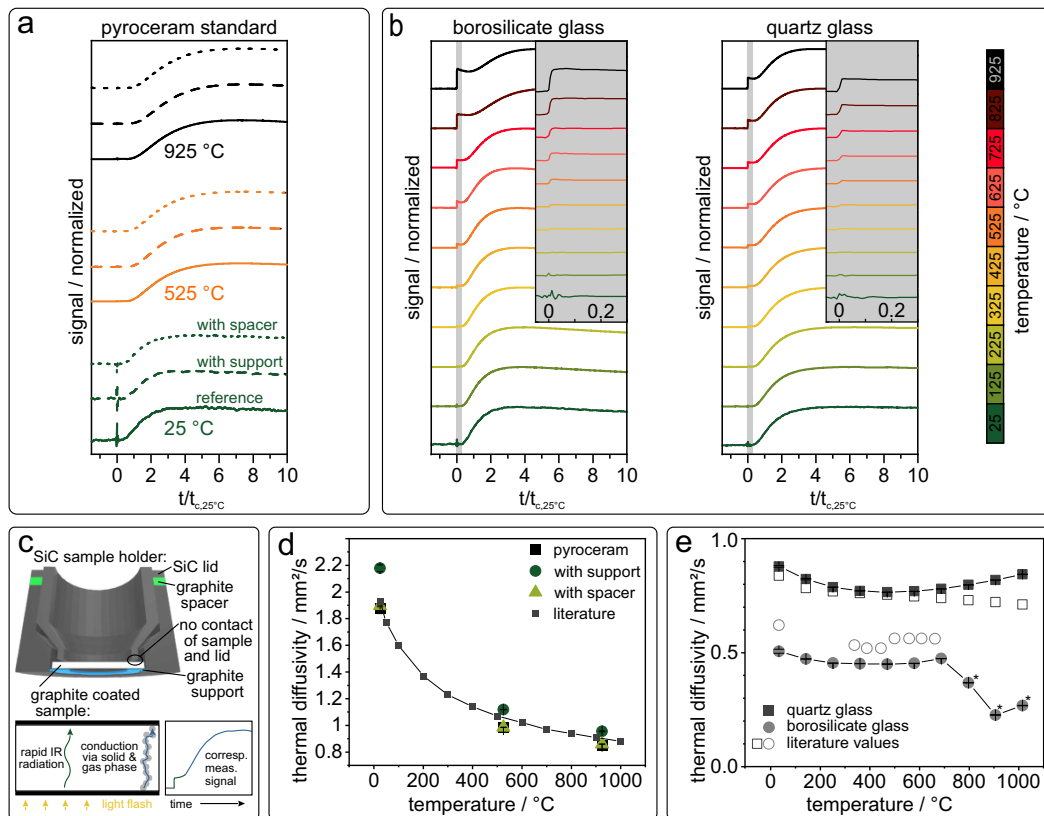


Fig. 7.2: Temperature-dependent LFA signal of pyroceram standard, measured with modified LFA sample holder (a). The corresponding pyroceram thermal diffusivity, in comparison with literature values (d). Temperature-dependent LFA signal of bulk borosilicate glass and quartz glass measured with the modified sample holder (b). The corresponding thermal diffusivity, in comparison to literature values[22-23] (e). Illustration of modified LFA sample holder, and sketch of heat transfer processes with the corresponding measurement signal in a LFA measurement (c).

The major difference between the pyroceram and the glass measurements is the appearance of an increasing step at $t_{c,25^\circ\text{C}} < 0.1$ for temperatures exceeding 425 °C. In contrast to the data of the hollow and solid particle samples, this radiative step is well-known and can be confidently fitted by the “transparent model” developed from the manufacturer. As outlined in Figure 7.2c, this steplike increase in temperature can be associated with radiative heat transport between the sample bottom and top surface. Thermalization of the Xenon light flash, as well as mid-infrared emission and absorption, respectively, happen much faster compared to the ms time resolution of the XFA experiment. Therefore, the sample’s top surface temperature is offset by a small amount, which is accounted for by the fitting procedure. When comparing the insets of Figure 7.2b and Figure 7.1, one recognizes a marked difference between the two early radiative events. A comparison of the radiation peak at $t_{c,25^\circ\text{C}} < 0.15$ is shown in Figure 7.11 in the supporting information. The granular samples demonstrate a marked loss in surface temperature after the initial increase, whereas

the bulk material reaches a plateau. Even more important is the apparently slower temperature increase, in particular in the case of the hollow sphere samples. Since all bulk and particulate samples have been prepared in a comparable way, this slow temperature increase cannot be assigned to the heating dynamics of the graphitic coating layers that may vary from sample to sample in a small and non-systematic way. When looking at longer measurement times, the relative magnitude of the first steplike process to the slower broad temperature increase is vastly different between the bulk and the particulate samples. Whereas for bulk samples only a small temperature increase can be assigned to the early radiative transport, it becomes the dominant transport mechanism for solid and hollow spheres. However, owing to the slow dynamics and high intensity the established models are not capable of fitting these two processes anymore. The fitting model becomes increasingly inaccurate for temperatures above 525 °C (Figure 7.12). Lunev *et al.* found a similar effect on alumina samples above 1000 °C and established a numerical model for their data.^[31]

For the hollow particles, the initial increase in temperature is reminiscent of the known temperature evolution of diffusive thermal transport. In a rough approximation we, therefore, treated our measurement as a superposition of two diffusive transport processes based on the model of Cape and Lehman, which includes losses to the environment. Note that this simplified treatment uses the same diffusive thermal transport formalism for radiative and conductive transport. The temperature evolution was modeled as:

$$T(L, t) = A \sum_{m=0}^{\infty} C_{m,1} \xi_{m,1} e^{(\omega_{m,1}(t-\Delta t)/t_{c,1})} + \sum_{m=0}^{\infty} C_{m,2} \xi_{m,2} e^{(\omega_{m,2}t/t_{c,2})} \quad (7.1)$$

A is a parameter for the ratio between the maximum intensities of the two processes, Δt is an initial time shift as the first process is not exclusively of diffusive nature.^[27] $C_{m,i} = (-1)^m (2\xi_{m,i}) / (\xi_{m,i}^2 + 2H_i + H_i^2)$, where H_i represents the axial Biot number and $\xi_{m,i}$ is determined by $(\xi_{m,i}^2 - H_i^2) \tan(\xi_{m,i}) = 2\xi_{m,i}H_i$. Furthermore $\omega_{m,i} = -\xi_{m,i}^2/\pi^2$ and the characteristic time $t_{c,i} = L^2/\pi^2\alpha$. An example of this data evaluation is shown in Figure 7.3a for the small hollow spheres at 725 °C (the evaluation of the big hollow particles can be found in the supporting information, Figure 7.13), where both transport processes display a similar order of magnitude. There is a convincing agreement between the measured data and the applied model, which can separate the individual transport processes. This simplified model is robust for a wide temperature range, where both processes occur (Figure 7.3b) and it could also be applied to the large hollow sphere sample (Figure 7.13). Limitations of this model are conditions where one of the two processes strongly dominates, in the cases shown here at room temperature and > 900 °C. The intensity mismatch between the two processes is then too large and the fitting sensitivity insufficient for the weaker

transport process. Another limitation is the timescale of the first diffusive process. The relatively slow nature in case of the hollow sphere samples could be well-described. This was not possible for the solid particles anymore, where the radiative increase appears to be slightly faster. Nevertheless, we can extract from our simplified description semiquantitative information (Figure 7.14). The thermal diffusivity assigned to both processes should certainly only be taken as a rough estimate. The precondition of one-dimensional heat transport is not valid anymore in this system, where two temperature gradients on different timescales are present within the sample. The thermal diffusivity of both processes differs by two orders of magnitude and shows a negligible temperature dependence in case of the slow, conduction-based process, whereas the fast process becomes significantly faster with increasing temperature. This is commensurate with previous reports on radiative thermal transport at high temperatures, where a strongly increasing thermal conductivity has been reported.^[32] Our model, furthermore, allows quantifying the temperature-dependent ratio, A , between the two processes, as shown in Figure 3c for the 278 nm hollow particle sample. This ratio follows a non-linear temperature dependency. It scales with T^4 , owing to its radiative nature obeying Stefan-Boltzmann's law.^[16]

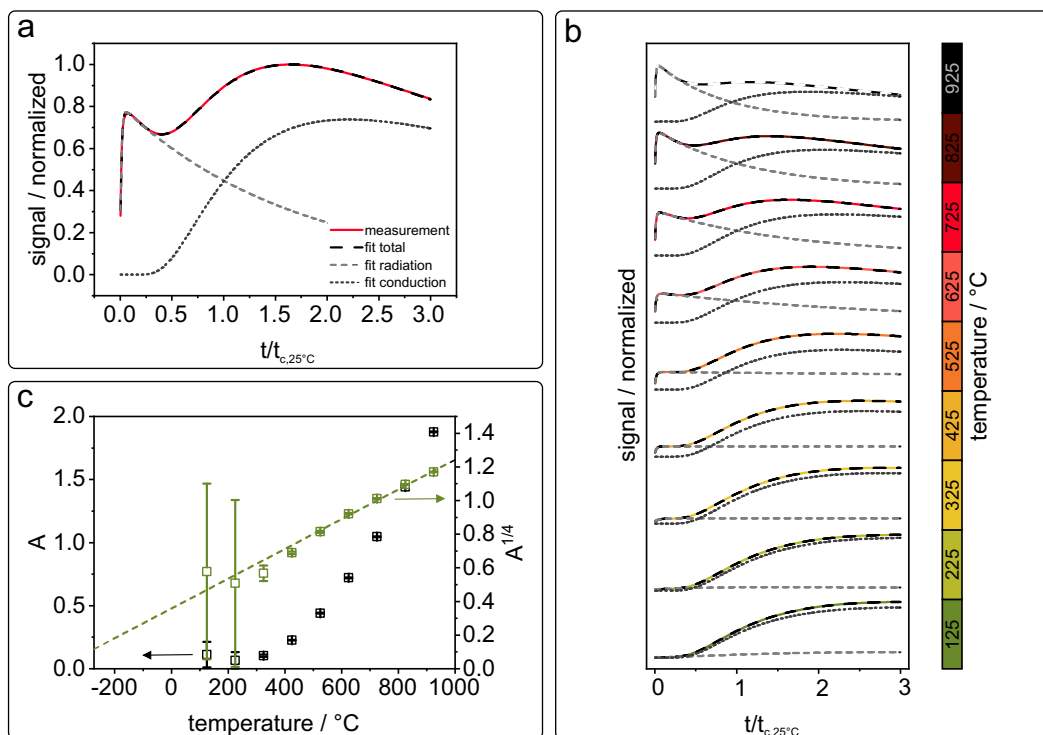


Fig. 7.3: Double-diffusive model applied on 278 nm hollow particle measurements. Example of measurement at 725 °C (a). Application at all temperatures (b). Resulting ratio, A , of first and second diffusive process (c).

Having outlined the direct observation of such two transport processes, we now want to turn the focus on the influence of the optical properties onto the radiative transport. The transmission spectra are shown in Figure 7.4. We find that all samples are transparent in the IR detector region between 3-5 μm (yellow hatched area),

except for the 8 μm solid silica particles. This correlates to the LFA results that did not show a distinct radiation peak for the 8 μm species. Optical transparency in this wavelength range is a precondition for radiative transport. Sub-micron sized TiO_2 hollow spheres, for instance, have a comparable mesostructure to the SiO_2 hollow spheres, yet, they are fully opaque from the UV/Vis to the MIR range (Figure 7.15). Consequently, no radiative transport process could be observed (Figure 7.16). A slight reduction of the mid-infrared transmission can be achieved by inert calcination conditions of the hollow spheres, which retain a small fraction of carbon in the particles. Whereas the optical appearance changed strongly (Figure 7.17 and 7.18), the opacity in the 3-5 μm range is not sufficient to suppress the radiative process (Figure 7.19).

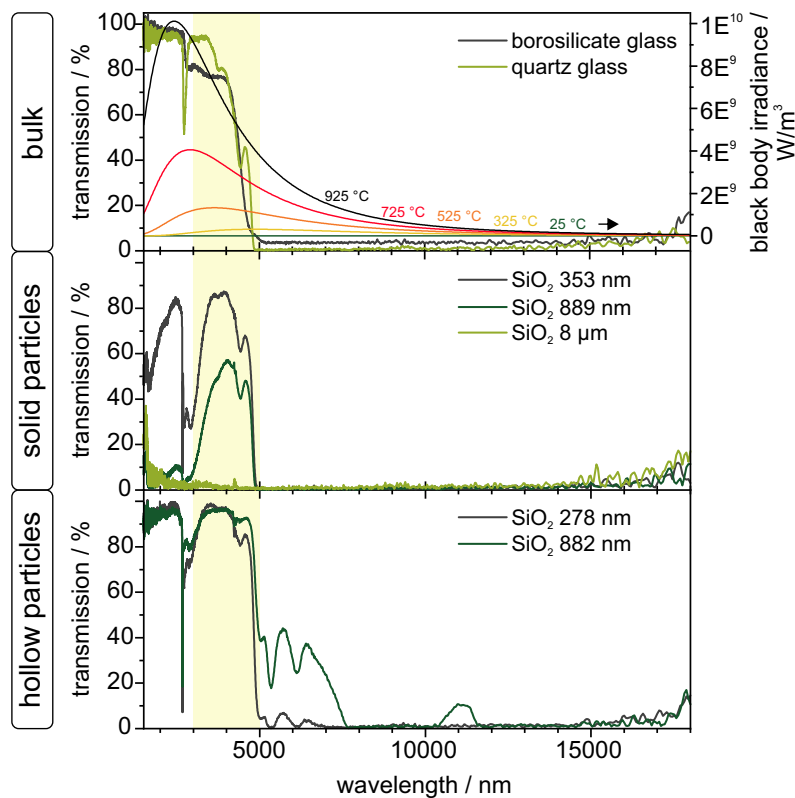


Fig. 7.4: IR transmission data of bulk, solid particle, and hollow particle samples in comparison to black body irradiance. The LFA detection region between 3 and 5 μm is highlighted.

To gain a deeper understanding of the radiative transport mechanism through such bulk and particulate materials, we used simulations based on the S-matrix method. These multibody calculations have been performed on a simplified two-dimensional multilayer models representing the most relevant structural parameters of our samples (Figure 7.5, left column). The model consists of top and bottom reservoirs representing the graphite coatings and in between one bulk SiO_2 layer or several SiO_2 layers with a thickness of 353 nm and 20 nm gaps, representing the small solid particle structures. Here, the assumption was made that the interparticle distance

is 6 % of the particle diameter, which was calculated with a 3D radial distribution function of an MD simulated particle structure (Figure 7.20). The big hollow particle structure is represented by 30 nm SiO₂ layers with 800 nm gaps, representing the hollow particle part, and 50 nm gaps, representing the interparticle distance. The calculated transmission spectra of the multilayer structure are in good agreement with the experimental data (Figure 7.5 middle column), and, therefore, can be considered a reasonable approximation to the particle structure. These models allow calculating the transmission coefficients \mathcal{T}_j^{12} ($j = s, p$), which mainly determine the modes contributing to the radiative heat flow between the two graphite layers. They contain the contributions of waves that are propagating ($\kappa < k_0$) and waves that are evanescent ($\kappa > k_0$) in vacuum, where κ is the wave vector component parallel to the interface and k_0 is the wavenumber in vacuum.^[33] Figure 7.5 (right column) shows the transmission \mathcal{T}_p^{12} , in the $\lambda - \kappa$ plane. In case of bulk SiO₂ radiative transport only occurs for wavelengths $< 5 \mu\text{m}$ with a considerable contribution of evanescent waves. Due to the fact that in the transparency window, the lateral wave vector κ of the waves which can propagate within SiO₂ is limited by $\sqrt{\text{Re}(\epsilon_{\text{SiO}_2})}k_0 \approx 1.4k_0$. In case of the solid sphere analogous structure, we find a layer dependence of the transmission coefficient. When increasing the number of layers to from $N = 9$ to $N = 3121$ (Figure 7.21), only waves in the transparency window with $\lambda < 5 \mu\text{m}$ can reach the second graphite layer. All other wavelengths are attenuated by the optical density of the SiO₂ particles. The solid spheres still show contributions of evanescent waves coupling to the graphitic reservoirs. It is interesting to note that there is no significant surface wave contribution in the reststrahlen band $\lambda = 8\text{--}9.3 \mu\text{m}$. We elaborated on the role of surface modes within the reststrahlen band more explicitly using a numerically exact boundary element method provided by SCUFF-EM for 800 nm spheres (Figure 7.23). This method takes far- and near-field contributions to the transmission function into account. For two adjacent SiO₂ particles, the heat flux is indeed dominated by a surface mode at $\lambda = 9 \mu\text{m}$. This mode, however, quickly attenuates when including more particles. Furthermore, when considering the transmission between two graphitic objects, the major contribution originates from modes with $\lambda < 8 \mu\text{m}$. This is due to the fact that damping of the coupled surface modes is too strong to ensure an efficient coupling over long distances. Considering the radiative transport case through hollow silica spheres, one recognizes the absence of evanescent contributions in \mathcal{T}_p^{12} . We attribute this to the increased distance between the silica surfaces. The major distance is governed by the hollow space (800 nm) inside of the silica capsules. The absence of evanescent waves is counteracted by a reduced optical density between $5 \mu\text{m} < \lambda < 7.5 \mu\text{m}$, where some transmission is also possible.

We used the transmission coefficients to calculate the heat transfer coefficients (htc), describing the radiative heat flow h^{12} from the graphite bottom at temperature T_1 and the heat flow h^{23} from the middle layer 2 at temperature T_2 towards the

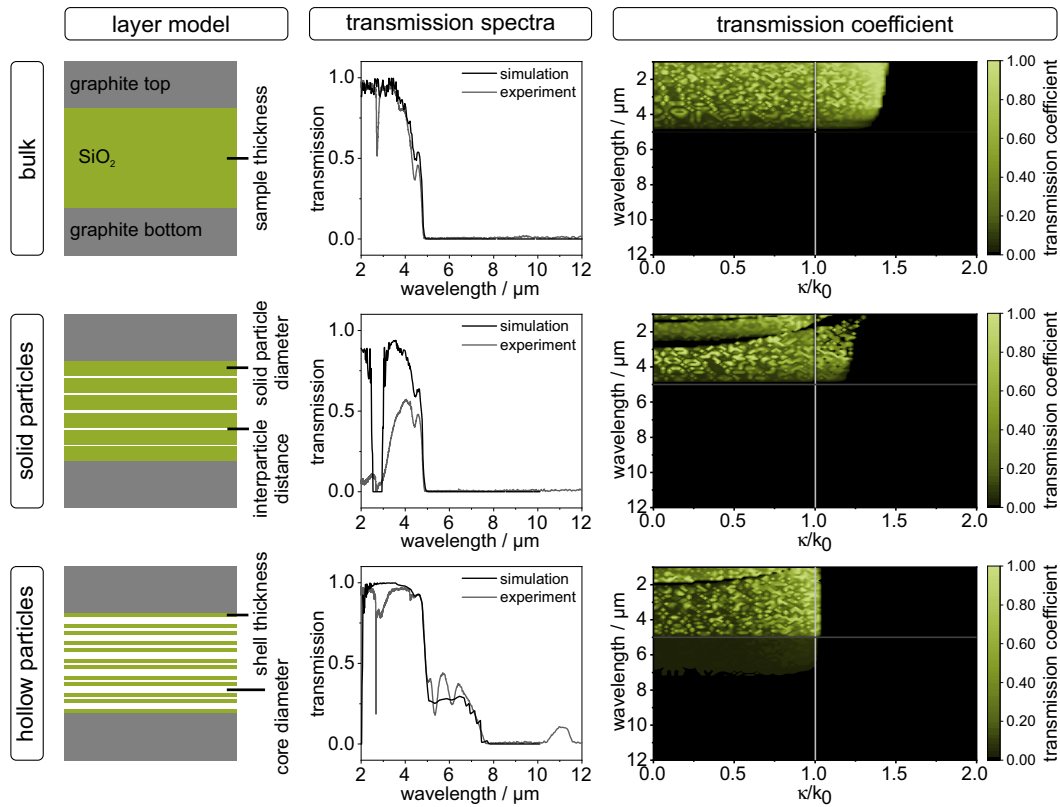


Fig. 7.5: Sketches of the layer model (1. column) used for calculation of transmission spectra (2. column) and transmission coefficients (3. column) of bulk, solid particle, and hollow particle structures.

graphite top 3 at temperature T_3 , where h^{12} is for small time scales the dominant contribution (see supporting information for details). The integrated htc of the multilayer models is shown in Figure 7.6 (left). The heat flow through the bulk silica film is larger than for the multilayer structure due to the larger contribution of the evanescent waves in the bulk film. Both particle structures feature comparable htc, which we rationalize by a compensation of the contributions of evanescent waves in case of the solid spheres and higher wavelength modes in case of the hollow spheres. Combining our double diffusive transport evaluation with the radiative transport analysis, we can draw several conclusions. Surface wave modes do not play a major role in the high-temperature transport through particulate SiO₂ materials – the reststrahlen band is too far red-shifted. The optical density of the particle packing determines which wavelengths can be transported through such structures, with a first window opening below 7.5 μm and the major contribution originating from < 5 μm. Evanescent waves are suppressed by the large porosity in the case of hollow silica beads.

We finally extended the multilayer model to also include thermal conduction through the individual layers (Figure 7.6, right, see supporting information for details). This calculation is based on a set of coupled differential equations, which include the

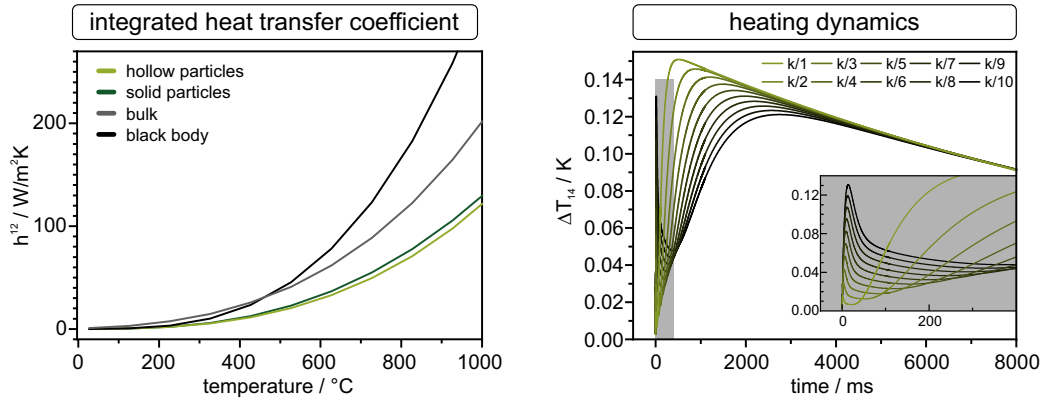


Fig. 7.6: Integrated heat transfer coefficient h^{12} for hollow and solid SiO_2 particles, and bulk quartz glass, in comparison with black body radiation. The data was calculated using the multilayer model described in Figure 7.5 (left). Heating dynamics without lateral losses of the multilayer model from Figure 7.24 at a temperature of 925°C (right).

conductive and radiative heat flow between discrete layers. Two main conclusions can be drawn from this analysis. Firstly, the main features of the time-dependent temperature evolution observed in the LFA experiment are well captured by this analytic description. This corroborates our interpretation of the direct observation of a radiative and conductive heat transport process. Secondly, the systematic variation of the thermal conductivity of the solid skeleton stresses the importance of the relative heat transport capacity of these two channels. In case of a low conducting matrix, radiative transport becomes the dominant process. In case of a highly conducting matrix, radiative transport plays a subordinate role.

7.4 Summary and Conclusion

We demonstrated a direct observation of two distinct heat transport processes in mesostructured silica materials. We fabricated colloidal glasses comprising solid and hollow silica particles of 800 nm and 400 nm, respectively. The temperature evolution of the sample's top surface in an LFA experiment is dominated by a fast and a slow process. At room temperature, heat conduction along the silica network dominates, rendering such silica particle packings efficient thermal insulators comparable to polymer foams. With increasing temperatures, however, thermal radiation becomes more important and finally dominant, owing to the T^4 increase in radiation power and the blue-shift of the radiated wavelengths. Optical transparency in the mid-infrared range and good thermal emitters at the boundaries are preconditions to open this radiative heat transport pathway. Consequently, the silica materials become at high temperatures much better thermal conductors as compared to their room-temperature behavior. Surface wave modes within the reststrahlen band do not contribute to this radiative transport process. Evanescent waves, on the contrary, do

contribute to the overall heat transport and are most prominent for bulk materials and ensembles of solid silica particles. The large intra-particle gaps caused by the hollow core in the case of silica capsules attenuates the contribution from evanescent waves. The radiative heat transport in hollow particle structures is slow enough to be described by a diffusive transport fit. Our results give a direct and detailed insight into the various transport mechanisms that govern high-temperature heat transport. Controlling the optical properties in the mid-infrared range either by means of the composition, the structure, or by adding additives is of paramount importance to maintain a strong thermal insulation behavior. The time-dependence of LFA measurements is a unique benefit to directly observe radiative and conductive thermal processes.

7.5 Experimental Section / Methods

7.5.1 Materials

Borosilicate glass (microscope slide, Menzel glass, Thermo Scientific) and quartz glass were cleaned with Hellmanex III (Hellma GmbH) and cut in pieces of 1 x 1 cm before the measurements. Sapphire discs ($d = 1$ cm, Edmund optics) were used as received. SiO₂ solid particles in three different sizes (353 nm, 889 nm, 8 μm) were purchased from microParticles GmbH and used as received. The synthesis of the SiO₂ and TiO₂ hollow particles is described in detail in the supporting information.

The particles were assembled using the vacuum filtration method described by Ruckdeschel *et al.*^[34] A vacuum filtration system from Merck Millipore was used in combination with MF Millipore membrane filters with pore sizes of 0.2 μm and 0.45 μm. A Teflon funnel with a diameter of 1 cm has been used for the SiO₂ particles. A funnel with a diameter of 1.2 cm has been used for the TiO₂ particles because shrinkage of the samples during calcination has been considered. All samples have been dried at 40 °C in a vacuum overnight before calcination. The samples have been calcinated at 500 °C or 925 °C to remove organic components and avoid structural changes during the measurements.

7.5.2 Methods

UV-Vis measurements were conducted on a Cary 5000 (Agilent Technologies) in transmission mode with the Ulbricht sphere in the range of 250 and 2500 nm. A holder for the round-shaped samples was 3D printed for UV-Vis and IR measurements.

Infrared (IR) measurements were conducted on a VERTEX 70 spectrometer (Bruker) in the range of 1.5 and 18 μm . Transmission measurements have been made using a gold-coated integrating sphere with an MCT detector.

Laser scanning microscopy was performed using a LEXT OLS5000-SAF microscope (Olympus) to determine the sample thicknesses and volumes. Laser Flash Analysis was conducted on a LFA 467 HT HyperFlash apparatus (Netzsch) in the range of 25 and 925 $^{\circ}\text{C}$ under a slight nitrogen stream (50 ml/min). The samples were coated with a thin layer of graphite on the top and bottom side and placed in the sample holder, equipped with self-made graphite support and spacer (Figure 7.2c).

Acknowledgements

We thank Stefan Rettinger and Tanja Feller for the help with STA and LEXT measurements, Thomas Tran for the determination of the mean particle distance and help with data evaluation, and Kishin Matsumori for some additional optical calculations. We also thank the Bavarian Polymer Institute, especially Ulrich Mansfeld and Markus Drechsler, for their help with SEM and TEM measurements.

Funding information

This project was funded by the German Research Foundation (DFG RE3550/2–1). T.L. acknowledges funding by ERC Starting Grant VISIRday under Grant No. 714968, K.H acknowledges funding by SFB840, TP B7. S.-A. B. acknowledges support from the Heisenberg Programme of the German Research Foundation (DFG, project No. 404073166).

7.6 References

- [1] A. Du, B. Zhou, Z. Zhang, and J. Shen, „A special material or a new state of matter: A review and reconsideration of the aerogel“, *Materials*, vol. 6, no. 3, pp. 941–968, Mar. 2013.
- [2] P. Ruckdeschel, A. Philipp, and M. Retsch, „Understanding thermal insulation in porous, particulate materials“, *Advanced Functional Materials*, vol. 27, no. 38, p. 1702256, Sep. 2017.

- [3] E. Cohen and L. Glicksman, „Analysis of the transient hot-wire method to measure thermal conductivity of silica aerogel: Influence of wire length, and radiation properties“, *Journal of Heat Transfer*, vol. 136, no. 4, Jan. 2014.
- [4] J. Fricke and T. Tillotson, „Aerogels: Production, characterization, and applications“, *Thin Solid Films*, vol. 297, no. 1-2, pp. 212–223, Apr. 1997.
- [5] U. Gross and L.-T.-S. Tran, „Radiation effects on transient hot-wire measurements in absorbing and emitting porous media“, *International Journal of Heat and Mass Transfer*, vol. 47, no. 14-16, pp. 3279–3290, Jul. 2004.
- [6] U. Heinemann, R. Caps, and J. Fricke, „Radiation-conduction interaction: An investigation on silica aerogels“, *International Journal of Heat and Mass Transfer*, vol. 39, no. 10, pp. 2115–2130, Jul. 1996.
- [7] X. Lu, R. Caps, J. Fricke, C. Alviso, and R. Pekala, „Correlation between structure and thermal conductivity of organic aerogels“, *Journal of Non-Crystalline Solids*, vol. 188, no. 3, pp. 226–234, Aug. 1995.
- [8] G. Wei, Y. Liu, X. Zhang, F. Yu, and X. Du, „Thermal conductivities study on silica aerogel and its composite insulation materials“, *International Journal of Heat and Mass Transfer*, vol. 54, no. 11-12, pp. 2355–2366, May 2011.
- [9] P. Ruckdeschel and M. Retsch, „Interface and morphology control of the thermal conductivity in core-shell particle colloidal crystals“, *Advanced Materials Interfaces*, vol. 4, no. 24, p. 1700963, Nov. 2017.
- [10] S. A. Mofid, B. P. Jelle, X. Zhao, *et al.*, „Utilization of size-tunable hollow silica nanospheres for building thermal insulation applications“, *Journal of Building Engineering*, vol. 31, p. 101336, Sep. 2020.
- [11] M. Wiener, G. Reichenauer, S. Braxmeier, F. Hemberger, and H.-P. Ebert, „Carbon aerogel-based high-temperature thermal insulation“, *International Journal of Thermophysics*, vol. 30, no. 4, pp. 1372–1385, Jun. 2009.
- [12] J. Feng, J. Feng, Y. Jiang, and C. Zhang, „Ultralow density carbon aerogels with low thermal conductivity up to 2000°C“, *Materials Letters*, vol. 65, no. 23-24, pp. 3454–3456, Dec. 2011.
- [13] P. Ruckdeschel, T. W. Kemnitzer, F. A. Nutz, J. Senker, and M. Retsch, „Hollow silica sphere colloidal crystals: Insights into calcination dependent thermal transport“, *Nanoscale*, vol. 7, no. 22, pp. 10059–10070, 2015.
- [14] S. N. Schiffres, K. H. Kim, L. Hu, *et al.*, „Gas diffusion, energy transport, and thermal accommodation in single-walled carbon nanotube aerogels“, *Advanced Functional Materials*, vol. 22, no. 24, pp. 5251–5258, Aug. 2012.
- [15] G. Wedler and H. Freund, *Lehrbuch der Physikalischen Chemie*, ser. Wiley VCH Lehrbuchkollektion 1. Wiley-VCH, 2012.
- [16] F. Incropera, D. DeWitt, T. Bergman, and A. Lavine, *Fundamentals of Heat and Mass Transfer*. Wiley, 2007.

- [17] T. Xie, Y.-L. He, and Z.-J. Hu, „Theoretical study on thermal conductivities of silica aerogel composite insulating material“, *International Journal of Heat and Mass Transfer*, vol. 58, no. 1-2, pp. 540–552, Mar. 2013.
- [18] S. Zeng, A. Hunt, and R. Greif, „Theoretical modeling of carbon content to minimize heat transfer in silica aerogel“, *Journal of Non-Crystalline Solids*, vol. 186, pp. 271–277, Jun. 1995.
- [19] H. Liu, T. Li, Y. Shi, and X. Zhao, „Thermal insulation composite prepared from carbon foam and silica aerogel under ambient pressure“, *Journal of Materials Engineering and Performance*, vol. 24, no. 10, pp. 4054–4059, Sep. 2015.
- [20] V. G. Parale, H.-N.-R. Jung, W. Han, *et al.*, „Improvement in the high temperature thermal insulation performance of y2o3 opacified silica aerogels“, *Journal of Alloys and Compounds*, vol. 727, pp. 871–878, Dec. 2017.
- [21] S.-A. Biehs, R. Messina, P. Venkataram, *et al.*, „Near-field radiative heat transfer in many-body systems“, *Reviews of Modern Physics*, vol. 93, no. 2, Jun. 2021.
- [22] P. Ben-Abdallah, S.-A. Biehs, and K. Joulain, „Many-body radiative heat transfer theory“, *Physical Review Letters*, vol. 107, no. 11, Sep. 2011.
- [23] P. Ben-Abdallah, R. Messina, S.-A. Biehs, *et al.*, „Heat superdiffusion in plasmonic nanostructure networks“, *Physical Review Letters*, vol. 111, no. 17, Oct. 2013.
- [24] E. Tervo, M. Francoeur, B. Cola, and Z. Zhang, „Thermal radiation in systems of many dipoles“, *Physical Review B*, vol. 100, no. 20, Nov. 2019.
- [25] D. Becerril and C. Noguez, „Near-field energy transfer between nanoparticles modulated by coupled multipolar modes“, *Physical Review B*, vol. 99, no. 4, Jan. 2019.
- [26] N. Sakatani, K. Ogawa, Y. Iijima, *et al.*, „Thermal conductivity model for powdered materials under vacuum based on experimental studies“, *AIP Advances*, vol. 7, no. 1, p. 015310, Jan. 2017.
- [27] J. A. Cape and G. W. Lehman, „Temperature and finite pulse-time effects in the flash method for measuring thermal diffusivity“, *Journal of Applied Physics*, vol. 34, no. 7, pp. 1909–1913, Jul. 1963.
- [28] A. Philipp, J. F. Eichinger, R. C. Aydin, *et al.*, „The accuracy of laser flash analysis explored by finite element method and numerical fitting“, *Heat and Mass Transfer*, vol. 56, no. 3, pp. 811–823, Oct. 2019.
- [29] O. A. Sergeev, A. G. Shashkov, and A. S. Umanskii, „Thermophysical properties of quartz glass“, *Journal of Engineering Physics*, vol. 43, no. 6, pp. 1375–1383, Dec. 1982.

- [30] L. F. Johnson, D. P. H. Hasselman, and E. Minford, „Thermal diffusivity and conductivity of a carbon fibre-reinforced borosilicate glass“, *Journal of Materials Science*, vol. 22, no. 9, pp. 3111–3117, Sep. 1987.
- [31] A. Lunev, V. Zborovskii, and T. Aliev, „Complexity matters: Highly-accurate numerical models of coupled radiative–conductive heat transfer in a laser flash experiment“, *International Journal of Thermal Sciences*, vol. 160, p. 106 695, Feb. 2021.
- [32] T. J. Shankland, U. Nitsan, and A. G. Duba, „Optical absorption and radiative heat transport in olivine at high temperature“, *Journal of Geophysical Research*, vol. 84, no. B4, p. 1603, 1979.
- [33] R. Messina, P. Ben-Abdallah, B. Guizal, M. Antezza, and S.-A. Biehs, „Hyperbolic waveguide for long-distance transport of near-field heat flux“, *Physical Review B*, vol. 94, no. 10, Sep. 2016.
- [34] P. Ruckdeschel, A. Philipp, B. A. F. Kopera, *et al.*, „Thermal transport in binary colloidal glasses: Composition dependence and percolation assessment“, *Physical Review E*, vol. 97, no. 2, Feb. 2018.

7.7 Supporting Information

7.7.1 Synthesis and Characterization of SiO₂ and TiO₂ Hollow Particles

Materials

Ammonium hydroxide solution (NH₄OH, Sigma-Aldrich GmbH, 30-33 %), 2,2'-azobis-(isobutyramidine) dihydrochloride (AIBA, Sigma-Aldrich GmbH, 97 %), ethanol abs. (Sigma-Aldrich GmbH, ≥99.8 %), 2-methacryloxyethyltrimethylammonium chloride (MTC, Sigma-Aldrich GmbH, 75 % soln. in water), polyvinylpyrrolidone (PVP, Sigma-Aldrich GmbH), styrene (Sigma-Aldrich GmbH, >99 %), tetraethyl orthosilicate (TEOS, Sigma-Aldrich GmbH, 98 %) titanium butoxide (TBT, Sigma Aldrich GmbH, 97 %) were used as received. Millipore water was taken from a Millipore Direct Q3UV unit (Merck Millipore). 2,2'-Azobis(2-methylpropionitril) (AIBN, Sigma-Aldrich GmbH) was recrystallized from ethanol before use.

Microscopy

Scanning electron microscopy (SEM) was performed using a Zeiss Ultraplus instrument using acceleration voltages of 3 kV. InLens and Everhard-Thornley detectors were used. A MATLAB circle detection function was used to evaluate the diameter of the particles. Transmission electron microscopy (TEM) measurements were performed with a JEOL JEM-2200FS field emission energy filtering transmission electron microscope (FE-EFTEM) operated at an acceleration voltage of 200 kV. Zero-loss filtered micrographs ($\Delta E \sim 0$ eV) were recorded with a bottom mounted CMOS camera system (OneView, Gatan) and processed with DM 3.3 image processing software (Gatan).

Polystyrene template particles

217 nm particles (Figure 7.7) were synthesized via emulsifier free emulsion polymerization.^[1] For the synthesis, 1.8 g PVP (360 kg/mol), 235 ml Millipore water, 26 ml styrene, and 25 μ l MTC were added to a 500 ml three-neck flask equipped with a gas inlet and reflux condenser. The emulsion was stirred at a stirring speed of 850 rpm using a large egg-shaped magnetic stirrer bar and heated to 70 °C under a slight argon flow. After 60 min 0.6 g AIBA, dissolved in 5 ml Millipore water, was added

to initiate the polymerization. After the nucleation the stirring speed was reduced to 450 rpm and the reaction was allowed to continue over night. The polymerization was stopped by exposing the dispersion to ambient air and filtrated using a 125 μm nylon filter sieve. No further purification was required.

The 845 nm particles (Figure 7.7) were synthesized via dispersion polymerization.^{[2],[3]} 12 g PVP (40 kg/mol), 194 ml of ethanol, 40 ml Millipore water, 12 ml styrene and 1.2 g AIBN were added to a 1 l three-necked flask equipped with a reflux condenser and a gas inlet. The solution was degassed while stirring with an egg-shaped stirring bar with a speed of 150 rpm. After 30 min, the mixture was heated to the reaction temperature of 70 °C. After 90 min 194 ml ethanol, 12 ml styrene, and 450 μl MTC were premixed in an Erlenmeyer flask and added to the reaction. The reaction was carried out overnight under a slight argon flow. The polymerization was stopped by exposing the dispersion to ambient air and filtrated using a 125 μm nylon filter sieve. No further purification was required.

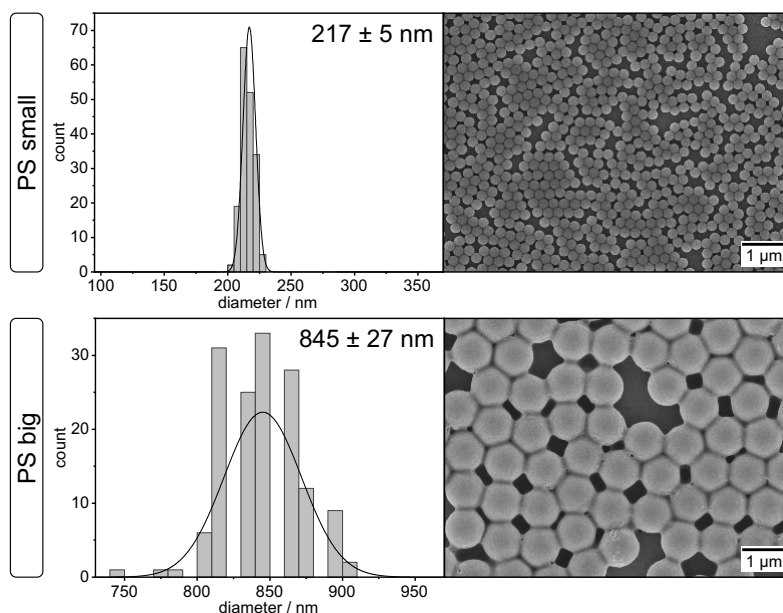


Fig. 7.7: Histograms and SEM images of polystyrene particles that were used as template for the SiO_2 and TiO_2 hollow particles.

SiO_2 and TiO_2 Hollow Particles

A modified Stöber process was used for the synthesis of the silica shell to get PS@SiO_2 core-shell particles.^{[4],[5]} For the synthesis, 40 ml (60 ml) dispersion of the 217 nm (845 nm) particles were diluted with 280 ml (450 ml) ethanol and 1/10 of 13.44 ml (1.8 ml) TEOS and stirred at 400 rpm at room temperature. After 20 min equilibration time, 20.8 ml (31 ml) NH_4OH solution was added. The remaining TEOS was added in nine more steps in time intervals bigger than 15 min and the reaction

was stirred at room temperature over night. The particles were centrifuged and washed twice with ethanol and three times with Millipore water for purification.

PS@TiO₂ core-shell particles were prepared using a method described by Cheng *et al.* and Lechner *et al.*^{[2],[3]} 40 ml dispersion of 845 nm particles and 234 ml ethanol were added to an Erlenmeyer flask equipped with a septum. The dispersion was stirred at 350 rpm with a magnetic stirrer bar. After 10 min of degassing, a solution of 4.8 ml TBT in 20 ml ethanol was added within 30 min using a syringe pump. After another 30 min the stirrer was stopped and the dispersion was allowed to age for 24 h. The core-shell particles were washed three times with ethanol for purification.

In order to remove the PS core of the core-shell particles, the assembled samples were calcinated either in air or inert argon gas atmosphere using a modified temperature profile of Schroden *et al.*^{[3],[6]} A heating rate of 2 K/min was used for all heating steps. The samples were heated to 300 °C, followed by an isothermal step of 2 h. They were then heated to 400 °C, followed by an isothermal step of 5 h. After that the samples were heated to 500 °C or 925 °C, followed by an isothermal step of 5 h. Finally, the samples were cooled down to room temperature. The resulting hollow particles can be seen in Figure 7.8.

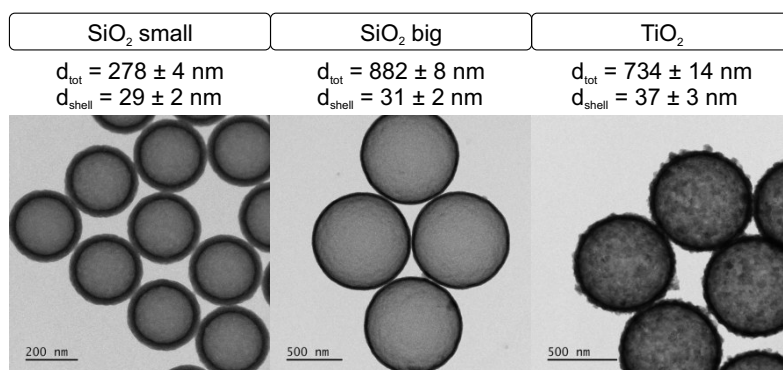


Fig. 7.8: TEM images of SiO₂ and TiO₂ hollow particles after calcination at 500 °C.

Figure 7.9 shows sideview SEM images of the calcinated colloidal glasslike structures. All structures stayed stable at calcination temperatures up to 925 °C. The broken shells of the TiO₂ particles came from cutting the sample in half with a knife.

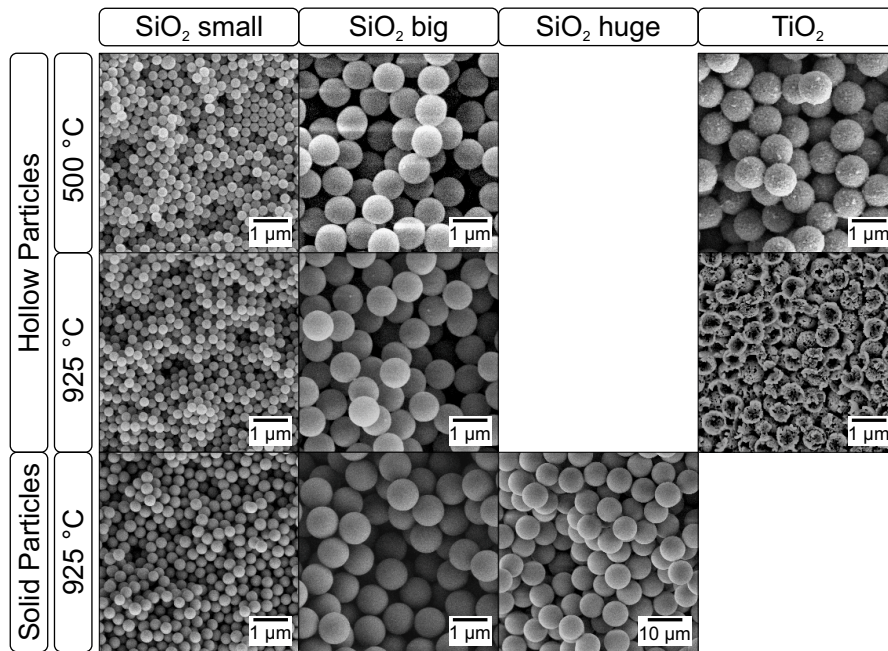


Fig. 7.9: Sideview SEM images of all colloidal glasslike structures after calcination at 500 °C or 925 °C.

7.7.2 X-ray powder diffraction of TiO₂ samples

X-ray powder diffraction was performed to investigate the titania phase of the hollow particles before and after LFA measurements at 925 °C. X-ray powder diffraction patterns for the TiO₂ samples were recorded on an Empyrean diffractometer in Bragg-Brentano-geometry (PANalytical B.V.; the Netherlands) using Cu-K_α radiation ($\lambda = 1.54187 \text{ \AA}$). The samples were first calcinated in air atmosphere at 500 °C and then calcinated in inert gas atmosphere up to 925 °C. The results are shown in Figure 7.10. Both samples consist of 100 % anatase.

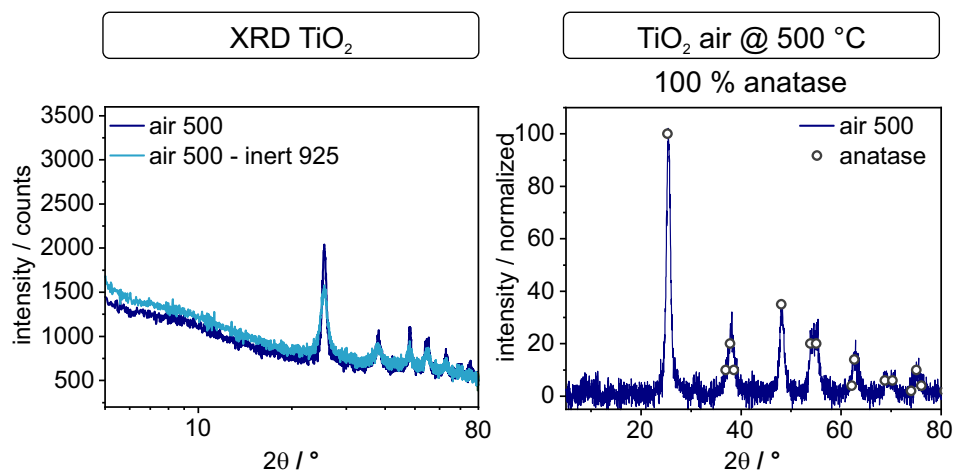


Fig. 7.10: XRD spectra of TiO₂ hollow particles calcinated under different conditions, as well as peak evaluation for the 500 °C particles calcinated in air.

7.7.3 Transparent fit of radiation data

Figure 7.12 shows measurement data with the transparent fit of the Protheus software (Netzsch) for hollow and solid particle and bulk quartz samples. It can be seen that the fit model was working perfectly for the bulk sample. However, it failed to fit the particle samples. The fit started getting inaccurate at 625 °C for the solid particle samples and 525 °C for the hollow particle samples. At 825 °C (solid) and 725 °C (hollow), the fit model could not fit the data anymore. This fit problem originated from the different peak shapes of the radiation peak, as shown in Figure 7.11. The bulk signal had a sharp initial temperature increase, followed by a decrease. The hollow particle signal had a diffusive-like shape. The solid particle signal is in between with a sharp initial increase, followed by a diffusive-like increase.

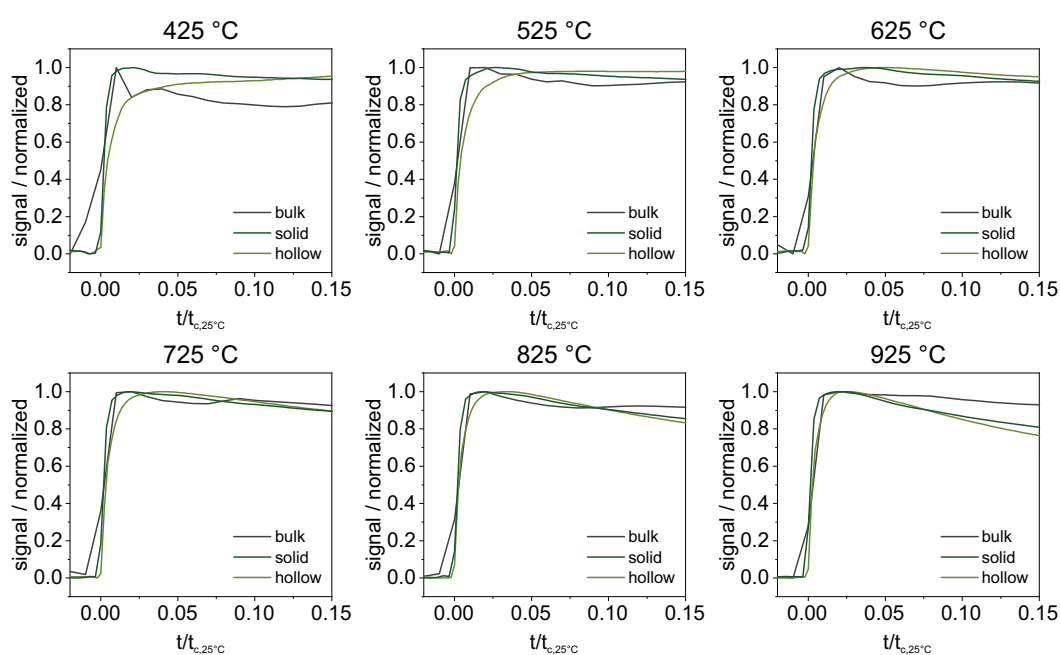


Fig. 7.11: Peak shape of radiation peak of hollow and solid particles, and bulk quartz glass from 425 to 925 °C.

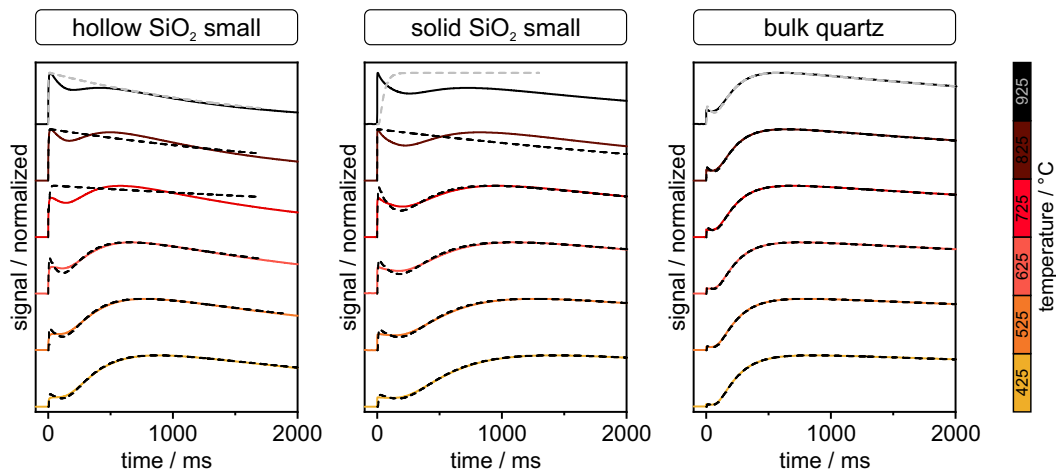


Fig. 7.12: Transparent fit on LFA data of hollow and solid particles, and bulk quartz. The colored lines show the measurement signal at 425–925 °C, the dashed lines show the corresponding fit.

7.7.4 Double-diffusive model of LFA data of hollow particle samples

From the double-diffusive model, it was possible to determine the thermal diffusivity of the radiation and conduction process of the hollow particle samples. The results are shown in Figure 7.3 and Figure 7.13. The radiation diffusivity was increasing with increasing temperature. An increasing radiative thermal conductivity is known from the geophysical science and measurements and calculations on olivine samples, where the conductivity is calculated from high-temperature absorption data.^[7] The conductive thermal diffusivity is almost constant in both samples. It has to be noted that the values do not represent the actual values because of two reasons. First, at higher temperatures, the conduction peak has almost vanished and the fit may be inaccurate. Second, the double-diffusive model is simplified and does not take into account reflection of heat at the sample-graphite-boundary. Therefore, an accurate evaluation of the conductive thermal diffusivity was not achieved with this fit.

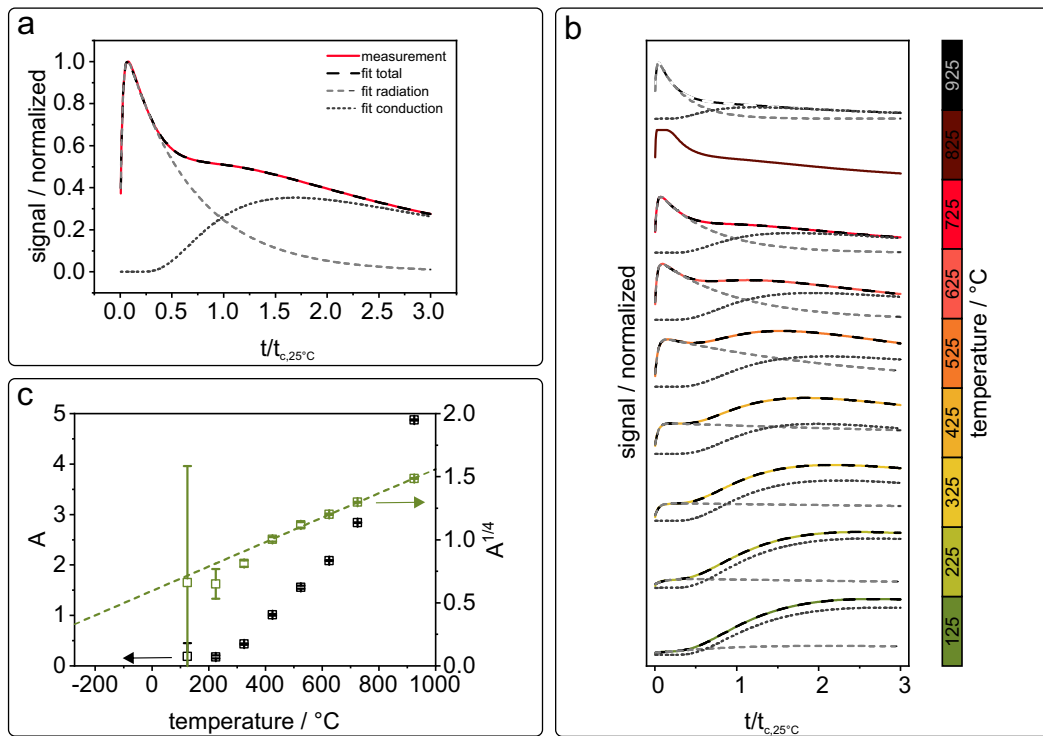


Fig. 7.13: Double diffusive model applied to temperature-dependent measurements of big hollow particle samples.

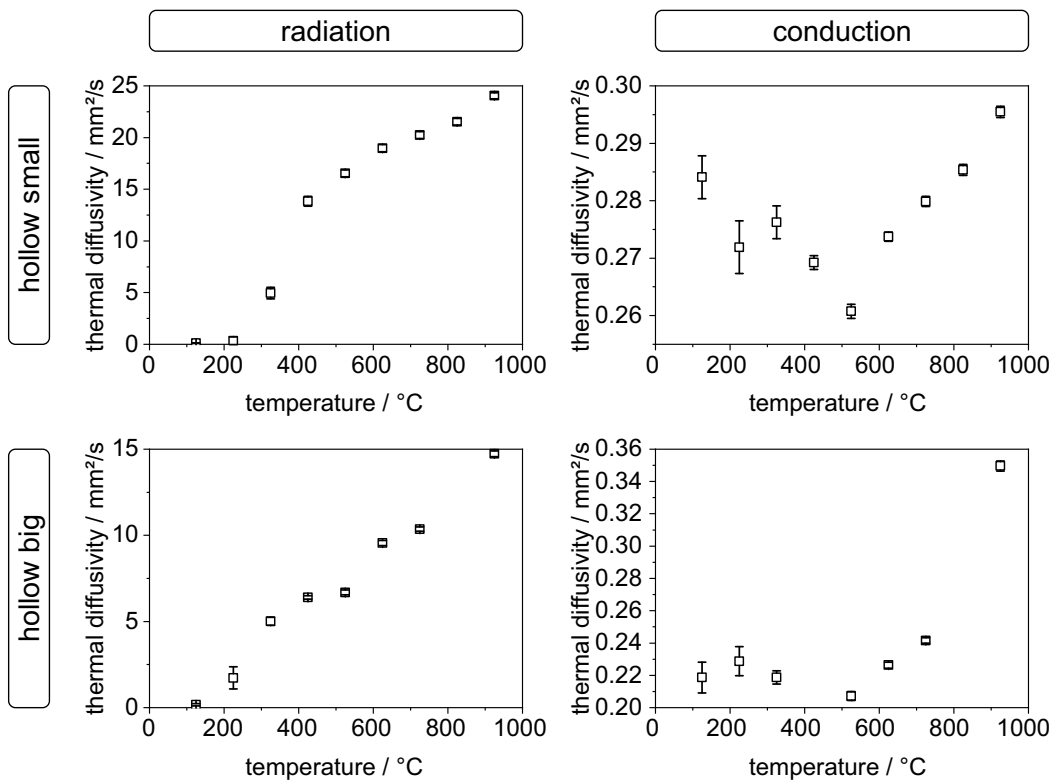


Fig. 7.14: Thermal diffusivity of radiation and conduction of hollow particle samples, calculated by the double diffusive model.

7.7.5 TiO₂ hollow particle sample

Similar to the 8 μm solid SiO₂ particles, the TiO₂ hollow particles have almost no transmission in the IR region (Figure 7.15). Because of the missing bandgap between 3 and 5 μm , radiation does not contribute to the thermal transport in the sample. Therefore, no radiation peak is visible in the measurements (Figure 7.16). The sample consisting of particles with a diameter of 734 nm and a shell thickness of 37 nm, has a density of 0.385 g/c³m, a thermal diffusivity of 0.613 mm²/s, and a thermal conductivity of 0.163 W/mK at 25 $^{\circ}\text{C}$.

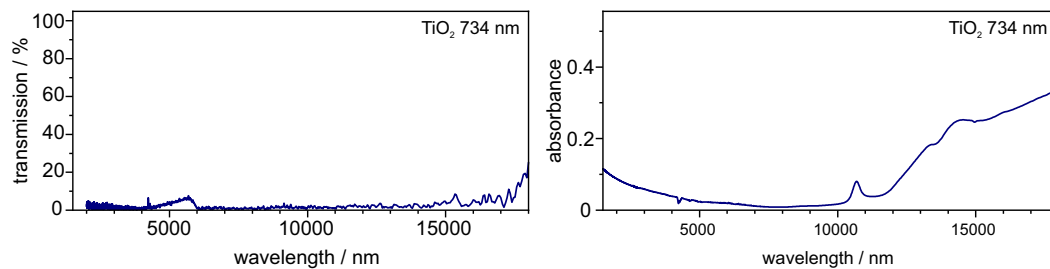


Fig. 7.15: Transmission and absorbance spectra of TiO₂ hollow particles in the IR region.

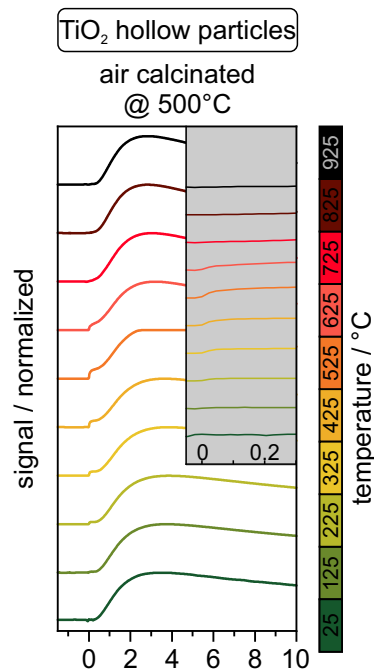


Fig. 7.16: Temperature-dependent LFA measurement signals of TiO₂ hollow particle samples that were calcinated at 500 $^{\circ}\text{C}$ in air or inert atmosphere before the measurement.

7.7.6 Inert calcined SiO₂ hollow particle samples

Figure 7.17 shows a picture of whole samples of SiO₂ hollow particles after calcination in air and inert atmosphere. The color of the inert calcinated samples comes from carbon residues in the hollow particles, as described by Wang *et al.*^[8] The samples have totally different optical properties in the visible region, however in the IR region the transmission is barely reduced (Figure 7.18). Therefore, the thermal behavior, especially the intensity of the radiation peak, does not change, which can be seen in Figure 7.19.

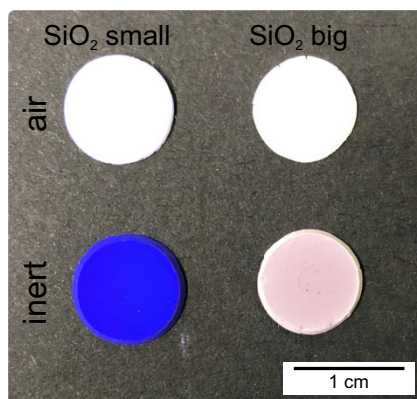


Fig. 7.17: Picture of colloidal glasslike assemblies of SiO₂ hollow particles after calcination at 925 °C in air and inert atmosphere.

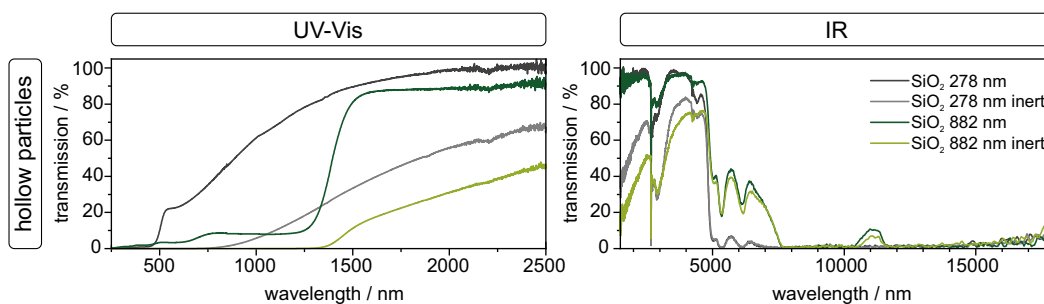


Fig. 7.18: Optical properties of air and inert calcinated colloidal assemblies of hollow SiO₂ particles in the UV-Vis and IR region.

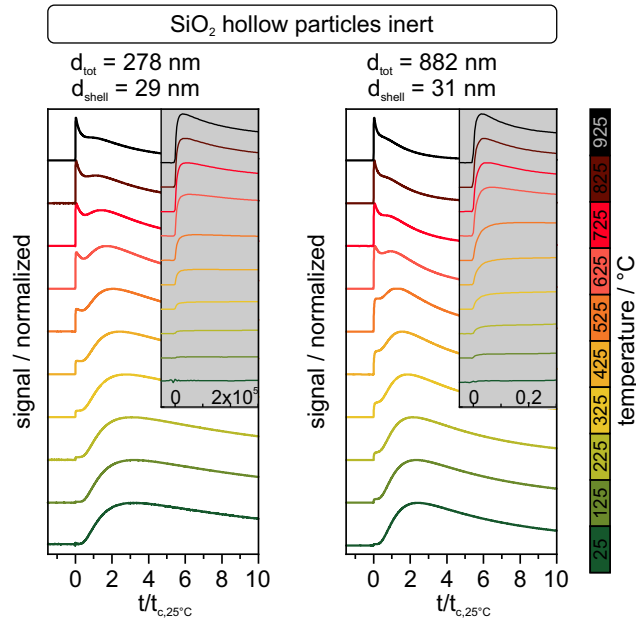


Fig. 7.19: Temperature dependent LFA measurement signals of SiO₂ hollow particle samples that were calcinated in argon atmosphere at 925 °C before the measurement. The time is normalized by the characteristic thermal response time t_c .

7.7.7 Mean particle distance for multilayer model

To get the mean interparticle distance in colloidal glasses, a MD simulation of particles with a diameter of 1 μm with a compression rate of $1e^{-2}$ has been performed. The resulting packing density was 61.1 %, which is comparable to the experimental data. The 3D radial distribution function of the simulated structure was calculated, according to Kopera *et al.*^[9] An interparticle distance of 63 nm was determined. Thus, we assumed to have a mean distance of 6 % of the total particle diameter for all samples.

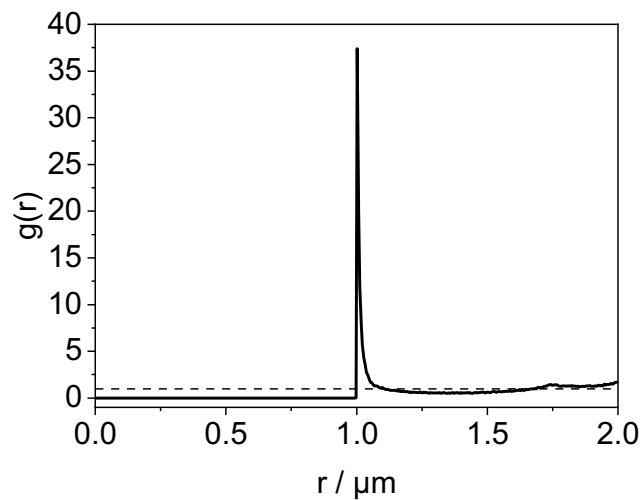


Fig. 7.20: 3D radial distribution function of a colloidal glass with a packing density of 61.1 % and particles with a diameter of 1 μm .

7.7.8 Transmission coefficient: influence of number of particle layers

In Figure 7.21 we show the Transmission coefficient \mathcal{T}_p^{12} for the p-polarized waves (which include possible surface wave contributions) in the $\lambda - \kappa$ plane choosing $\delta = 20$ nm and the multilayer structure, which models the structure of solid 353 nm silica particles. It can be seen how the number of the Fabry-Pérot modes is increasing when increasing the number of layers from $N = 9$ ($d = 2.5 \mu\text{m}$) to $N = 3121$ ($d = 827 \mu\text{m}$) forming Bloch band structures^[10] due to the periodicity of the structure. The same behavior can be expected for highly ordered nanoparticle structures. It can be further seen that when increasing the number of layers from $N = 9$ to $N = 3121$, only waves in the transparency window of glass for $\lambda < 5 \mu\text{m}$ can reach the second graphite layer, and all the other waves are damped out due to the losses in the glassy part of the structure. The waves reaching the second graphite layer also include evanescent contributions because the wavevector in glass can be larger than in vacuum. In the transparency window, the lateral wave vector κ is limited by $\sqrt{R(\epsilon_{\text{SiO}_2})}k_0 \approx 1.4k_0$ due to the material and those waves which can tunnel between the layers of the multilayer structure will finally heat up the graphite layer. It is interesting to note that there is no significant surface wave contribution for h^{12} in the restrahlen band $\lambda \in [8 \mu\text{m} : 9.3 \mu\text{m}]$. This is due to the fact that damping of the coupled surface modes is too strong to ensure an efficient coupling over long distances.

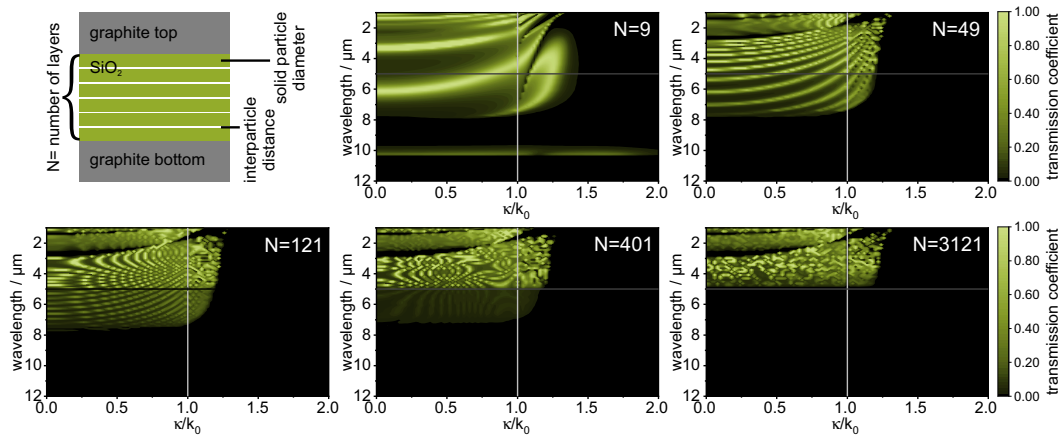


Fig. 7.21: Transmission coefficients of a model representing solid SiO_2 particle glasses with an increasing number of layers, N , from 9 to 3121.

7.7.9 Heat transfer coefficient

The radiative heat flux in the multilayer systems was calculated by using the theory of fluctuational electrodynamics. The heat transfer coefficient describing the radiative heat flow h^{12} from the graphite layer 1 at temperature T_1 and the heat flow h^{23} from

the intermediate film 2 at temperature T_2 towards the second graphite layer 3 at temperature T_3 are given by the expressions^{[11]–[13]}

$$h^{12/23} = \int_0^\infty \frac{d\omega}{2\pi} \sum_{j=s,p} \int \frac{d^2\kappa}{(2\pi)^2} \frac{\partial \Theta(T)}{\partial T} \mathcal{T}_j^{12/23}(\omega, \kappa). \quad (7.2)$$

Here $\Theta(T) = \hbar\omega / (\exp(\hbar\omega/k_B T) - 1)$ is the mean energy of a harmonic oscillator at temperature T ; k_B is the Boltzmann and \hbar the reduced Planck constant. The transmission coefficients $\mathcal{T}_j^{12/23}$ ($j = s, p$) are the functions of the frequency ω and the lateral wavevector κ for s- and p-polarized waves and can have values between 0 and 1. They contain the contributions of propagating waves ($\kappa < k_0$) but also evanescent waves ($\kappa > k_0$) in vacuum introducing the vacuum wavevector $k_0 = \omega/c$ and the light velocity c . The complex expressions can be found in Messina *et al.*^[14] However, they mainly depend on the distances δ and the layer thickness d as well as on the optical properties of the three layers. For example they depend on the corresponding amplitude transmission and reflection coefficients so that they can be evaluated as soon as the optical properties of the three layers are known. For the intermediate multilayer structure, we used the standard S-matrix method to calculate the needed reflection and transmission coefficients. The optical data for the permittivity of silica and graphite are taken from literature values in Ref.^{[11]–[13]}

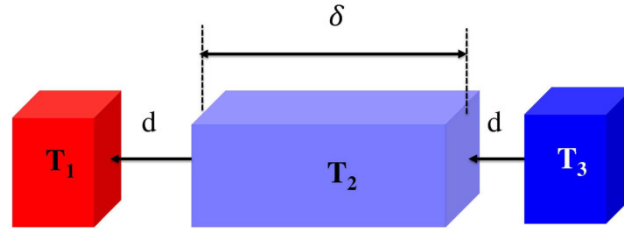


Fig. 7.22: Sketch of the three-layer structure. Layer 1 and 3 are graphite sheets, and the intermediate layer 2 is the nanoparticle glass of thickness d .

The radiative heat flux Φ (W/m^2) to the graphite layer 3 is within this model simply given as

$$\Phi = h^{12} (T_1 - T_2) + h^{23} (T_2 - T_3). \quad (7.3)$$

That means that in the first instance where the graphite layer 1 is heated by the laser flash, we have $T_1 > T_2 = T_3$ so that h^{12} describes the radiative coupling between the first and second graphite layers. Therefore the modes contributing to the radiative heat flow between the two graphite layers are mainly determined by \mathcal{T}_j^{12} ($j = s, p$).

7.7.10 Influence of coupling surface modes on transmission of heat radiation

To clarify the role of the surface mode contribution to the radiative heat flux, we have made exact numerical calculations using the open-source program SCUFF-EM developed by Homer Reid at MIT.^[15] It uses a boundary element method to determine the transmission functions $F_{ij}(\omega)$ between two objects i and j so that the exchanged power P between these objects due to thermal radiation (far- and near-field) can then be determined by

$$P_{ij} = \int_0^\infty d\omega (\Theta(T_i) - \Theta(T_j)) F_{ij}(\omega). \quad (7.4)$$

In Figure 7.23 we show the transmission functions for the heat flux between two, three, and four nanoparticles of diameter 800 nm and an interparticle distance of 50 nm. As can be expected, the heat flux between adjacent silica nanoparticles is dominated by the surface mode resonance at $\lambda \approx 9 \mu\text{m}$, and it becomes weaker and weaker when considering the coupling between nanoparticles with one or two nanoparticles in between them. When replacing the outer nanoparticles in the chain of 3 and 4 nanoparticles with a graphite particle, it can be nicely seen that the transmission of heat radiation will be mainly in the transparency region below $8 \mu\text{m}$, i.e., below the reststrahlen band. The surface mode resonance contribution becomes already relatively weak for a chain of 4 nanoparticles, and it can be expected that it is negligible for chains of 3000 to 4000 nanoparticles.

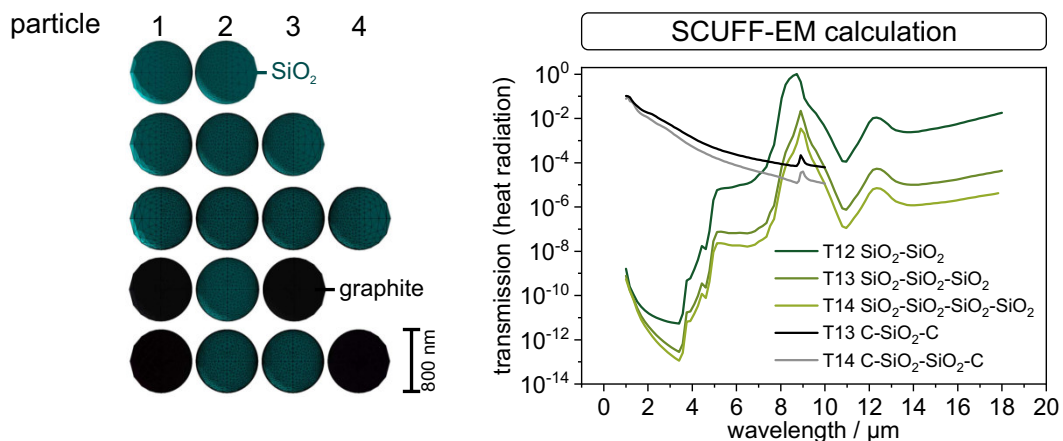


Fig. 7.23: SCUFF-EM calculation of transmission functions for heat flux between first and last particle in a row of two to four particles.

7.7.11 Influence of material thermal conductivity on radiation

We have used a set of 14 coupled differential equations to describe the temperature evolution of the system. The first and last graphite layers are in this model split into a $d_{\text{surf}} = 200\text{nm}$ thin surface layer (the skin depth of graphite for $\lambda = 1\ \mu\text{m} - 10\ \mu\text{m}$ is $100\ \text{nm} - 200\ \text{nm}$) with temperatures T_1 and T_{14} standing for the surface temperatures of the laser flash heated first layer and the measured surface temperature of the last layer, and a layer of thickness d_C with temperatures T_2 and T_{13} . The glass film is divided into 10 layers of thickness d_{SiO_2} with temperatures T_3, T_4, \dots, T_{12} . In this model, we assume that the adjacent layers are coupled via thermal conduction and that the graphite layers are coupled to the 3 glass layers by h^{23} and between each other by h^{12} . Then using Newton's law of cooling, we have the set of equations

$$C_{\rho,C,\text{surf}} \frac{dT_1}{dt} = h_{\text{cond},C}(T_2 - T_1) + h_{\text{rad}}(T_m - T_1) + h_{\text{cond, lat}}(T_m - T_1), \quad (7.5)$$

$$\begin{aligned} C_{\rho,C} \frac{dT_2}{dt} = & h^{12}(T_{13} - T_{\text{mean}}) + h^{23}(T_3 - T_2) \\ & + h_{\text{cond, C-SiO}_2}(T_3 - T_2) + h_{\text{cond},C}(T_1 - T_2) + h_{\text{cond, lat}}(T_m - T_2), \end{aligned} \quad (7.6)$$

$$\begin{aligned} C_{\rho,\text{SiO}_2} \frac{dT_3}{dt} = & h_{\text{cond, C-SiO}_2}(T_2 - T_3) + h_{\text{cond, SiO}_2}(T_4 - T_3) + h^{23}(T_2 - T_3) \\ & + h_{\text{cond, lat}}(T_m - T_3), \end{aligned} \quad (7.7)$$

$$C_{\rho,\text{SiO}_2} \frac{dT_4}{dt} = h_{\text{cond, SiO}_2}(T_3 - T_4) + h_{\text{cond, SiO}_2}(T_5 - T_4) + h_{\text{cond, lat}}(T_m - T_4), \quad (7.8)$$

... = ...

$$\begin{aligned} C_{\rho,C} \frac{dT_{13}}{dt} = & h^{12}(T_2 - T_{\text{mean}}) + h^{23}(T_{12} - T_{13}) + h_{\text{cond, C-SiO}_2}(T_{12} - T_{13}) \\ & + h_{\text{cond},C}(T_{14} - T_{13}) + h_{\text{cond, lat}}(T_m - T_{13}), \end{aligned} \quad (7.9)$$

$$C_{\rho,C,\text{surf}} \frac{dT_{14}}{dt} = h_{\text{rad}}(T_m - T_{14}) + h_{\text{cond, C}}(T_{13} - T_{14}) + h_{\text{cond, lat}}(T_m - T_{14}). \quad (7.10)$$

In these equations T_m is the ambient temperature, T_{mean} is the mean temperature in the glass medium, and

$$C_{\rho,C,\text{surf}} = C_C \rho_C d_{\text{surf}}, \quad C_{\rho,C} = C_C \rho_C d_C, \quad C_{\rho,\text{SiO}_2} = C_{\text{SiO}_2} \rho_{\text{SiO}_2} d_{\text{SiO}_2} \quad (7.11)$$

are the products of the heat capacities of graphite and silica, the corresponding mass densities (Table 7.2), and the layer thicknesses where $d_{\text{SiO}_2} = d/10$, $d_{\text{surf}} = 200\text{nm}$, and d_C can vary from $10\ \mu\text{m} - 30\ \mu\text{m}$. The heat transfer coefficients h^{12} and h^{23} are defined above h_{rad} is the htc of the graphite layer into vacuum, and takes the radiative cooling of the surface layers into account. The heat transfer coefficients

caused by thermal conduction in graphite, in silica, or between graphite and silica are defined as

$$h_C = \frac{\kappa_C}{d_{\text{surf}} + d_C}, \quad h_{\text{SiO}_2} = \frac{\kappa_{\text{SiO}_2}}{d_{\text{SiO}_2}}, \quad h_{\text{C-SiO}_2} = \frac{1}{\frac{1}{h_{\text{SiO}_2}} + \frac{1}{h_C}}. \quad (7.12)$$

The values of the thermal conductivities κ_C and κ_{SiO_2} are taken from literature (Table 7.2). Since the Kapitza resistance between graphite and silica is extremely small, we have neglected it. $h_{\text{cond, lat}}$ is a parameter which can be used to model lateral conductive losses in the sample.

This model neglects the thermal radiation channels within the graphite and silica media. That means it is assumed that within the materials conduction is more important than radiation. The numerical results also suggest that h^{23} has negligible impact for the used parameters underlining the assumption that the radiative coupling between adjacent layers by the surface mode interaction is small compared to the conductive one. Note that in this model, there are only three more or less unknown parameters: the conductivity of the glass medium κ_{SiO_2} which is actually measured by the LFA (i.e. by fitting the model to the data), the thickness of the graphite layers which are estimated to be 20 μm – 30 μm (dependent on the number of coated layers), and the lateral conductivity $h_{\text{cond, lat}}$.

Tab. 7.2: Specific heat capacity, c_P , and thermal conductivity, κ , of quartz glass and graphite. c_P of quartz glass was taken from Smyth *et al.*^[16], κ was calculated using the thermal diffusivity from our measurements on bulk quartz (Figure 7.2) and a density of 2.201 g/cm³. The c_P of graphite was calculated according to Butland *et al.*^[17], κ was calculated according to McEligot *et al.*^[18]

T [°C]	quartz		graphite	
	c_P [J/gK]	κ [W/mK]	c_P [J/gK]	κ [W/mK]
25	0.744	1.439	0.713	131.338
125	0.879	1.593	0.980	121.156
225	0.981	1.700	1.193	111.718
325	1.057	1.793	1.360	103.023
425	1.110	1.870	1.491	95.072
525	1.153	1.952	1.596	87.865
625	1.189	2.041	1.681	81.402
725	1.217	2.137	1.751	75.683
825	1.242	2.238	1.809	70.707
925	1.263	2.345	1.857	66.476

In Figure 7.24 we show the simulation of the LFA experiment by plotting the temporal temperature evolution $\Delta T_{14} = T_{14} - T_m$ of the second graphite surface temperature for $T_m = 925$ °C with initial conditions $T_1 = T_m + 10$ K and $T_2 = T_3 = \dots = T_{14} = T_m$ at time $t = 0$ ms and $d_C = 20$ μm . The values for h^{12} and h^{23} are calculated for the multilayer structure replacing the solid 353 nm nanoparticles with $N = 3121$ layers

(so that $d = 827 \mu\text{m}$) and $\delta = 20 \text{ nm}$. To show the impact of the conductivity of the intermediate glass layer, we have varied k_{SiO_2} . It can be seen that the relative strengths of the peaks, which are due to heating by thermal radiation or conduction, highly depend on the thermal conductivity of the glass layer.

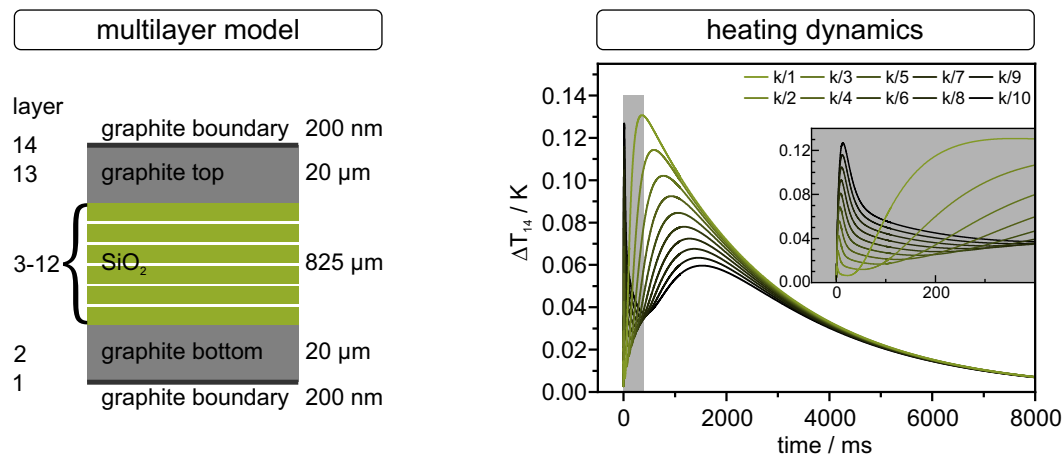


Fig. 7.24: Multilayer model for heating dynamics calculations of a solid SiO_2 colloidal structure with a particle diameter of 353 nm (left). Heating dynamics with lateral losses of the multilayer model at a temperature of $925 \text{ }^\circ\text{C}$ (right).

7.7.12 References

- [1] J. W. Goodwin, J. Hearn, C. C. Ho, and R. H. Ottewill, „Studies on the preparation and characterisation of monodisperse polystyrene latices“, *Colloid and Polymer Science*, vol. 252, no. 6, pp. 464–471, Jun. 1974.
- [2] X. Cheng, M. Chen, L. Wu, and G. Gu, „Novel and facile method for the preparation of monodispersed titania hollow spheres“, *Langmuir*, vol. 22, no. 8, pp. 3858–3863, Mar. 2006.
- [3] A. M. Lechner, T. Feller, Q. Song, *et al.*, „Scalable synthesis of smooth PS@TiO₂ core-shell and TiO₂ hollow spheres in the (sub) micron size range: Understanding synthesis and calcination parameters“, *Colloid and Polymer Science*, vol. 298, no. 7, pp. 867–878, Mar. 2020.
- [4] W. Stöber, A. Fink, and E. Bohn, „Controlled growth of monodisperse silica spheres in the micron size range“, *Journal of Colloid and Interface Science*, vol. 26, no. 1, pp. 62–69, Jan. 1968.
- [5] C. Graf, D. L. J. Vossen, A. Imhof, and A. van Blaaderen, „A general method to coat colloidal particles with silica“, *Langmuir*, vol. 19, no. 17, pp. 6693–6700, Aug. 2003.
- [6] R. C. Schroden, M. Al-Daous, C. F. Blanford, and A. Stein, „Optical properties of inverse opal photonic crystals“, *Chemistry of Materials*, vol. 14, no. 8, pp. 3305–3315, Aug. 2002.

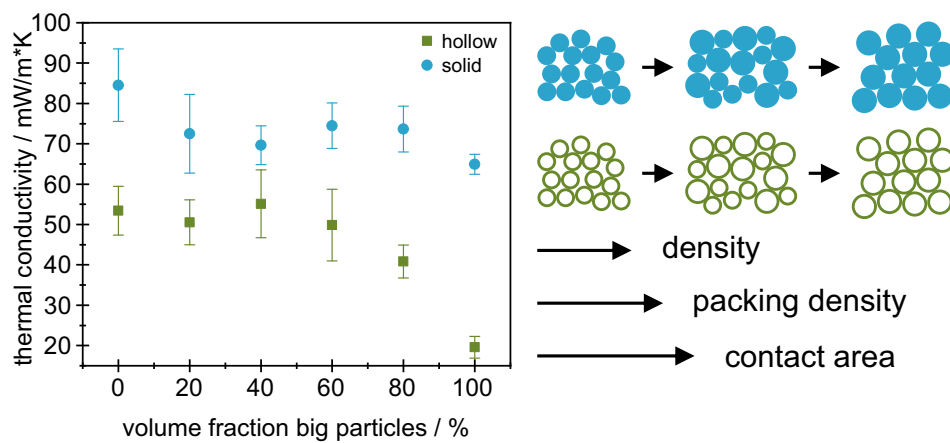
- [7] T. J. Shankland, U. Nitsan, and A. G. Duba, „Optical absorption and radiative heat transport in olivine at high temperature“, *Journal of Geophysical Research*, vol. 84, no. B4, p. 1603, 1979.
- [8] F. Wang, X. Zhang, J. Zhu, and Y. Lin, „Preparation of structurally colored films assembled by using polystyrene@silica, air@silica and air@carbon@silica core–shell nanoparticles with enhanced color visibility“, *RSC Advances*, vol. 6, no. 44, pp. 37 535–37 543, 2016.
- [9] B. A. F. Kopera and M. Retsch, „Computing the 3d radial distribution function from particle positions: An advanced analytic approach“, *Analytical Chemistry*, vol. 90, no. 23, pp. 13 909–13 914, Nov. 2018.
- [10] P. Yeh and M. Hendry, „Optical waves in layered media“, *Physics Today*, vol. 43, no. 1, pp. 77–78, Jan. 1990.
- [11] R. Kitamura, L. Pilon, and M. Jonasz, „Optical constants of silica glass from extreme ultraviolet to far infrared at near room temperature“, *Applied Optics*, vol. 46, no. 33, p. 8118, Nov. 2007.
- [12] A. B. Djurišić and E. H. Li, „Optical properties of graphite“, *Journal of Applied Physics*, vol. 85, no. 10, pp. 7404–7410, May 1999.
- [13] I. H. Malitson, „Interspecimen comparison of the refractive index of fused silica“, *Journal of the Optical Society of America*, vol. 55, no. 10, p. 1205, Oct. 1965.
- [14] R. Messina, P. Ben-Abdallah, B. Guizal, M. Antezza, and S.-A. Biehs, „Hyperbolic waveguide for long-distance transport of near-field heat flux“, *Physical Review B*, vol. 94, no. 10, Sep. 2016.
- [15] M. T. H. Reid and S. G. Johnson, „Efficient computation of power, force, and torque in BEM scattering calculations“, *IEEE Transactions on Antennas and Propagation*, vol. 63, no. 8, pp. 3588–3598, Aug. 2015.
- [16] H. T. SMYTH, H. S. SKOGEN, and W. B. HARSELL, „Thermal capacity of vitreous silica“, *Journal of the American Ceramic Society*, vol. 36, no. 10, pp. 327–328, Oct. 1953.
- [17] A. Butland and R. Maddison, „The specific heat of graphite: An evaluation of measurements“, *Journal of Nuclear Materials*, vol. 49, no. 1, pp. 45–56, Nov. 1973.
- [18] D. McEligot, W. D. Swank, D. L. Cottle, and F. I. Valentin, „Thermal properties of g-348 graphite“, Tech. Rep., May 2016.

Thermal Transport in Binary Colloidal Glasses

Anna M. Neuhöfer¹ and Markus Retsch¹

¹ Physical Chemistry I, University of Bayreuth, Universitätsstraße 30, 95440 Bayreuth, Germany

² Bavarian Polymer Institute (BPI), University of Bayreuth, Universitätsstraße 30, 95440 Bayreuth, Germany



unpublished

8.1 Abstract

Making thermal insulation materials more efficient is still a big challenge. A popular material for thermal insulation applications is silica because of its inherent low thermal conductivity, high melting temperature, and chemical inertness. In contrast to aerogels, colloidal silica particles and hollow particles offer a good base material for model systems because of its controllable shape and pore sizes. This contribution focuses on the parameters material density, packing density, disorder, and particle size of particle based insulation materials. Therefore, binary mixtures of monodisperse particles with diameters in the range of 500 and 900 nm have been prepared. We compare the influence of the material density based on two distinct particle motifs: solid and hollow particle structures. The packing density of the ensemble was reduced by a fast filtration method. We find that the influence of the particle size exceeds the influence of the binary mixing ratio in terms of thermal conductivity reduction. Since the particle size is directly related to the material density in the case of the hollow particles, a reduction of the thermal conductivity up to 60 % was achieved through a switch from small to big particles. This study contributes to research on thermal insulation materials by demonstrating the complex interplay of the disorder, packing density, and effective density.

8.2 Introduction

The efficient insulation of buildings is still a big challenge. To reduce the overall wall thickness, conventional insulation materials, such as mineral wool and expanded polystyrene, need to be improved in terms of thermal insulation efficiency, lifetime, recyclability, and breathability. Since 1931, aerogels have been researched and optimized for thermal insulation applications.^[1] A typical backbone material is silica, which is particularly suitable for this task due to its low bulk thermal conductivity, high melting temperature, and chemical inertness. A further advantage of silica is the natural abundance and the possibility to recycle it after usage. Aerogels typically require a supercritical drying step, which leads to high production costs. An alternative route requires surface modification of the lyogel, followed by ambient pressure drying. This alternative is promising because it is less expensive. However, a further synthesis step is necessary.^[2] Another weakness of aerogels is the fragility that may lead to puncturing and, consequently, a reduced lifetime.^[3] Another drawback is the difficult structural characterization of aerogel materials, limiting the possibilities for a targeted performance improvement based on structure-property relationships.^[4] Since 1931, aerogels have been researched and optimized for thermal insulation materials.^[5] An emerging field of studies is the research on insulation materials based on silica hollow particles in the sub-micrometer region. Only ten years ago,

Liao *et al.* published their results on the thermal conductivity of silica hollow sphere powders, measured by the 3ω technique.^[6] Since then, the research on silica hollow particle samples was mainly driven by the groups of Gao, working with raspberry-like silica shells^{[3],[7],[8]} and Retsch, working with smooth silica shells^{[9],[10]}. Besides the shell structure, both groups reported consistent results of thermal conductivities down to about 20 mW/mK. In addition to these insulation properties, further advantages of this material class are the controllability of the average pore sizes, shell thickness, and the superstructure. This high control over the particle geometry helps developing structure-property-relationships, which in turn can be utilized for a specific optimization of the insulation capability in the future. Consequently, hollow particle materials have the potential to become the next generation of thermal insulation materials.

There are three contributions that determine the thermal conductivity of porous materials: radiation, gaseous and solid conduction. Radiation is based on an energy transfer by electromagnetic waves that are emitted by matter above 0 K. At ambient temperature measurements its contribution is comparably small in the case of silica aerogels and hollow particle structures. Experimentally, this was shown before by Herrmann *et al.*, who compared the thermal conductivities of pure and opacified silica aerogels. Below 50 °C, there was no significant difference between the different samples. Above 50 °C, the thermal conductivities of the opacified samples were reduced due to the suppression of the radiation.^[11] Reim *et al.* also characterized the thermal properties of packed silica aerogels beds, completed by calculations using a parallel line thermal transport model. They also saw a significant influence of thermal radiation above 50 °C.^[12] In 2017, Fang *et al.* published a numerical method to solve the conduction-radiation equation and also confirmed a minor influence of radiation at room-temperature.^[13] Furthermore, a decreasing influence of the radiative thermal transport with increasing density was found. Hollow silica particle structures, that can be classified as high-density aerogels^{[10],[14]}, therefore, do not have a significant influence of radiative thermal transport at room-temperature. This was verified experimentally by Neuhöfer *et al.* who saw an increasing radiative influence above 200 °C.^[15]

In the aerogels' pores and hollow nanoparticle specimen, gaseous conduction takes place. A lot of research on pressure dependent thermal transport of aerogels and hollow silica samples has been done by various groups. Collectively, all studies showed increasing thermal conductivities with increasing gas pressure due to the additional diffusion pathways through the gaseous phase.^{[4],[8],[10],[12],[16]} Furthermore, the gaseous conductivity is dependent on the gas species, temperature and pore structure.^[8] Decisive is the Knudsen number that is defined as the ratio of the mean free path of the gas molecules and the pore size.^[17] When the mean free path is larger than the mean pore size, gas-wall interactions dominate over the gas-gas interactions,

leading to a significant reduction in the gaseous thermal conductivity. In the case of nanostructured pores ($< 1 \mu\text{m}$) this reduction in bulk thermal conductivity is even retained at ambient pressure.^[10]

Therefore the main thermal transport in aerogel and silica hollow particle samples occurs through the solid backbone. The thermal conductivity, κ , is calculated from the thermal diffusivity, α , the density, ρ , and specific heat capacity, c_P : $\kappa = \alpha\rho c_P$. Consequently, the thermal conductivity is directly proportional to the sample density. With decreasing density, the thermal conductivity decreases due to a restriction of the propagation of heat to the transport pathways in the tenuous structure. Fricke and Tillotson performed a series of thermal conductivity measurements with densities between 50 and 250 kg/m³ and revealed that the solid conduction is proportional to $\rho^{1.6}$.^[4] The solid backbone of an aerogel is made of interconnected silica nanoparticles with sizes up to 10 nm.^{[8],[16],[18],[19]} In the case of silica hollow particle samples, the particle diameters are ~ 10 -100 times larger. However, in both cases the amount and area of the contact points is critical for the thermal transport. It is possible to calculate the contact area and its influence on the thermal conductivity using the Hertzian theory. Experimentally, particle beds have been compressed with different loading pressures^{[20],[21]} or polymer particles have been heated above the glass transition temperature^[22] to increase the contact areas without changing the number of contact points. Both experiments resulted in an increased thermal conductivity with increasing contact area. Up to now, far too little attention has been paid to the influence of the particle size that will be addressed in this paper.

Besides the contact area, the number of contact points is strongly affecting the thermal conductivity by limiting the number of transport paths. This can be achieved by increasing the disorder of the system. A measure for the order in a colloidal assembly is the solid volume fraction, ϕ . In 1986, the first phase diagrams on the ϕ -dependent colloidal superstructure have been published by Pusey and Megan.^[23] The structures can be divided in equilibrium (liquid, crystalline) and non-equilibrium (supercooled, glassy) states.^{[24]-[28]} Crystalline colloidal structures, that are often used as model systems for thermal transport investigations, have the highest possible solid volume fraction of $\phi_{\text{hcp}} \approx 0.74$ due to a hexagonal closed packaging.^{[9],[29]} To decrease the order of a colloidal system, it is necessary to increase ϕ fast enough to avoid crystallization, for example through a filtration method.^[30] In that case, the assemblies first undergo supercooling, passing a glassy region that is limited by the random-close-packaging boundary. The exact values for the phase boundaries depend strongly on several parameters, such as the particle diameter, repulsive Yukawa pair potential, and the Debye length.^{[23],[31]} However, typical values are $\phi_{\text{glass}} \approx 0.58$, and $\phi_{\text{rcp}} \approx 0.64$.^[24] Another possibility to achieve non-equilibrium states is increasing the dispersity of the colloidal system by mixing two particle sizes, resulting in a polydispersity of $> 5\%$.^{[27],[28]} The resulting lowered number of

particle contact points was shown by Nutz *et al.* who performed molecular dynamic simulations on binary particle assemblies with size ratios of 0.54, 0.8, and 0.9. They showed that for all size ratios, the number of next neighbors decreased from 12 to 10-11. For the thermal transport this resulted in extended streamline lengths and consequently lower thermal conductivities.^[29]

Considering all of the above parameters, the thermal conductivity of a material can be strongly decreased by decreasing the material density, lowering the solid volume fraction, and number of contact points. This study focuses on the influence of material density and disorder on the thermal properties of solid and hollow silica particle structures. While a controlled reduction of the density is achieved by a switch from solid to hollow particles, the disorder is introduced by binary particle mixtures and a fast assembly process. Our contribution provides new insights into the influences of these parameters and helps to design better insulation materials in the future.

8.3 Materials and Methods

8.3.1 Materials

503 nm and 902 nm SiO₂ solid particles were purchased from microParticles GmbH and used as received. The synthesis of the PS@SiO₂ core-shell particles is described in detail in the supporting information.

The particles were assembled using the vacuum filtration method described by Ruckdeschel *et al.*^[30] A vacuum filtration system from Merck Millipore was used in combination with MF Millipore membrane filters with pore sizes of 0.45 μm, and a Teflon funnel with a diameter of 1 cm has been used.

All samples have been dried at 40 °C in a vacuum overnight before calcination. The samples have been calcined at 500 °C for 12 h to remove organic components and avoid structural changes during the measurements.

8.3.2 Methods

Scanning electron microscopy (SEM) was performed using a Zeiss Ultraplus instrument using acceleration voltages of 3 kV. InLens and Everhard-Thornley detectors were used. MATLAB circle detection function was used to evaluate the diameter of the particles.

Laser scanning microscopy was performed using a LEXT OLS5000-SAF microscope (Olympus) to determine the sample thicknesses and volumes. The volume and mass of the sample were used for the density determination.

Differential Scanning Calorimetry (DSC) measurements were performed on a Discovery 2500 DSC (TA Instruments) between -50 and 450 °C with a heating and cooling rate of 20 K/min. The samples were measured in a heat-cool-heat cycle, only the second heating data was used for evaluation. The specific heat capacity, c_P , was determined according to ASTM E1269.^[32]

Laser Flash Analysis (LFA) was conducted on a LFA 467 HT HyperFlash apparatus (Netzsch) at 25 °C in vacuum. The samples were sputtered with a 1 μm gold layer on the bottom side and coated with a thin layer of graphite on both sides before inserting in the sample holder. The sample holder was equipped with self-made graphite support and spacer.^[15]

8.4 Results and Discussion

We base our analysis on two types of porous materials, one comprising *hollow* silica, the other comprising *solid* silica spheres. Silica was used because of its high thermal insulation capability, especially in the case of colloidal crystals consisting of hollow silica particles. As explained in the introductory part, the thermal transport can be further reduced by switching from crystalline to disordered structures and by reducing the material density. Here, the disorder was generated by two complementary mechanisms. On the one hand, binary mixtures of two particle sizes with 20, 40, 60, and 80 vol% of the big particles have been prepared. Additionally, the pure small and big particles have been measured. It is well known that the addition of a second particle size prevents crystallization. Furthermore, it was shown before on polystyrene particles that a particle size ratio of 0.6 is the optimum for reducing the thermal transport.^[29] Therefore, the hollow silica particles have been chosen to be 568 nm with 36 nm shells and 966 nm with 32 nm shells. The solid particles were 503 nm and 902 nm (Figure 8.4 and 8.5). The diameter ratios were therefore 0.59 and 0.56 for the hollow and solid particles, respectively. A second way to increase the particle disorder is a fast assembly strategy, which attenuates crystallization. Therefore, the filtration method was used for the assembly in this work. It reduces the assembly process from several days to one hour by removing the water of the particle dispersions through a filter paper, instead of drying the dispersion in a beaker. Figure 8.1 shows sideview SEM images of the resulting particle structures of the hollow (top) and solid (bottom) particles. For a better visualization, the respective big particles were highlighted in green (hollow) and blue (solid). It can

be seen, that all assemblies are disordered. Crystallization was suppressed by the filtration method for all samples, even the 0 and 100 vol% samples, that would have been able to crystallize owing to their monodispersity. The binary mixtures may additionally contribute to the disorder in case of the 20, 40, 60, and 80 vol% samples.

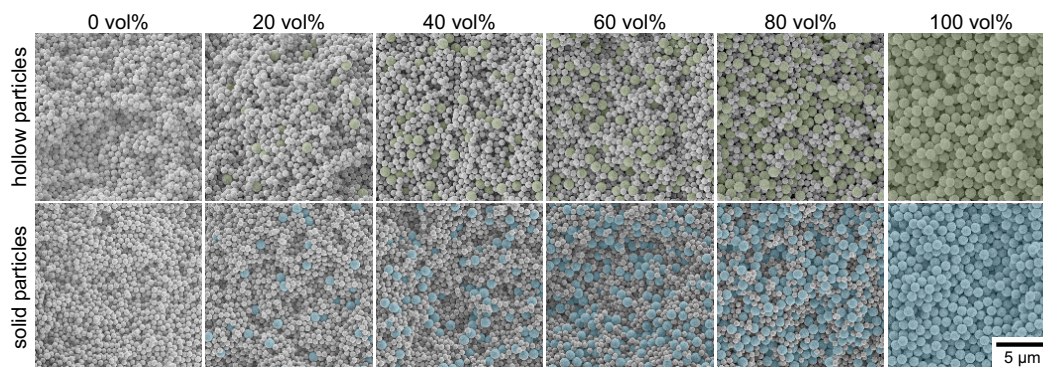


Fig. 8.1: SEM sideview images of colloidal glasses with increasing amount of big particles. Top row: hollow binary mixtures. Bottom row: solid binary mixtures.

The second way to tune and reduce the thermal transport in colloidal systems is the material density. In our case the density was reduced by switching from solid to hollow particles. As base material, PS@SiO₂ particles have been used. All particles have been assembled before calcination. The core-shell particles exhibit a substantially higher density compared to their hollow particle analogues. Therefore, to maintain a high comparability to the solid silica sphere samples, we decided to conduct the self-assembly process with core-shell particles. Consequently, we can assume that the mesostructure of the hollow and solid samples is similar. After calcination, the overall density was reduced in the best controllable way. The particles retain their spherical shape and do not crack or disintegrate during the calcination process (Figure 8.4, supporting information). Figure 8.2A shows the sample density in dependence of the volume fraction of the big particles for the solid and hollow particle samples. The sample densities were determined by dividing the sample mass by the volume. The volume was determined by the analysis of three-dimensional sample images recorded by a laser scanning microscope. For each ratio, 5-6 samples have been measured. In case of the solid particles, the density remains almost constant around 1.2 g/cm³. The switch to hollow particles reduces the sample density to about 1/3 of the solid particle density for the 0% big particle samples. In contrast to the solid particles, the density expectedly decreases by 47% from 0.38 to 0.18 g/cm³. This makes sense when having in mind that the specific particle density decreases by 53% from the small to the big particles, considering the comparable shell thickness of ~ 35 nm.

The sample densities were used to calculate the packing densities, ϕ , of the samples, which are shown in figure 8.2B for the solid and hollow particles. The packing density

is used to classify the degree of crystallinity and order in the different samples. Remarkable are the overall high deviations within one sample group, especially in the case of the 20% big particle samples. This unveils the drawback of the filtration method – a high degree of variability between the individual experiments.

However, the main advantage of the filtration method was successfully utilized, that the particle assembly was fast enough to suppress the crystallization process, which can be seen by the data of the monodisperse small and big particle samples. The values for the solid particles are $\phi_{s,0} = 0.65$ and $\phi_{s,100} = 0.69$ and, therefore, in the range of a random-close-packing state. It is interesting that the packing density of the hollow particles is even lower. The small hollow particles led to a packing density of $\phi_{h,0} = 0.62$, which is in the glassy state. What stands out is the packing density of $\phi_{h,100} = 0.54$ for the big hollow particle samples, that is very low and in the supercooled region. A possible explanation for the low packing densities could be found in the particle stabilization. In contrast to the solid silica particles, the polystyrene and core-shell particles are sterically stabilized with PVP. The polymer is added during the synthesis of the polystyrene particles and is necessary for the Stöber synthesis of the silica shell. For the synthesis of the big polystyrene particles, more than the 3-fold amount of PVP was inserted, compared to the small polystyrene particle synthesis. This large amount of PVP may have increased the steric stabilization of the big core-shell particles and hindered a closer packing of the particles during the filtration process.

There are also significant differences between the packing densities of the mixed particle samples in the case of the solid and hollow particles. While the values for the solid samples are all in the random-close-packing region, the values for the hollow samples scatter randomly between the supercooled region for $\phi_{h,20} = 0.57$ and the random-close-packed region for $\phi_{h,60} = 0.72$. In the case of the solid samples, no dependence between the packing density and the binary particle mixture could be found relative to the large standard deviations. The extraordinary scattering in the case of the hollow samples may also be a result of the different steric stabilization of the particles.

The thermal diffusivity of all samples was determined at 25 °C in vacuum using the light flash method. Figure 8.3A shows the thermal diffusivity data of the solid and hollow particle samples. The thermal diffusivity of the hollow samples is up to two times higher than the solid samples. The data of the monodisperse small and big particle samples shows a drop of $\sim 25\%$ of the thermal diffusivity from the 0 to the 100 vol% big particle samples for both, the solid and hollow samples. In contrast, the data of the mixed samples behaves differently for solid and hollow samples. In the case of the solid particles, the thermal diffusivity of the mixed samples lays in between both limiting values. The thermal diffusivity of the hollow particle mixtures

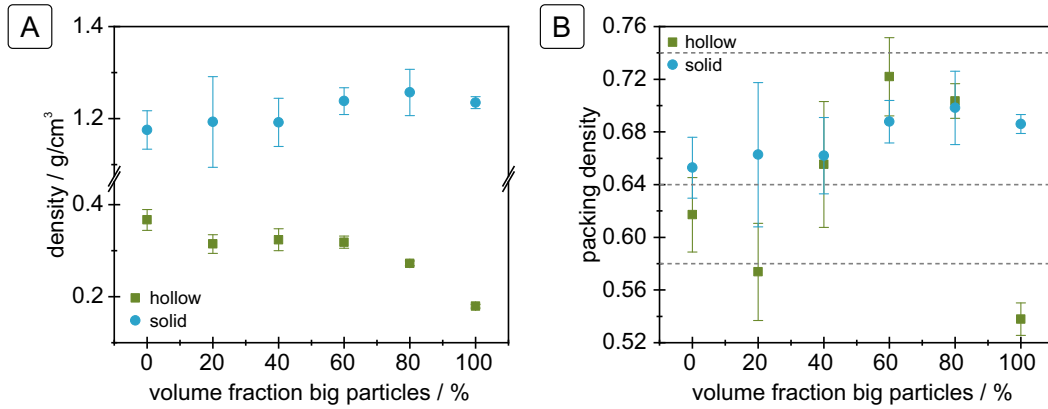


Fig. 8.2: (A) Density of samples made from hollow and solid binary mixtures. (B) Resulting packing density of the samples, calculated with a silica shell density of 1.8 g/cm^3 , according to Ruckdeschel *et al.*^[10] The dashed lines show the literature transition values from the supercooled to the glassy state ($\phi_g \approx 0.58$), from the glassy to the random-close-packing state ($\phi_{\text{rcp}} \approx 0.64$), and the upper solid volume fraction, given by the hexagonal-close-packaging of monodisperse particles ($\phi_{\text{hcp}} \approx 0.74$).^[33]

exceeds both limiting values. However, especially in the case of the hollow samples, the big error bars also indicate a high variability within one mixing ratio.

From the thermal diffusivity and sample density the thermal conductivity of all samples was calculated, using the density and specific heat capacity, c_P , using $\kappa = \alpha \cdot \rho \cdot c_P$. The specific heat capacity was determined from differential scanning calorimetry measurements. It is $c_{P,s} = 0.68 \pm 0.02 \text{ J/gK}$ for the solid particles and $c_{P,h} = 0.83 \pm 0.06 \text{ J/gK}$ for the hollow particles. As expected, the thermal conductivity of the solid samples is larger than for the hollow samples. Again, there is a drop from the 0 to 100 vol% big particle samples. In the case of the thermal conductivity, the decrease is different for the solid and hollow samples. For the hollow samples, the decrease is about 60%, which is a significantly higher reduction compared to the solid samples with 20%. The thermal conductivities of the particle mixtures are in between both limiting values and follow the trend that was observed by Nutz *et al.* on binary polymer particle mixtures before.^[29]

The data presented here shows the complexity of thermal transport in particular systems, since the particles itself and their assembly have an influence on the thermal properties. Crucial parameters for the thermal diffusivity and conductivity are the specific heat capacity, packing density, and the number of contact points and contact areas of the individual particles. In addition to the above mentioned multiple parameters, the variability of the particle assembly makes the characterization more difficult. However, it is still possible to deduce trends from the presented data: The introduction of disorder by binary mixtures of solid silica spheres plays a subordinate role compared to the fast filtration process. This is shown by the thermal conductivity data of the solid particle assemblies, that does not change when varying

the mixing ratios. The thermal conductivity data of the solid particles also reveals the influence of the particle size. The smaller the particle diameter, the larger is the thermal conductivity. This is due to the fact that the ratio of the contact areas and the particle surface increases with decreasing particle diameter. The increased contact areas, in turn, lead to a higher thermal conductivity, which was shown in literature before.^{[20]–[22]} Reducing the material density, by switching from solid to hollow particles, leads to a systematic reduction of the thermal conductivity. The density drop from the small to the large hollow particle assemblies, influences the thermal conductivity of the corresponding structures in addition to the influence of the degree of disorder, particle size, and contact area. Overall, the influence of the a reduction in density dominates over the degree of disorder when it comes to thermal insulation materials.

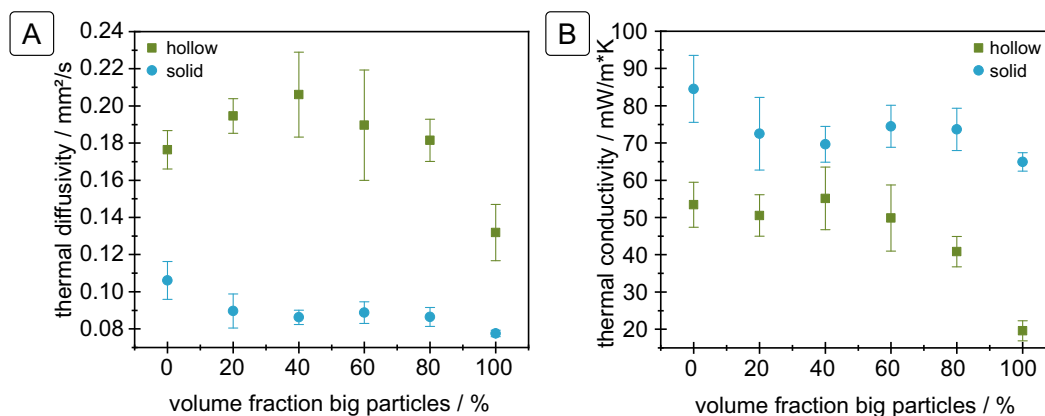


Fig. 8.3: Absolute values for thermal diffusivity (A) and thermal conductivity (B) of binary colloidal glasses.

8.5 Summary and Conclusions

The aim of the present research was to examine the influence of material density and disorder on the thermal properties of colloidal silica structures. For that, two strategies have been followed: reduction of the density by a switch from solid to hollow particles and enhancement of the degree of disorder by using binary particle mixtures and fast assembly through a filtration method. Therefore, binary mixtures of solid and hollow silica particles in the size range of 500 and 900 nm have been prepared successfully, which was confirmed by SEM sideview images. It was possible to reduce the material density of the hollow particle samples of 33% up to 85% compared to the solid particles. While the solid samples' densities stayed almost constant for all compositions, it decreased with increasing amount of the big hollow particles. This finding already indicated the strong influence of the particle size on the material properties in case of the hollow samples. The calculated packing densities provided more information about the degree of disorder of the samples. Again, it was more comparable for the solid samples, while the hollow samples had

strong fluctuations reaching from the random-close-packed structures down to the supercooled region for the 100 % big particle structures. The density measurements unveiled also a high degree of variability between the individual experiments as disadvantage of the fast filtration method. The presented thermal conductivity data showed the complex interplay of the different parameters density, disorder, and particle size, that are closely connected and cannot be examined in a disentangled way. However, two main trends have been observed: First, the influence of the particle size was more pronounced than the influence of the degree of disorder in a sample. Increasing the particle size from 500 to 900 nm, reduced the thermal conductivity of about 20 %, due to smaller contact areas between the individual particles. The second trend is that the influence of the sample density was more pronounced than the influence of the degree of disorder in a sample. For the hollow sample series, the influence of the density leads to a more pronounced drop in the thermal conductivity of 60 % from the small to the large particles. Conclusively, this study sets the basis for further research on the influence of the solid and hollow particle diameters on the materials' thermal properties.

Acknowledgements

We thank Stefan Rettinger for the help with LEXT measurements. We also thank the Bavarian Polymer Institute, especially Markus Drechsler, for his help with TEM measurements.

Funding information

This project was funded by the German Research Foundation (DFG RE3550/2-1).

8.6 References

- [1] S. S. Kistler, „Coherent expanded aerogels and jellies“, *Nature*, vol. 127, no. 3211, pp. 741–741, May 1931.
- [2] A. S. Dorcheh and M. Abbasi, „Silica aerogel; synthesis, properties and characterization“, *Journal of Materials Processing Technology*, vol. 199, no. 1-3, pp. 10–26, Apr. 2008.
- [3] L. I. C. Sandberg, T. Gao, B. P. Jelle, and A. Gustavsen, „Synthesis of hollow silica nanospheres by sacrificial polystyrene templates for thermal insulation

- applications“, *Advances in Materials Science and Engineering*, vol. 2013, pp. 1–6, 2013.
- [4] J. Fricke and T. Tillotson, „Aerogels: Production, characterization, and applications“, *Thin Solid Films*, vol. 297, no. 1-2, pp. 212–223, Apr. 1997.
- [5] S. S. KISTLER, „Coherent expanded aerogels and jellies“, *Nature*, vol. 127, no. 3211, pp. 741–741, May 1931.
- [6] Y. Liao, X. Wu, H. Liu, and Y. Chen, „Thermal conductivity of powder silica hollow spheres“, *Thermochimica Acta*, vol. 526, no. 1-2, pp. 178–184, Nov. 2011.
- [7] S. A. Mofid, B. P. Jelle, X. Zhao, *et al.*, „Utilization of size-tunable hollow silica nanospheres for building thermal insulation applications“, *Journal of Building Engineering*, vol. 31, p. 101336, Sep. 2020.
- [8] G. Tang, C. Bi, Y. Zhao, and W. Tao, „Thermal transport in nano-porous insulation of aerogel: Factors, models and outlook“, *Energy*, vol. 90, pp. 701–721, Oct. 2015.
- [9] P. Ruckdeschel, T. W. Kemnitzer, F. A. Nutz, J. Senker, and M. Retsch, „Hollow silica sphere colloidal crystals: Insights into calcination dependent thermal transport“, *Nanoscale*, vol. 7, no. 22, pp. 10059–10070, 2015.
- [10] P. Ruckdeschel, A. Philipp, and M. Retsch, „Understanding thermal insulation in porous, particulate materials“, *Advanced Functional Materials*, vol. 27, no. 38, p. 1702256, Sep. 2017.
- [11] G. Herrmann, R. Iden, M. Mielke, F. Teich, and B. Ziegler, „On the way to commercial production of silica aerogel“, *Journal of Non-Crystalline Solids*, vol. 186, pp. 380–387, Jun. 1995.
- [12] M. Reim, G. Reichenauer, W. Körner, *et al.*, „Silica-aerogel granulate – structural, optical and thermal properties“, *Journal of Non-Crystalline Solids*, vol. 350, pp. 358–363, Dec. 2004.
- [13] W.-Z. Fang, H. Zhang, L. Chen, and W.-Q. Tao, „Numerical predictions of thermal conductivities for the silica aerogel and its composites“, *Applied Thermal Engineering*, vol. 115, pp. 1277–1286, Mar. 2017.
- [14] Y.-J. Dai, Y.-Q. Tang, W.-Z. Fang, H. Zhang, and W.-Q. Tao, „A theoretical model for the effective thermal conductivity of silica aerogel composites“, *Applied Thermal Engineering*, vol. 128, pp. 1634–1645, Jan. 2018.
- [15] A. M. Neuhöfer, K. Herrmann, F. Lebeda, *et al.*, „High-temperature thermal transport in porous silica materials: Direct observation of a switch from conduction to radiation“, *Advanced Functional Materials*, p. 2108370, Nov. 2021.

- [16] K. Swimm, G. Reichenauer, S. Vidi, and H.-P. Ebert, „Gas pressure dependence of the heat transport in porous solids with pores smaller than 10 nm“, *International Journal of Thermophysics*, vol. 30, no. 4, pp. 1329–1342, Jul. 2009.
- [17] M. Knudsen, „Die molekulare wärmeleitung der gase und der akkommodationskoeffizient“, *Annalen der Physik*, vol. 339, no. 4, pp. 593–656, 1911.
- [18] D. Dan, H. Zhang, and W.-Q. Tao, „Effective structure of aerogels and decomposed contributions of its thermal conductivity“, *Applied Thermal Engineering*, vol. 72, no. 1, pp. 2–9, Nov. 2014.
- [19] B. Himmel, T. Gerber, H. Bürger, G. Holzhüter, and A. Olbertz, „Structural characterization of SiO₂@Al₂O₃ aerogels“, *Journal of Non-Crystalline Solids*, vol. 186, pp. 149–158, Jun. 1995.
- [20] J. Mo and H. Ban, „Measurements and theoretical modeling of effective thermal conductivity of particle beds under compression in air and vacuum“, *Case Studies in Thermal Engineering*, vol. 10, pp. 423–433, Sep. 2017.
- [21] D. Garrett and H. Ban, „Compressive pressure dependent anisotropic effective thermal conductivity of granular beds“, *Granular Matter*, vol. 13, no. 5, pp. 685–696, Jun. 2011.
- [22] F. A. Nutz, P. Ruckdeschel, and M. Retsch, „Polystyrene colloidal crystals: Interface controlled thermal conductivity in an open-porous mesoparticle superstructure“, *Journal of Colloid and Interface Science*, vol. 457, pp. 96–101, Nov. 2015.
- [23] P. N. Pusey and W. van Megen, „Phase behaviour of concentrated suspensions of nearly hard colloidal spheres“, *Nature*, vol. 320, no. 6060, pp. 340–342, Mar. 1986.
- [24] E. Zaccarelli, C. Valeriani, E. Sanz, *et al.*, „Crystallization of hard-sphere glasses“, *Physical Review Letters*, vol. 103, no. 13, Sep. 2009.
- [25] A.-P. Hynninen and M. Dijkstra, „Phase diagrams of hard-core repulsive yukawa particles“, *Physical Review E*, vol. 68, no. 2, Aug. 2003.
- [26] P. N. Pusey, E. Zaccarelli, C. Valeriani, *et al.*, „Hard spheres: Crystallization and glass formation“, *Philosophical Transactions of the Royal Society A: Mathematical, Physical and Engineering Sciences*, vol. 367, no. 1909, pp. 4993–5011, Dec. 2009.
- [27] S. Auer and D. Frenkel, „Suppression of crystal nucleation in polydisperse colloids due to increase of the surface free energy“, *Nature*, vol. 413, no. 6857, pp. 711–713, Oct. 2001.

- [28] H. J. Schöpe, G. Bryant, and W. van Meegen, „Effect of polydispersity on the crystallization kinetics of suspensions of colloidal hard spheres when approaching the glass transition“, *The Journal of Chemical Physics*, vol. 127, no. 8, p. 084 505, Aug. 2007.
- [29] F. A. Nutz, A. Philipp, B. A. F. Kopera, M. Dulle, and M. Retsch, „Low thermal conductivity through dense particle packings with optimum disorder“, *Advanced Materials*, vol. 30, no. 14, p. 1 704 910, Feb. 2018.
- [30] P. Ruckdeschel, A. Philipp, B. A. F. Kopera, *et al.*, „Thermal transport in binary colloidal glasses: Composition dependence and percolation assessment“, *Physical Review E*, vol. 97, no. 2, Feb. 2018.
- [31] H.-J. Butt, K. Graf, and M. Kappl, *Physics and Chemistry of Interfaces*. Wiley, Sep. 2003.
- [32] *Standard test method for determining specific heat capacity by differential scanning calorimetry*, ASTM, West Conshohocken, ASTM International, 2011.
- [33] G. L. Hunter and E. R. Weeks, „The physics of the colloidal glass transition“, *Reports on Progress in Physics*, vol. 75, no. 6, p. 066 501, May 2012.

8.7 Supporting Information

8.7.1 Synthesis and Characterization of SiO₂ (Hollow) Nanoparticles

Materials

Ammonium hydroxide solution (NH₄OH, Sigma-Aldrich GmbH, 30-33 %), 2,2'-azobis-(isobutyramidine) dihydrochloride (AIBA, Sigma-Aldrich GmbH, 97 %), ethanol abs. (Sigma-Aldrich GmbH, ≥99.8 %), 2-methacryloxyethyltrimethylammonium chloride (MTC, Sigma-Aldrich GmbH, 75 % soln. in water), polyvinylpyrrolidone (PVP, Sigma-Aldrich GmbH), styrene (Sigma-Aldrich GmbH, > 9 %), tetraethyl orthosilicate (TEOS, Sigma-Aldrich GmbH, 98 %) were used as received. Millipore water was taken from a Millipore Direct Q3UV unit (Merck Millipore). 2,2'-Azobis(2-methylpropionitril) (AIBN, Sigma-Aldrich GmbH) was recrystallized from ethanol before use.

The SiO₂ particles (SiO₂-F-SC122 and SiO₂-F-SC86-2, microParticles GmbH, 5 wt%) were used as received.

Additional Methods

Transmission electron microscopy (TEM) measurements were performed with a JEOL JEM-2200FS field emission energy filtering transmission electron microscope (FE-EFTEM) operated at an acceleration voltage of 200 kV. Zero-loss filtered micrographs ($\Delta E \sim 0$ eV) were recorded with a bottom mounted CMOS camera system (OneView, Gatan) and processed with DM 3.3 image processing software (Gatan).

Polystyrene Template Particles

530 nm particles (Fig. 8.4) were synthesized via emulsifier free emulsion polymerization.^[1] For the synthesis, 1.8 g PVP (360 kg/mol), 235 ml Millipore water, and 26 ml styrene were added to a 500 ml three-neck flask equipped with a gas inlet and reflux condenser. The emulsion was stirred at a stirring speed of 850 rpm using a large egg-shaped magnetic stirrer bar and heated to 70 °C under a slight argon flow. 0.8 g AIBA was dissolved in 5 ml Millipore water, was added to initiate the

polymerization after 60 min. After the nucleation the stirring speed was reduced to 450 rpm and the reaction was allowed to continue over night. The polymerization was stopped by exposing the dispersion to ambient air and filtrated using a 125 μm nylon filter sieve. No further purification was required.

The 928 nm particles (Fig. 8.4) were synthesized via dispersion polymerization.^{[2],[3]} 6 g PVP (40 kg/mol), 112 ml of ethanol, 20 ml Millipore water, 10 ml styrene and 0.6 g AIBN were added to a 1 l three-necked flask, equipped with a reflux condenser and a gas inlet. The whole reaction was carried out under a slight argon flow. The solution was stirred with an egg-shaped stirring bar with a speed of 150 rpm. After 30 min, the mixture was heated to the reaction temperature of 70 °C. 112 ml ethanol, 10 ml styrene, and 450 μl MTC were premixed in an Erlenmeyer flask and added to the reaction after 90 min. The reaction was carried out overnight and stopped by exposing the dispersion to ambient air. The dispersion was filtrated using a 125 μm nylon filter sieve. No further purification was required.

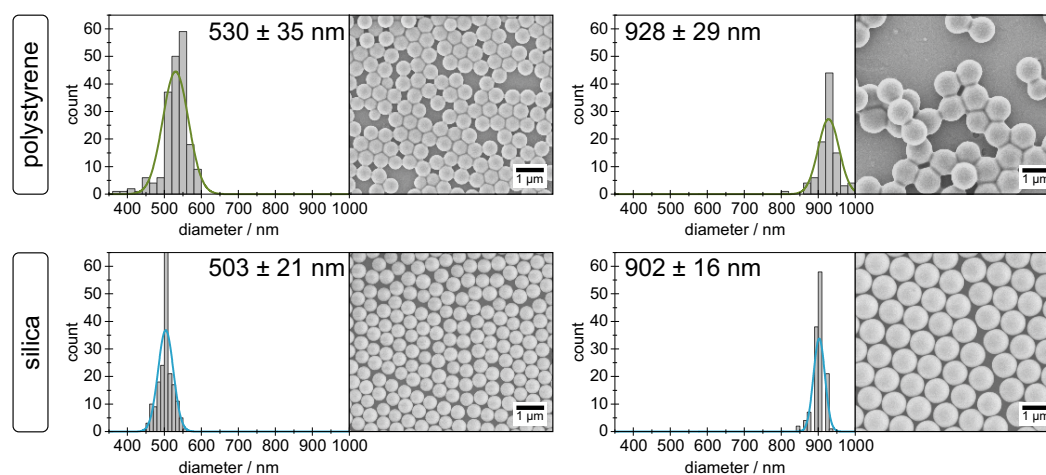


Fig. 8.4: Histograms and SEM images of polystyrene particles that were used as template for the SiO_2 hollow particles, and of the silica particles, that were used as reference material.

PS@ SiO_2 Core-Shell Particles

A modified Stöber process was used for the synthesis of the silica shell to get PS@ SiO_2 core-shell particles.^[4] For the synthesis, 100 ml dispersion of the 530 nm (928 nm) particles were diluted with 700 ml ethanol and 1/10 of 20 ml (5.5 ml) TEOS and stirred at 400 rpm at room temperature. After 20 min equilibration time, 52 ml NH_4OH solution was added. The remaining TEOS was added in nine more steps in time intervals bigger than 15 min and the reaction was stirred at room temperature over night. The particles were centrifuged and washed twice with ethanol and three times with Millipore water for purification.

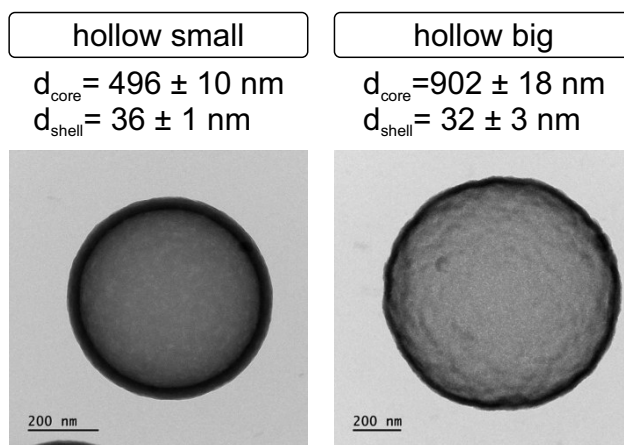


Fig. 8.5: TEM images of small and big silica hollow particles after calcination at 500 °C.

8.7.2 References

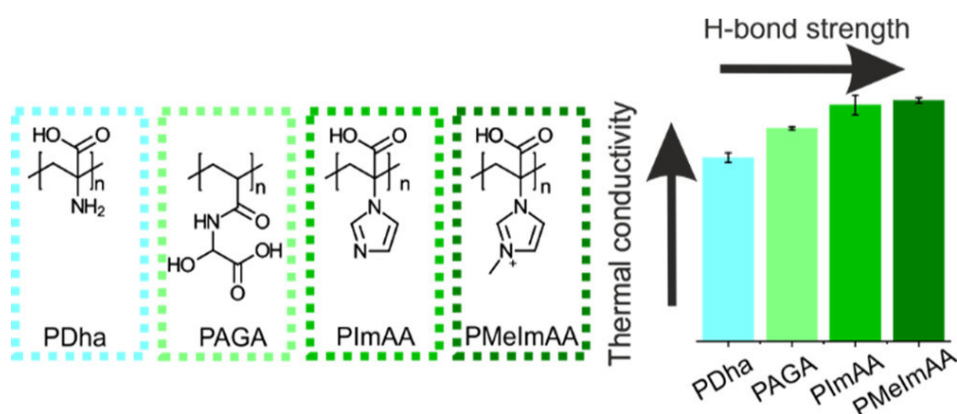
- [1] J. W. Goodwin, J. Hearn, C. C. Ho, and R. H. Ottewill, „Studies on the preparation and characterisation of monodisperse polystyrene latices“, *Colloid and Polymer Science*, vol. 252, no. 6, pp. 464–471, Jun. 1974.
- [2] X. Cheng, M. Chen, L. Wu, and G. Gu, „Novel and facile method for the preparation of monodispersed titania hollow spheres“, *Langmuir*, vol. 22, no. 8, pp. 3858–3863, Mar. 2006.
- [3] A. M. Lechner, T. Feller, Q. Song, *et al.*, „Scalable synthesis of smooth PS@TiO₂ core-shell and TiO₂ hollow spheres in the (sub) micron size range: Understanding synthesis and calcination parameters“, *Colloid and Polymer Science*, vol. 298, no. 7, pp. 867–878, Mar. 2020.
- [4] W. Stöber, A. Fink, and E. Bohn, „Controlled growth of monodisperse silica spheres in the micron size range“, *Journal of Colloid and Interface Science*, vol. 26, no. 1, pp. 62–69, Jan. 1968.

Thermal Transport in Ampholytic Polymers: The Role of Hydrogen Bonding and Water Uptake

Patrick Hummel¹, Anna M. Lechner¹, Kai Herrmann¹, Philip Biehl², Carsten Rössel², Lisa Wiedenhöft², Felix H. Schacher², and Markus Retsch¹

¹ Department of Chemistry, Physical Chemistry I and Bavarian Polymer Institute, University of Bayreuth, 95447 Bayreuth, Germany

² Institute of Organic Chemistry and Macromolecular Chemistry and Jena Center for Soft Matter (JCSM), Friedrich Schiller University Jena, D-07743 Jena, Germany



Published in *Macromolecules*, **2020**, DOI: 10.1021/acs.macromol.0c00596
 Reprinted with permission from Hummel *et al.*, *Macromolecules* 2020, 53,
 5528-5537. Copyright 2020 American Chemical Society.

9.1 Abstract

The low thermal conductivity of amorphous polymers typically prevents their usage in thermal management applications. Therefore, increasing their intrinsic thermal conductivity poses an exciting scientific challenge. One approach is to promote attractive interchain interactions. Here, we investigate the thermal conductivity of several ampholytic polymers. This unique class of polymers offers H bond donor and acceptor groups in each repeat unit and constitutes a one-component system. We use IR spectroscopy to characterize the bonding strength and motifs based on the carbonyl peak. For the dry ampholytic polymers, we find a correlation between H bond strength and thermal conductivity. We also characterized the influence of hydration under various relative humidity conditions, which mostly led to an increase in thermal conductivity. This increase can be rationalized by the formation of a water-polymer nanocomposite material and can be described by volume-weighted mixing models.

9.2 Introduction

Easy processability, lightweight, low cost, and electrical insulation make polymers promising candidates for various applications in electronic devices. The continuously increasing energy density in such electronic devices demands a wholistic concept for thermal management at the same time.^[1] The usually low thermal conductivity of polymers represents a significant obstacle in this context. For that reason, the ambitious goal of polymer chemists is to create thermally highly conducting polymers. Similar to the discovery of (semi)conducting polymers, this would open up an entirely new space for the application of amorphous polymers. Two general strategies have been pursued to reach this goal: the creation of polymer (nano)composites and polymer processing. In the case of processing, a variety of methods such as mechanical stretching,^{[1],[2]} electrospinning,^[3] and nanotemplating^[4] have been investigated. In these cases, an increase in thermal conductivity is mostly attributed to a high chain orientation.^{[5],[6]} The polymer chain orientation is often accompanied by some degree of crystallization. The chain alignment can be further enhanced by the proper design of the polymer backbone to promote stiffer polymer chains.^[7] Consequently, impressively high thermal conductivities, of around 20 W/mK, were measured along the axis of crystalline polymer fibers with a high modulus.^[2] However, the radial thermal conductivity stays low.^[8] Even a commercial product is already available, making use of stretched polymers with a high degree of crystallinity. The organic heat spreader Temprion OHS (DuPont) with a crystallinity of 99.9% demonstrates a remarkable in-plane thermal conductivity of 45 W/mK and a typical polymer-like cross-plane thermal conductivity of 0.2 W/mK. Amorphous polymers, in general,

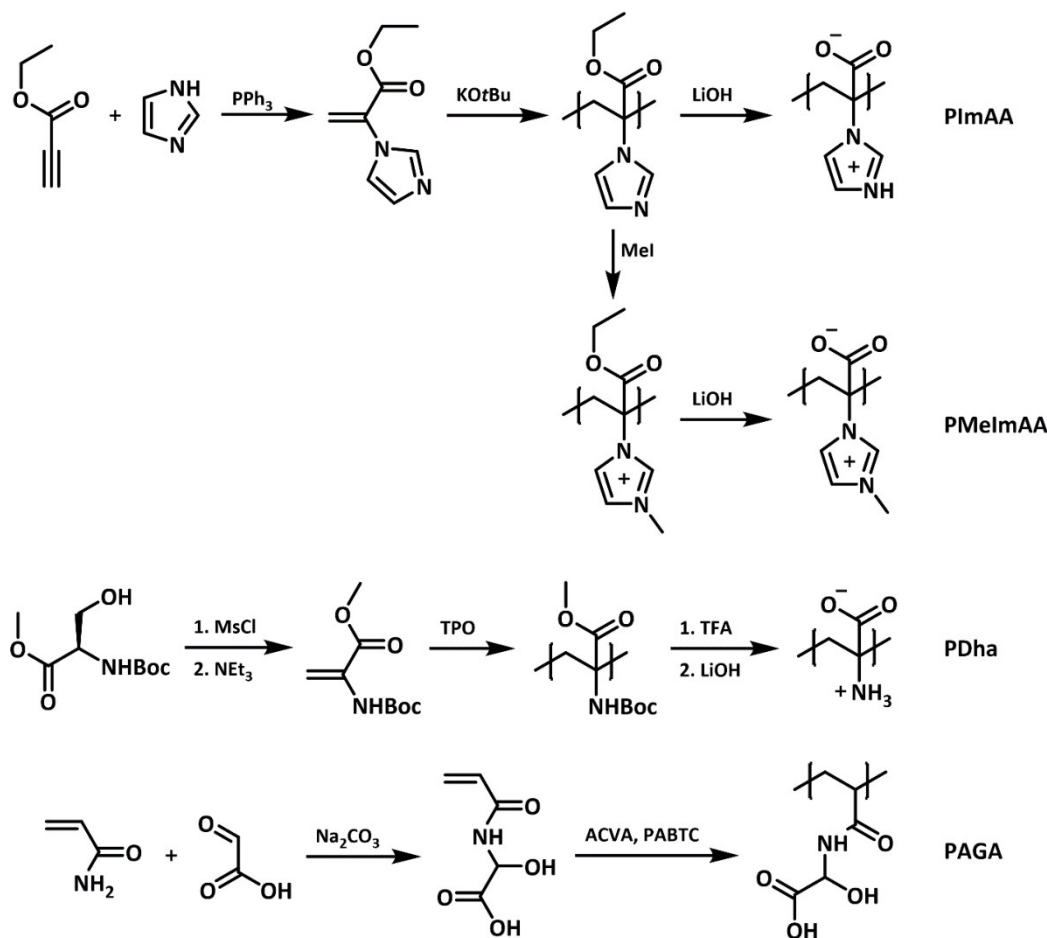
have a lower thermal conductivity than crystalline ones. However, their heat-spreading capabilities would be less affected by the orientation in space owing to the random polymer coiling. Furthermore, the processing of amorphous polymers is less sophisticated because of the lack of a nucleation and growth phase compared to (semi)crystalline samples. Ways to beat the intrinsically low thermal conductivity of amorphous polymers are mixing with highly conducting components or the introduction of functional groups.

In that regard, the field of (nano)composite materials has been actively investigated over the past years. The effective material properties strongly depend on a multitude of parameters such as the filler shape and composition, the interfacial interaction between the filler and matrix, and the filler concentration.^{[9],[10]} Depending on the filler shape, anisotropic thermal transport properties may evolve at the same time.^{[11],[12]}

The introduction of functional groups to the polymer backbone or its side groups is an alternative approach to increase the thermal conductivity. The main driving force for an increased thermal conductivity is stretching of the polymer to a more elongated conformation and an improved interchain transfer of heat. Amorphous polymers with hydrogen bond-forming functional groups are consequently well-suited to realize improved thermal conductivities.^[13] The strong hydrogen bonding between adjacent polymer chains could improve the transfer of thermal energy. In addition to this, the thermal conductivity can be further increased by the use of polyelectrolytes.^{[14],[15]} Polyelectrolytes react sensitively to external stimuli such as ionic strength or pH, which influence the polymer conformation and polymer packing.

The engineering of these interchain interactions can lead to high thermal conductivities of up to 1.5 W/mK, as shown in amorphous polymer blends.^[16] However, demixing is a significant issue in polymer blends, and controversial findings on the role of H bonds were published.^[13] Miscibility is always an enormous challenge in polymer blends, and the resulting microstructure can be hard to characterize.

In this work, we present a new approach to prevent the issue of miscibility. Ampholytic polymers exhibit donor and acceptor groups for the formation of H bonds covalently attached to one polymer chain, which inevitably prevents demixing. We present four different ampholytic polymers (Scheme 9.1) with a detailed characterization of their microstructure (measured by IR spectroscopy) and their thermal transport properties (measured by the photoacoustic method).



Scheme 9.1: Synthesis of PImAA, PMeImAA, PDha, and PAGA

9.3 Materials and methods

9.3.1 Polymer Synthesis

Synthesis of poly(2-(imidazole-1-yl)acrylic acid) (PImAA), (Scheme 9.1): The synthesis of ethyl 2-(imidazole-1-yl)acrylate (EImA) and anionic polymerization in tetrahydrofuran (THF) with potassium tert-butoxide (KOtBu) as an initiator, as well as the polymer modifications, were performed as described in the literature.^[17] The polymers were characterized by proton nuclear magnetic resonance (¹H NMR) (300 MHz, D₂O) and size exclusion chromatography (SEC, 0.1 M NaCl/0.3 % TFA in water, P2VP calibration).

Synthesis of polydehydroalanine (PDha), (Scheme 9.1): PDha was synthesized as reported by Günther *et al.* or von der Lühe *et al.*^{[18],[19]} Briefly, a solution of 2.9 mg (0.0084 mmol) of Lucirin TPO in 300 μ L of 1,4-dioxane was added to 300 mg (1.49 mmol) of tert-butoxycarbonylaminoethyl acrylate (tBAMA; M/I = 200:1). The mixture was placed in an ultraviolet (UV) cube (100 W) for 5 min. Afterward, the polymer was precipitated in 4 mL of n-hexane and subsequently deprotected. Therefore, 500 mg of the obtained PtBAMA was dissolved in 7.5 mL of trifluoroacetic acid and stirred at 50 °C for 1 h. The mixture was precipitated in methanol. The so-obtained PAMA was dissolved in 10 mL of 1,4-dioxane, and a saturated solution of LiOH (10 mL) was added. The mixture was stirred at 100 °C for 3 h and neutralized with diluted HCl_{aq}. During neutralization, PDha precipitated. PDha was characterized by ¹H NMR (300 MHz, D₂O/NaOD, pH 8).

Synthesis of poly(2-acrylamido glycolic acid) (PAGA), (Scheme 9.1): 2-acryloylamido glycolic acid was synthesized as described in the literature.^[20] Reversible addition-fragmentation chain transfer (RAFT) polymerization was performed according to a previously published protocol^[21] with [M]/[CTA]/[I] = 145:1:0.3. PAGA was characterized by ¹H NMR (D₂O, 300 MHz) and SEC (0.1 M NaNO₃/0.05 % NaN₃, PEO calibration).

Synthesis of poly(methyl methacrylate) (PMMA): The RAFT synthesis of PMMA was adapted from Mayadunne *et al.*^[22] Therefore, 38.25 g (0.382 mol) of MMA, 750.6 mg (2.17 mmol) of 2-cyano-2-propyl dodecyl trithiocarbonate (CPDTTC), 3.7 mg (0.0225 mmol) of azobisisobutyronitrile (AIBN), and 11.9 g (0.129 mol) of toluene were placed in a flask. The mixture was heated to 80 °C for 33.5 h. The polymer was precipitated in methanol.

Poly(acrylic acid) (PAA) was purchased from Sigma-Aldrich as a sodium salt solution. The pH of the solution was adjusted to 1. The sodium ions were removed by dialysis of the solution against Milli-Q water until pH was constant.

9.3.2 Sample Preparation

Spin-Coating

The polymers were dissolved in the respective solvent to achieve concentrations between 15 and 25 wt%. PMMA was dissolved in toluene and PDha was dissolved in DMSO, while all other polymers were processed from water. The solutions were then spin-casted on glass substrates with dimensions of 25 × 25 mm at 3000 rpm

for 150 s. These samples were used for thermal conductivity measurements and IR investigations. The dry samples were kept in a vacuum oven at 100 °C for 24 h.

Humidity Annealing

Saturated salt solutions in a desiccator achieved different relative humidities. We used MgCl_2 , NaCl , and K_2SO_4 for relative humidities of 45, 77, and 92 %, respectively.^[23] The spin-cast samples were equilibrated in a humid atmosphere for 24 h before further investigations. The transducer layer surface is shown in Figure 9.15 and demonstrates holes or cracks. Therefore, equilibration with the environment is not prevented by the evaporated transducer layer on top of the polymer. Photoacoustic (PA), atomic force microscopy (AFM), and IR measurements were conducted immediately after receiving the samples from the humidity-adjusted desiccator.

Thermal Conductivity Measurements

The PA method was used to determine the thermal conductivity of the spin-coated polymer films.^{[24],[25]} A gold transducer layer was applied to the top of the sample before the measurement. The sample is fixed to the measurement cell. The cell is gas-tight and filled with 20 psi helium. A modulated laser heats the transducer layer periodically. The induced temperature change on the surface of the sample leads to an acoustic wave propagating into the gas. The acoustic signal is detected using a microphone and coupled to a lock-in amplifier. The frequency-dependent phase shift between the modulated laser beam and the acoustic wave is measured. The experimental data are fitted using a multilayer model, describing the temperature distribution in the sample. The primary fitting result is the total layer resistance. Dividing the total layer resistance by the film thickness, the effective thermal conductivity is obtained. Each sample was measured three times. The mean values of these measurements are presented with the standard deviations as error bars. The humidity-dependent data were measured without additional external control of the surrounding humidity. We did not observe a drift in the photoacoustic signal during the measurement time and conclude that the humidity water uptake remains constant for this duration (Figure 9.6c). More details can be found in the Supporting Information Section 9.7.1.

Fourier Transform Infrared Spectroscopy

The Fourier transform infrared (FTIR) measurements were conducted on a Bruker (Billerica, MA, USA) VERTEX 70 IR spectrometer with an attenuated total reflection (ATR) measurement unit. The measurements were performed from 380 to 4000 cm^{-1} with a resolution of 4 cm^{-1} and 128 scans. The samples were taken from the desiccators or vacuum oven, respectively, and directly measured under ambient conditions. Normalized spectra were used to calculate the difference spectra relative to the dry polymer samples.^[26] Therefore, the normalized spectrum of the dry sample was subtracted from the spectra at the different relative humidities. The CH_2 deformation vibration at 1450 cm^{-1} was used as a reference peak for normalization, which is unaffected by water adsorption.

Fourier Self-Deconvolution

Fourier self-deconvolution (FSD) is a mathematical method to increase spectral resolution. By this, it is possible to separate overlapping absorption bands in an IR spectrum.^[27] We applied the FSD according to Hu *et al.*^[28] The software OPUS 7.5 (Bruker, Billerica, MA, USA) was used for all steps. First, the carbonyl region (between 1800 and 1540 cm^{-1}) was cut-off. A baseline correction with one iteration was performed, and the spectrum was smoothed by 5-9 points. In the next step, the FSD was performed with a Lorentzian shape with a half-bandwidth of 25 and a noise reduction of 0.30. Another baseline correction was conducted before the peaks were selected according to the minima of the second derivative of the initial spectrum. Finally, the peaks were fitted with a Gaussian profile with the Levenberg-Marquardt method.

Differential Scanning Calorimetry

Differential scanning calorimetry (DSC) measurements were performed on a TA instruments Discovery DSC 2500. Two heating cycles were conducted; only the second cycle was used for evaluation. The temperature profile ranged from -40 to 140 °C using a heating rate of 10 K/min with a nitrogen flow of 50 mL/min. The measurements are shown in Figure 9.13.

Modulated DSC (MDSC) measurements were performed to determine the cp of the samples. The optimum MDSC parameters have been calculated and evaluated following the instructions described in the literature.^[29] The modulations in the

transition range and the modulation period were controlled and adjusted to a heating rate of 2 K/min, a period of 80 s, and an amplitude of 1.6 K. The final samples were measured in hermetic pans to avoid loss of water during the measurement. The experiments were performed in a temperature range from 5 to 60 °C. C_P at 25 °C of each polymer is given in Table 9.1.

Tab. 9.1: Summary of the Measured Polymer Properties^a

name	M_n [g/mol]	PDI	density [g/cm ³]	c_p [J/gK]
PImAA	5500 ^b	1.31 ^b	1.48	1.045
PMeImAA	3300 ^b	1.45 ^b	1.37	0.896
PDha	13,000 ^c	2.5 ^c	1.24	1.009
PAGA	28,500 ^d	1.32 ^d	1.22	1.245
PAA	15,000		1.26	1.202
PMMA	17,400 ^e	1.15	1.15	1.217

^aThe density and c_p values were used for the determination of thermal conductivity. ^bDetermined by SEC using aqueous 0.3 % TFA/0.1 M NaCl as an eluent and calibrated against P2VP standards. ^cDetermined for the protected precursor of PDha by SEC using 0.1 % LiCl in DMAc as an eluent and calibrated against PMMA standards. ^dDetermined by SEC using 0.1 M NaNO₃/0.05 % NaN₃ as an eluent and calibrated against PEO standards. ^eDetermined by SEC using THF as an eluent and calibrated against PMMA standards.

Helium Pycnometer

An Ultrapyc 1200e (Quantachrome Instruments, Boynton Beach, FL, USA) was used for the determination of the density of the dry samples. Before each run, the volume of the measurement cell was calibrated. Subsequently, a defined mass of the polymer was put into the cell. The volume of the polymer was determined by 100 runs. The division of mass and volume calculated the density. The obtained values are summarized in Table 9.1.

9.4 Results and Discussion

We investigate the effective thermal conductivity of four different ampholytic polymers, PDha, PAGA, PImAA, and its methylated derivative poly(2-(3-methylimidazolium-1-yl)acrylic acid) (PMeImAA, Figure 1a). All polymers have at least two different functional groups per repetition unit. We also analyzed PAA with only one func-

tional group, which was reported to play a crucial role in the formation of a highly conducting pathway.^[16] PMMA is not able to form hydrogen bonds and was also measured as a reference system.

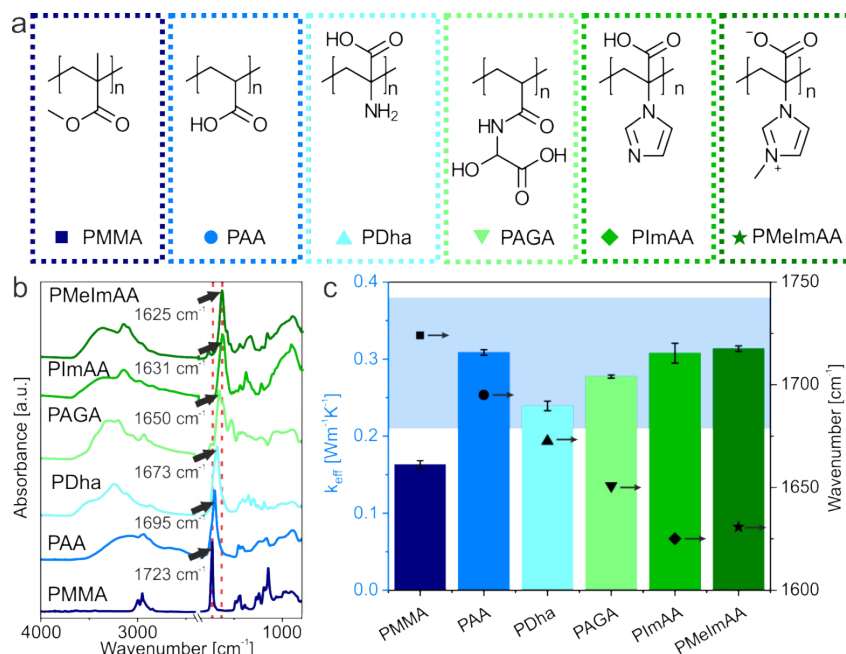


Fig. 9.1: (a) Structure of the ampholytic polymers and the reference polymers PAA and PMMA. The ampholytic polymers have at least two functional groups per repetition unit. (b) IR spectra of all investigated polymer samples in the dry state. The red dashed lines present the carbonyl peak position of PMMA and PMelAA, respectively. (c) Measured effective thermal conductivity of all samples (solid bars). The thermal conductivity correlates with the peak position (black symbols) of the carbonyl band measured by IR spectroscopy (except for PAA). The light blue area indicates the range of literature values for amorphous, water-soluble polymers.^[13]

We start our analysis by the polymer characterization under dry conditions, that is, after storing the samples in a vacuum oven. In the IR spectra shown in Figure 9.1b, it can be seen that, except PMMA, all polymers form intra- and intermolecular hydrogen bond interactions as indicated by the broad bands between 2500 and 3600 cm^{-1} . These bands originate from the O-H and N-H stretching vibrations. OH-wagging at 900 cm^{-1} is another indicator for the presence of COOH under these vacuum-dried conditions. This band is broad due to various spatial orientations of the H bond-forming functional groups. Because of this variety of possible bonds, the underlying C-H stretching vibrations, and several overtones, this region of an IR spectrum is challenging to evaluate.

We, consequently, focus our analysis on another strong peak connected to hydrogen bonds: the carbonyl stretching vibration around 1700 cm^{-1} . This peak is very strong, possesses a small full width at half-maximum, and is sensitive to the local environment.^{[28],[30],[31]} Therefore, it provides a suitable target for further investigations of

H bonds. Furthermore, it was shown that the absorption coefficient of the carbonyl stretching vibration, in comparison with the O-H and N-H stretching, does not depend significantly on the strength of the H bonds.^{[32],[33]} One disadvantage is that H bonds between functional groups without a carbonyl group contribution cannot be resolved. A first indication of the strength of a hydrogen bond is the position of the carbonyl peak, whereby lower frequencies indicate an increasing strength of the H bond.^[34] We see a systematic shift of the carbonyl peak from PAA to PMeImAA, indicating an overall increase in strength of the carboxylic H bonds.

The effective thermal conductivities (Figure 9.1c) show typical values for water-soluble amorphous polymers compared to values reported in the literature (shaded area).^[13] Comparing our values for PMMA (0.16 W/mK) and PAA (0.31 W/mK) with the literature (0.20 W/mK^[13] and 0.34 W/mK^[15]/0.37 W/mK^[13]), we find slightly lower values. The lower values are reasonable because the PA method determines the total layer resistance of the sample. The effective thermal conductivity is calculated based on the polymer film thickness. Also, it takes the thermal resistances between the polymer layer and the support structure and transducer layer, respectively, into account. We attribute the relatively large standard deviation of the PImAA sample to the lowest layer thickness (<1 μm) of the PImAA sample, which reduces the fitting accuracy.

Considering the systematic increase in H bond strength derived from the carbonyl peak position, we find the expected increase in thermal conductivity for the ampholytic samples under investigation. Rather unexpected from this point of view is the exceptionally high thermal conductivity of PAA.

For further insight into the strength of the H bonds, we provide a detailed analysis of the IR spectra. We base our analysis on FSD of the carbonyl resonance between 1600 and 1750 cm^{-1} , according to Hu *et al.*^[28] The fitted spectra are shown in Figure 9.2. The peaks are assigned to different configurations of the carbonyl group. Dark yellow is anhydrides (1805-1760 cm^{-1}), green is free carbonyl groups (1740-1730 cm^{-1}), cyan is the terminal oligomeric form of carboxylic acid (1716-1680 cm^{-1}), blue is the cyclic dimer (1700-1665 cm^{-1}), and gray-blue is the inner oligomeric form (1675-1650 cm^{-1}). These peaks can be found in all samples containing a carboxylic acid group. The assignment is based on Dong *et al.*,^[30] who investigated different H bond motifs in PAA samples. The introduction of amino groups in our ampholytic polymers introduces additional peaks marked in purple, ascribed to H bonds with primary or secondary amino groups (PDha and PAGA). A final category of H bonds is assigned to the interaction of the carbonyl group with the imidazole ring in PImAA and PMeImAA depicted in dark blue. Further contributions arising from vibrations other than the carbonyl stretching, such as NH bending vibration/Amide II and

vibrations of the aromatic ring, are summarized in orange. As a consequence, the orange bands were excluded for the evaluation of the carbonyl ratio.

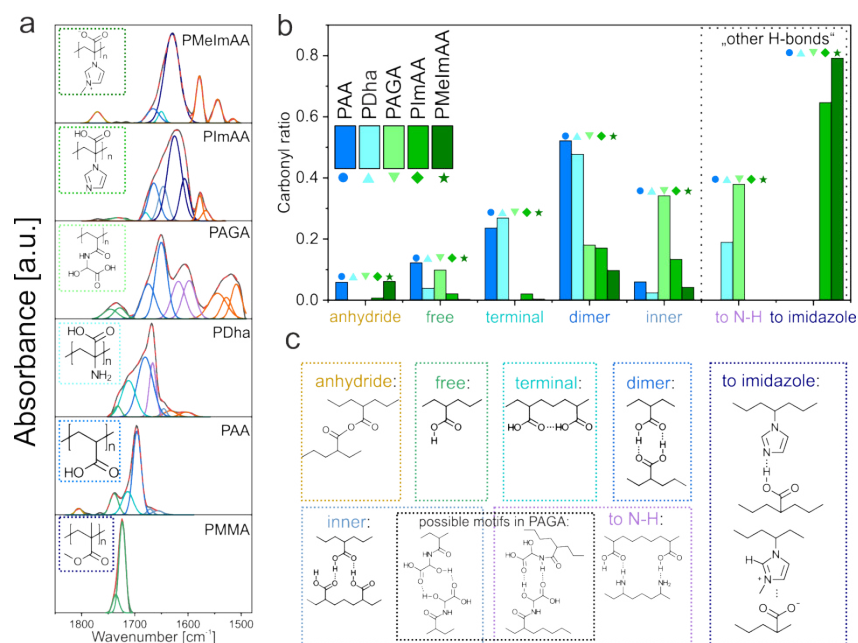


Fig. 9.2: (a) Deconvoluted IR spectra of all investigated samples. The films were dried before the measurements. (b) Relative ratio of different motifs of the carbonyl bond. (c) Schematic illustration of different H bond motifs.

The relative contribution of all these different classes of hydrogen bonds is summarized in Figure 9.2b. Most notably, PAA comprises a range of strongly coordinated H bonds (dimer, inner, terminal) and even covalently condensed moieties (anhydride). The interplay of these structural motifs facilitates thermal transport between the polymer chains. Please note that the strength of the H bond is the lowest in the case of PAA compared to all other ampholytic polymers (Figure 9.1b, 1723 cm^{-1} peak position of the carbonyl band). Thus, the bonding scheme in PAA may additionally facilitate an elongated conformation, which also improves thermal transport. As soon as an additional functional group is introduced (NH_2 in the case of PDha), the thermal conductivity drops considerably. However, the nature of the H bond environment is still comparable to PAA. Merely, the anhydride and free-carboxyl bonds are replaced by O-H-N moieties (“other bonds” in Figure 9.2b). The overall stiffer carbonyl peak (1695 cm^{-1}) should even favor a higher thermal conductivity. Thus, it is difficult to unambiguously relate the thermal conductivity reduction to subtle differences in the way hydrogen bonds are formed in the respective polymers. Additional contributions, such as the side chain structure^[14] or the influence of the side groups on the polymer morphology,^[7] are important at the same time. Thus, the alleged beneficial influence of additional hydrogen bonds to the primary amino group is counteracted by conformational changes that cannot be resolved by IR characterization. The transition from PDha to PAGA, PImAA, and PMeImAA demonstrates a monotonic increase in the class of other hydrogen bonds. Along this

direction, the strength of the carbonyl bond also increases. The combination of both effects translates into the general trend of increasing thermal conductivity.

PAA and all herein used ampholytic polymers are strongly sensitive to humidity. We, consequently, determined its influence on the effective thermal conductivity. We gravimetrically measured the moisture content after prolonged exposure to specific humidities (Figure 9.3a). PMMA, as a control, demonstrates no sensitivity to increasing humidity. PAA exhibits a considerable absorption of water on the order of 40 %, whereas in the case of the herein used, ampholytic polymer values from 35 to 60 % are found. The quaternized P_{MeIm}AA exhibits the most significant water uptake and doubles its weight. These mass changes are comparable to literature data on PAA^[35] and other polyelectrolytes,^[36] respectively. The uptake of water influences not only the H bonding within the polymers but also the specific heat capacity and density. Both quantities are highly relevant when determining the thermal conductivity under these conditions. The measurement of the effective polymer density under various humidity conditions is not possible in a direct manner. We, therefore, used the measured moisture content to calculate the humidity-dependent density. The specific heat capacity was determined experimentally by MDSC measurements, using hermetic pans (Figure 9.3b). The shaded areas indicate the expected c_p based on a mass-weighted mixing model considering the measured moisture contents. Although the overall trend of an increasing c_p is well-captured in all cases, some degree of variability in a range of $\sim 20\%$ is seen. This variation can be explained by the difficulty of accurately retaining the moisture uptake and polymer conformation during the measurement itself.

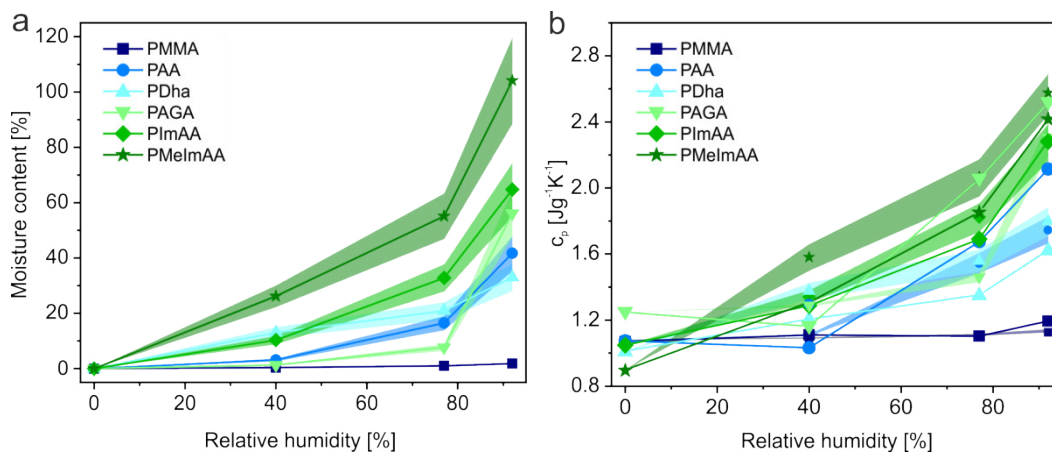


Fig. 9.3: Humidity dependence of the samples. (a) Moisture content increases with humidity for all polymers with functional groups. Shaded areas mark the variability. (b) c_p , measured by MDSC, increases with humidity (solid lines and symbols). Shaded areas rationalize the expected trend of the c_p based on the water uptake in (a) calculated using a mass-weighted mixing model.

The uptake of water also affects the polymer microstructure and H bond environment. Consistently, with our previous analysis, we used FSD of the carbonyl peak of our

FTIR spectra. Figure 9.4 summarizes three distinct cases: PAA, PImAA, and PMeImAA. The spectra show a distinctly different way of water uptake in the case of PAA compared to PImAA and PMeImAA. In the literature, there is a differentiation between unbound and bound water.^{[35],[37]} We define bound water as directly coordinated to the polymer, while unbound water interacts with other water molecules and forms clusters.

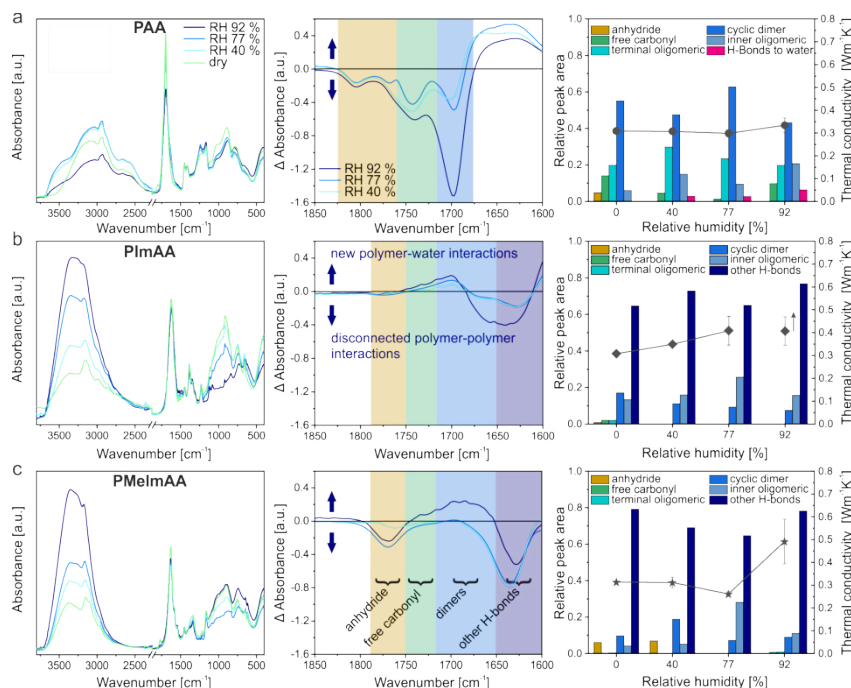


Fig. 9.4: From left to right: IR spectra of samples stored at different relative humidities. Difference spectra in the region of the carbonyl stretching vibration. The relative peak area of different H bond structures dependent on the relative humidity. (a) PAA, (b) PImAA, and (c) PMeImAA.

Our results of the absorbed amount of water in PAA (moisture content of 0.42 g/g polymer) are in good agreement with the literature value (0.47 g/g polymer).^{ccc} Also, the FTIR difference spectrum is in good agreement with the findings of Daniliuc *et al.*^[35] They reported a negative contribution in the difference spectra for free C=O (around 1735 cm^{-1}) and dimer (around 1700 cm^{-1}) and a positive peak between 1672 and 1634 cm^{-1} . The negative contributions are attributed to disconnected polymer-polymer interactions, while the positive contributions are newly formed polymer-water interactions.^[35] They interpreted the spectra such that only bound water exists in their PAA sample.

Despite a higher moisture content, the difference spectra of PImAA and PMeImAA show overall fewer variations. Although the negative contributions between 1675 and 1600 cm^{-1} represent disconnected polymer-polymer interactions, the overall lack of significant positive contributions indicates that the water is adsorbed in

a less bound state in the case of PImAA and PMeImAA. The variation between these two polymers is smaller because polymers with similar functional groups show similar peaks in IR spectroscopy when adsorbing/absorbing water.^[38] The same data evaluation and representation for PDha and PAGA are summarized in Figure 9.13.

When considering the deconvoluted peaks (right panels of Figure 9.4), one has to be cautious while interpreting the respective contributions. The major difficulty is that the thermal conductivity is governed by various parameters, which were already pointed out in the discussion of the dry samples. We can, however, extract reasonable trends. PAA shows that the adsorption of bound water hardly influences the thermal conductivity. Consequently, bound water intercalates tightly between the PAA chains without affecting its conformation nor impeding interchain thermal transport. The IR spectra of PImAA do not show significant changes in the carbonyl peak region. Consequently, the uptake of bound and unbound water itself seems to be the driving force for the monotonic increase in thermal conductivity. PMeImAA hints toward the fact that the creation of inner oligomeric groups on the expense of anhydride, cyclic dimer, and charged heterocycle interactions impedes thermal transport up to the humidity of RH \sim 77%. Finally, considering reports in the literature, the uptake of water was also reported to increase the effective thermal conductivity strongly. Mehra *et al.*^[39] worked with polyvinylalcohol and ascribed the thermal conductivity increase to the formation of thermal bridges by bound water molecules. All these examples demonstrate that the influence of humidity on the thermal transport in hydrophilic polymers is hard to predict and certainly depends on the specific polymer-water combination.

Although the previous discussion focused on a microscopic interpretation of inter- and intramolecular interaction between the constituting polymers, we also want to draw the attention to an alternative consideration comprising a much more coarse-grained point of view. The uptake of unbound water can be understood as a way to generate a two-phase material, where water clusters are formed.^[37] This heterogeneous material can then be analyzed in a similar way to other nanocomposite materials using effective medium models as described by Carson.^[40] For this, we use the vacuum (dry) polymer thermal conductivity as the pure phase of one component and literature data of the thermal conductivity of water as the second component. In combination with our data of the moisture uptake (Figure 3a) and two volume-weighted mixing models (parallel mixing model and effective medium model^[40]), the humidity-dependent thermal conductivity is calculated (Figure 9.5). For PDha, PAGA, and PImAA, both mixing models describe the experimental data adequately well, particularly when considering the accuracy of the mixing models themselves and the thermal conductivity determination. For the case of PAA, where a high amount

of bound water can be expected, both mixing models systematically overestimate the effective thermal conductivity.

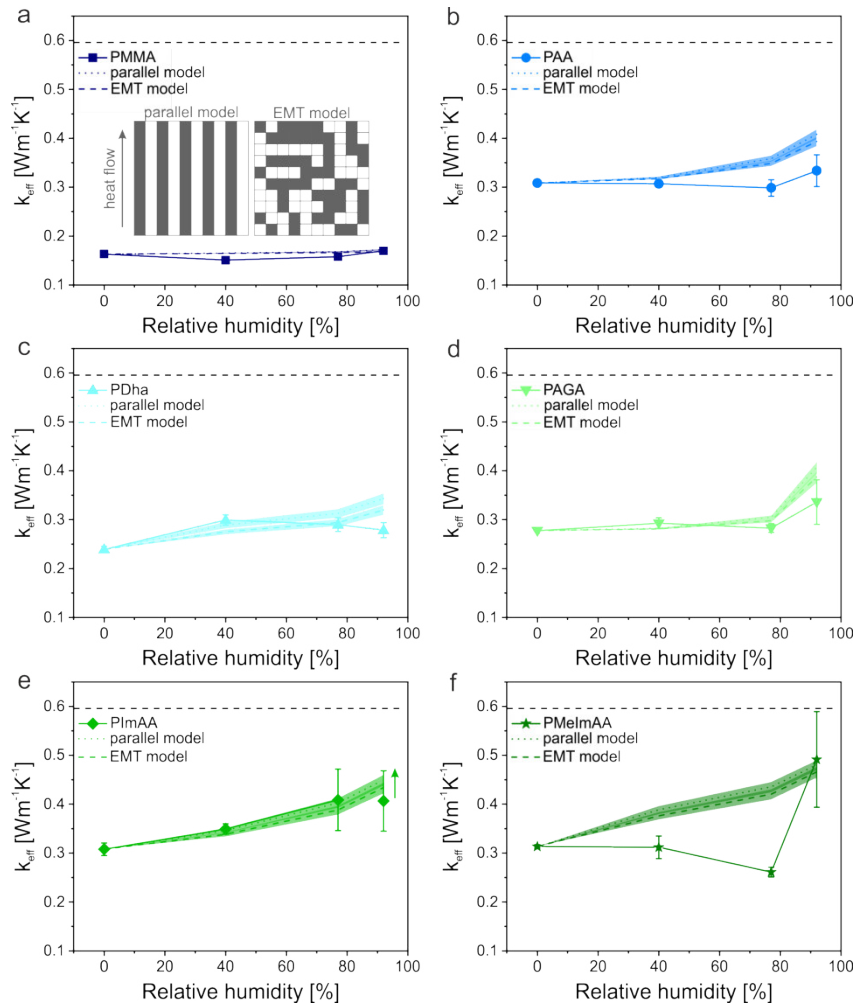


Fig. 9.5: Effective thermal conductivity vs relative humidity for all investigated polymer samples. From (a-f) PMMA, PAA, PDha, PAGA, PImAA, and PMeImAA. The solid symbols depict the experimental data, while the dashed and dotted lines are calculated values using the parallel and the EMT mixing model, respectively. A schematic illustration of these models is shown as an inset in (a). The shaded areas consider the variability because of the deviation of the moisture content determination. The dashed black line represents the thermal conductivity of water.

The parallel mixing model is based on the presence of extended percolation paths through the entire polymer structure. In contrast, if the water uptake happened in a random and dispersed fashion within the polymer, it should be better represented by the EMT mixing model (also compared to the schematic depiction in the inset of Figure 9.5a).^[40] The small difference between the pure polymer and the pure water thermal conductivity prevents an unambiguous judgment on the presence of dispersed or percolated water inside the polymer. Both mixing models, however, support the straight-forward interpretation in the sense of a water-polymer nanocomposite material. Only the ionic PMeImAA sample deviates strongly from the mixing models, which could be understood in a way that the uptake of water first disrupts

thermal transport pathways. Once water condensation sets in at very high humidity (RH \sim 92%), the thermal conductivity is again dominated by the water phase.

9.5 Conclusions

We employed a set of polyampholytes featuring a high density of functional groups to investigate how thermal transport can be controlled by hydrogen bonding in amorphous polymers. We, therefore, compared four types of ampholytic polymers to PAA and PMMA as reference materials. The investigation of ampholytic polymers is particularly interesting because this opens an elegant pathway to study the influence of H-donor and H-acceptor groups in a one-phase system. We employed a detailed IR spectroscopy investigation for a holistic understanding of the involved H bond motifs.

In summary, we can deduce three major trends. First, PAA is an exceptionally well-conducting hydrophilic polymer, which we attribute to a stretched polymer conformation. Second, for all ampholytic polymers, we find an overall trend of increasing thermal conductivity along with an increase in the H bond strength under dry conditions. This can be deduced from a systematic red shift of the carbonyl peak. Third, the presence of humidity leads to a polymer-specific uptake of water and, consequently, to a variety of changes to the H bond motifs. However, the thermal transport in ampholytic polymers can be well-described using mixing models, where the uptake of water is considered as the formation of a nanocomposite material. Deviations from this straight-forward description are PAA, where a high amount of strongly bound water is observed, and PMeImAA, where ionic interactions are dominant. The deconvolution of the carbonyl resonance peak demonstrates a range of binding motifs between the respective polymers. However, an unambiguous assignment of a particular H bond moiety to an increased or decreased thermal transport behavior is not possible. Additional factors such as scattering effects along the polymer backbone or on polymer side groups have to be taken into account, as well as subtle changes to the polymer conformation. Overall, our contribution adds to a better understanding of the role of H bonds for thermal transport in polymer materials.

Most importantly, not only the specific design of H bond motifs determines the capability to conduct thermal energy. Even in the case of one-phase systems, the various influences of polymer conformation, side groups, and interaction have to be balanced. We are still far away from a predictive model to molecularly design amorphous polymers to a specific high or low thermal conductivity. This is an

ongoing challenge to be addressed by polymer chemists and engineers over the next years.

Acknowledgements

This project was funded through a Lichtenberg professorship by the Volkswagen Foundation and by the German Research Foundation by the SFB 840 (project B7). Additional support was provided by ERC StG VISIRday #714968, DFG RE3550/2-1, SCHA1640/12-1, and the collaborative research center SFB 1278 “PolyTarget” (project number 316213987, project C03). P.B. (Landesgraduiertenstipendium) and L. W. (CarlZeiss-Foundation) are grateful for Ph.D. fellowships.

Funding information

Volkswagen Foundation (Lichtenberg professorship); SFB 840 (project B7); DFG RE3550/2-1; VISIRday ERC StG #714968; SCHA1640/12-1; SFB 1278 “PolyTarget” (project number 316213987, project C03); Carl-Zeiss-Foundation (fellowship for L.W.)

9.6 References

- [1] A. L. Moore and L. Shi, „Emerging challenges and materials for thermal management of electronics“, *Materials Today*, vol. 17, no. 4, pp. 163–174, May 2014.
- [2] X. Wang, V. Ho, R. A. Segalman, and D. G. Cahill, „Thermal conductivity of high-modulus polymer fibers“, *Macromolecules*, vol. 46, no. 12, pp. 4937–4943, Jun. 2013.
- [3] Z. Zhong, M. C. Wingert, J. Strzalka, *et al.*, „Structure-induced enhancement of thermal conductivities in electrospun polymer nanofibers“, *Nanoscale*, vol. 6, no. 14, pp. 8283–8291, 2014.
- [4] V. Singh, T. L. Bougher, A. Weathers, *et al.*, „High thermal conductivity of chain-oriented amorphous polythiophene“, *Nature Nanotechnology*, vol. 9, no. 5, pp. 384–390, Mar. 2014.
- [5] A. Henry and G. Chen, „High thermal conductivity of single polyethylene chains using molecular dynamics simulations“, *Physical Review Letters*, vol. 101, no. 23, Dec. 2008.

- [6] J. Liu and R. Yang, „Length-dependent thermal conductivity of single extended polymer chains“, *Physical Review B*, vol. 86, no. 10, Sep. 2012.
- [7] T. Zhang and T. Luo, „Role of chain morphology and stiffness in thermal conductivity of amorphous polymers“, *The Journal of Physical Chemistry B*, vol. 120, no. 4, pp. 803–812, Jan. 2016.
- [8] Y. Lu, J. Liu, X. Xie, and D. G. Cahill, „Thermal conductivity in the radial direction of deformed polymer fibers“, *ACS Macro Letters*, vol. 5, no. 6, pp. 646–650, May 2016.
- [9] C. Huang, X. Qian, and R. Yang, „Thermal conductivity of polymers and polymer nanocomposites“, *Materials Science and Engineering: R: Reports*, vol. 132, pp. 1–22, Oct. 2018.
- [10] H. S. Kim, J.-u. Jang, H. Lee, *et al.*, „Thermal management in polymer composites: A review of physical and structural parameters“, *Advanced Engineering Materials*, vol. 20, no. 10, p. 1 800 204, Aug. 2018.
- [11] N. Song, D. Jiao, S. Cui, *et al.*, „Highly anisotropic thermal conductivity of layer-by-layer assembled nanofibrillated cellulose/graphene nanosheets hybrid films for thermal management“, *ACS Applied Materials & Interfaces*, vol. 9, no. 3, pp. 2924–2932, Jan. 2017.
- [12] Z. Wang, K. Rolle, T. Schilling, *et al.*, „Tunable thermoelastic anisotropy in hybrid bragg stacks with extreme polymer confinement“, *Angewandte Chemie International Edition*, vol. 59, no. 3, pp. 1286–1294, Jan. 2020.
- [13] X. Xie, D. Li, T.-H. Tsai, *et al.*, „Thermal conductivity, heat capacity, and elastic constants of water-soluble polymers and polymer blends“, *Macromolecules*, vol. 49, no. 3, pp. 972–978, Jan. 2016.
- [14] X. Xie, K. Yang, D. Li, *et al.*, „High and low thermal conductivity of amorphous macromolecules“, *Physical Review B*, vol. 95, no. 3, Jan. 2017.
- [15] A. Shanker, C. Li, G.-H. Kim, *et al.*, „High thermal conductivity in electrostatically engineered amorphous polymers“, *Science Advances*, vol. 3, no. 7, e1700342, Jul. 2017.
- [16] G.-H. Kim, D. Lee, A. Shanker, *et al.*, „High thermal conductivity in amorphous polymer blends by engineered interchain interactions“, *Nature Materials*, vol. 14, no. 3, pp. 295–300, Nov. 2014.
- [17] C. Rössel, M. Billing, H. Görls, *et al.*, „Synthesis and modification of poly(ethyl 2-(imidazol-1-yl)acrylate) (PEImA)“, *Polymer*, vol. 127, pp. 182–191, Oct. 2017.
- [18] U. Günther, L. V. Sigolaeva, D. V. Pergushov, and F. H. Schacher, „Polyelectrolytes with tunable charge based on polydehydroalanine: Synthesis and solution properties“, *Macromolecular Chemistry and Physics*, vol. 214, no. 19, pp. 2202–2212, Aug. 2013.

- [19] M. von der Lühe, A. Weidner, S. Dutz, and F. H. Schacher, „Reversible electrostatic adsorption of polyelectrolytes and bovine serum albumin onto polyzwitterion-coated magnetic multicore nanoparticles: Implications for sensing and drug delivery“, *ACS Applied Nano Materials*, vol. 1, no. 1, pp. 232–244, Dec. 2017.
- [20] C. Sidot and Y. Christidis, *Pure crystallized anhydrous acrylamidoglycolic acid and process for its preparation*. June 9, 1964.
- [21] L. Volkmann, M. Köhler, F. H. Sobotta, *et al.*, „Poly(2-acrylamidoglycolic acid) (PAGA): Controlled polymerization using RAFT and chelation of metal cations“, *Macromolecules*, vol. 51, no. 18, pp. 7284–7294, Sep. 2018.
- [22] R. T. A. Mayadunne, E. Rizzardo, J. Chiefari, *et al.*, „Living polymers by the use of trithiocarbonates as reversible addition-fragmentation chain transfer (RAFT) agents: ABA triblock copolymers by radical polymerization in two steps“, *Macromolecules*, vol. 33, no. 2, pp. 243–245, Jan. 2000.
- [23] P. W. Winston and D. H. Bates, „Saturated solutions for the control of humidity in biological research“, *Ecology*, vol. 41, no. 1, pp. 232–237, Jan. 1960.
- [24] H. Hu, X. Wang, and X. Xu, „Generalized theory of the photoacoustic effect in a multilayer material“, *Journal of Applied Physics*, vol. 86, no. 7, pp. 3953–3958, Oct. 1999.
- [25] X. Wang, H. Hu, and X. Xu, „Photo-acoustic measurement of thermal conductivity of thin films and bulk materials“, *Journal of Heat Transfer*, vol. 123, no. 1, pp. 138–144, Jun. 2000.
- [26] Y. Park, S. Lee, S. S. Ha, *et al.*, „Crosslinking effect on thermal conductivity of electrospun poly(acrylic acid) nanofibers“, *Polymers*, vol. 11, no. 5, p. 858, May 2019.
- [27] J. K. Kauppinen, D. J. Moffatt, H. H. Mantsch, and D. G. Cameron, „Fourier self-deconvolution: A method for resolving intrinsically overlapped bands“, *Applied Spectroscopy*, vol. 35, no. 3, pp. 271–276, May 1981.
- [28] X. Hu, D. Kaplan, and P. Cebe, „Determining beta-sheet crystallinity in fibrous proteins by thermal analysis and infrared spectroscopy“, *Macromolecules*, vol. 39, no. 18, pp. 6161–6170, Sep. 2006.
- [29] L. C. Thomas. (2005). Modulated dsc basics; optimization of mdsc experimental conditions modulated dsc paper, [Online]. Available: http://www.tainstruments.com/pdf/literature/TP_008_MDSC_num_3_Optimization_of_Experimental_Conditions.pdf
- [30] J. Dong, Y. Ozaki, and K. Nakashima, „Infrared, raman, and near-infrared spectroscopic evidence for the coexistence of various hydrogen-bond forms in poly(acrylic acid)“, *Macromolecules*, vol. 30, no. 4, pp. 1111–1117, Feb. 1997.

- [31] M. M. Coleman, M. Sobkowiak, G. J. Pehlert, P. C. Painter, and T. Iqbal, „Infrared temperature studies of a simple polyurea“, *Macromolecular Chemistry and Physics*, vol. 198, no. 1, pp. 117–136, Jan. 1997.
- [32] D. J. Skrovanek, S. E. Howe, P. C. Painter, and M. M. Coleman, „Hydrogen bonding in polymers: Infrared temperature studies of an amorphous polyamide“, *Macromolecules*, vol. 18, no. 9, pp. 1676–1683, Sep. 1985.
- [33] D. J. Skrovanek, P. C. Painter, and M. M. Coleman, „Hydrogen bonding in polymers. 2. infrared temperature studies of nylon 11“, *Macromolecules*, vol. 19, no. 3, pp. 699–705, May 1986.
- [34] Z. Shen, F. Luo, H. Bai, *et al.*, „A study on mediating the crystallization behavior of PBT through intermolecular hydrogen-bonding“, *RSC Advances*, vol. 6, no. 21, pp. 17 510–17 518, 2016.
- [35] L. Daniliuc and C. David, „Intermolecular interactions in blends of poly(vinyl alcohol) with poly(acrylic acid): 2. correlation between the states of sorbed water and the interactions in homopolymers and their blends“, *Polymer*, vol. 37, no. 23, pp. 5219–5227, Nov. 1996.
- [36] M. Wieland, C. Dingler, R. Merkle, J. Maier, and S. Ludwigs, „Humidity-controlled water uptake and conductivities in ion and electron mixed conducting polythiophene films“, *ACS Applied Materials & Interfaces*, vol. 12, no. 5, pp. 6742–6751, Jan. 2020.
- [37] S. Popineau, C. Rondeau-Mouro, C. Sulpice-Gaillet, and M. E. Shanahan, „Free/bound water absorption in an epoxy adhesive“, *Polymer*, vol. 46, no. 24, pp. 10 733–10 740, Nov. 2005.
- [38] K. Ichikawa, T. Mori, H. Kitano, *et al.*, „Fourier transform infrared study on the sorption of water to various kinds of polymer thin films“, *Journal of Polymer Science Part B: Polymer Physics*, vol. 39, no. 18, pp. 2175–2182, 2001.
- [39] N. Mehra, L. Mu, T. Ji, Y. Li, and J. Zhu, „Moisture driven thermal conduction in polymer and polymer blends“, *Composites Science and Technology*, vol. 151, pp. 115–123, Oct. 2017.
- [40] J. K. Carson, S. J. Lovatt, D. J. Tanner, and A. C. Cleland, „Thermal conductivity bounds for isotropic, porous materials“, *International Journal of Heat and Mass Transfer*, vol. 48, no. 11, pp. 2150–2158, May 2005.

9.7 Supporting Information

9.7.1 Thermal conductivity measurements

The thermal conductivity was determined by the photoacoustic method. For photoacoustic characterization, the samples were spin-coated on glass substrates. The layout of the measurement set-up is described in the literature.^[1]

The frequency-dependent phase-shift is plotted in Figure 9.6 - two measurements and the respective fits are shown in Figures 9.6a and b. They correspond to the dry and the RH 77 % PImAA sample, respectively. The phase shift data are fitted by a multilayer model developed by Hu *et al.*^[2] The fit was performed according to Singh *et al.*^[3], which yields the total layer resistance. Figure 9.6c shows three consecutive measurements. The change of the phase shift is minimal. Therefore, we conclude that the moisture content keeps constant over the course of at least three measurements, which corresponds to about 30 min.

The thickness was obtained by AFM measurements (Table S1). For each humidity condition, a separate and individual sample was prepared using the same stock solution and spin coating parameters. Overall the layer thicknesses show a good consistency from sample to sample. The applied humidity conditions do not lead to an excessive degree of swelling. Only for PImAA, the layer thickness at RH 92 % could not be quantified by AFM directly. The low molecular weight of PImAA (5500 g/mol) - in comparison to the other polymer samples (13000 - 28 000 g/mol) - led to a viscous polymer film that prevented the evaluation of the step height at a scratch in the sample. Consequently, we provide for this single case a lower estimate of the thermal conductivity based on the dry polymer layer thickness of ~ 900 nm. The humidity dependent specific heat capacity was determined by MDSC measurements. The density of the dry samples was measured with a helium pycnometer. The density of the samples with absorbed water was calculated from the moisture content, and the bulk densities of water and the polymers. Dividing the total layer resistance by the sample thickness leads to the effective thermal conductivity. All relevant data are shown in Table 9.2.

Tab. 9.2: Summary of the data used for the determination of the effective thermal conductivity.

Sample	Relative humidity [%]	Total layer resistance [mm ² K/W]	SD	Thick-ness [μm]	SD	Effective thermal conductivity [W/mK]	SD
PMMA	0	9.44	0.28	1.540	0.071	0.163	0.005
PMMA	45	10.41	0.11	1.569	0.011	0.151	0.002
PMMA	77	9.94	0.17	1.569	0.024	0.158	0.003
PMMA	92	9.26	0.25	1.570	0.016	0.170	0.004
PAA	0	3.74	0.18	1.182	0.010	0.309	0.004
PAA	45	4.10	0.06	1.258	0.052	0.307	0.005
PAA	77	4.26	0.25	1.270	0.005	0.299	0.017
PAA	92	4.56	0.42	1.511	0.197	0.334	0.032
PDha	0	7.10	0.19	1.697	0.017	0.239	0.006
PDha	45	6.28	0.20	1.680	0.022	0.299	0.011
PDha	77	5.96	0.29	1.724	0.025	0.290	0.014
PDha	92	6.20	0.33	1.723	0.020	0.279	0.016
PAGA	0	5.70	0.04	1.580	0.194	0.277	0.002
PAGA	45	5.77	0.22	1.688	0.108	0.293	0.011
PAGA	77	6.50	0.21	1.838	0.143	0.283	0.009
PAGA	92	3.31	0.42	1.100	0.016	0.336	0.046
PImAA	0	2.87	0.12	0.881	0.035	0.307	0.013
PImAA	45	2.57	0.08	0.891	0.024	0.349	0.011
PImAA	77	2.45	0.35	0.983	0.071	0.409	0.062
PImAA	92	2.25	0.33	> 0.900	-	0.407	0.061
PMeImAA	0	3.54	0.04	1.110	0.048	0.314	0.004
PMeImAA	45	3.64	0.28	1.132	0.170	0.312	0.023
PMeImAA	77	4.08	0.16	1.064	0.071	0.261	0.010
PMeImAA	92	2.47	0.35	1.200	0.096	0.492	0.098

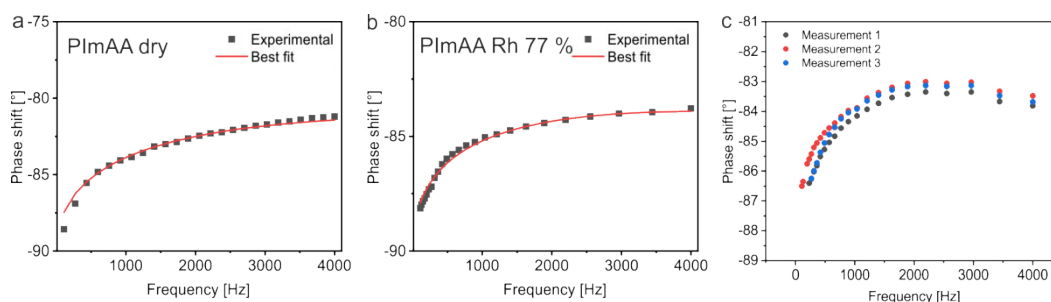


Fig. 9.6: The frequency-dependent phase shift of (a) the dry PImAA sample and (b) the PImAA sample at 77% humidity. The red lines present the best fit. (c) Three consecutive measurements of PAA at 77% humidity. The data shows only slight deviations between the measurements. Therefore, we conclude that the moisture content of the sample is stable over the time of the measurements.

9.7.2 IR Spectroscopy of dry samples

PAA

In Figure 9.7 the IR spectrum of a dry PAA film in the region of the C=O stretching vibration is shown. We attributed the different peaks in the deconvoluted spectrum to specific configurations of the C=O bond, according to Dong *et al.*^[4]. Therefore, we could distinguish between the free, the dimeric, and two oligomeric forms of the C=O bond. The peak with the highest wavenumber of 1735 cm^{-1} is attributed to the free monomer of the COOH group, whereas the peak at around 1700 cm^{-1} represents the cyclic dimer. The linear oligomeric forms of the terminal COOH groups lie in between, at 1716 cm^{-1} , while the inner COOH appears at two peaks with the lowest wavenumbers around 1674 cm^{-1} . The H-bond conformations are illustrated in Figure 9.8. At least some anhydride groups have formed due to the drying process, as indicated by the bands at 1806 cm^{-1} and 1765 cm^{-1} .

Extending the assignment from Dong *et al.*, we attributed different forms of H-bonds in the other investigated polymers.

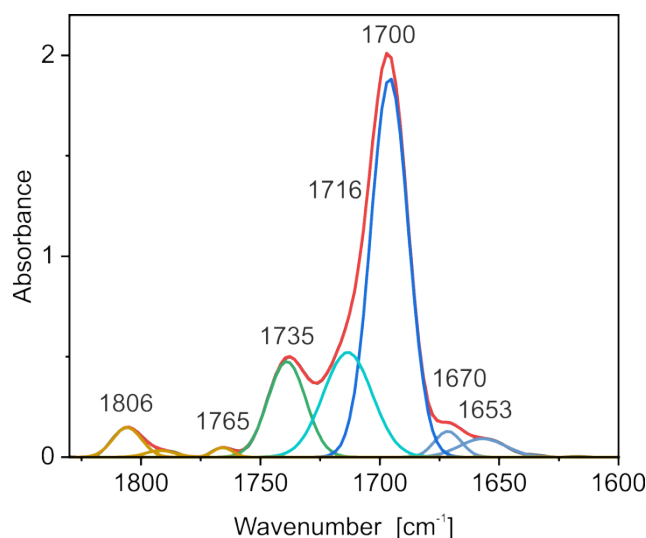


Fig. 9.7: IR spectrum of PAA in the region of the C=O band. The spectrum was deconvoluted for better interpretation. The bands were attributed to distinct configurations of the C=O bond, according to Ref.^[4]

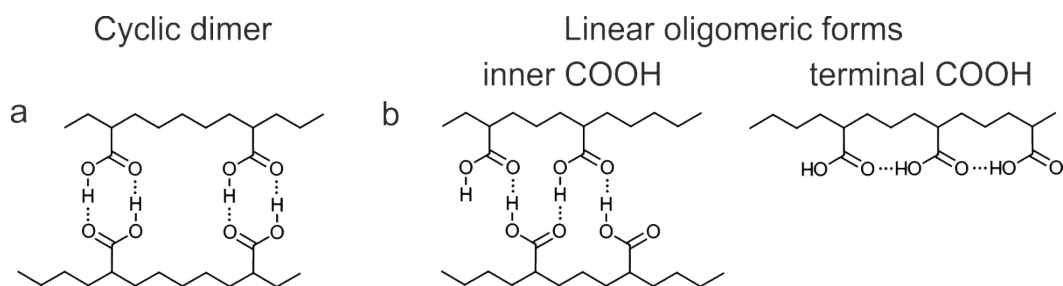


Fig. 9.8: Forms of hydrogen bonding in PAA.^[4]

PDha

Compared to PAA, an amino group is added to the repetition unit of PDha. Therefore, more motifs to form H-bonds are available. Similar peaks for the PAA sample could be detected (Figure 9.9). However, we found a slight shift to lower frequencies of all peaks. While the shift is only a few wavenumbers for the free C=O stretching and the terminal Hbonds, the shift is 20 cm^{-1} and 50 cm^{-1} for the cyclic dimers and the inner H-bonds. The shift is an incidence of the increased strength of the H-bonds.

Furthermore, new peaks arose at 1667 cm^{-1} , 1634 cm^{-1} , and 1603 cm^{-1} . The peak at 1667 cm^{-1} is ascribed to the H-bonds formed between the carbonyl and the amino group. The peaks at 1634 cm^{-1} and 1603 cm^{-1} belong to the NH_2 deformation vibration and are, therefore, excluded from the evaluation of the C=O stretching vibration. We want to note that it is also possible that H-bonds between two

amino groups are formed. The analysis of these H-bonds is not approachable by the investigation of the carbonyl stretching vibration.

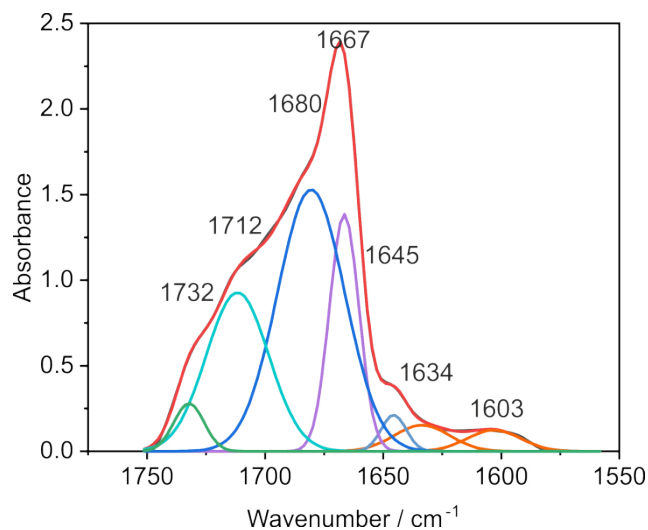


Fig. 9.9: Deconvoluted IR spectrum of the dry PDha sample in the region of the C=O stretching vibration.

PAGA

Due to the presence of two different carbonyl groups, the spectrum of PAGA exhibits many peaks in the region between 1500 cm^{-1} and 1800 cm^{-1} . Besides the carboxylic acid group, also another carbonyl group is located in the amide bond. As a consequence, we detect amide I and amide II vibrations. While the amide I band derives from the C=O stretching of the amide carbonyl group, the amide II band consists of N-H bending and C-N stretching. Therefore, the amide II band is not relevant for the H-bond analysis, which is focused on the carbonyl bands. Stretching vibrations of free carbonyl groups from the carboxylic acid appear at 1735 cm^{-1} . The peak at 1675 cm^{-1} is attributed to the carboxylic acid dimer, as this is a wavenumber comparable to the other samples. The band at 1650 cm^{-1} is ascribed to the inner H-bonds of the COOH group. Additional H-bonds to the single OH group could be a reason for the exceptional strength of this band. The two bands at 1618 cm^{-1} and 1598 cm^{-1} belong to different conformations of H-bonds but are not easily distinguishable.

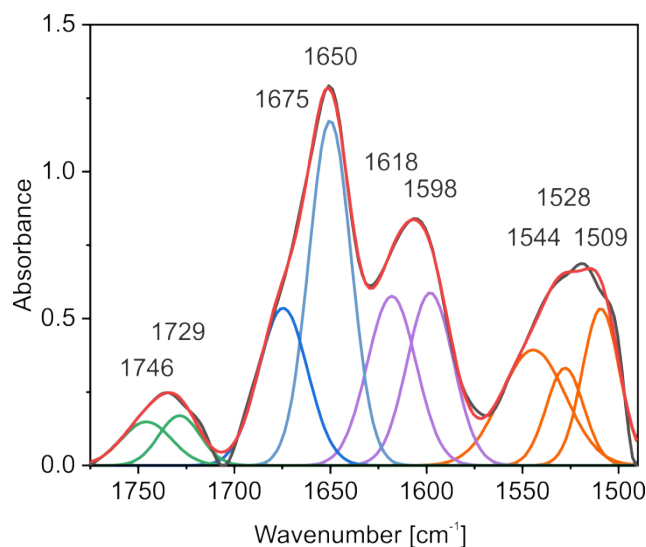


Fig. 9.10: Deconvoluted IR spectrum of the dry PAGA sample in the region of the C=O stretching vibration.

PImAA

In the literature, it has been described that mixing PAA with poly(vinyl imidazole) (PVI) leads to a decrease of the carbonyl band of the PAA at 1716 cm^{-1} and to a new peak at 1547 cm^{-1} . The new peak is explained by the exchange of the proton from the carboxylic acid group to the imidazole group. Hence, the new peak is ascribed to the asymmetric stretching vibration of COO^- .^[5]

In comparison, the PImAA film shows a strong carbonyl stretching peak at 1625 cm^{-1} . The peak 1578 cm^{-1} is ascribed to the C=C and C=N stretching in the aromatic ring. We do not attribute any of those peaks to the asymmetric stretching vibration of COO^- , because of the high wavenumber of the first and the missing of the symmetric stretching vibration around 1330 cm^{-1} . Nevertheless, the low frequency of the C=O peak is an incident for a strong interaction between the carboxylic acid and the imidazole groups. This band, in turn, is relatively broad, which indicates a variety of interactions with different coordinations and bond strengths. The two peaks with the highest wavenumbers at 1770 cm^{-1} and 1732 cm^{-1} are ascribed to anhydride bonds and free carbonyl groups, respectively. Both show a very weak intensity and are almost overlooked. Accordingly, most of the carbonyl groups participate in H-bond interactions. We distinguish the Hbonds in two categories: H-bonds between acid groups like in PAA (1680 cm^{-1} , 1664 cm^{-1} , and 1647 cm^{-1}) and H-bonds between the carboxylic acid and an imidazole group (“other H-bonds”, 1625 cm^{-1} and 1606 cm^{-1}).

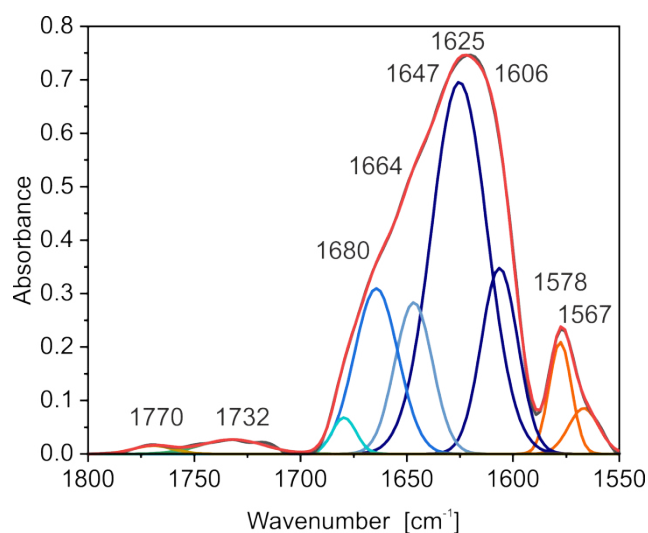


Fig. 9.11: Deconvoluted IR spectrum of the dry PImAA sample in the region of the C=O stretching vibration.

PMelMAA

In comparison to PImAA, PMelMAA has a methyl group attached to the imidazole ring, leading to a positive charge. Consequently, there is no free electron pair available at the nitrogen. The C=O band is again composed of different parts. At 1770 cm^{-1} a relatively strong anhydride band is detected, whereas the vibration of free carbonyl at 1733 cm^{-1} is only marginal. Also, the H-bonds between the carboxylic acid groups decreased in intensity. The very narrow peak at 1629 cm^{-1} is ascribed to the interactions between carbonyl and imidazole ring. The narrow width of the peak indicates a relative uniform strength and conformation of the interactions. The bands at 1579 cm^{-1} and 1515 cm^{-1} are ascribed to the C=C and C=N stretching in the aromatic ring.

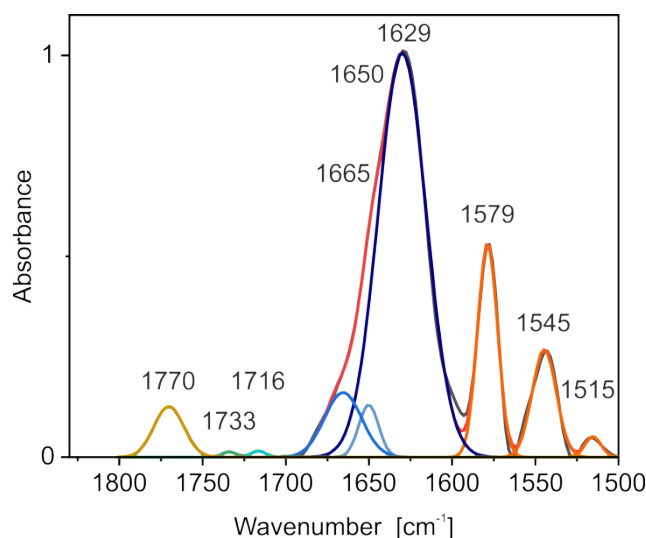


Fig. 9.12: Deconvoluted IR spectrum of the dry PMeImAA sample in the region of the C=O stretching vibration.

9.7.3 Humidity dependent IR spectra

Figure S8 shows the humidity dependent IR analysis for PDha and PAGA analogous to the presentation in Figure 9.4 in the main manuscript.

PDha shows a comparable behavior to PAA. The difference IR spectra show negative and positive contributions in the same wavenumber regions. However, the effects are less pronounced. This indicates a similar mechanism of water absorption in PAA and PDha.

PAGA shows moderate water uptake for RH 40 % and RH 77 %. At RH 92 %, the moisture content strongly increases. This behavior is also observed in the IR spectrum, with a drastic increase of the OH stretching vibration at 3500 cm⁻¹. The difference spectra in the carbonyl region show small deviations. The spectra for RH 40 % and RH 77 % show a slight decrease in H-bonds, whereas a small positive contribution is observed for the RH 92 % sample. The newly formed interactions probably also lead to a slight increase in thermal conductivity at RH 92 %.

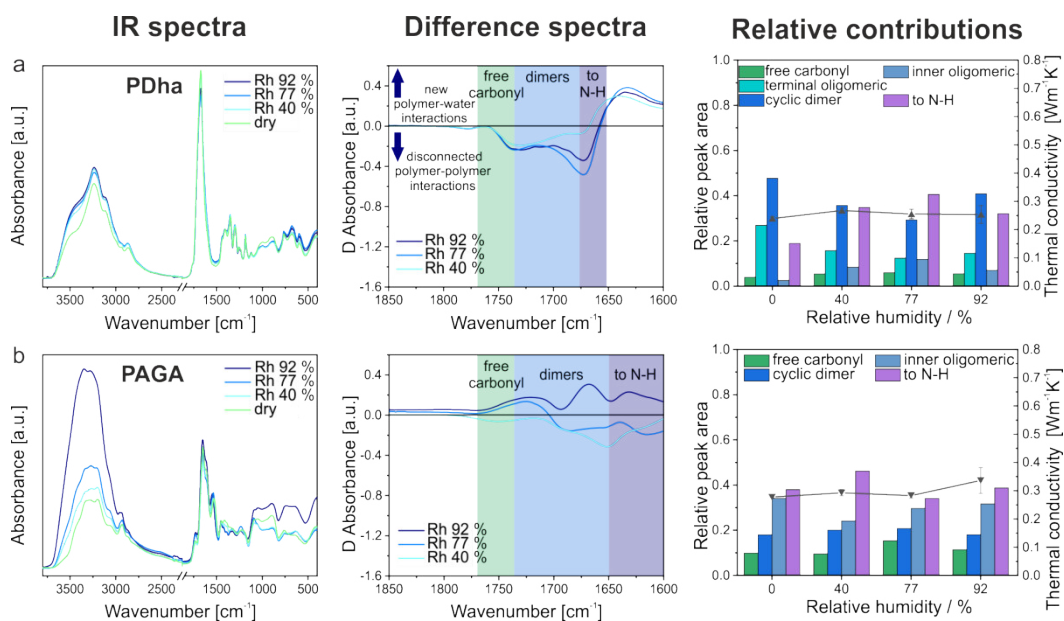


Fig. 9.13: (a) PDha, and (b) PAGA. From left to right: IR-spectra of samples with various humidity exposure. Difference spectra in the region of the carbonyl stretching vibration. The relative peak area of different H-bond structures dependent on the relative humidity.

9.7.4 DSC measurements

Besides the MDSC measurements, to determine the c_p of all samples, we performed DSC measurements of the dry samples in the range between $-40\text{ }^\circ\text{C}$ and $140\text{ }^\circ\text{C}$. Figure 9.14 shows direct DSC measurements with a heat rate of 10 K/min .

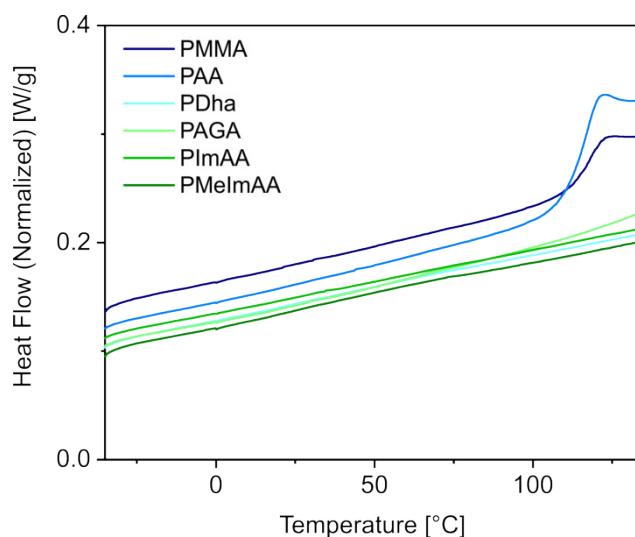


Fig. 9.14: DSC measurements of dry polymer samples. The experiments were performed in the range from $-40\text{ }^\circ\text{C}$ to $140\text{ }^\circ\text{C}$ with a heating rate of 10 K/min under nitrogen atmosphere.

9.7.5 Polymer/water effective medium model (EMT)

The following equations were used to calculate the values for the parallel mixing model and the effective medium model, according to Carson *et al.*^[6]

Parallel mixing model:

$$k_{\text{parallel}} = (1 - x_2)k_1 + x_2k_2 \quad (9.1)$$

Effective medium model:

$$k_{\text{EMT}} = \frac{1}{4}((3x_2 - 1)k_2 + [3(1 - x_2) - 1]k_1) + \sqrt{[(3x_2 - 1)k_2 + (3(1 - x_2) - 1)k_1]^2 + 8k_1k_2} \quad (9.2)$$

With $x_{1,2}$ and $k_{1,2}$, the volume ratio, and the thermal conductivity of components 1 and 2, respectively.

9.7.6 Transducer layer

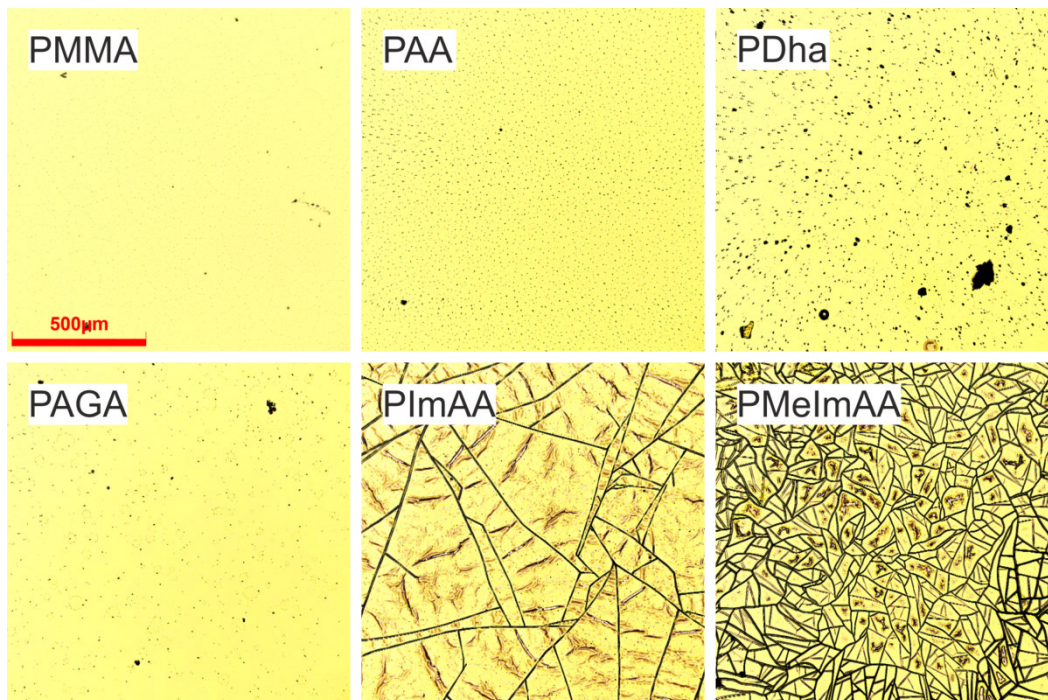


Fig. 9.15: Optical microscopy of the surface of the Au transducer layer after measuring at humid conditions. Dark speckles and cracks indicate imperfections in the Au transducer layer, which facilitates equilibration to environmental conditions.

9.7.7 References

- [1] Z. Wang, K. Rolle, T. Schilling, *et al.*, „Tunable thermoelastic anisotropy in hybrid bragg stacks with extreme polymer confinement“, *Angewandte Chemie International Edition*, vol. 59, no. 3, pp. 1286–1294, Jan. 2020.
- [2] H. Hu, X. Wang, and X. Xu, „Generalized theory of the photoacoustic effect in a multilayer material“, *Journal of Applied Physics*, vol. 86, no. 7, pp. 3953–3958, Oct. 1999.
- [3] V. Singh, T. L. Bougher, A. Weathers, *et al.*, „High thermal conductivity of chain-oriented amorphous polythiophene“, *Nature Nanotechnology*, vol. 9, no. 5, pp. 384–390, Mar. 2014.
- [4] J. Dong, Y. Ozaki, and K. Nakashima, „Infrared, raman, and near-infrared spectroscopic evidence for the coexistence of various hydrogen-bond forms in poly(acrylic acid)“, *Macromolecules*, vol. 30, no. 4, pp. 1111–1117, Feb. 1997.
- [5] A. Arslan, S. Kıralp, L. Toppare, and A. Bozkurt, „Novel conducting polymer electrolyte biosensor based on poly(1-vinyl imidazole) and poly(acrylic acid) networks“, *Langmuir*, vol. 22, no. 6, pp. 2912–2915, Mar. 2006.
- [6] J. K. Carson, S. J. Lovatt, D. J. Tanner, and A. C. Cleland, „Thermal conductivity bounds for isotropic, porous materials“, *International Journal of Heat and Mass Transfer*, vol. 48, no. 11, pp. 2150–2158, May 2005.

Tunable thermoelastic anisotropy in hybrid Bragg stacks with extreme polymer confinement

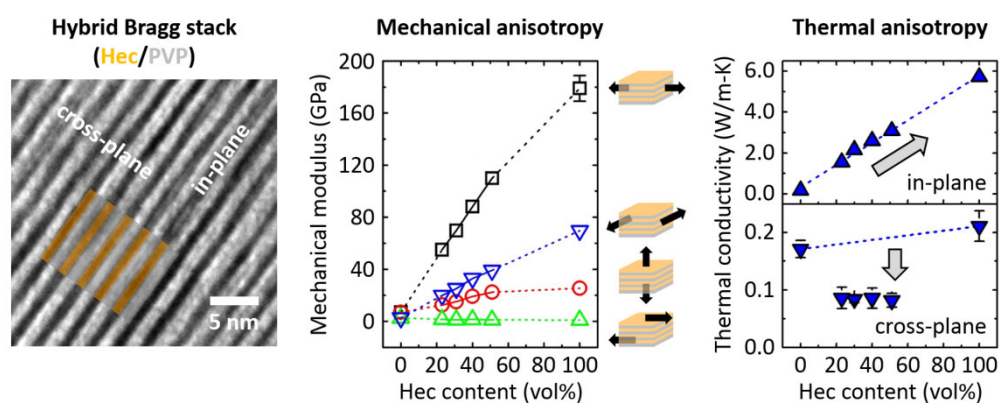
Zuyuan Wang¹, Konrad Rolle¹, Theresa Schilling^{2,3}, Patrick Hummel^{2,3}, Alexandra Philipp^{2,3}, Bernd A. F. Kopera^{2,3}, Anna M. Lechner^{2,3}, Markus Retsch^{2,3}, Josef Breu^{2,3}, and George Fytas^{1,4}

¹ Max Planck Institute for Polymer Research, Ackermannweg 10, 55128 Mainz, Germany

² Bavarian Polymer Institute, University of Bayreuth, Universitätsstraße 30, 95447 Bayreuth, Germany

³ Department of Chemistry, University of Bayreuth, Universitätsstraße 30, 95447 Bayreuth, Germany

⁴ Institute of Electronic Structure and Laser, F.O.R.T.H., 70013 Heraklion, Greece



Published in *Angewandte Chemie Int. Ed.*, **2019**, DOI: 10.1002/anie.201911546
 Reprinted with permission from Wang *et al.*, *Angew. Chem. Int. Ed.*, 2020, 59,
 1286- 1294. Copyright 2019 The Authors.

10.1 Abstract

Controlling thermomechanical anisotropy is important for emerging heat management applications such as thermal interface and electronic packaging materials. Whereas many studies report on thermal transport in anisotropic nanocomposite materials, a fundamental understanding of the interplay between mechanical and thermal properties is missing, due to the lack of measurements of direction-dependent mechanical properties. In this work, exceptionally coherent and transparent hybrid Bragg stacks made of strictly alternating mica-type nanosheets (synthetic hectorite) and polymer layers (polyvinylpyrrolidone) were fabricated at large scale. Distinct from ordinary nanocomposites, these stacks display long-range periodicity, which is tunable down to angstrom precision. A large thermal transport anisotropy (up to 38) is consequently observed, with the high in-plane thermal conductivity (up to 5.7 W/mK) exhibiting an effective medium behavior. The unique hybrid material combined with advanced characterization techniques allows correlating the full elastic tensors to the direction-dependent thermal conductivities. We, therefore, provide a first analysis on how the direction-dependent Young's and shear moduli influence the flow of heat.

10.2 Introduction

Heat management is crucial in many applications important for fueling the growth of our technology-driven society. It needs to address not only very small length scales to dissipate the heat produced, for example, by electronic circuits, but also very large length scales to realize air conditioning, for instance, for commercial buildings. The ubiquity of heat makes it obvious that heat management is a key-technology to realize international long-term goals regarding global warming. Controlling the elusive flow of heat is a complex challenge across multiple materials, length scales, and ultimately devices. This results in stringent requirements for directional control over the heat flux based on advanced material design. Whereas heat transport represents an effective, far-field phenomenon, it is decisively governed by the material structure^{[1]–[3]} and chemistry^{[4],[5]} on the microscale. Extreme phenomena of both heat dissipation and thermal insulation have been demonstrated in nanostructured and hybrid materials. For heat dissipation, surprisingly high thermal conductivities have been reported for one-dimensional (1D) fibers comprising synthetic^[6] and natural polymers.^{[7],[8]} For thermal insulation, unusually low thermal conductivities have been shown for (disordered) stacks of two-dimensional (2D) materials.^{[9],[10]} Extremely efficient anisotropic thermal insulation materials have been demonstrated with various mixtures of polymers and nanoparticles or 2D materials.^{[11]–[13]}

The combination of inherently different materials, such as soft and hard matter, is attractive, as new properties, deviating from those based on the simple linear interpolation, could emerge. This is often accompanied by improved processability, which is aided by the complementary properties of the constituent components. For instance, the soft component can serve as a binder to enable fabrication of large-area, thin films of an otherwise brittle, hard component. On the contrary, the expected effective material properties, such as mechanical reinforcement, optical transparency, and electrical or thermal conductivity, have been often found inferior to the high expectations. The reason for such shortcomings is that the nanocomposite structure, particularly the soft-hard interface, is poorly controlled. Furthermore, although many characterization techniques, such as tensile testing, indentation, and abrasion tests, are capable of assessing engineering properties, they are unsuitable for directly identifying and quantifying anisotropies or microscopic contributions to the effective properties.

Nevertheless, hybrid systems have been reported to drastically alter the materials' thermal transport properties,^{[6]–[13]} depending on the geometry, dimensionality, crystallographic symmetry, and confinement. Interestingly, layered structures inherently exhibit structural anisotropy, a feature that can be detrimental or desirable depending on the application.^[14] In particular, when polymer films are filled with nanosheets of huge aspect ratio, the resulting nanocomposite properties ought to be exceedingly anisotropic. Yet, only effective material properties such as electrical or thermal conductivity have been reported in a direction-dependent manner. Direction-dependent mechanical properties, which fundamentally translate into thermal transport properties are still missing. Strong anisotropies in hybrid materials are preferentially achieved at small stacking periodicities^[10] or by combining components with a large property contrast.^[15]

For a thorough characterization of such nanosheet/polymer stacks (also known as “nacre-mimics”^{[16]–[19]}), macroscopically oriented and homogeneous systems are paramount. Such ideal model system should also exhibit translational crystallographic symmetry, tunability, and strong anisotropy. Direction-dependent studies benefit significantly from the availability of various light scattering methods, rendering a transparent filler such as the synthetic clay hectorite with a mica-type structure desirable. For fundamental investigations of elastic properties, Brillouin light spectroscopy (BLS) has established itself as a technique of choice, as it allows for microscopic observations of high frequency (GHz) dynamics, at which viscoelasticity effects are usually negligible.^{[20],[21]} On the other hand, lock-in thermography and photoacoustic techniques have been proven reliable in accessing the in-plane and cross-plane thermal conductivities of thin films.^{[22],[23]} Here, we show for the first time the complete mechanical properties of clay/polymer Bragg stacks that are fabricated using a uniquely defined, scalable spray-coating process meeting all aforementioned

specifications of a suitable model system. We, therefore, introduce 1D hybrid Bragg stacks based on nacre-mimetic clay/polymer with small stacking periods and large property contrast. These Bragg stacks are scalable in both lateral extension and thickness, and they are macroscopically oriented. The fully controlled microstructure allows a detailed orientation dependent characterization of the thermal and mechanical properties. We couple the thermal and mechanical analyses to achieve an in-depth understanding of the interplay between the thermal conductivities and mechanical moduli in a direction-dependent manner. The extreme confinement of polymer between the clay sheets further prompts a question regarding the validity of continuum mechanics that we also address. The combination of unique hybrid materials and advanced characterization techniques provides an unprecedented insight into the physics of direction-dependent nanomechanical and thermal transport properties in strongly anisotropic materials with polymer confinement.

10.3 Results and Discussion

10.3.1 Hybrid Bragg stacks with extreme polymer confinement

The Bragg stacks comprise synthetic clay sodium fluorohectorite (Hec, $[\text{Na}_{0.5}]^{\text{inter}}[\text{Mg}_{2.5}\text{Li}_{0.5}]^{\text{oct}}[\text{Si}_4]^{\text{tet}}\text{O}_{10}\text{F}_2$) and polyvinylpyrrolidone (PVP, $M_w = 40\,000$ g/mol). Like layered titanates^[24] and antimony phosphates,^[25] Hec belongs to a handful of compounds showing a rare phenomenon of osmotic swelling.^[26] In contrast to mechanical exfoliation by e.g. sonication in the liquid phase,^[27] osmotic swelling is a thermodynamically favored, repulsive process,^[28] allowing for complete and gentle delamination that preserves the diameter of the parent crystals. In general, exfoliation describes the process of slicing tactoids into thinner stacks, whereas by delamination, the layered material is exfoliated to the level of individual single nanosheets.^[29] For Hec, nanosheets with a thickness of 10 \AA and a median diameter of $20\text{ }\mu\text{m}$ (Figure 10.5) are obtained by simply immersing the material into deionized water.^[30] Phase purity and a homogeneous charge density guaranteeing a uniform intracrystalline reactivity are prerequisite for such a well-controlled delamination. For Hec this is achieved by long-term annealing, while less uniform natural or other synthetic clays commonly applied for nacre-mimics comprise mixtures of auxiliary minerals, mono-, few- and multilayer stacks.^[30] Because of the large aspect (diameter to thickness) ratio, polar rotation of the nanosheets in suspension is hindered, leading to parallel nanosheets after osmotic swelling. Even dilute ($<1\text{ vol}\%$) suspensions of Hec represent nematic phases.^[31] The parallel pre-orientation of adjacent nanosheets in the highly swollen dispersion is indispensable for the fabrication of homogeneous and periodic Bragg stacks via spray coating. Similar to titanate nanosheets,^[32] Hec

nanosheets adopt this cofacial arrangement due to strong electrostatic repulsion with inter-nanosheet distances exceeding 50 nm. Polymers can easily diffuse into these spacious galleries. By mixing Hec suspensions with varying aliquots of an aqueous PVP solution, we obtained perfectly homogeneous, nematic dispersions, as evidenced by small-angle X-ray scattering (SAXS) measurements (Figure 10.6).

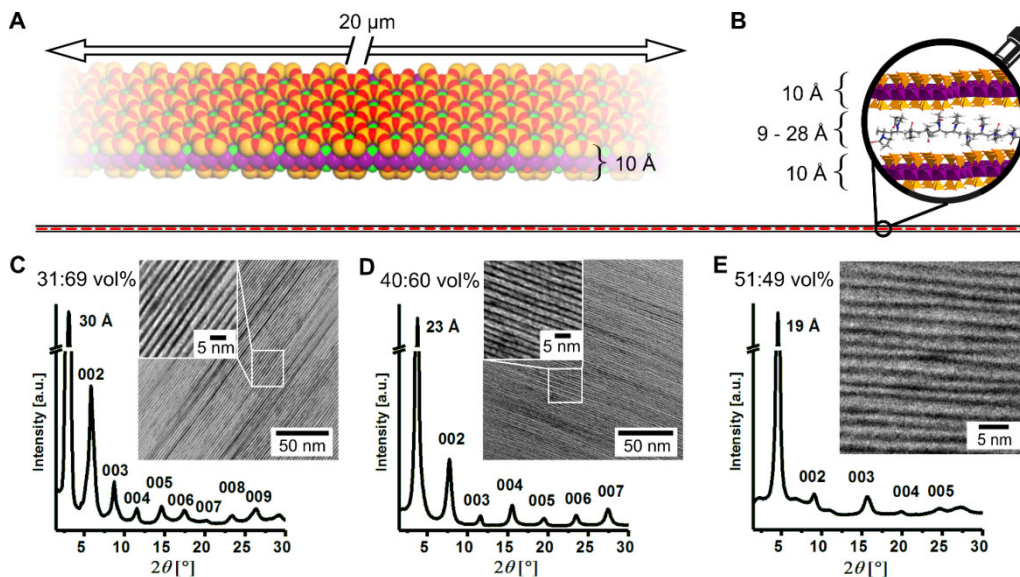


Fig. 10.1: Schematic and microscopic images of ultra-anisotropic and extremely confined Hec/PVP Bragg stacks. (A) Space-filling model of one single Hec nanosheet emphasizing the anisotropy of the nanosheet and the corrugation of the clay nanosheet allowing for interdigitation with PVP. (B) True to scale schematic of the pronounced structural anisotropy. The ultra-high-aspect-ratio nanosheets stretch from left to right and have lateral dimensions much larger than the length of the PVP polymer chains. The gallery height is on the order of magnitude of the molecular dimensions. (C-D) XRD patterns of Hec31/PVP69 and Hec40/PVP60 (defect-free materials) showing intense 001-reflections and a rational series of basal reflections up to the ninth order. The cross-sectional TEM images show exceptionally periodic homogeneity of these hybrid films over large length scales. (E) XRD patterns and cross-sectional TEM image of Hec51/PVP49 displaying a random stacking of two gallery heights.

Through spray coating of dilute nematic mixtures of high-aspectratio Hec nanosheets with PVP (1-2 wt% total solid content, see Section 10.7.1) highly coherent Bragg stack films with tunable gallery spacings are fabricated.^[33] The transverse flexibility of clay monolayers^[34] and their large aspect ratio are essentials assuring the high degree of precision obtained in the self-assembly.^[35] Both, all nanosheets and the macroscopic film are aligned parallel to a polyethylene terephthalate substrate. The microscopic orientation of the Hec nanosheets prescribes the macroscopic film orientation, which is prerequisite for the direction-dependent measurements. The macroscopic film orientation is, consequently, equivalent to the microscopic polymer/clay direction and allows using far-field and integrating characterization techniques to reveal direction-dependent properties. After drying, self supporting

hybrid films with lateral extensions of several square centimeters are peeled off the substrate and used in the BLS and thermal conductivity measurements. Only by generating a nematic phase consisting of a homogeneous mixture of large aspect ratio and flexible nanosheets allows for fabrication of large area, self-standing 1D single crystals referred to in literature as Bragg-stacks or smectic films.^[35] Furthermore, appropriate processing like spray coating fostering the thermodynamic equilibration of the hybrid structure during drying has to be employed.

In total, we prepared six samples: pure polymer, pure Hec, and four hybrid Bragg stacks, which are denoted as Hec0/PVP100, Hec100/PVP0, Hec23/PVP77, Hec31/PVP69, Hec40/PVP60, and Hec51/PVP49, respectively. Here, the numbers indicate the volume fractions (vol%) of Hec and PVP, as confirmed by thermogravimetric analysis (Table 10.1 and Figure 10.7).

The Hec surface is corrugated (Figure 10.1A) allowing for interdigitation and anchoring of PVP chains. Such interdigitation has been documented for intercalated molecular moieties, where structures based on single crystal data refinement are available.^{[36],[37]} An in-scale impression of the ultra-high aspect ratio provided by the Hec nanosheet gallery is shown in Figure 10.1B, where the length of the line corresponds to the typical lateral size of a clay nanosheet, and the thickness of the line to the height of a Hec/PVP/Hec layer. The magnifying lens highlights the extreme polymer confinement in the cross-plane direction. The perfect homogeneous arrangement of Hec nanosheets and PVP is demonstrated by TEM and SEM images over different dimensions (Figure 10.1C-E, Figure 10.11). Note that the lateral dimensions of the Hec nanosheets are much larger than the typical persistence and even contour lengths of the PVP chains. While for the polymer chains the Hec nanosheet confinement appears infinite, at the length scale of the Bragg-stack films extending over tens of centimeters, they are of course finite. At the magnification where single 1 nm thick nanosheets are observable (Figure 10.1C-E, Figure 10.9), the occurrence of nanosheet edges is very rare (fewer than one per 2500 nm²). Careful inspection, however, reveals few (Figure 10.10) of these nanosheet edges. The clay nanosheets show in-plane crystalline order resembling the structure of mica. While mica possesses 3D crystalline order, our nanocomposite films belong to the transversely isotropic symmetry class, because the adjacent Hec nanosheets are positioned randomly in the lateral direction. However, all hybrid films show translational crystallographic symmetry along 001 (the cross-plane direction), as indicated by several orders of Bragg reflections (Figure 10.1C-E and Figure 10.9). By varying the PVP content, the basal spacing was tuned in the range from 19 to 38 Å, leading to PVP layer thicknesses ranging from 9 to 28 Å. For all samples, the gallery height is, therefore, significantly smaller than the PVP chains' radius of gyration (R_g , PVP ≈ 15 nm^[38]), implying strong polymer confinement.

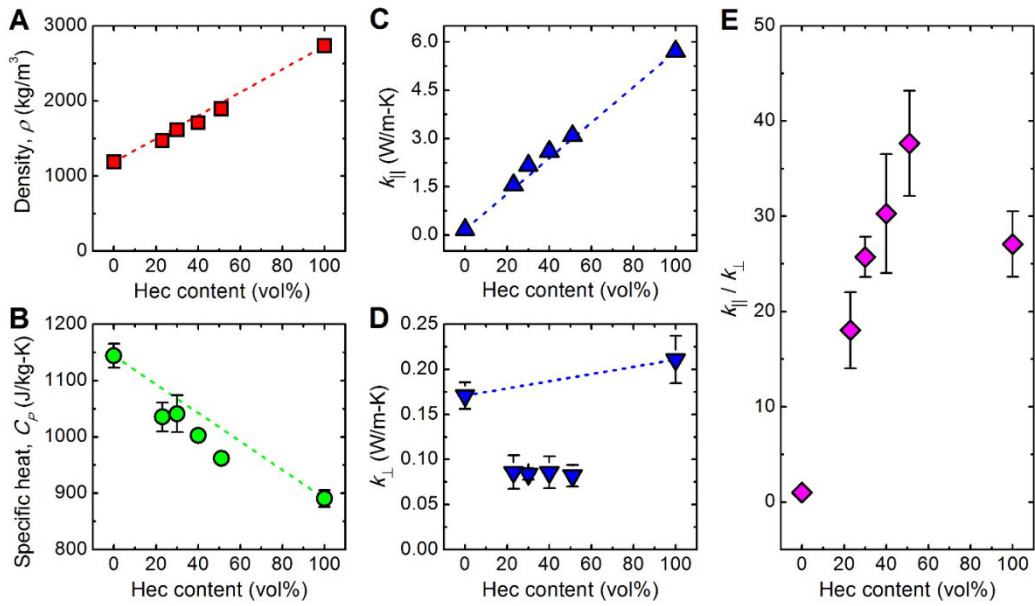


Fig. 10.2: Direction-dependent thermal conductivities of Hec/PVP hybrid Bragg stacks. (A) Film density, (B) specific heat, and effective (C) in-plane and (D) cross plane thermal conductivities, as a function of the Hec volume fraction. The red, green, and blue dashed lines in (A)-(D) show linear trends based on a simple mixing model, $A(x) = (1 - x)A(0\%) + xA(100\%)$, where A represents ρ , C_p , k_{\parallel} , or k_{\perp} , and x denotes the Hec volume fraction. (E) Ratio of the in-plane to cross-plane thermal conductivities vs. the Hec volume fraction. For clarity, error bars smaller than the symbol size are not shown.

In contrast to known nanocomposite films,^{[17],[39]} Hec and PVP are thermodynamically miscible over a wide range of compositions. This miscibility is a prerequisite for tuning the basal spacing over a wide range with angstrom precision, which typically is only observed when vapour-phase deposition techniques are applied.^[9] The miscibility is also reflected in an agreement of the basal spacing observed by X-ray diffraction (d_{XRD}) with the nominal values calculated based on the Hec and PVP volume fractions (d_{nominal} , Table 10.1). To the best of our knowledge, our Hec/PVP Bragg stack films are the first of its kind showing such an agreement. Because the polymer confinement, however, is getting to the point where the gallery height is on the order of the size of an individual polymer chain, it is not possible to vary the gallery height continuously but only in incremental steps that relate to the diameter of the polymer chain. Consequently, only discrete polymer volume fractions lead to essentially defect-free Bragg stacks, as seen in Hec40/PVP60 and Hec31/PVP69. XRD patterns reflect this with a rational 001-series, where the average basal spacing (d_{XRD}) calculated from individual reflections shows a low coefficient of variation with the reflection peaks being sharp and intense (Table 10.1). The two gallery heights of the two defect free hybrid materials (1.3 nm for Hec40/PVP60 and 2.0 nm for Hec31/PVP69) might be attributed to the elliptical nature of PVP chains with principle axes of 1.0 nm and 1.3 nm (Figure 10.8A). The observed gallery heights

correspond to a monolayer with the longer principal axis (Figure 10.8B) oriented perpendicular to the Hec nanosheets and a bilayer with the longer principle axis (Figure 10.8C) lying in the plan of the Hec nanosheets, respectively.

In the two cases where the volume ratios do not happen to match (Hec23/PVP77 and Hec51/PVP49), the miscibility is nevertheless assured at small length scale by random interstratification of two gallery heights (Figure 10.1E; transmission electron microscopy (TEM) close-up), and the coefficient of variation of the 001-series increases^[40] (Table 10.1) with the reflection peaks being less intense (Figure 10.1E and Figure 10.9).

10.3.2 In-plane and cross-plane thermal conductivities

The in-plane and cross-plane thermal conductivities of the Hec/PVP hybrid Bragg stacks were characterized by lock-in thermography and photoacoustic measurements,^{[22],[23],[41]} respectively. Since the density, ρ , and specific heat, C_p , are prerequisites for the thermal conductivity analysis, they were also determined experimentally by using helium pycnometry and differential scanning calorimetry (DSC) (Section 10.7.4), respectively. As the Hec volume fraction increases from 0 to 100%, the density increases from 1190 to 2730 kg/m³ (Figure 10.2A). This is well captured by a volume fraction-based mixing model (dashed line in Figure 10.2A). Correspondingly, the specific heat decreases from 1140 to 890 J/kgK (Figure 10.2B), which also follows the prediction by an effective medium model (Figure 10.12B). Both analyses indicate that despite the extreme polymer confinement the properties of the hybrid stacks could be described by linearly interpolating the properties of the two bulk constituents. The polymer confinement, however, leads to a significant increase in the glass transition temperature (T_g) of PVP, with no discernable T_g below 250 °C even at the lowest Hec composition (Figure 10.12A). Expectedly, the thermal conductivity of the Bragg stacks strongly depends on the direction. The in-plane thermal conductivity achieves its maximum, $k_{\parallel,\max} = 5.71$ W/mK, in Hec100/PVP0, which is even higher than typical in-plane thermal conductivities of natural micas (Figure 10.4A).^[42] The lower end is given by the isotropic thermal conductivity of Hec0/PVP100, i.e., $k_{\parallel,\min} = 0.17$ W/mK (only determined by photoacoustic characterization). The four hybrid Bragg stacks have in-plane thermal conductivities between these limiting values following a parallel mixing model (Figure 10.2 C).^[43] This is again surprising, as it implies that the confinement of PVP has no effect on the in-plane thermal conductivity of the Hec/PVP hybrid stacks compared to bulk PVP. The cross-plane thermal conductivity exhibits a broad minimum at $k_{\perp} \approx 0.09$ W/mK, which is comparable to previously reported data for organoclay laminates.^[10] The deviation of the cross-plane thermal conductivities from an effective medium behavior (Figure 10.2D, dashed line) could be attributed

to the Hec/PVP interfaces, which are the dominating contributors to the cross-plane thermal resistance, as discussed below. The thermal conductivity anisotropy, k_{\parallel}/k_{\perp} , depends strongly on the hybrid composition, attaining a maximum of 38 in Hec51/PVP49 (Figure 10.2E). We note that this anisotropy is exceptionally high for electrically insulating hybrid materials^[44] and outperforms natural nacre by a factor of ≈ 20 .^[45] All in all, the structural perfection of the pure components and hybrid Bragg stacks translate into a record-high in-plane thermal conductivity and thermal transport anisotropy.

10.3.3 Anisotropic mechanical properties

The unique macroscopic orientation in the hybrid Bragg stacks allows us to track down the origin of their high thermal conductivity anisotropy by measuring their full mechanical tensors. The measurements were conducted by using BLS, which probes the phonon wave vector, q , dependent sound velocity, v , through inelastic light scattering by thermally excited, high frequency (GHz) phonons.^{[20],[21]} Since the hybrid Bragg stacks are transversely isotropic, only q vectors in a single plane containing the symmetry axis have to be considered. For such a q vector, the direction can be denoted by α , the angle between q and the normal to the sample film, and because of symmetry α can be restricted in the range from 0° to 90° . The measurements corresponding to $\alpha = 0^\circ$, $0^\circ < \alpha < 90^\circ$ and $\alpha = 90^\circ$ were conducted in the reflection, backscattering, and transmission scattering geometries, respectively, while the polarization of the phonon mode was selected using different incident and scattered light polarization configurations (e.g., VV for quasi-longitudinal (Q-L) and quasi-transverse (Q-T) modes, and VH for a pure-transverse (P-T) mode).^[46] This flexibility of accessible parameters makes BLS particularly suitable for characterizing anisotropic or crystalline structures, as demonstrated in previous experiments on mica crystals.^[47] Since this work is the first one to apply the BLS technique to a hybrid Bragg stack material, we briefly outline the BLS measurement and data analysis.

Consider Hec31/PVP69 as an example. A typical BLS spectrum from the reflection geometry (inset to Figure 10.18A) displays a cross-plane longitudinal (L_{\perp}) mode in the VV polarization configuration (Figure 10.18B). A typical BLS spectrum from the backscattering geometry (Figure 10.3A, top-right inset) depicts a Q-L and a Q-T mode in the VV polarization configuration (Figure 10.2A) and a weak P-T mode in the VH polarization configuration (Figure 10.3A, top-left inset). Comparatively richer information exists in a typical BLS spectrum from the transmission geometry (Figure 10.3B, top-right inset). In the VV polarization configuration, the BLS spectrum features an in-plane longitudinal (L_{\parallel}) and a Q-L mode at a small laser incident angle, β , and an additional Q-T mode at a large β (Figure 10.3B). In the

VH polarization configuration, a weak P-T mode at all β (Figure 10.3B, top-left inset) is clearly resolved. In the transmission BLS spectra, the intensity ratio of the Q-L and Q-T peaks yields additional information (Figure 10.19B) and the Q-T mode intensity increases noticeably at higher Hec contents. By comparing the backscattering and transmission spectra, it becomes clear that the appearance of the Q-L and Q-T peaks in the latter (Figure 10.3B) results from the scattering of the laser beam internally reflected on the sample's backside.^[48]

Based on the frequency shift, f , from the BLS spectrum and the phonon wave vector, q , from the momentum conservation analysis, we calculated the sound velocity along a certain q as $\nu = 2\pi f/|q|$. Whereas the reflection measurements give the ν_{*+} , at $\alpha = 0^\circ$ and the transmission measurements result in the ν_{*+} , and ν_{-+} . at $\alpha = 90^\circ$, the backscattering measurements provide sound velocities for all the Q-L, Q-T, and P-T modes at intermediate α angles, as limited by the sample's refractive index. These direction-dependent sound velocities are reported in Figure 10.3C for Hec31/PVP69; additional data for the other samples are shown in Figure 10.20A-D. Since sound velocities are intimately related to the elastic stiffness tensor in the framework of the Christoffel equation,^{[49],[50]} the availability of the former together with the measured sample densities (Figure 10.2A and Table 10.4) enables unique determination of the latter. For a transversely isotropic material, the elastic stiffness tensor contains five independent elastic constants (e.g., C_{11} , C_{12} , C_{13} , C_{33} , and C_{44}).^{[51],[52]} Through χ^2 fitting,^[53] we obtained the elastic stiffness constants (Figure 10.20E and Table 10.4), which allow theoretical representation of the direction-dependent sound velocities (solid lines in Figure 10.3C and Figure 10.20A-D) as well as determination of the engineering mechanical properties (Figure 10.3D and Table 10.5). In addition, we analyzed the error bars (standard deviations) of the quantities according to principles of uncertainty propagation (Section 10.7.11).

This analysis provides the first direction-dependent insights into the mechanical properties of hybrid Bragg stacks in general and of clay/polymer nanocomposites in particular. The Young's moduli, E_{\parallel} and E_{\perp} , and torsional shear modulus, G_{12} , all increase with increasing Hec volume fraction. The sliding shear modulus, G_{13} , however, decreases from 2.6 GPa in Hec0/PVP100 to 1.0 GPa in Hec100/PVP0. A reduction in polymer chain entanglement upon confinement could be the cause of the decrease in G_{13} .^[54] Since the elastic moduli of polymer nanocomposites depend on the specific filler-polymer and polymer-polymer interactions, a rationalization of the increase (E_{\parallel} , E_{\perp} , G_{12}) or decrease (for G_{13}) with Hec content would require computer simulations.^[54] All the mechanical moduli of the Bragg stacks display an effective medium behavior, assuming values between those of the two bulk components. We point out that even though the PVP chains are strongly confined between the adjacent Hec nanosheets (note $R_{g, \text{PVP}} > 5(d_{\text{XRD}} - d_{\text{Hec}})$), bulk properties (e.g., ρ_{PVP} , ρ_{Hec}) are sufficient to fully capture the BLS measurements. As expected

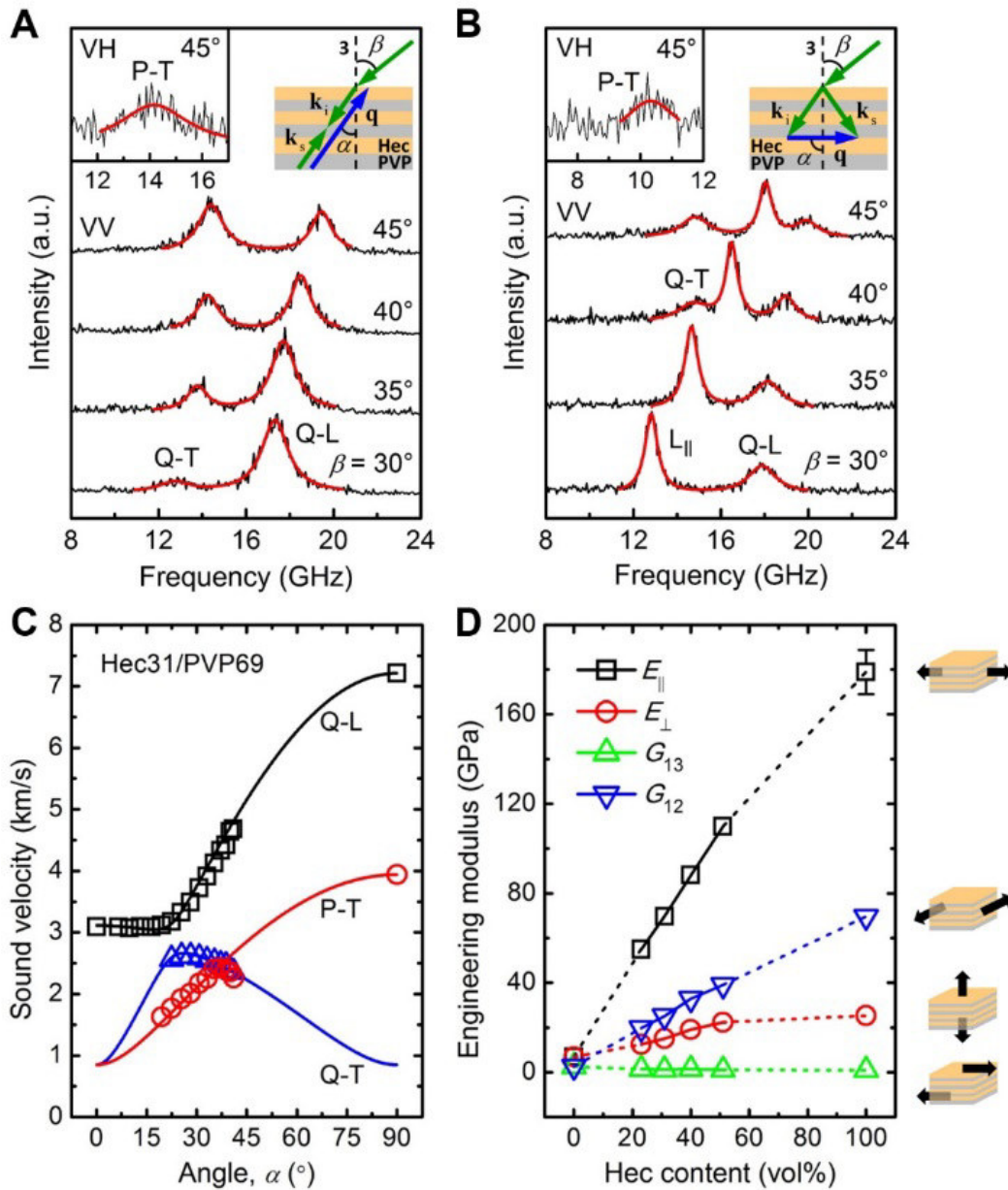


Fig. 10.3: BLS measurements and strong mechanical anisotropy of Hec/PVP hybrid Bragg stacks. (A-B) Polarized BLS spectra (anti-Stokes side) of the Hec31/PVP69 hybrid stack film recorded in (A) the backscattering geometry with q forming a variable angle, α , with the normal to the sample film (top-right inset to (A)) and (B) the transmission geometry with the phonon wave vector, q , directed in-plane ($\alpha = 90^\circ$; top-right inset to (B)). k_i and k_s are the wave vectors of the incident and scattered light beams, respectively. β is the incident angle of the laser beam. The quasi-longitudinal (Q-L), quasi-transverse (Q-T), and in-plane longitudinal (L_{\parallel}) phonon modes are indicated in (A) and (B). The much weaker depolarized VH spectra of the pure transverse modes are shown in the top-left insets. Notice the correspondence between the Q-L and Q-T modes in (A) and those in (B). (C) Direction-dependent sound velocities of the observed acoustic phonons in the BLS spectra of Hec31/PVP69. The three solid lines indicate theoretical representations (Equations (10.6)-(10.8)) of the experimental sound velocities of the three modes. (D) Composition dependence of four engineering moduli. The moduli of the anisotropic hybrid films are extrapolated to those of the pure PVP and pure Hec films, as shown by the dashed lines. The four schematics beside (D) visualize the physical meanings of the corresponding moduli.

from the structural anisotropy, the Young's moduli exhibit large differences between the in-plane and cross-plane directions (Figure 10.3D). As the Hec volume fraction increases from 0 to 100 %, the mechanical anisotropy ratio, E_{\parallel}/E_{\perp} , increases from 1 to 7. Concomitantly, the two characteristic Poisson's ratios, ν_{23} and ν_{24} , vary in ranges of 0.02-0.05 (nearly zero or cork-like values) and 0.34-0.41 (typical polymer values), respectively (Table 10.5). The reasonable values of the mechanical properties corroborate the validity of continuum mechanics at length scales of a few nanometers and in the presence of extreme polymer confinement.

In the last section, we summarize the new insights onto the anisotropic thermoelasticity that can be gained from this wholistic analysis. We firstly exploit the directly measured direction-dependent sound velocities, and secondly correlate the derived mechanical moduli to the direction-dependent thermal conductivities. We first apply a kinetic theory model, $k = C_v \bar{v}_g \bar{\Lambda} / 3$ to estimate the average phonon mean free path $\bar{\Lambda}$; along different directions in the Bragg stacks.^[55] We use $C_v = C_p$ and $\bar{v}_g = \bar{v}_{s,\parallel} = (\nu_{Q-L,\parallel} + \nu_{Q-T,\parallel} + \nu_{P-T,\parallel}) / 3$; a similar analysis is done for k_{\perp} . The in-plane $\bar{\Lambda}$; strongly depends on the hybrid composition, ranging from 14 Å for Hec100/PVP0 to 2 Å for Hec0/PVP100 (Figure 10.4A). We note that these $\bar{\Lambda}$ values significantly underestimate the presence of longer ranged phonons, which are typically better described by a phonon mean free path accumulation function.^{[55],[56]} It is well known that thermal transport involves phonons over a wide range of frequencies which have different specific heat capacities, group velocities, and mean free paths. The underestimated $\bar{\Lambda}$; in our analysis could be attributed to the overestimated \bar{v}_g from the BLS measurements, which mainly characterizes the propagation speed of a small fraction of the low frequency (long wavelength) phonons. These low frequency phonons carry only a negligible fraction of the overall heat. For the in-plane direction, the lateral size of the Hec nanosheets by far exceeds the average phonon mean free path. Hence, the high in-plane thermal conductivities are governed by the intrinsic material properties, not by the presence of grain boundaries between the aligned Hec nanosheets. The complementary analysis for k_{\perp} demonstrates a strong reduction of $\bar{\Lambda}$; down to less than 1 Å (Figure 10.4B) with no discernible composition dependence along the cross-plane direction. Interfacial effects apparently dominate the thermal transport in this direction, which is better analyzed using a series resistance model (SRM, Figure 10.4C and F) as outlined by Losego *et al.*^[10] The fitted value of the interfacial conductance, $G_{\text{Hec/PVP}} = 89 \pm 8 \text{ MW/m}^2\text{K}$ (see Section 10.7.10), falls well into the range of reported values for other inorganic/organic interfaces.^{[4],[57]} The intercalation of PVP between the clay sheets leads to a strong reduction of the interfacial conductance, which is $G_{\text{Hec/Hec}} = 291 \pm 28 \text{ MW/m}^2\text{K}$ for the pure hectorite.

We next address the correlation between the anisotropic mechanical moduli and thermal conductivities. Two distinct conclusions can be drawn.

- (i) In the direction parallel to the Hec nanosheets, a correlation between the thermal conductivity and all mechanical moduli is found. Along this direction the phonon mean free path is considerably shorter than the typical lateral size of a Hec nanosheet, rendering grain boundary effects insignificant. The influence of E_{\parallel} , E_{\perp} , and G_{12} on the thermal transport dominates over G_{13} since the former moduli show a direct relation to the in-plane thermal conductivity. E_{\parallel} and G_{12} show a power scaling law close to one (0.93) between in-plane thermal conductivity and modulus (E_{\perp} scales with 0.38). Whereas we find a clear correlation between the moduli and the thermal conductivity, we cannot deduce which change in mechanical modulus causes which effect to the thermal transport. The applicability of a simple mixing model along the parallel direction as outlined in Figure 10.2 A-C is certainly surprising in view of the strong polymer confinement effect on the glass transition (Figure 10.12).
- (ii) In the direction perpendicular to the Hec nanosheets, the phonon mean free path is comparable to the periodicity of the Bragg stacks. Here, the composition dependence of the mechanical properties does not influence the reduction of the cross-plane thermal conductivity (vertical spread of the data points in Figure 10.4E). Thus, changes to the gallery height are insignificant, which indicates the overwhelming contribution of the interfacial conductance. Considering changes to the pure components we find that reducing the sliding shear modulus G_{13} decreases the cross-plane thermal transport properties of the polymer component. The reduction in k_{\perp} of the hybrid stacks relative to pure hectorite correlates to losses in E_{\parallel} , E_{\perp} , and G_{12} that apparently counteract the increase in G_{13} .

Overall, the mechanical and thermal properties are uncorrelated along the perpendicular direction, and the thermal transport is governed by the Hec/PVP interfaces.

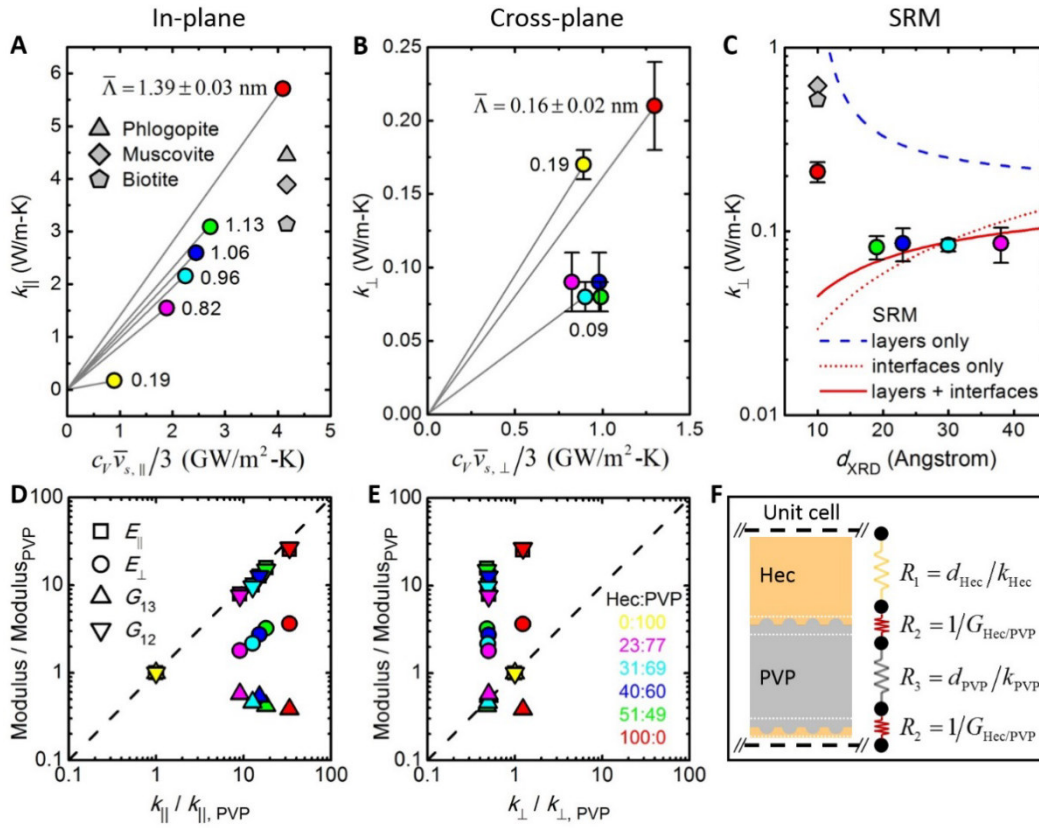


Fig. 10.4: Analysis of anisotropic thermomechanical coupling in Hec/PVP hybrid Bragg stacks. (A) Effective in-plane thermal conductivity, k_{\parallel} , vs. $C_v \bar{v}_{s,\parallel}/3$. The yellow, purple, cyan, blue, green, and red colored symbols represent the Hec0/PVP100, Hec23/PVP77, Hec31/PVP69, Hec40/PVP60, Hec51/PVP49, and Hec100/PVP0 samples, respectively. The phlogopite data point is from our additional measurements; muscovite and biotite data points are from reference.^[42] (B) Effective cross-plane thermal conductivity, k_{\perp} , vs. $C_v \bar{v}_{s,\perp}/3$. In (A) and (B), the numbers beside the data points indicate the average phonon mean free paths, $\bar{\Lambda}$; (i.e., the slope of the gray lines). (C) Effective cross-plane thermal conductivity, k_{\perp} , vs. the basal spacing of the Bragg stacks. The red solid line is a fit to the experimental data based on the series resistance model (SRM) shown in (F). As a comparison, the blue dashed line considers only the thermal resistances of the Hec and PVP layers, and the red dotted line considers only the thermal resistances of the Hec/PVP interfaces. (D) Normalized mechanical moduli vs. normalized effective inplane thermal conductivity, k_{\parallel} . The dashed line shows a direct correlation between the two axes with a power of one. (E) Normalized mechanical moduli vs. normalized effective cross-plane thermal conductivity, k_{\perp} . In (D) and (E), the following values of the pure PVP film, $E_{\parallel} = E_{\perp} = 7.0$ GPa, $G_{13} = G_{12} = 2.6$ GPa, and $k_{\parallel} = k_{\perp} = 0.17$ W/mK, are used as references in the normalization. (F) A schematic of the SRM used to analyze the Hec/PVP interfacial thermal conductance.

10.4 Conclusion

In conclusion, fully delaminated hectorite platelets can be processed into hybrid Bragg stacks with unique properties, with the polymer polyvinylpyrrolidone being the intercalated second component. Such long-range 1D ordered materials become accessible by simply spray coating the desired nematic dispersions of adjusted volume fractions, which at the same time controls the periodicity of the hybrid stacks down to the angstrom level. The macroscopic lattice alignment enables the determination of direction-dependent thermoelastic properties, which we assessed by thermal transport characterization techniques and Brillouin light spectroscopy. We found a record high anisotropy between the in-plane and cross-plane thermal conductivities in clay/polymer hybrid materials. This is corroborated by the first report of direction-dependent Young's and shear moduli that are also strongly anisotropic. The effective gallery spacing, density, specific heat, and in-plane thermal conductivity were found to conform to composition-dependent simple mixing models. Despite the nanometer-level lattice periodicity and angstrom-level polymer confinement, the Christoffel-equation-based model, derived in the framework of continuum mechanics, remains applicable for determining the anisotropic elasticity. Of general relevance is the direction dependency of the way that the mechanical moduli and thermal conductivities correlate. In the in-plane direction, where grain boundaries are negligible relative to the phonon mean free path, E_{\parallel} , E_{\perp} , and G_{12} directly correlate with the in-plane thermal conductivity. In the cross-plane direction, where the phonon mean free path is comparable to the lattice periodicity, the thermal transport is governed by the clay/polymer interfaces. We are convinced that a wholistic understanding of direction-dependent thermoelastic properties will have a broad impact on important applications such as electronic packaging and thermoelectrics. This contribution is only a first step towards this goal. More work needs to be done for the deterministic - maybe even independent - design of mechanical and thermal properties. Future studies should also address the role of enthalpic interaction at the clay/polymer interface, interdigitation of the confined polymer, size effects of the platelets, and other nanosheet materials.

10.5 Experimental Section

10.5.1 Sample Preparation

The synthetic clay sodium fluorohectorite (Hec, $[\text{Na}_{0.5}]^{\text{inter}}[\text{Mg}_{2.5}\text{Li}_{0.5}]^{\text{oct}}[\text{Si}_4]^{\text{tet}}\text{O}_{10}\text{F}_2$) was delaminated by immersing it into Millipore water (0.5 wt%). The aqueous PVP solution (1 wt%) was added in the desired weight ratio. The suspension was mixed for at least one day in an overhead shaker. The homogeneity of the suspension was crosschecked by SAXS measurements. Self-supporting films were prepared using a fully automatic spray coating system. Every spraying cycle is followed by a drying cycle of 90 s at a temperature of 55 °C. We prepared pure PVP, pure Hec, and four hybrid Hec/PVP films. The self supporting films were characterized by thermogravimetric analysis, XRD, and TEM. Additional information about the sample preparation can be found in Section 10.7.1.

10.5.2 In-plane thermal conductivity measurements

Lock-in thermography measures the temperature spreading across the free-standing samples upon thermal excitation by a focused laser beam with a modulated intensity. To prevent convective heat losses, the experiments are conducted in a vacuum chamber. The amplitude and phase data are extracted from the radial temperature distribution. The thermal diffusivity is then fitted by the slope method for thermally thin films. With the density, determined by helium pycnometry, and the specific heat, determined by differential scanning calorimetry (DSC), the thermal conductivity can be calculated. More details are provided in Section 10.7.4.

10.5.3 Cross-plane thermal conductivity measurements

The photoacoustic method uses a modulated laser beam to periodically heat a transducer layer in intimate contact with the sample. The heat is converted into an acoustic wave propagating into a gas tight cell above the sample, which is filled with helium at 20 psi. A sensitive microphone detects the phase shift between the acoustic signal and the modulated laser by a lock-in amplifier. The frequency-dependent phase shift is then compared to a multilayer model, assuming one-dimensional heat transfer. Therefrom, the total layer resistance is obtained. With the film thickness determined by AFM, the effective thermal conductivity is calculated. More details are provided in Section 10.7.4.

10.5.4 Brillouin light spectroscopy (BLS)

BLS measures the phonon dispersion, $\omega(q)$, by detecting the Doppler frequency shift, ω , of the inelastically scattered light by sound waves (“phonons”) with a wave vector, q . We recorded BLS spectra utilizing three scattering geometries (transmission, reflection, and backscattering) and two polarization configurations of the incident ($\lambda = 532$ nm) and scattered light (polarized VV, depolarized VH), which allowed us to establish the nature of the observed phonons. We varied the incident angle to obtain the direction dependent sound velocities necessary for the determination of the anisotropic elasticity. The elastic stiffness tensors were obtained from the representation of the direction-dependent sound velocities by the Christoffel equation assuming transverse isotropy. The characteristic Young’s moduli, shear moduli, and Poisson’s ratios of the Bragg stacks were subsequently calculated. More details can be found in Section 10.7.9.

Acknowledgements

We thank Sabine Rosenfeldt for conducting SAXS measurements on the gel samples. We also thank Marco Schwarzmann for preparing TEM samples and taking TEM micrographs. The Volkswagen Foundation funded this project through a Lichtenberg professorship. DFG RE 3550/2-1 provided additional support. Z. W., K. R., and G. F. acknowledge the financial support by ERC AdG SmartPhon (Grant No. 694977).

10.6 References

- [1] B. Graczykowski, A. E. Sachat, J. S. Reparaz, *et al.*, „Thermal conductivity and air-mediated losses in periodic porous silicon membranes at high temperatures“, *Nature Communications*, vol. 8, no. 1, 2017.
- [2] M. E. Siemens, Q. Li, R. Yang, *et al.*, „Quasi-ballistic thermal transport from nanoscale interfaces observed using ultrafast coherent soft x-ray beams“, *Nature Materials*, vol. 9, no. 1, pp. 26–30, 2009.
- [3] J. A. Tomko, A. Pena-Francesch, H. Jung, *et al.*, „Tunable thermal transport and reversible thermal conductivity switching in topologically networked bio-inspired materials“, *Nature Nanotechnology*, vol. 13, no. 10, pp. 959–964, 2018.

- [4] M. D. Losego, M. E. Grady, N. R. Sottos, D. G. Cahill, and P. V. Braun, „Effects of chemical bonding on heat transport across interfaces“, *Nature Materials*, vol. 11, no. 6, pp. 502–506, 2012.
- [5] G.-H. Kim, D. Lee, A. Shanker, *et al.*, „High thermal conductivity in amorphous polymer blends by engineered interchain interactions“, *Nature Materials*, vol. 14, no. 3, pp. 295–300, 2014.
- [6] S. Shen, A. Henry, J. Tong, R. Zheng, and G. Chen, „Polyethylene nanofibres with very high thermal conductivities“, *Nature Nanotechnology*, vol. 5, no. 4, pp. 251–255, 2010.
- [7] X. Huang, G. Liu, and X. Wang, „New secrets of spider silk: Exceptionally high thermal conductivity and its abnormal change under stretching“, *Advanced Materials*, vol. 24, no. 11, pp. 1482–1486, 2012.
- [8] R. Fuente, A. Mendioroz, and A. Salazar, „Revising the exceptionally high thermal diffusivity of spider silk“, *Materials Letters*, vol. 114, pp. 1–3, 2014.
- [9] C. Chiritescu, D. G. Cahill, N. Nguyen, *et al.*, „Ultralow thermal conductivity in disordered, layered WSe₂ crystals“, *Science*, vol. 315, no. 5810, pp. 351–353, 2007.
- [10] M. D. Losego, I. P. Blitz, R. A. Vaia, D. G. Cahill, and P. V. Braun, „Ultralow thermal conductivity in organoclay nanolaminates synthesized via simple self-assembly“, *Nano Letters*, vol. 13, no. 5, pp. 2215–2219, 2013.
- [11] B. Wicklein, A. Kocjan, G. Salazar-Alvarez, *et al.*, „Thermally insulating and fire-retardant lightweight anisotropic foams based on nanocellulose and graphene oxide“, *Nature Nanotechnology*, vol. 10, no. 3, pp. 277–283, 2014.
- [12] T. Li, J. Song, X. Zhao, *et al.*, „Anisotropic, lightweight, strong, and super thermally insulating nanowood with naturally aligned nanocellulose“, *Science Advances*, vol. 4, no. 3, eaar3724, 2018.
- [13] M. Chau, B. A. F. Kopera, V. R. Machado, *et al.*, „Reversible transition between isotropic and anisotropic thermal transport in elastic polyurethane foams“, *Materials Horizons*, vol. 4, no. 2, pp. 236–241, 2017.
- [14] J. Xiao, Q. Kuang, S. Yang, *et al.*, „Surface structure dependent electrocatalytic activity of CO₃O₄ anchored on graphene sheets toward oxygen reduction reaction“, *Scientific Reports*, vol. 3, no. 1, 2013.
- [15] N. Song, D. Jiao, S. Cui, *et al.*, „Highly anisotropic thermal conductivity of layer-by-layer assembled nanofibrillated cellulose/graphene nanosheets hybrid films for thermal management“, *ACS Applied Materials & Interfaces*, vol. 9, no. 3, pp. 2924–2932, 2017.
- [16] A. Eckert, T. Rudolph, J. Guo, T. Mang, and A. Walther, „Exceptionally ductile and tough biomimetic artificial nacre with gas barrier function“, *Advanced Materials*, vol. 30, no. 32, p. 1802477, 2018.

- [17] T. Verho, M. Karesoja, P. Das, *et al.*, „Hydration and dynamic state of nanoconfined polymer layers govern toughness in nacre-mimetic nanocomposites“, *Advanced Materials*, vol. 25, no. 36, pp. 5055–5059, 2013.
- [18] T. Szabó, M. Szekeres, I. Dékány, *et al.*, „Layer-by-layer construction of ultrathin hybrid films with proteins and clay minerals“, *The Journal of Physical Chemistry C*, vol. 111, no. 34, pp. 12 730–12 740, 2007.
- [19] Z. Tang, N. A. Kotov, S. Magonov, and B. Ozturk, „Nanostructured artificial nacre“, *Nature Materials*, vol. 2, no. 6, pp. 413–418, 2003.
- [20] T. Still, *High Frequency Acoustics in Colloid-Based Meso- and Nanostructures by Spontaneous Brillouin Light Scattering*. Springer Berlin Heidelberg, 2010.
- [21] E. Alonso-Redondo, M. Schmitt, Z. Urbach, *et al.*, „A new class of tunable hypersonic phononic crystals based on polymer-tethered colloids“, *Nature Communications*, vol. 6, no. 1, 2015.
- [22] V. Singh, T. L. Bougher, A. Weathers, *et al.*, „High thermal conductivity of chain-oriented amorphous polythiophene“, *Nature Nanotechnology*, vol. 9, no. 5, pp. 384–390, 2014.
- [23] A. Mendioroz, R. Fuente-Dacal, E. Apiñaniz, and A. Salazar, „Thermal diffusivity measurements of thin plates and filaments using lock-in thermography“, *Review of Scientific Instruments*, vol. 80, no. 7, p. 074 904, 2009.
- [24] L. Wang and T. Sasaki, „Titanium oxide nanosheets: Graphene analogues with versatile functionalities“, *Chemical Reviews*, vol. 114, no. 19, pp. 9455–9486, 2014.
- [25] P. Davidson, C. Penisson, D. Constantin, and J.-C. P. Gabriel, „Isotropic, nematic, and lamellar phases in colloidal suspensions of nanosheets“, *Proceedings of the National Academy of Sciences*, vol. 115, no. 26, pp. 6662–6667, 2018.
- [26] A. Lerf, „Storylines in intercalation chemistry“, *Dalton Trans.*, vol. 43, no. 27, pp. 10 276–10 291, 2014.
- [27] V. Nicolosi, M. Chhowalla, M. G. Kanatzidis, M. S. Strano, and J. N. Coleman, „Liquid exfoliation of layered materials“, *Science*, vol. 340, no. 6139, pp. 1 226 419–1 226 419, 2013.
- [28] M. Daab, N. J. Eichstaedt, A. Edenharter, S. Rosenfeldt, and J. Brey, „Layer charge robust delamination of organo-clays“, *RSC Advances*, vol. 8, no. 50, pp. 28 797–28 803, 2018.
- [29] J. E. F. C. Gardolinski and G. Lagaly, „Grafted organic derivatives of kaolinite: II. intercalation of primary n-alkylamines and delamination“, *Clay Minerals*, vol. 40, no. 4, pp. 547–556, 2005.

- [30] M. Stöter, D. A. Kunz, M. Schmidt, *et al.*, „Nanoplatelets of sodium hectorite showing aspect ratios of 20000 and superior purity“, *Langmuir*, vol. 29, no. 4, pp. 1280–1285, 2013.
- [31] S. Rosenfeldt, M. Stöter, M. Schlenk, *et al.*, „In-depth insights into the key steps of delamination of charged 2d nanomaterials“, *Langmuir*, vol. 32, no. 41, pp. 10 582–10 588, 2016.
- [32] K. Sano, Y. S. Kim, Y. Ishida, *et al.*, „Photonic water dynamically responsive to external stimuli“, *Nature Communications*, vol. 7, no. 1, 2016.
- [33] H. Kalo, W. Milius, and J. Breu, „Single crystal structure refinement of one- and two-layer hydrates of sodium fluorohectorite“, *RSC Advances*, vol. 2, no. 22, p. 8452, 2012.
- [34] D. A. Kunz, J. Erath, D. Kluge, *et al.*, „In-plane modulus of singular 2:1 clay lamellae applying a simple wrinkling technique“, *ACS Applied Materials & Interfaces*, vol. 5, no. 12, pp. 5851–5855, 2013.
- [35] M. Wong, R. Ishige, K. L. White, *et al.*, „Large-scale self-assembled zirconium phosphate smectic layers via a simple spray-coating process“, *Nature Communications*, vol. 5, no. 1, 2014.
- [36] W. Seidl and J. Breu, „Single crystal structure refinement of tetramethyl ammonium-hectorite“, *Zeitschrift für Kristallographie - Crystalline Materials*, vol. 220, no. 2/3, 2005.
- [37] A. Baumgartner, K. Sattler, J. Thun, and J. Breu, „A route to microporous materials through oxidative pillaring of micas“, *Angewandte Chemie International Edition*, vol. 47, no. 9, pp. 1640–1644, 2008.
- [38] N. L. McFarlane, N. J. Wagner, E. W. Kaler, and M. L. Lynch, „Poly(ethylene oxide) (PEO) and poly(vinyl pyrrolidone) (PVP) induce different changes in the colloid stability of nanoparticles“, *Langmuir*, vol. 26, no. 17, pp. 13 823–13 830, 2010.
- [39] E. S. Tsurko, P. Feicht, F. Nehm, *et al.*, „Large scale self-assembly of smectic nanocomposite films by doctor blading versus spray coating: Impact of crystal quality on barrier properties“, *Macromolecules*, vol. 50, no. 11, pp. 4344–4350, 2017.
- [40] D. M. Moore and R. C. Reynolds, *X-ray Diffraction and the Identification and Analysis of Clay Minerals*, Second. New York: Oxford University Press, 1997.
- [41] A. Philipp, N. W. Pech-May, B. A. F. Kopera, *et al.*, „Direct measurement of the in-plane thermal diffusivity of semitransparent thin films by lock-in thermography: An extension of the slopes method“, *Analytical Chemistry*, vol. 91, no. 13, pp. 8476–8483, 2019.

- [42] C. Clauser and E. Huenges, *Thermal Conductivity of Rocks and Minerals*. American Geophysical Union, 2013, pp. 105–126.
- [43] J. K. Carson, S. J. Lovatt, D. J. Tanner, and A. C. Cleland, „Thermal conductivity bounds for isotropic, porous materials“, *International Journal of Heat and Mass Transfer*, vol. 48, no. 11, pp. 2150–2158, 2005.
- [44] Y.-F. Huang, Z.-G. Wang, H.-M. Yin, *et al.*, „Highly anisotropic, thermally conductive, and mechanically strong polymer composites with nacre-like structure for thermal management applications“, *ACS Applied Nano Materials*, vol. 1, no. 7, pp. 3312–3320, 2018.
- [45] L. P. Tremblay, M. B. Johnson, U. Werner-Zwanziger, and M. A. White, „Relationship between thermal conductivity and structure of nacre from *haliotis fulgens*“, *Journal of Materials Research*, vol. 26, no. 10, pp. 1216–1224, 2011.
- [46] R. W. Gammon, „Brillouin scattering experiments in the ferroelectric crystal triglycine sulfate“, PhD thesis, John Hopkins University, 1967.
- [47] L. E. McNeil and M. Grimsditch, „Elastic moduli of muscovite mica“, *Journal of Physics: Condensed Matter*, vol. 5, no. 11, pp. 1681–1690, 1993.
- [48] J. Krüger, L. Peetz, and M. Pietralla, „Brillouin scattering of semicrystalline poly(4-methyl-1-pentene): Study of surface effects of bulk and film material“, *Polymer*, vol. 19, no. 12, pp. 1397–1404, 1978.
- [49] S. P. Cheadle, R. J. Brown, and D. C. Lawton, „Orthorhombic anisotropy: A physical seismic modeling study“, *Geophysics*, vol. 56, no. 10, pp. 1603–1613, 1991.
- [50] M. Mah and D. R. Schmitt, „Experimental determination of the elastic coefficients of an orthorhombic material“, *Geophysics*, vol. 66, no. 4, pp. 1217–1225, 2001.
- [51] S. Cusack and A. Miller, „Determination of the elastic constants of collagen by brillouin light scattering“, *Journal of Molecular Biology*, vol. 135, no. 1, pp. 39–51, 1979.
- [52] Y. C. Chu and S. I. Rokhlin, „Comparative analysis of through-transmission ultrasonic bulk wave methods for phase velocity measurements in anisotropic materials“, *The Journal of the Acoustical Society of America*, vol. 95, no. 6, pp. 3204–3212, 1994.
- [53] M. Zgonik, P. Bernasconi, M. Duelli, *et al.*, „Dielectric, elastic, piezoelectric, electro-optic, and elasto-optic tensors of batio crystals“, *Physical Review B*, vol. 50, no. 9, p. 5941, 1994.
- [54] J. Midya, Y. Cang, S. A. Egorov, *et al.*, „Disentangling the role of chain conformation on the mechanics of polymer tethered particle materials“, *Nano Letters*, vol. 19, no. 4, pp. 2715–2722, 2019.

- [55] G. A. Elbaz, W.-L. Ong, E. A. Doud, *et al.*, „Phonon speed, not scattering, differentiates thermal transport in lead halide perovskites“, *Nano Letters*, vol. 17, no. 9, pp. 5734–5739, 2017.
- [56] A. S. Henry and G. Chen, „Spectral phonon transport properties of silicon based on molecular dynamics simulations and lattice dynamics“, *Journal of Computational and Theoretical Nanoscience*, vol. 5, no. 2, pp. 141–152, 2008.
- [57] W.-L. Ong, S. M. Rupich, D. V. Talapin, A. J. H. McGaughey, and J. A. Malen, „Surface chemistry mediates thermal transport in three-dimensional nanocrystal arrays“, *Nature Materials*, vol. 12, no. 5, pp. 410–415, 2013.

10.7 Supporting Information

10.7.1 Sample Preparation

10.7.2 Materials

The synthetic clay sodium fluorohectorite (Hec, $[\text{Na}_{0.5}]^{\text{inter}}[\text{Mg}_{2.5}\text{Li}_{0.5}]^{\text{oct}}[\text{Si}_4]^{\text{tet}}\text{O}_{10}\text{F}_2$) was synthesized via melt synthesis followed by long-term annealing, according to an established procedure. The material featured a cation exchange capacity of 1.27 mmol/g (References^{[1],[2]}). Polyvinylpyrrolidone (PVP; $M_w = 40.000$ g/mol) was provided by Sigma Aldrich.

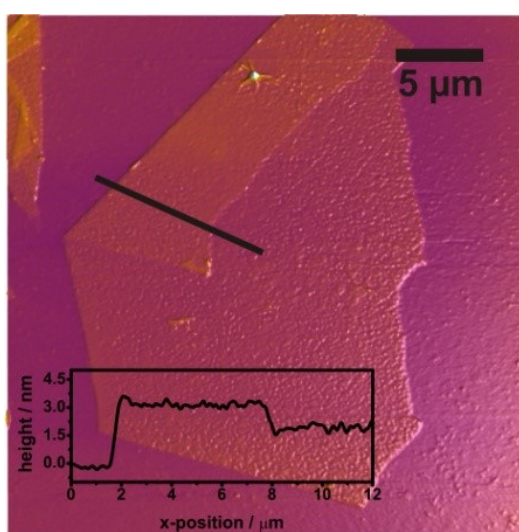


Fig. 10.5: Atomic force microscopy image of a single delaminated Hec nanosheet. Reprinted with permission from Langmuir.^{[1],[2]} Copyright 2019 American Chemical Society.

10.7.3 Film preparation

For the delamination, the synthetic Hec was immersed into Millipore water (0.5 wt%). The complete delamination was studied by small angle X-ray scattering (SAXS). The aqueous PVP solution (1 wt%) was added in the desired weight ratio. The suspension was mixed for at least 1 day in the overhead shaker. Homogeneity of the suspensions was cross-checked by SAXS measurements. All SAXS data were measured using the small-angle X-ray system “Double Ganesha AIR” (SAXSLAB, Denmark). The X-ray source of this laboratory-based system is a rotating anode (copper, MicroMax 007HF, Rigaku Corporation, Japan) providing a micro-focused beam. The data were recorded by a position sensitive detector (PILATUS 300 K, Dectris). To cover the range of scattering vectors between 0.004 - 1.0 \AA^{-1} , different

detector positions were used. The measurements of the suspensions were done in 1 mm glass capillaries (Hilgenberg, code 4007610, Germany) at room temperature. To improve the detection limit of the in-house machine, the suspensions were first concentrated to ≈ 10 wt% by centrifugation at 10 000 rpm for 1 hour. A rational basal series was found for all suspensions, indicating that all clay nanosheets were separated to exactly the same distance by water and PVP (Figure 10.6). Within experimental errors reaggregation to stacks of Hec can be excluded by the absence of a reflection typical for crystalline hydrated Hec phases at $q = 0.65 - 0.41 \text{ \AA}^{-1}$.

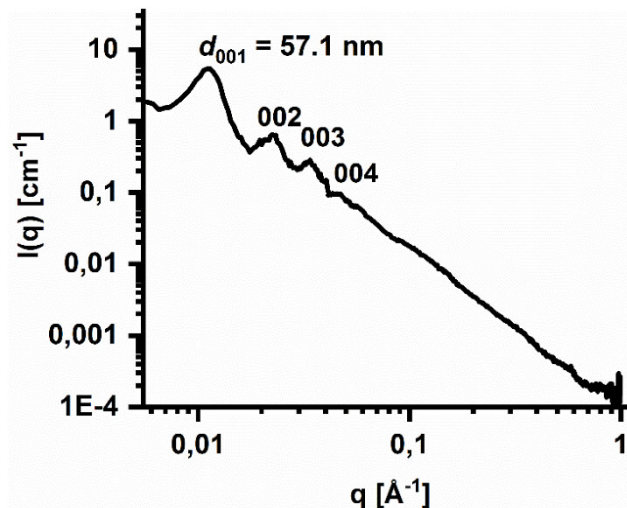


Fig. 10.6: 1D SAXS pattern of the concentrated gel sample Hec40/PVP60.

The self-supporting films were prepared by spray coating. The fully automatic spray coating system was equipped with a SATA 4000 LAB HVLP 1.0 mm spray gun (SATA GmbH & Co. KG, Germany). Suspensions were sprayed on a corona-treated polyethylene terephthalate (PET) foil (optimont 501, bleher Folientechnik, Germany). The spraying and nozzle pressure were set constant at values of 2 and 4 bar, respectively. The round per flat fan control was set to 6 with a flow speed of 3 mL/s. The distance between the spraying gun and the substrate was 17 cm. The thickness of the suspension layer applied in one spraying step is $\approx 2 \mu\text{m}$ which corresponds to ≈ 20 nm dry nanocomposite film thickness. For drying the suspension layer, the sample is stopped under infrared lamps until evaporation of the solvent is complete. After every spraying cycle, a drying cycle of 90 s with a temperature of $55 \text{ }^\circ\text{C}$ took place. The spraying/drying cycle is repeated until the desired barrier film thickness of $50 \mu\text{m}$ is obtained. Afterwards, the film was dried at $100 \text{ }^\circ\text{C}$ for 3 days and peeled off from the PET foil to achieve self-supporting films. For characterization by photoacoustic analysis thinner films on the order of a few μm were spray coated onto clean 1 mm thick microscopy glass slides. In total, we prepared six samples, which are denoted as Hec0/PVP100, Hec23/PVP77, Hec31/PVP69, Hec40/PVP60, Hec51/PVP49, and Hec100/PVP0, respectively (Table 10.1). Throughout the

manuscript, all samples are referred to by the nominal volume fractions (vol%) of Hec and PVP, respectively. To rule out compositional changes during spray coating, these ratios were cross-checked (Table 10.1) by thermogravimetric analysis (TGA), using a Linseis STA PT 1600 (Linseis Messgeräte GmbH, Germany). Changes in mass observed upon heating in synthetic air up to 800 °C were attributed to the combustion of PVP.

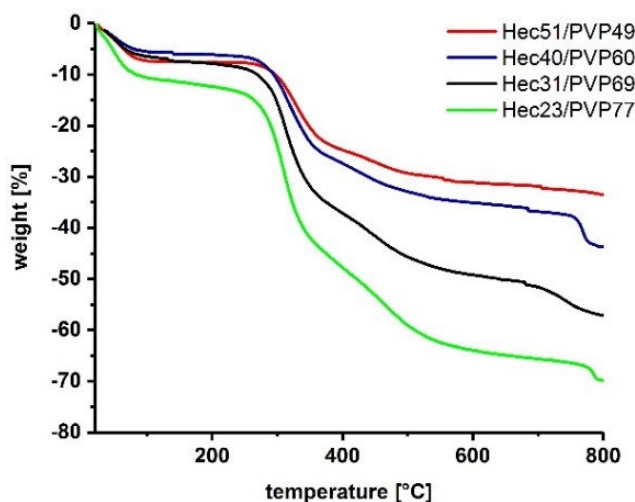


Fig. 10.7: TGA curves of four hybrid Bragg stacks. The weight loss below 200 °C corresponds to the water.

X-ray diffraction (XRD) patterns for the films were recorded in Bragg-Brentano-geometry on an Empyrean diffractometer (PANalytical B.V.; the Netherlands) using Cu K_{α} radiation ($\lambda = 1.54187 \text{ \AA}$). The self-supporting films were placed on glass slides (Menzel-Gläser; Thermo Scientific). Prior to the XRD measurements, the samples were dried at 100 °C in a vacuum chamber for one week.

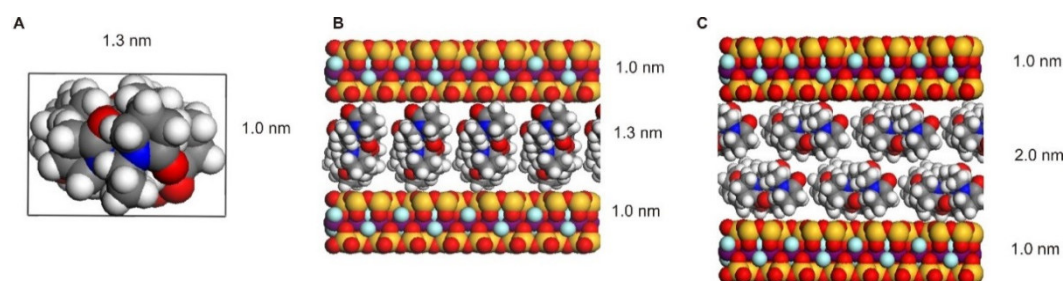


Fig. 10.8: Space filling models. (A) PVP viewed along the polymer backbone chain. (B) Monolayer of PVP oriented with the longer principal axis perpendicular to the Hec nanosheet. (C) Bilayer of PVP lying in the plane of the Hec nanosheets.

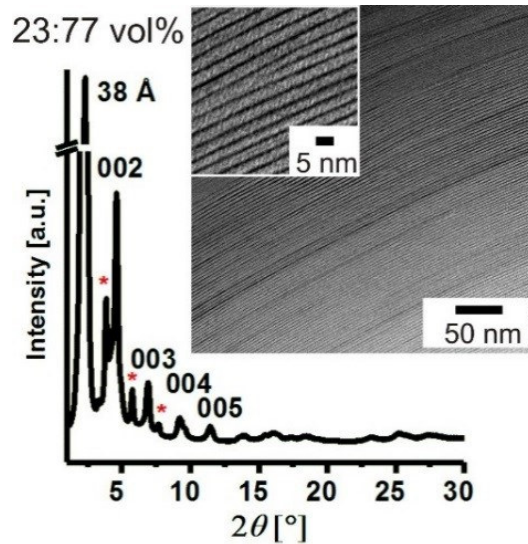


Fig. 10.9: XRD pattern and TEM image of the nanocomposite film Hec23/PVP77. The red asterisks denote a second series of basal reflections of a minority phase ($d = 2.3$ nm).

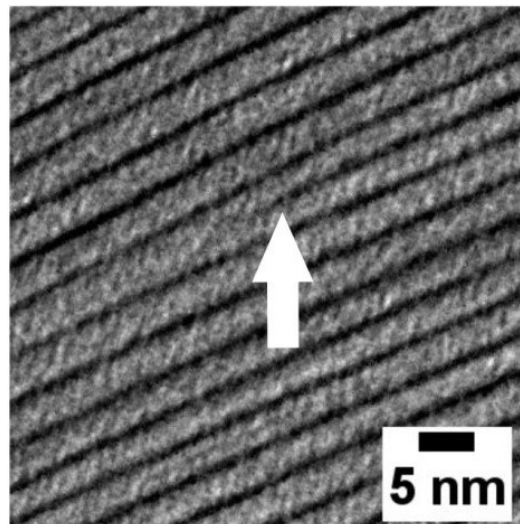


Fig. 10.10: Lattice plane termination of a single Hec nanosheet.

As a measure of the quality of the one-dimensional crystallinity of the films, the coefficient of variation (CV) and the full width at half maximum (FWHM) were determined (Table 10.1). Large CV-values ($\approx 3\%$ ^[3]) and large FWHM indicate non-rationality of the diffraction pattern as caused by a random interstratification of different interlayer heights. Assuming PVP and Hec densities of 1.2 g/cm and 2.7 g/cm, respectively, nominal d-spacings can be calculated for the various volume ratios (d_{nominal} in Table 10.1).^[4] They agree reasonably with those obtained from XRD measurements (d_{XRD} in Table 10.1). In analyzing the cross-plane thermal conductivity using the series resistance model, we used the d_{XRD} values.

Tab. 10.1: Overview of the structural and chemical characterization.

	nominal Hec:PVP ratio [wt%]	nominal Hec:PVP ratio [vol%]	PVP content [a] [wt%]	PVP content [b][vol%]	d_{nominal} [Å]
Hec100/PVP0	100:0	100:0	-	-	10
Hec51/PVP49	70:30	51:49	27	45	18
Hec40/PVP60	60:40	40:60	38	58	23
Hec31/PVP69	50:50	31:69	49	68	30
Hec23/PVP77	40:60	23:77	59	76	41
Hec0/PVP100	0:100	0:100	100	100	-
	d_{XRD} [Å]	gallery height (PVP) [c][nm]	CV [%]	FWHM [°2θ]	
Hec100/PVP0	10	-	-	-	
Hec51/PVP49	19	0.9	5.9	0.4	
Hec40/PVP60	23	1.3	1.3	0.3	
Hec31/PVP69	30	2.0	1.0	0.3	
Hec23/PVP77	38	2.8	2.8	0.3	
Hec0/PVP100	-	-	-	-	

^a determined by TGA

^b calculated with the PVP content determined by TGA

^c gallery height corresponds to the d-spacing minus the Hec platelet height of 1 nm

Scanning electron microscopy (SEM) images were taken with a Zeiss LEO 1530 (Carl Zeiss AG, Germany) at an operating voltage of 3 kV. Cross sections were prepared by cutting with a razor blade. The samples with Hec were sputtered with 10 nm carbon.

Transmission electron microscopy (TEM) images were taken on a JEOL JEM-2200FS (JEOL GmbH, Germany) at an acceleration voltage of 200 kV. Cross-section pictures of the self-supporting films were prepared with a Cryo Ion Slicer IB-09060CIS (JEOL, Germany).

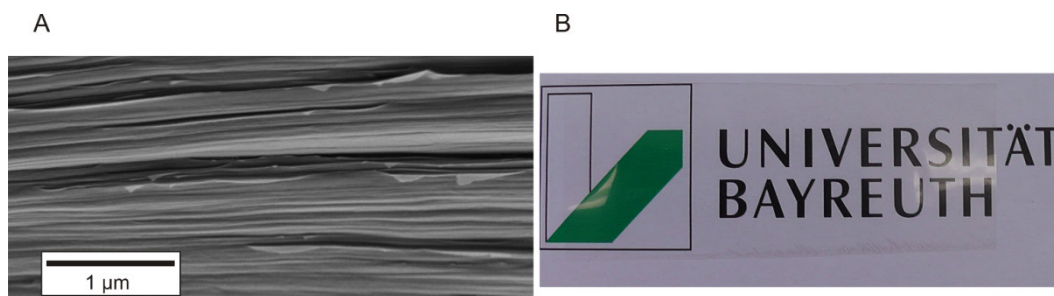


Fig. 10.11: SEM image and photograph of the hybrid film. A) The SEM image displays the ordered arrangement of hectorite sheets at the macro-scale. B) As the hectorite platelets arrange highly ordered, light scattering is prevented and the films is transparent.

10.7.4 Thermal measurements

For the determination of the in-plane and cross-plane thermal conductivity, the density and the specific heat are needed. Therefore, Helium pycnometry and differential scanning calorimetry (DSC) were used. We determined the in-plane thermal diffusivity by lock-in thermography, and the cross-plane thermal conductivity by the photoacoustic method. Prior to the measurements, the samples were dried at 100 °C in a vacuum chamber for one week.

10.7.5 Helium pycnometry

The density of the samples was measured by helium pycnometry. Therefore, an Ultrapyc 1200e (Quantachrome Instruments) was used. Prior to each measurement the volume of the empty measurement cell was measured. Afterwards, small pieces of the freestanding films were weighed into the sample cell with a nominal volume of 1.8 cm³. One hundred runs were performed to determine the volume of the films at room temperature. By knowing the mass (measured on a fine balance) and the volume, the density of the samples was calculated.

10.7.6 Differential scanning calorimetry

The specific heat was determined by DSC measurements according to the ASTM E1269 standard. The samples were freeze ground for better processability and contact to the DSC pans. The measurements were performed on a TA instruments Discovery DSC 2500. An isothermal step (1 h, 100 °C) was conducted prior to the measurement to ensure dry conditions. Then two heating cycles were used and only the second cycle evaluated. The temperature profile ranged from -40 to 250 °C using a heating rate of 20 K/min with a nitrogen flow of 50 mL/min.

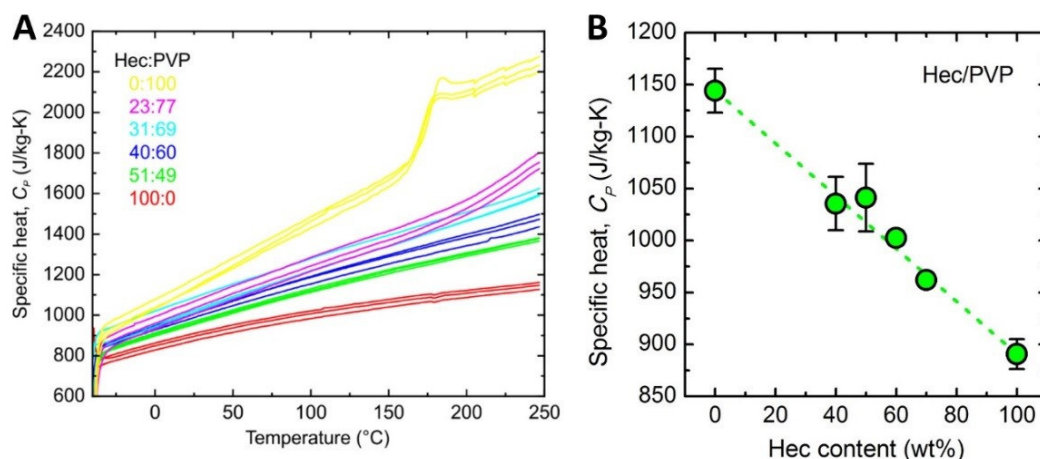


Fig. 10.12: Temperature and composition dependencies of the specific heat. (A) Three samples per Hec/PVP composition were measured. The average specific heat at 25 °C was used to calculate the thermal conductivity. (B) The green dashed line shows the prediction by a simple mixing model, $C_p(x) = (1-x)C_p(0\%) + xC_p(100\%)$, with x being the hectorite weight fraction

10.7.7 Lock-in thermography

The in-plane thermal diffusivity of free-standing Hec/PVP stack films was obtained by lock-in thermography (LIT). The self-built LIT set-up is shown in Figure 10.13.

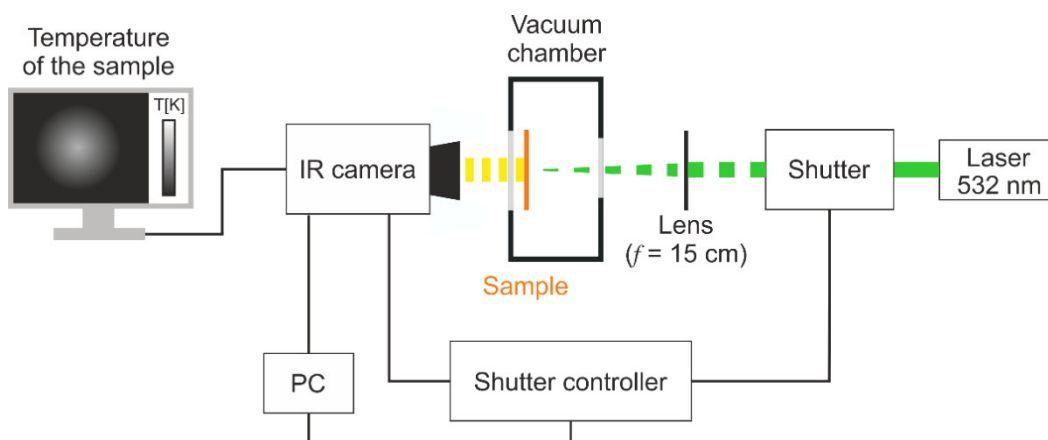


Fig. 10.13: Scheme of the lock-in thermography set-up. The samples were measured in a vacuum chamber to avoid convective heat losses to the environment.

The sample is heated by a laser beam (Genesis MX 532-1000 SLM OPS, Coherent, $\lambda = 532$ nm) focused onto the sample surface by a lens of 150 mm focal length. The intensity of the laser is modulated using a shutter (SH05/M, Thorlabs) controlled by a shutter controller (SC10, Thorlabs). The emitted infrared (IR) radiation of the sample surface is detected by an Infratec VarioCAM HD research IR camera (spectral window: 7.5-14 μm). The camera is equipped with a close-up lens. In this

configuration, the minimum spatial resolution is $29\ \mu\text{m}$ (working distance: $33\ \text{mm}$). Since heat losses to the environment lead to an overestimation of the thermal diffusivity^{[5],[6]} all samples were measured under vacuum conditions ($\approx 3 \times 10^{-3}$ mbar). Furthermore, all samples were coated with a $20\ \text{nm}$ carbon layer for enhanced laser absorption. The coating of the sample was facing to the IR camera. LIT measurements were performed using Infratec's IRBISactiveonline software. Measurements were conducted at several lock-in frequencies between 0.219 and $1.765\ \text{Hz}$ (depending on the Hec/PVP composition). Furthermore, each measurement was averaged over several (600-2000) lock-in periods to enhance the signal to noise ratio, with the first 60-100 periods being discarded. The software calculates automatically the amplitude and phase of the temperature oscillations (Figure 10.14). The red point marks the midpoint of the laser excitation and thus the midpoint of the radial distribution.

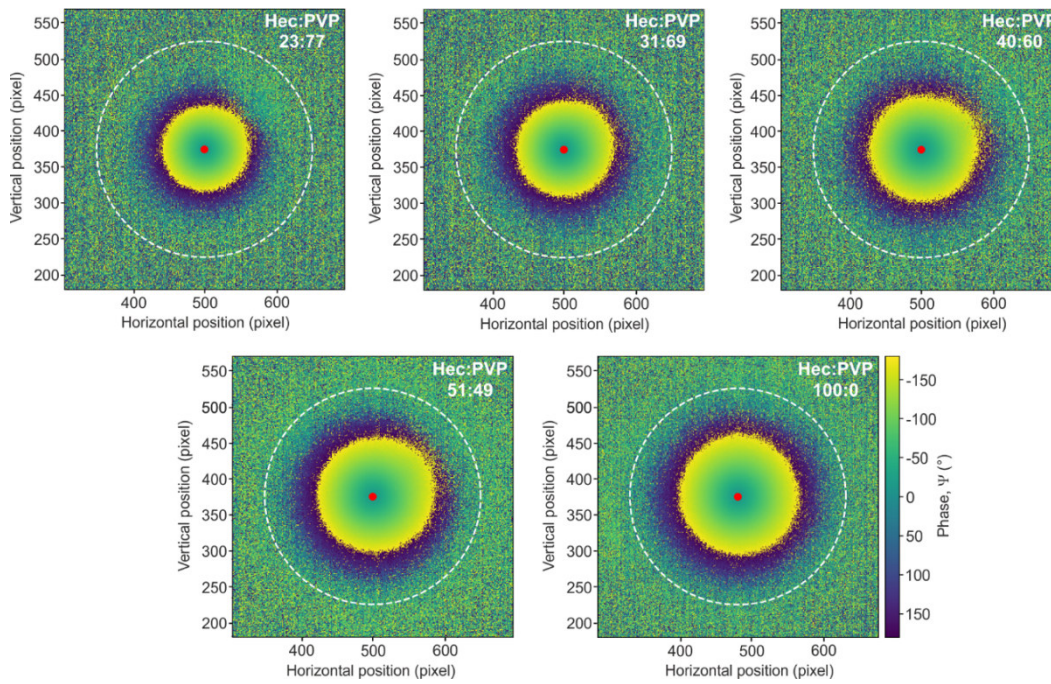


Fig. 10.14: Exemplary two-dimensional phase images measured at a frequency of $1.111\ \text{Hz}$. The penetration depth of the temperature oscillations increases with increasing thermal diffusivity of the Hec/PVP films. The focal point of the laser is marked by a red point in the center of the IR image

A self-written Python script is used to extract radial profiles for the phase and amplitude images (Figure 10.15). The thermal diffusivity is calculated from the phase and amplitude slopes according to the slope method of a thermally thin film:^[6]

$$m_{\Psi} \cdot m_{\ln(T \cdot \sqrt{r})} = \frac{\pi f_{\text{lock-in}}}{\alpha_{\parallel}} \quad (10.1)$$

Here, m_{Ψ} , is the slope of the linear relation of the phase and the radial distance, r , $m_{\ln(T \cdot \sqrt{r})}$ is the slope of the linear relation of the natural logarithm of the

amplitude T multiplied by the square root of the radial distance r , flock-in is the lock-in frequency, and α_{\parallel} is the in-plane thermal diffusivity. Three films have been measured for each Hec/PVP composition. An average in-plane thermal diffusivity and a standard deviation were calculated for each composition, as summarized in Table 10.2.

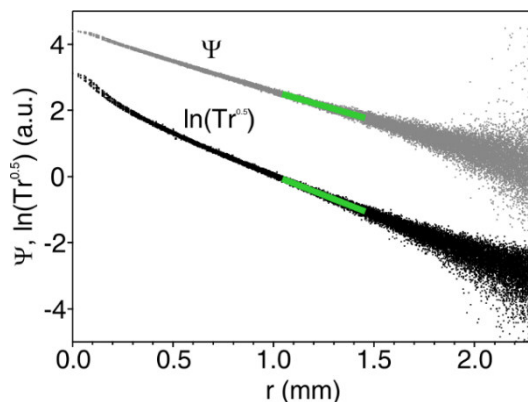


Fig. 10.15: Exemplary phase Ψ and amplitude profiles. The green line indicates the region, where the linear fit was evaluated. This is sufficiently far away from the central excitation spot.

Tab. 10.2: In-plane thermal diffusivity values of Hec/PVP stack films. Three films per Hec/PVP composition were measured, based on which an average in-plane thermal diffusivity and a standard deviation were calculated

Sample	In-plane thermal diffusivity (mm^2s^{-1})
Hec23/PVP77	1.02 ± 0.04
Hec31/PVP69	1.28 ± 0.02
Hec40/PVP60	1.52 ± 0.04
Hec51/PVP49	1.69 ± 0.03
Hec100/PVP0	2.35 ± 0.03

The in-plane thermal conductivity was calculated from the in-plane thermal diffusivity (α_{\parallel}), density (ρ), and specific heat (C_p) as

$$k_{\parallel} = \alpha_{\parallel} \cdot \rho \cdot C_p \quad (10.2)$$

10.7.8 Photoacoustic method

The cross-plane thermal conductivity was determined by the photoacoustic method. It uses the photoacoustic effect to determine the thermal properties of a sample. Therefore, a modulated laser beam ($\lambda = 488 \text{ nm}$) periodically heats the sample. For good absorption of the laser energy a thin Au transducer layer ($\approx 150 \text{ nm}$) was

coated on the sample surface. For photoacoustic characterization, the samples were spray-coated on a glass substrate. The layout of the measurement cell above the sample is shown in Figure 10.16A. The gas tight cell is filled with a helium pressure of 20 psi. The microphone (Bruel&Kjaer, 4398-A-011) connected to the cell measures an acoustic wave, which is induced by the periodic heat conduction from the transducer layer surface to the gas phase. As shown in Figure 10.16B, the microphone is linked to a lock-in amplifier with integrated signal generator (Zurich instruments, HF2LI). The signal generator controls the electro-optic modulator (EOM, Conoptics, M25A) and therefore the frequency of the modulated laser beam. The acoustic signal detected by the microphone is then transferred into a phase and amplitude shift in relation to the modulation of the incident laser beam.

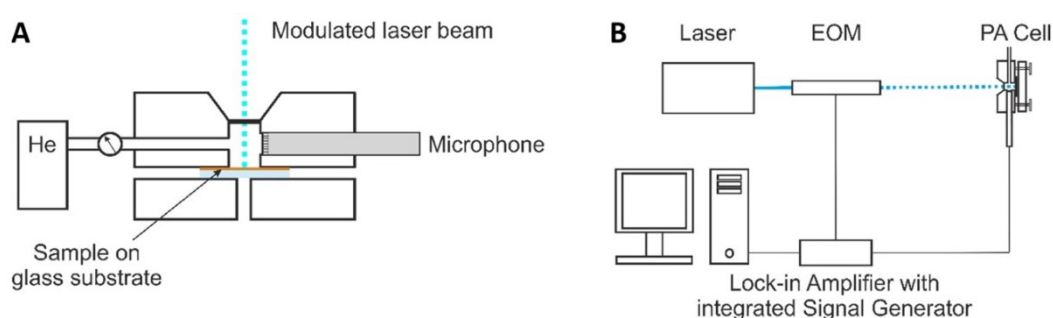


Fig. 10.16: Scheme of photoacoustic measurements. (A) The photoacoustic cell. (B) The whole setup.

The phase shift is detected as a function of the frequency in a range from 110 Hz to 4000 Hz. The signal is then normalized with the phase shift signal of a thermally thick glass sample (1 mm) with known thermal properties. A representative frequency sweep is shown in Figure 10.17. The red line indicates the best fit according to the fitting procedure presented by Singh *et al.*^[7] They used the generalized multilayer model of Hu *et al.*^[8] assuming one-dimensional heat transfer. The unknown fitting parameters are the contact resistance between the gold layer and the sample, the thermal diffusivity of the sample, and the contact resistance between sample and substrate. For thin films the fit is not very sensitive to the individual parameters, but to the total layer resistance. Therefore, only the total layer resistance is reported. From the total layer resistance it is possible to calculate the effective thermal conductivity by dividing with the thickness. The thickness of the samples was determined by AFM measurements. The values of the total layer resistance and sample thickness are summarized in Table 10.3. For each Hec/PVP ratio samples with three different thicknesses were measured to exclude influences from the sample thickness.

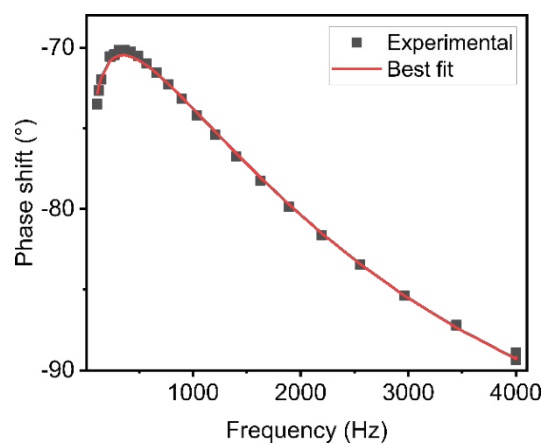


Fig. 10.17: Normalized photoacoustic phase signal. Representative photoacoustic measurement of the Hec31/PVP69 sample with a thickness of 1.979 μm . The red line shows the best fit.

Tab. 10.3: Summary of the photoacoustic measurements. The total layer resistance, the thickness, and the resulting effective cross-plane thermal conductivity are given for each sample.

Sample	Total layer resistance [$\text{mm}^2\text{K}/\text{W}$]	Thickness [μm]	Effective cross-plane thermal conductivity [W/mK]
Hec100/PVP0	1.58	0.28	0.177
Hec100/PVP0	2.55	0.595	0.234
Hec100/PVP0	4.34	0.94	0.217
Hec51/PVP49	3.69	0.255	0.069
Hec51/PVP49	7.74	0.722	0.093
Hec51/PVP49	11.53	0.957	0.083
Hec40/PVP60	6.54	0.463	0.071
Hec40/PVP60	14.03	1.139	0.081
Hec40/PVP60	18.96	1.987	0.105
Hec31/PVP69	8.20	0.744	0.091
Hec31/PVP69	17.58	1.382	0.079
Hec31/PVP69	24.06	1.979	0.082
Hec23/PVP77	8.81	0.568	0.064
Hec23/PVP77	17.45	1.677	0.096
Hec23/PVP77	26.37	2.568	0.097
Hec0/PVP100	2.26	0.351	0.155
Hec0/PVP100	4.50	0.792	0.176

10.7.9 Brillouin light spectroscopy

Brillouin Light Spectroscopy (BLS) measures the phonon dispersion, i.e., the wave vector, q , dependent sound velocity, $\nu_i(q)$, by detecting the Doppler frequency shift, f , in laser light inelastically scattered by sound waves (“phonons”). Since the phonon modes in question are thermally populated, the Bragg condition for light scattering is satisfied independent of the scattering angle, in contrast to the kindred time-domain (“picosecond ultrasonic”) techniques that require external phonon injection via special sample preparation. Since the latter typically involves deposition of non-transparent metallic transducer films, they also do not readily allow for transmission and backscattering measurements, further limiting the potential of these techniques for probing anisotropic materials. Assuming a planar sample, BLS can be conducted in three scattering geometries: transmission, reflection, and backscattering. For angle-dependent measurements in the transmission and reflection geometries, the laser source ($\lambda = 532$ nm) was mounted on a goniometer and rotated around the sample, similar to a wide-angle X-ray (WAXS) setup. For the transmission geometry (top-right inset to Figure 10.3B), the propagation vector, q , of the sound wave lies in the plane of the sample and its modulus, $|q|$, is independent of the refractive index according to $|q|_{\parallel} = \left(\frac{4\pi}{\lambda} \sin(\beta)\right)$, with β being the light incident angle. For the reflection geometry, the Bragg condition is fulfilled for sound waves with q along the normal to the sample plane, so that $|q|_{\perp} = \left(\frac{4\pi}{\lambda} \sqrt{n^2 - \sin^2(\beta)}\right)$ with n being the refractive index of the sample.^[9] In order to find n , several points at different β were acquired, and then fit linearly; n was determined under the constraint that the fit has to pass through the origin (Figure 10.18A), and the obtained values are reported in Table 10.4. In contrast to the transmission geometry, the range of the dispersion relationship that can be scanned by varying $|q|_{\perp}$ is more restricted due to refraction of the laser beam at the air-sample boundary. Finally, backscattering measurements can be conducted, where the incident and scattered light traverse the same path, and the sample is mounted on a rotating stage with angular gradation marks. Only a single dispersion point, corresponding to q directed opposite to k_i in the film and of a magnitude, $|q| = \frac{4\pi n}{\lambda}$ is accessible in the backscattering geometry, but all possible $\frac{q}{|q|}$ directions can be probed.

Because backscattering measurements use the same lens for focusing the incident and collimating scattered light, the alignment of the setup is generally much easier, so that all the backscattering spectra were acquired with microscope objectives (typically 10x) to reduce the spectrum accumulation time. From the given formulas, it is easy to see that the Brillouin frequency shift does not exceed $2\nu/\lambda$, where ν is sound velocity. These frequencies render viscoelasticity effects negligible and are detected using a high-resolution six-pass Tandem Fabry Perot (TFP) interferometer (JRS Instruments, Switzerland) optimized for the 1-50 GHz range. Values still further

out on the dispersion relationship can be accessed using, for example, picosecond ultrasonic interferometry (PUI), but at the expense of great effort and without any gain in information for the problem at hand.^[10] Finally, BLS also offers direct access to the shear moduli, simply by analyzing scattered light in different polarizations: VV (i.e., vertical incident and vertical scattered light) corresponds to quasi-longitudinal and quasi-transverse phonon modes, and VH (i.e., vertical incident and horizontal scattered light) to the pure-transverse phonon mode (for transversely isotropic samples, HV does not show a transverse peak). Before the BLS measurements, the samples were dried at 100 °C in a vacuum chamber for one week to remove any residual water content.

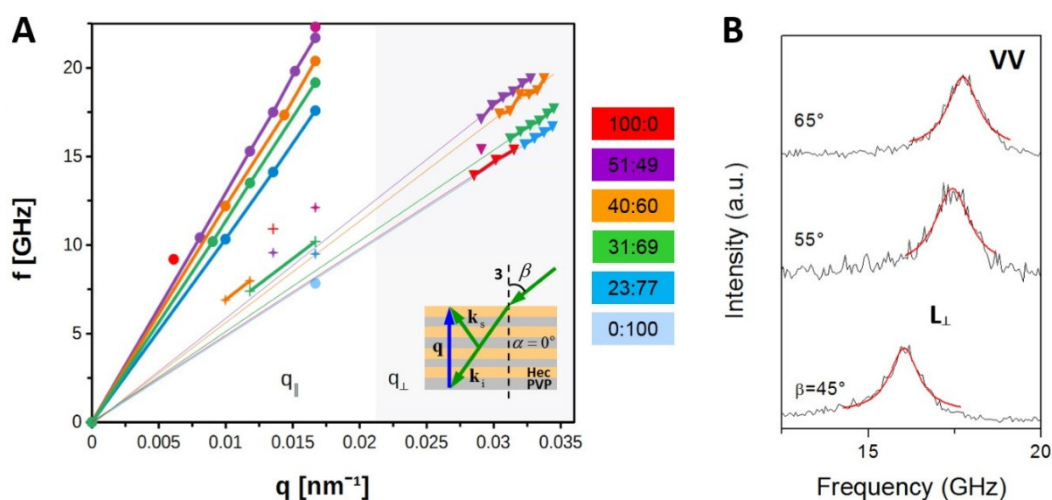


Fig. 10.18: BLS experiments in the reflection geometry. (A) Dispersion (frequency vs. wave vector) of the longitudinal (L) and transverse (T) phonons in the hybrid stacks and the two constituent components (see the color code) obtained from the polarized (VV) and depolarized (VH) BLS spectra recorded in the reflection geometry (inset). (B) Typical VV spectra of the Hec31/PVP69 hybrid film at three laser incident angles.

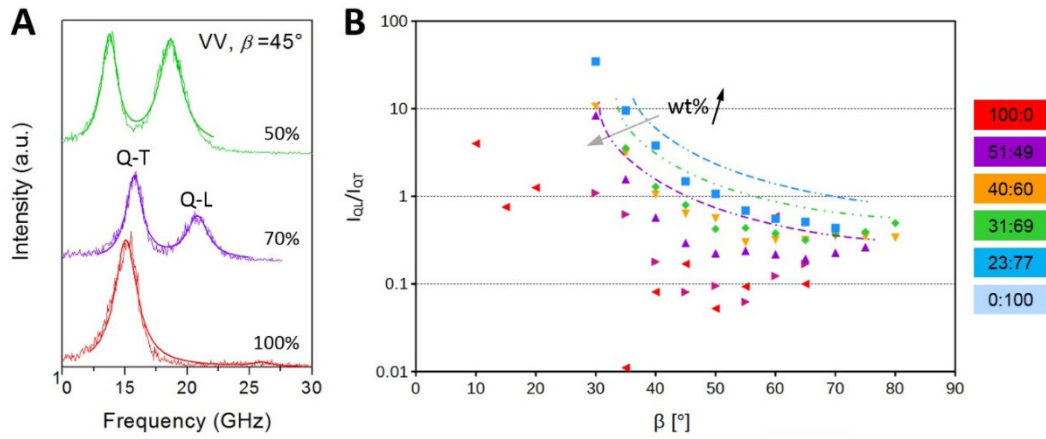


Fig. 10.19: BLS spectra and peak intensity. (A) Polarized (VV) BLS spectra recorded in the backscattering geometry (inset to Figure 10.3A) for two hybrid stacks and the pure Hec film at an incidence angle of 45° . (B) The intensity ratio of the Q-L to Q-T peaks in (A) vs. the laser incident angle.

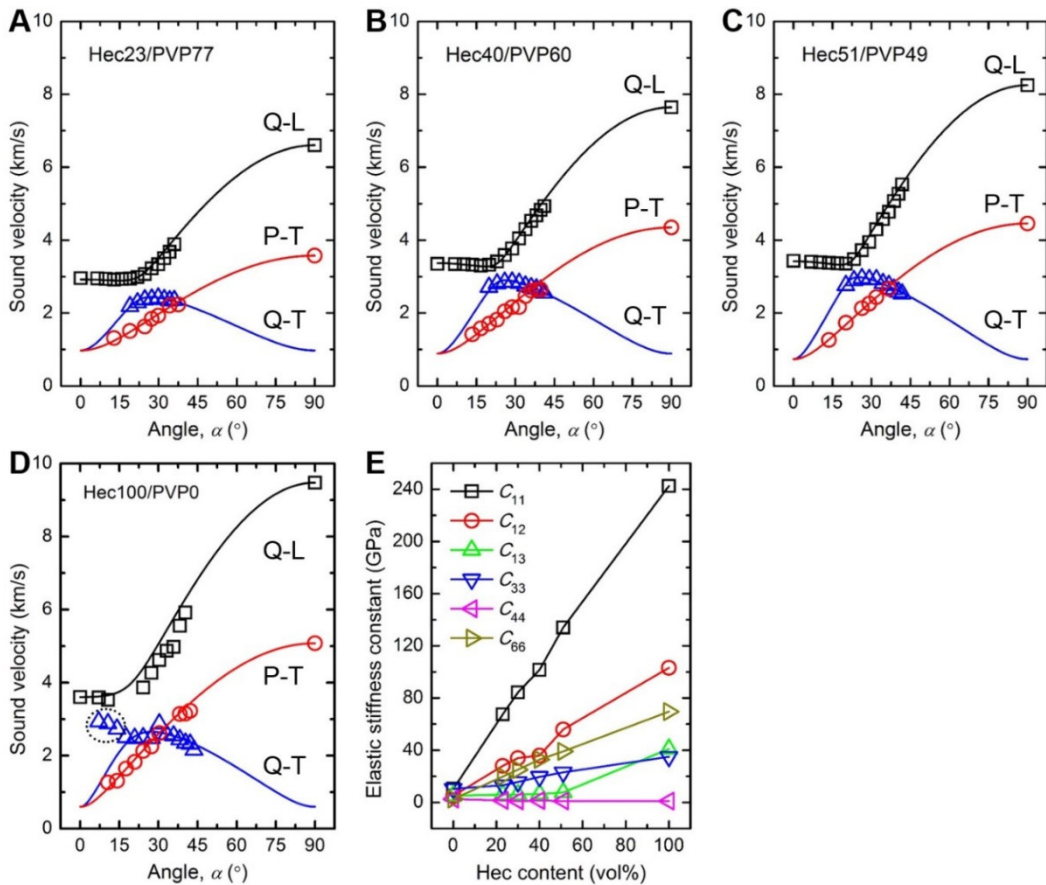


Fig. 10.20: Direction-dependent sound velocities of hybrid stack films. (A) Hec23/PVP77, (B) Hec40/PVP60, (C) Hec51/PVP49, and (D) Hec100/PVP0 (the data points in the dotted circle were not used in the fitting). Q-L, P-T, and Q-T represent the quasi-longitudinal, pure-transverse, and quasi-transverse phonon modes, respectively. (E) Variation of the elastic stiffness constants with the Hec volume fraction.

Based on the BLS-measured direction-dependent sound velocities, we obtained the elastic tensor within the framework of the Christoffel equation.^{[11],[12]}

$$\begin{bmatrix} \Gamma_{11} - \rho\nu^2 & \Gamma_{12} & \Gamma_{13} \\ \Gamma_{21} & \Gamma_{22} - \rho\nu^2 & \Gamma_{23} \\ \Gamma_{31} & \Gamma_{32} & \Gamma_{33} - \rho\nu^2 \end{bmatrix} \begin{bmatrix} u_1 \\ u_2 \\ u_3 \end{bmatrix} = \begin{bmatrix} 0 \\ 0 \\ 0 \end{bmatrix} \quad (10.3)$$

where ρ is the density of the sample, ν is the sound velocity, $\mathbf{u} = [u_1, u_2, u_3]^T$ is the displacement vector, and Γ_{ik} ($i, k = 1, 2, 3$) is the Christoffel stress, which is defined as

$$\Gamma_{ik} = \sum_{j=1}^3 \sum_{l=1}^3 C_{ijkl} n_j n_l. \quad (10.4)$$

Here, C_{ijkl} denotes an element of the 4th rank elastic tensor, and $\mathbf{n} = [n_1, n_2, n_3]^T$ represents the phonon propagation direction. For a transversely isotropic material, the elastic tensor, in the Voigt notation, has the following form.^[13]

$$\mathbf{C} = \begin{bmatrix} C_{11} & C_{12} & C_{13} & & & \\ C_{12} & C_{11} & C_{13} & & & \\ C_{13} & C_{13} & C_{33} & & & \\ & & & C_{44} & & \\ & & & & C_{44} & \\ & & & & & C_{44} = \frac{C_{11} - C_{12}}{2} \end{bmatrix}, \quad (10.5)$$

and contains five independent stiffness constants. After some algebra, the sound velocities of the Q-L, Q-T, and P-T modes along a direction defined by α can be represented as follows,

$$\nu_{\text{Q-L}}(\alpha) = \sqrt{\frac{-A_1 + \sqrt{A_1^2 - 4A_2}}{2\rho}} \quad (10.6)$$

$$\nu_{\text{Q-T}}(\alpha) = \sqrt{\frac{-A_1 - \sqrt{A_1^2 - 4A_2}}{2\rho}} \quad (10.7)$$

$$\nu_{\text{P-T}}(\alpha) = \sqrt{\frac{A_3}{\rho}} \quad (10.8)$$

where,

$$A_1 = -\left(\sin(\alpha C_{11})^2 + \cos(\alpha C_{33})^2 + C_{44}\right) \quad (10.9)$$

$$A_2 = \sin(\alpha C_{11} C_{44})^4 + \sin(\alpha)^2 \cos(\alpha)^2 \left(C_{11} C_{33} - C_{13}^2 - 2C_{13} C_{44}\right) + \cos(\alpha C_{33} C_{44})^4 \quad (10.10)$$

$$A_3 = \sin(\alpha C_{66})^2 + \cos(\alpha C_{44})^2 \quad (10.11)$$

Through nonlinear χ^2 fitting of the BLS-measured sound velocities (i.e., ν vs. α) with Equations (10.6)-(10.8), we obtained the elastic stiffness constants as well as their uncertainties.^[14] The χ^2 is defined as

$$\chi^2 = \sum_i \frac{[\nu_{i,\text{fit}}(C_{11}, C_{12}, C_{13}, C_{33}, C_{33}, \alpha) - \nu_{i,\text{exp}}(\alpha)]^2}{(\Delta\nu_{i,\text{exp}})^2} \quad (10.12)$$

where $\nu_{i,\text{fit}}$ and $\nu_{i,\text{exp}}$ are the fitted and experimental sound velocities, respectively, $\Delta\nu_{i,\text{exp}}$ is the uncertainty of the measured sound velocity, and the summation is over all experimental sound velocities. By considering the uncertainties of the measured angles, refractive indices, and phonon frequencies, we estimated $\nu_{i,\text{exp}}$ to be $0.02 \nu_{i,\text{exp}}$. We imposed the following constraints for the elastic stiffness constants:^[15]

1. $C_{11} > |C_{12}|$
2. $C_{44} > 0$
3. $C_{33}(C_{11} + C_{12}) > 2C_{13}^2$,

which ensure positive Young's and shear moduli. The availability of experimental data for all the Q-L, Q-T, and P-T modes allows unique determination of C_{11} , C_{12} , C_{13} , C_{33} , and C_{44} .

After that, we calculated the engineering mechanical properties,^[13] which include the in-plane Young's modulus (E_{\parallel}), cross-plane Young's modulus (E_{\perp}), sliding shear modulus (G_{13}), torsional shear modulus (G_{12}), and two characteristic Poisson's ratios (ν_{13} and ν_{12}). Note that only five of the engineering mechanical properties are independent (typically, E_{\parallel} , E_{\perp} , G_{13} , G_{12} , and one of ν_{13} and ν_{12} are chosen). Also note that to be consistent with the direction-dependent thermal conductivity results, we used subscripts, “ \parallel ” and “ \perp ”, to represent directions parallel and perpendicular to the sample film, respectively, rather than directions parallel and perpendicular to the “3”-axis (i.e., the symmetry axis), as seen in typical analysis of transversely isotropic materials. The relevant mechanical properties are summarized in Tables 10.4 and 10.5.

Tab. 10.4: Summary of elastic stiffness constants. Composition (Hec vol%, Hec wt%), density (ρ), refractive index (n), and elastic stiffness constants (C_{11} , C_{12} , C_{13} , C_{33} , C_{44} , and C_{66}) of the Hec/PVP hybrid Bragg stack films.

Sample ID	Hec vol%	Hec vw%	ρ (g/cm ³)	n		
Hec0/PVP100	0	0	1.2	1.53*		
Hec23/PVP77	23	40	1.55	1.54		
Hec31/PVP69	31	50	1.62	1.50		
Hec40/PVP60	40	60	1.74	1.47		
Hec51/PVP49	51	70	1.97	1.45		
Hec100/PVP0	100	100	2.70	1.40		

Sample ID	C_{11} (GPa)	C_{12} (GPa)	C_{13} (GPa)	C_{44} (GPa)	C_{44} (GPa)	C_{66} (GPa)
Hec0/PVP100	10.4	5.2	5.2	10.4	2.6	2.6
Hec23/PVP77	67.6±1.7	28.0±1.9	6.0 ± 1.2	13.2±0.3	1.5 ± 0.1	19.8±0.5
Hec31/PVP69	84.3±1.5	34.0±1.8	6.1 ± 1.5	15.7±0.3	1.2 ± 0.2	25.1±0.5
Hec40/PVP60	101.6 ± 1.8	35.9±2.2	6.5 ± 1.8	19.7±0.4	1.4 ± 0.1	32.9±0.6
Hec51/PVP49	134.1 ± 2.2	55.9±2.9	7.7 ± 2.3	23.0±0.5	1.1 ± 0.1	39.1±0.9
Hec100/PVP0	242.5 ± 6.2	103.2 ± 6.7	40.9±5.2	35.0±0.9	1.0 ± 0.1	69.6±1.2

*Source:

<https://refractiveindex.info/?shelf=organic&book=polyvinylpyrrolidone&page=Konig>.

Tab. 10.5: Summary of engineering mechanical properties. Composition (Hec vol%, Hec wt%) and engineering mechanical properties of the Hec/PVP hybrid Bragg stack films. E_{\parallel} : in-plane Young's modulus; E_{\perp} : cross-plane Young's modulus; G_{13} , G_{23} : sliding shear moduli; G_{12} : torsional shear modulus; $\nu_{13}, \nu_{23}, \nu_{12}$: Poisson's ratios (ν_{13} represents the strain response in the j -direction due to a stress in the i -direction).

Sample ID	Hec vol%	Hec vw%	E_{\parallel} (GPa)	E_{\perp} (GPa)	$\frac{E_{\parallel}}{E_{\perp}}$
Hec0/PVP100	0	0	7.0	7.0	1
Hec23/PVP77	23	40	55.0 ± 2.5	12.5 ± 0.4	4.4
Hec31/PVP69	31	50	69.7 ± 2.3	15.1 ± 0.4	4.6
Hec40/PVP60	40	60	88.1 ± 2.6	19.1 ± 0.5	4.6
Hec51/PVP49	51	70	109.9 ± 3.5	22.4 ± 0.6	4.9
Hec100/PVP0	100	100	178.9 ± 9.9	25.4 ± 2.6	7.0

Sample ID	$G_{13} = G_{23}$ (GPa)	G_{12} (GPa)	$\nu_{13} = \nu_{23}$	ν_{12}
Hec0/PVP100	2.6	2.6	0.33 (as- sumed)	0.33 (as- sumed)
Hec23/PVP77	1.5 ± 0.1	19.8 ± 0.5	0.06 ± 0.01	0.39 ± 0.03
Hec31/PVP69	1.2 ± 0.2	25.1 ± 0.5	0.05 ± 0.01	0.39 ± 0.2
Hec40/PVP60	1.4 ± 0.1	32.9 ± 0.9	0.05 ± 0.01	0.34 ± 0.02
Hec51/PVP49	1.1 ± 0.1	39.1 ± 0.9	0.04 ± 0.01	0.41 ± 0.02
Hec100/PVP0	1.0 ± 0.1	69.6 ± 1.2	0.12 ± 0.02	0.29 ± 0.06

10.7.10 Evaluation of interfacial thermal conductance

The series resistance model (SRM) shown in Figure 10.4F illustrates a hybrid stack unit cell consisting of one Hec layer and one PVP layer. We describe the corrugation of the Hec nanosheet (Figure 10.1B) by a thermal interface conductance, $G_{\text{Hec/PVP}}$. For the unit cell in Figure 10.4F, the total thermal resistance can be calculated as

$$\frac{d_{\text{XRD}}}{k_{\perp}} = \frac{d_{\text{Hec}}}{k_{\text{Hec}}} + \frac{d_{\text{PVP}}}{k_{\text{PVP}}} + \frac{2}{G_{\text{Hec/PVP}}}, \quad (10.13)$$

where d_{XRD} is the basal spacing as determined by XRD (Table 10.1), is the effective cross-plane thermal conductivity, $d_{\text{Hec}} = 10 \text{ \AA}$, and $d_{\text{PVP}} = d_{\text{XRD}} - d_{\text{Hec}}$. For the thermal conductivity of the two components, we used the following values: $k_{\text{Hec}} = 5.71 \text{ W/mK}$, and $k_{\text{PVP}} = 0.17 \text{ W/mK}$. The Hec/PVP interfacial conductance, $G_{\text{Hec/PVP}}$, is determined by least squares fitting of the experimental k_{\perp} data (red solid line in Figure 10.4C) to be $89 \pm 8 \text{ MW/m}^2\text{K}$, which falls well into the range of interfacial conductance reported for inorganic/organic interfaces.^{[16],[17]} We also

obtained the Hec/Hec interfacial conductance, $G_{\text{Hec/Hec}} = 219 \pm 28 \text{ MW/m}^2\text{K}$, by considering a unit cell consisting of one Hec layer and one Hec/Hec interface i.e.

$$\frac{d_{\text{XRD}}}{k_{\perp}} = \frac{d_{\text{Hec}}}{k_{\text{Hec}}} + \frac{1}{G_{\text{Hec/Hec}}}. \quad (10.14)$$

10.7.11 Uncertainty analysis

The uncertainties (standard deviations) of the data reported in this work were analyzed by taking into account the instrument accuracy, repetitive measurements, and propagation of uncertainties. The sound velocities were estimated to have an error bar of 2%. The uncertainties of the elastic stiffness constants were determined according to Zgonik *et al.*^[14] The uncertainties of the engineering mechanical properties were calculated according to principles of uncertainty propagation. For instance,

$$E_{\perp} = C_{33} - \frac{2C_{13}^2}{C_{11} + C_{12}} \quad (10.15)$$

$$\Delta E_{\perp} = \sqrt{\sum_{ij=11,12,13,33} \left(\frac{\partial E_{\perp}}{\partial C_{ij}} \right)^2 (\Delta C_{ij})^2 + \sum_{ij < kl}^{ij,kl=11,12,13,33} 2 \frac{\partial E_{\perp}}{\partial C_{ij}} \frac{\partial E_{\perp}}{\partial C_{kl}} \Delta C_{ij|kl}} \quad (10.16)$$

where

$$\frac{\partial E_{\perp}}{\partial C_{11}} = \frac{2C_{13}^2}{(C_{11} + C_{12})^2}, \quad (10.17)$$

$$\frac{\partial E_{\perp}}{\partial C_{12}} = \frac{2C_{13}^2}{(C_{11} + C_{12})^2}, \quad (10.18)$$

$$\frac{\partial E_{\perp}}{\partial C_{13}} = -\frac{4C_{13}}{C_{11} + C_{12}}, \quad (10.19)$$

$$\frac{\partial E_{\perp}}{\partial C_{33}} = 1, \quad (10.20)$$

Similar expressions can be derived for the other engineering moduli and the Poisson's ratios. The uncertainties of the thermal measurement results are analyzed in a similar way, i.e., by considering uncertainty propagation. For example,

$$k_{\parallel} = \alpha_{\parallel} \rho C_{\text{P}} \quad (10.21)$$

$$\Delta k_{\parallel} = \sqrt{\left(\frac{\partial k_{\parallel}}{\partial \alpha_{\parallel}} \right)^2 (\Delta \alpha_{\parallel})^2 + \left(\frac{\partial k_{\parallel}}{\partial \rho} \right)^2 (\Delta \rho)^2 + \left(\frac{\partial k_{\parallel}}{\partial C_{\text{P}}} \right)^2 (\Delta C_{\text{P}})^2} \quad (10.22)$$

where

$$\frac{\partial k_{\parallel}}{\partial \alpha_{\parallel}} = \rho C_{\text{P}} \quad (10.23)$$

$$\frac{\partial k_{\parallel}}{\partial \rho} = \alpha_{\parallel} C_{\text{P}} \quad (10.24)$$

$$\frac{\partial k_{\parallel}}{\partial C_{\text{P}}} = \alpha_{\parallel} \rho \quad (10.25)$$

Here we assumed negligible covariance terms. Similar expressions can be derived for k_{\perp} , k_{\parallel}/k_{\perp} , $\bar{\Lambda}$, etc. The uncertainties of the data are reported as error bars in the figures shown in the main text and Supporting Information. For clarity, error bars smaller than the symbol size are not shown.

10.7.12 References

- [1] J. Breu, W. Seidl, A. J. Stoll, K. G. Lange, and T. U. Probst, „Charge homogeneity in synthetic fluorohectorite“, *Chemistry of Materials*, vol. 13, no. 11, pp. 4213–4220, 2001.
- [2] M. Stöter, D. A. Kunz, M. Schmidt, *et al.*, „Nanoplatelets of sodium hectorite showing aspect ratios of 20000 and superior purity“, *Langmuir*, vol. 29, no. 4, pp. 1280–1285, 2013.
- [3] D. M. Moore and R. C. Reynolds, *X-ray Diffraction and the Identification and Analysis of Clay Minerals* -, Second. New York: Oxford University Press, 1997.
- [4] E. S. Tsurko, P. Feicht, F. Nehm, *et al.*, „Large scale self-assembly of smectic nanocomposite films by doctor blading versus spray coating: Impact of crystal quality on barrier properties“, *Macromolecules*, vol. 50, no. 11, pp. 4344–4350, 2017.
- [5] A. Salazar, A. Mendioroz, and R. Fuente, „The strong influence of heat losses on the accurate measurement of thermal diffusivity using lock-in thermography“, *Applied Physics Letters*, vol. 95, no. 12, p. 121 905, 2009.
- [6] A. Mendioroz, R. Fuente-Dacal, E. Apiñaniz, and A. Salazar, „Thermal diffusivity measurements of thin plates and filaments using lock-in thermography“, *Review of Scientific Instruments*, vol. 80, no. 7, p. 074 904, 2009.
- [7] V. Singh, T. L. Bougher, A. Weathers, *et al.*, „High thermal conductivity of chain-oriented amorphous polythiophene“, *Nature Nanotechnology*, vol. 9, no. 5, pp. 384–390, 2014.
- [8] H. Hu, X. Wang, and X. Xu, „Generalized theory of the photoacoustic effect in a multilayer material“, *Journal of Applied Physics*, vol. 86, no. 7, pp. 3953–3958, 1999.

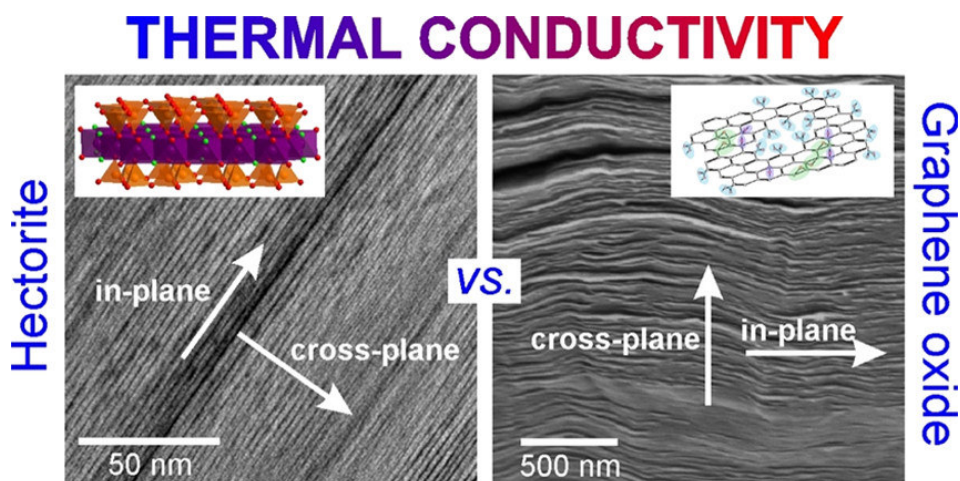
- [9] T. Still, *High Frequency Acoustics in Colloid-Based Meso- and Nanostructures by Spontaneous Brillouin Light Scattering*. Springer Berlin Heidelberg, 2010.
- [10] C. Klieber, *Ultrafast photo-acoustic spectroscopy of super-cooled liquids*. Massachusetts Institute of Technology, 2010.
- [11] S. P. Cheadle, R. J. Brown, and D. C. Lawton, „Orthorhombic anisotropy: A physical seismic modeling study“, *Geophysics*, vol. 56, no. 10, pp. 1603–1613, 1991.
- [12] M. Mah and D. R. Schmitt, „Experimental determination of the elastic coefficients of an orthorhombic material“, *Geophysics*, vol. 66, no. 4, pp. 1217–1225, 2001.
- [13] S. Cusack and A. Miller, „Determination of the elastic constants of collagen by brillouin light scattering“, *Journal of Molecular Biology*, vol. 135, no. 1, pp. 39–51, 1979.
- [14] M. Zgonik, P. Bernasconi, M. Duelli, *et al.*, „Dielectric, elastic, piezoelectric, electro-optic, and elasto-optic tensors of BaTiO₃ crystals“, *Physical Review B*, vol. 50, no. 9, pp. 5941–5949, 1994.
- [15] F. Mouhat and F.-X. Coudert, „Necessary and sufficient elastic stability conditions in various crystal systems“, *Physical Review B*, vol. 90, no. 22, 2014.
- [16] M. D. Losego, M. E. Grady, N. R. Sottos, D. G. Cahill, and P. V. Braun, „Effects of chemical bonding on heat transport across interfaces“, *Nature Materials*, vol. 11, no. 6, pp. 502–506, 2012.
- [17] W.-L. Ong, S. M. Rupich, D. V. Talapin, A. J. H. McGaughey, and J. A. Malen, „Surface chemistry mediates thermal transport in three-dimensional nanocrystal arrays“, *Nature Materials*, vol. 12, no. 5, pp. 410–415, 2013.

Anisotropic Thermal Transport in Spray-Coated Single-Phase Two-Dimensional Materials: Synthetic Clay Versus Graphene Oxide

Alexandra Philipp¹, Patrick Hummel¹, Theresa Schilling¹, Patrick Feicht¹, Sabine Rosenfeldt¹, Michael Ertl¹, Marius Schöttle¹, Anna M. Lechner¹, Zhen Xu², Chao Gao², Josef Breu¹, and Markus Retsch¹

¹ Department of Chemistry and Bavarian Polymer Institute, University of Bayreuth, 95447 Bayreuth, Germany

² Department of Polymer Science and Engineering, Zhejiang University, Hangzhou, Zhejiang 310027, China



Published in *ACS Appl. Mater. Interfaces*, **2020**, DOI: 10.1021/acsami.9b22793
Reprinted with permission from Philipp *et al.*, *ACS Appl. Mater. Interfaces* 2020,
12, 16, 18785–18791. Copyright 2020 American Chemical Society.

11.1 Abstract

Directional control on material properties such as mechanical moduli or thermal conductivity are of paramount importance for the development of nanostructured next-generation devices. Two-dimensional materials are particularly interesting in this context owing to their inherent structural anisotropy. Here, we compare graphene oxide (GO) and synthetic clay sodium fluorohectorite (Hec) with respect to their thermal transport properties. The unique sheet structure of both allows preparation of highly ordered Bragg stacks of these pure materials. The thermal conductivity parallel to the platelets strongly exceeds that perpendicular to them. We find a significant difference in the performance between GO and synthetic clay. Our analysis of the textured structure, size of the platelets, and chemical composition shows that Hec is a superior two-dimensional component to GO. Consequently, synthetic clay is a promising material for thermal management applications in electronic devices where electrically insulating materials are prerequisites.

11.2 Introduction

Modern electronics crucially depend on materials and structures that are capable of dissipating their ever-increasing thermal energy density. Materials with a high thermal conductivity manage to divert heat away from hot spots efficiently. At the same time, the thermal management in the entire device needs to be considered where areas of high and low-temperature tolerance may be located in close vicinity.^[1] Consequently, materials that are capable of directing the flow of heat are required. Two-dimensional (2D) materials with an anisotropic thermal conductivity match this requirement.^[2] Well-known representatives of such materials are graphite^[3] and graphene.^[4] Both exhibit a high in-plane thermal conductivity, while their cross-plane thermal conductivity is much lower. However, they are both also electrically conductive and consequently not suitable in most electronic applications. To prevent shortcuts, the use of nonconductive materials is mandatory. This demand is represented in the field of thermal interface materials.^{[5],[6]} The right selection of the matrix and filler and the processing and structure formation are essential for achieving an optimum performance.^{[7],[8]}

Two materials have been widely used to prepare electrically nonconductive composites with anisotropic thermal conductivity, namely, graphene oxide (GO) and the graphene analog hexagonal boron nitride (hBN). Strong oxidation of graphite allows for the water processability of GO but significantly reduces the in-plane thermal conductivity compared to graphite/graphene. The degree of oxidation relates to the in-plane thermal conductivity.^[9] In most cases, GO is reduced (rGO)

to partially restore the high in-plane thermal conductivity. Concomitantly, the electrical conductivity increases.^{[10]–[13]} Consequently, the anisotropy ratios (i.e., the ratio between in-plane and cross-plane thermal conductivity) in GO-based materials depend on the oxidation state and can reach values of 19 for GO^[9] and up to 675 for rGO.^[10] An additional drawback of this reduction step is the necessity to apply either reducing chemicals (such as hydrazine) or high thermal temperatures, which are needed to be tolerated by the entire device or composite.

The structure and properties of hBN are comparable to those of graphite/graphene. The most significant difference exists in the electrical conductivity. In comparison to graphene, hBN is not electrically conductive. The thermal transport properties, however, are comparable, meaning a high in-plane thermal transport and, therefore, a high anisotropic thermal conductivity. A fundamental study of bulk single-crystalline hBN demonstrated a promising anisotropy ratio of 87.5.^[14] However, the sample was a 1 mm-sized flake, and it is not yet possible to produce large-area samples of single-crystalline hBN. Nevertheless, hBN can be mixed with polymers to achieve composite materials. In contrast to GO, hydrophobic hBN is still challenging to fully exfoliate, especially in water. A simple sonication-assisted hydrolyzation process in water leads only to a mixture of monolayers and multilayers.^[15] Therefore, studies about the anisotropic thermal conductivity of hBN/polymer composites lack structural control and cannot reach the value of the single crystal.^{[16]–[20]} A maximum ratio up to 39 could be realized by stretching the composite, which improves the alignment and therefore demonstrates the difficulty in controlling the composite structure during processing.^[19]

Synthetic clays are less-known materials in the context of thermal interface materials. Nevertheless, this material class offers a range of advantages, particularly regarding the structural control of the assembled composite structure. Due to their superior control over the aspect ratio and the delamination process, highly ordered composites with outstanding mechanical,^{[21]–[23]} gas barrier,^{[24],[25]} and fire resistance^{[22],[23]} properties have already been realized. Additionally, the high phase purity of Hec leads to optically clear and transparent films, which is relevant for optical applications. Furthermore, ultralow cross-plane thermal conductivity was demonstrated in organoclays^[26] and hybrid Bragg stacks.^[27] Although this hints toward the high potential of this material class for high anisotropic thermal conductivity, little is known about the direction-dependent heat spreading in the pure filler components.

Our contribution aims to close this knowledge gap. We focus on pure, single-phase components to elaborate the fundamental filler properties without introducing additional complications originating from filler/matrix interactions. Our study is based on a synthetic clay sodium fluorohectorite of different platelet diameter. For a better classification of this unnoticed material in the context of anisotropic thermal

conductivity, we compare our results to two types of GO samples stemming from different sources.

11.3 Results and Discussion

Our investigation is based on four samples: synthetic sodium fluorohectorite (Hec, $[\text{Na}_{0.5}]^{\text{inter}}[\text{Mg}_{2.5}\text{Li}_{0.5}]^{\text{oct}}[\text{Si}_4]^{\text{tet}}\text{O}_{10}\text{F}_2$) in its native form termed Hec-L, consisting of large platelets (tens of μm in lateral size) and Hec-S, consisting of small platelets (sub- μm) received after sonication of Hec-L. We compare the Hec samples to GO, which was synthesized following a modified Hummers–Offeman procedure^[28] termed GO-syn, and a commercially available GO, termed GO-com. In all samples, we focus on the contribution of the platelet dimension, platelet defect concentration, and chemical composition to the thermal transport anisotropy. All materials were processed by spray coating of a dilute aqueous dispersion (0.5 wt%) onto a substrate (polyethylene terephthalate (PET) film or glass). Thus, the Hec and GO sheets align parallel to the substrate introducing a macroscopic orientation to the individual nanosheets. After drying for 5 h at 100 °C, freestanding samples were obtained by peeling off the films from PET. These films were used to determine the in-plane thermal conductivity by lock-in thermography. The cross-plane thermal conductivity was measured using the photoacoustic method with thin films immobilized on a glass substrate. The obtained thermal conductivity values are summarized in Figure 11.1a. We found comparable in-plane and cross-plane thermal conductivities for Hec-L (in-plane: $5.7 \pm 0.1 \text{ W/mK}$, cross-plane: $0.21 \pm 0.03 \text{ W/mK}$) and for Hec-S (in-plane: $5.6 \pm 0.2 \text{ W/mK}$, cross-plane: $0.18 \pm 0.02 \text{ W/mK}$). Compared to literature values of related structures, the in-plane thermal transport of our pure Hec samples is exceptionally high. Muscovite and biotite single crystals show in-plane thermal conductivities of 3.89 and 3.14 W/mK, respectively.^[29] The montmorillonite sample, which was prepared from a suspension of delaminated platelets, showed an in-plane thermal conductivity of only 1.92 W/mK.^[30] The high in-plane thermal conductivity of pure Hec is very promising in the context of heat spreading, particularly since this high value is obtained without any further processing of the spray-coated film. By contrast, the cross-plane thermal conductivities of muscovite and biotite are 0.62 and 0.52 W/mK, respectively,^[29] and are therefore more than twice as high as in our synthetic Hec samples. The montmorillonite sample, by contrast, has a cross-plane thermal conductivity of 0.2 W/mK,^[30] which is comparable to our samples.

The in-plane and cross-plane thermal conductivities of the as-prepared GO samples are both lower than those of the clay samples. The in-plane values are $1.7 \pm 0.1 \text{ W/mK}$ for GO-syn and $1.0 \pm 0.1 \text{ W/mK}$ for GO-com, while the cross-plane values are 0.12 ± 0.01 and $0.13 \pm 0.01 \text{ W/mK}$, respectively. The values of

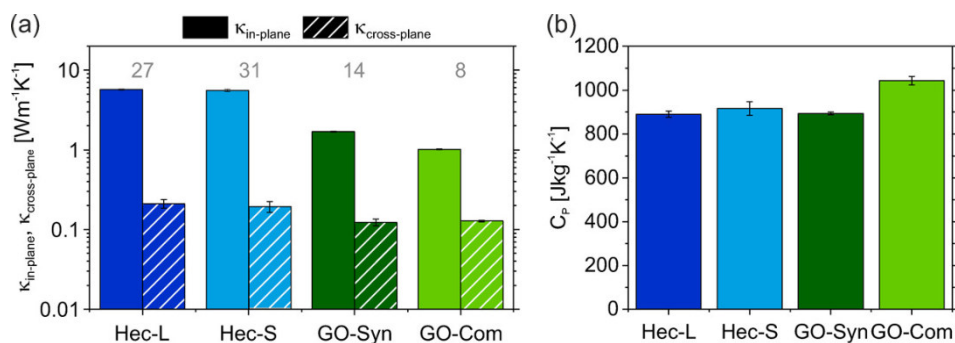


Fig. 11.1: Thermal properties: (a) in-plane ($\kappa_{\text{in-plane}}$) and cross-plane ($\kappa_{\text{cross-plane}}$) thermal conductivity. The numbers in the graph represent the anisotropy ratio of the thermal conductivity ($\kappa_{\text{in-plane}}/\kappa_{\text{cross-plane}}$). (b) Specific heat capacity (C_p).

the cross-plane thermal conductivity are comparable to reports in the literature of 0.18^[10] and 0.15 W/mK.^[9] The in-plane thermal conductivities show a much higher degree of variability. Renteria *et al.* reported a value of 2.94 W/mK,^[10] which is almost twice as high as the value for GO-syn. Meng *et al.* measured a value of 1.6 W/mK,^[9] which is in good agreement with our value for GO-syn. The variation of the GO results indicates that the in-plane thermal conductivity is strongly sensitive to the exact synthesis and preparation of the GO samples. This result is in line with reported large spreads of in-plane moduli ranging from 170 to 530 GPa,^[28] which was attributed to holes formed in the GO sheets due to overoxidation as proposed by Hofmann and König.^[31] This variation is also visible in the specific heat capacity (Figure 11.1b). Both Hec samples have comparable heat capacity, whereas GO-com has a higher heat capacity than GO-syn.

The Hec films exhibit a 2- to 3-fold higher anisotropy ratio ($\kappa_{\text{in-plane}}/\kappa_{\text{cross-plane}}$) of thermal conductivity than the GO samples (gray numbers in Figure 11.1a). The anisotropy ratio of the GO-syn sample of 14 is in good agreement with other studies,^[10] which reported a ratio of 16, while the anisotropy of GO-com^[8] is even lower. The anisotropy values of the synthetic Hec (~ 30) exceed the anisotropy ratios of natural clays, like boom clay^[32] (~ 1.7). Even the literature values of well-oriented samples like muscovite (6.3),^[29] biotite (6.0),^[29] and montmorillonite (9.6)^[30] hardly compare to the anisotropy in our synthetic structure. The superior anisotropy underlines the very high textured orientation of our structure.

We next focus on the structure and composition of the samples under investigation to work out any potential influence on the thermal conductivity. Hec belongs to the trioctahedral 2:1 smectite family and shows a sandwich-like structure comprising two tetrahedral and one octahedral layer (Figure 11.2a) with a nominal composition of $[\text{Na}_{0.5}]^{\text{inter}}[\text{Mg}_{2.5}\text{Li}_{0.5}]^{\text{oct}}[\text{Si}_4]^{\text{tet}}\text{O}_{10}\text{F}_2$. The thickness of an individual Hec platelet is ≈ 10 Å (Figure 11.2b). The synthetic Hec applied here has been shown to delaminate into individual single layers by repulsive osmotic swelling when immersed in deionized

water.^[33] For well-controlled delamination, a uniform intracrystalline reactivity is a prerequisite, which comes along with phase purity and a homogeneous charge density. For synthetic Hec, this is achieved by a melt synthesis followed by long-term annealing. The delamination was studied by small-angle X-ray scattering (SAXS). The high orientational lamellar order in liquid crystals leads typically to (a) anisotropic 2D scattering patterns and (b) a rational series of $00l$ -reflections due to the defined interlayer spacing d at $d = 2\pi/q$. Further, in that case, the swelling behavior of 2D lamellae with volume fraction Φ and thickness t is expected to be $d = t/\Phi$.^[34] The homogeneous intracrystalline reactivity assures a rational $00l$ -series, with adjacent Hec nanosheets being separated in suspension to 53 ± 6 (3 wt%) and 38 ± 4 nm (5 wt%) for Hec-L and Hec-S, respectively (Figure 11.2c). Due to the hindered polar rotation of Hec nanosheets in suspension, these Hec suspensions represent nematic phases. The observable rational series up to six higher-order reflections emphasizes the superior positional order of adjacent individual nanosheets. The high positional order is further proven by an anisotropic 2D scattering pattern (Figure 11.4). Spray coating these nematic phases of dilute Hec suspensions led to homogeneous, one-dimensional (1D) crystalline structures (smectic films) composed of largely overlapping individual sheets forming quasi-single crystalline band-like films.^[27] The exceptional periodic homogeneity can be seen from the cross-sectional transmission electron microscopy (TEM) image (Figure 11.2b). The white arrows highlight the directions of the in-plane and cross-plane thermal conductivity measurements. X-ray diffraction (XRD) patterns (Figure 11.2d) of both samples show a rational $00l$ -series up to the seventh order with sharp and intense basal reflections after spray coating. The quality of the 1D crystalline order is further confirmed by a low coefficient of variation of the $00l$ -series (Table 11.1) and a small full width at half-maximum. Furthermore, both Hec-L and Hec-S samples have a comparable basal spacing of ≈ 10 Å in the dry state, which represents the periodicity along the stacking direction. In Figure 11.5, the platelet areas, measured by scanning electron microscopy (SEM) followed by evaluating the area with ImageJ, are compared for samples Hec-L and Hec-S. The sample Hec-L (Figure 11.6), which was used as received from the synthesis, consists of large platelets with areas up to $800 \mu\text{m}^2$. We fabricated Hec-S from Hec-L by ultrasound treatment, which reduced the platelet area by more than 3 orders of magnitude ($< 0.4 \mu\text{m}^2$, Figures 11.5 and 11.6). Due to an ultrathin platelet thickness of 1 nm, both samples still have high aspect ratios (20000 and 300, respectively). The sonication procedure for platelet-size reduction leaves the structure and chemical composition of Hec unaltered. Infrared (IR) spectroscopy (Figure 11.2e) and X-ray photoelectron spectroscopy (XPS) spectra (Figure 11.8) of both samples were measured to demonstrate this. In the case of IR spectroscopy, four main signals are visible, which correspond to (i) OH stretching vibrations of water or cation-OH stretching vibrations at platelet edges, (ii) OH-bending vibrations of water, (iii) stretching vibration of SiO-groups in tetrahedral sheets, and (iv) bending vibration of SiO-groups and stretching vibration

of MgF-groups in octahedral sheets.^{[35]–[37]} Hec-L and Hec-S show good quantitative agreement of all these characteristic absorption peaks. Similarly, fitting of the element-specific bands in the XPS measurement results in comparable atomic ratios. Overall, sonication of Hec-L only reduced the size of the Hec platelets and did not affect the self-assembly, i.e., the basal spacing and order, as well as the chemical composition. Counterintuitively, we found that small Hec sheets are still great in-plane conductors. This can be explained by an in-plane mean free path that is still orders of magnitude smaller than the average platelet diameter. Consequently, boundary effects become negligible, which would typically lead to reduced thermal conductivity.^[27]

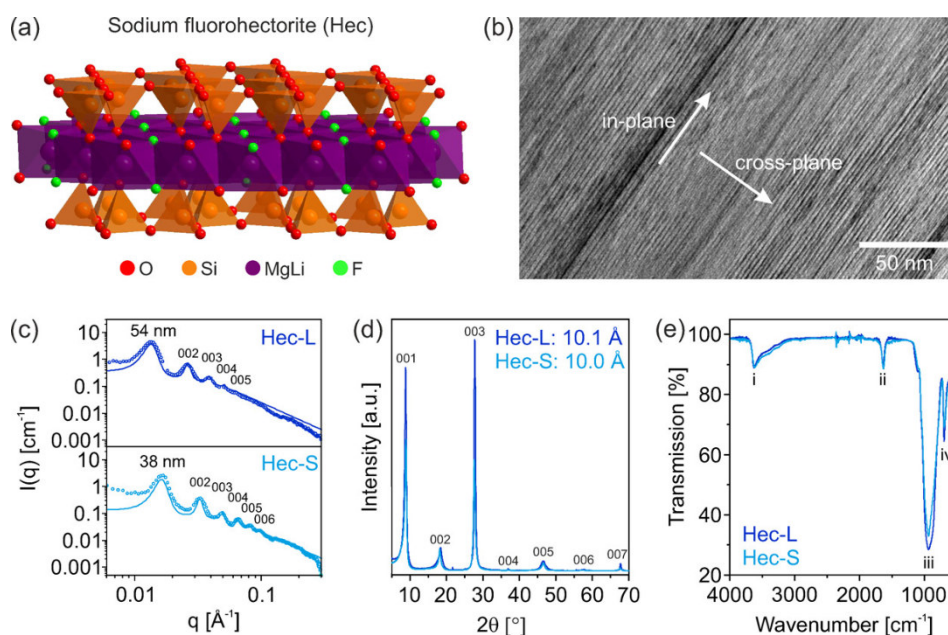


Fig. 11.2: (a) Structure of a sodium fluorohectorite (Hec) platelet. Sodium counter ions are located between two Hec platelets. (b) A cross-sectional TEM image of an aligned smectic Hec film. White arrows illustrate the in-plane and cross-plane directions. (c) SAXS results of aqueous Hec suspensions showing a rational series of $00l$ -reflections. (d) XRD patterns of the freestanding Hec films showing intense $00l$ -reflections. Both samples have a basal spacing around 10 Å. (e) IR spectra prove the same chemical composition of both samples.

For GO, it is not possible to provide a chemical formula. Its chemical structure is based on graphene, but GO is ill-defined, and the number of defects, i.e., vacancies/holes in the 2D structure and functional groups, strongly depends on the synthesis route.^[28] Figure 3a shows an exemplary structure of GO having various functional defects (epoxide, hydroxyl, and carboxylic groups) as well as a hole.^{[31],[38]} SAXS was used to further investigate the graphene oxide dispersions of about 3.5 wt%. Diluted graphene oxide dispersions are expected to form a nematic liquid crystalline phase in water via ordering of the sheets.^[39] The scattering intensity $I(q)$ values of the two GO suspensions decrease with the scattering vector q , following a q^{-2} power law (Figure 11.3c). This scaling law is typically obtained for

platelet-shaped scattering objects and proves the 2D morphology of the dispersed graphene oxide layers. The graphene oxide dispersions exhibit an anisotropic 2D SAXS pattern (Figure 11.4), indicating a nematic orientation. In contrast, Hec in a similar concentration shows additionally a series of $00l$ -reflection.^[34] The absence of these reflections in the case of GO is mainly attributed to a much more pronounced dislocation of the lamellar order by slipping or tilting of the individual GO layers. This strongly hints to a more heterogeneous charge distribution of the graphene oxide sheets. Similar to the Hec samples, spray coating of dilute GO dispersions led to aligned stacks of overlapping individual sheets, as can be seen from the SEM image (Figure 11.3b). The white arrows highlight the directions of the in-plane and cross-plane thermal conductivity measurements. The XRD patterns in Figure 11.3d show one weak, a rather broad, peak at 6 \AA ^[40] and no higher-order peaks as typical for randomly interstratified structures with varying layer separation. Thus, the stacking of the spray-coated GO sheets is less well-defined than that of the Hec platelets. Furthermore, the GO layers ($\sim 6 \text{ \AA}$) are thinner than the Hec platelets ($\sim 10 \text{ \AA}$). The analysis of the sheet area (Figure 11.5) revealed that GO-syn is much smaller than Hec-L, whereas GO-com is comparable to Hec-L but very broadly distributed (Figures 11.6 and 11.7). Both GO samples are, however, much larger than Hec-S. Additionally, we measured Raman spectra (Figure 11.10) and XPS (Figure 11.3e and Figure 11.9) to analyze the degree of functional defects of the GO samples. The intensity ratios of the D and G bands (I_D/I_G) of both samples are around 1, which is a measure for a high number of defects within the graphene-based structure. The overview XPS spectra (Figure 11.9) reveal the presence of carbon (C), oxygen (O), and sulfur (S). The latter stems from sulfate groups and is typical for GO made by the Hummers–Offeman protocols.^[28] Integrating over the various C1s species revealed that the main difference between the GO samples is the ratio of pristine sp^2 vs oxygenated C atoms. Figure 11.3e shows the C1s XPS spectra of GO-syn and GO-com. Three main peaks are visible, which are assigned to double-bonded carbon–oxygen (C=O; $\approx 288.3 \text{ eV}$), single-bonded carbon–oxygen (C–O; $\approx 286.8 \text{ eV}$), and sp^2 and sp^3 carbon (C=C/C–C; $\approx 284.7 \text{ eV}$).^[10] GO-com has a higher amount of oxygen-containing functional groups such as hydroxyl, epoxide, carbonyl, and carboxyl groups than GO-syn.

Since we found a 2 times lower in-plane thermal diffusivity for GO-com in comparison to GO-syn, we conclude that the difference in the degree of oxidation has a high impact on the in-plane thermal transport. These findings also support the results of Meng *et al.*^[9] They investigated GO samples with different degrees of oxidation. In agreement with our findings, the sample with a higher degree of oxidation showed a lower thermal conductivity. The reason is the decrease in sp^2 cluster size with an increasing amount of oxygen in the structure and holes in the 2D structure produced by overoxidation.^[31] Consequently, phonon scattering is enhanced by the likewise increased sp^2/sp^3 boundaries.^[9]

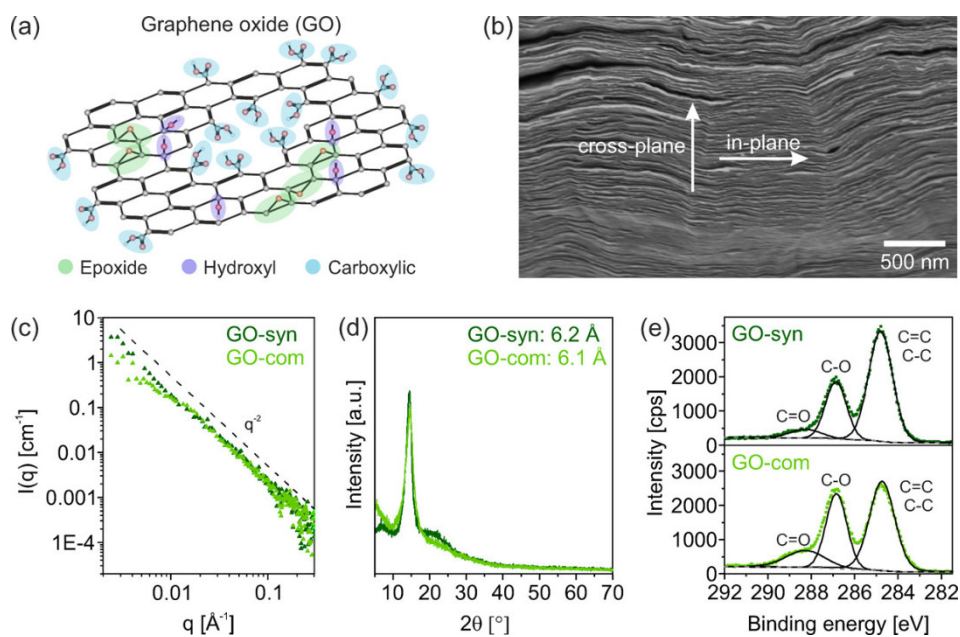


Fig. 11.3: (a) Exemplary structure of graphene oxide (GO). (b) SEM image of an aligned GO film. White arrows illustrate the in-plane and cross-plane directions. (c) SAXS results of GO suspensions showing a q^{-2} scaling of the scattering intensity. (d) XRD patterns show no long-range order. Both samples have a spacing of approximately 6 Å. (e) XPS data of the carbon signatures.

Before closing, we want to add a few words to put our results in the right context. Clearly, the absolute (in-plane) thermal conductivity values reported here are not as high as for hydrophobic graphitic materials or hexagonal boron nitride. The major distinction between such materials and our Hec and GO samples, however, lies in the processing conditions of water-dispersible two-dimensional materials with fully delaminated sheets. This makes especially Hec attractive for various applications where spray coating and mild processing conditions are indispensable for the final functional component. When comparing Hec and GO, we consider Hec to be superior owing to its well-defined chemical structure, better reproducibility, and higher thermal transport values. Furthermore, the Hec presented here has not yet been optimized for optimum thermal transport properties. In combination with other benign properties such as gas barrier properties or optical transparency, we expect that this material class will have an increasing impact on functional 2D materials.

11.4 Conclusions

In this study, we investigated the anisotropic thermal transport properties of thin films of synthetic clay sodium fluorohectorite (Hec) films and graphene oxide (GO). Whereas these materials are often used in the context of nanocomposite materials, we

focused on the pure phase components and their thermal transport properties. The properties of such 2D materials are strongly governed by the chemical composition, vacancy defects in the layer structure, and the platelet size. We, therefore, determined the thermal transport properties of four different samples. All of them were fabricated into (freestanding) thin films via spray coating of diluted dispersions of Hec and GO. The superior long-range order in Hec films results in a significantly higher anisotropy ratio than the GO samples. Quite remarkably, the in-plane thermal conductivity reaches very high values of up to 5.7 W/mK, which makes Hec an attractive material for heat spreading applications. GO in its oxidized form as received directly after spray coating features in-plane thermal conductivities on the order of only 1 W/mK. The thermal transport properties are strongly affected by the chemical composition of the GO samples. In particular, the in-plane thermal conductivity is reduced with increasing degree of functional groups containing oxygen. The cross-plane thermal conductivity is hardly affected and remains at a low value of ~ 0.12 W/mK. Surprisingly, the platelet size does not influence the in-plane thermal conductivity, which can be concluded from comparing Hec-L and Hec-S films. The chemical composition remained unaltered between large and small platelets of Hec. However, even though the platelet diameters were drastically reduced by approximately 2 orders of magnitude, the superior in-plane heat spreading properties were retained.

Overall, anisotropic heat transport is gaining increased attention in applications of thermal interface materials or heat management in light-emitting diodes or batteries. Our contribution provides a better understanding of the interplay between platelet size and chemical composition on the direction-dependent thermal conductivity. Furthermore, synthetic hectorite is an up-and-coming alternative to the more established GO and hBN heat spreading materials.

11.5 Materials and Methods

11.5.1 Sample Preparation and Characterization

The synthetic clay sodium fluorohectorite (Hec, $[\text{Na}_{0.5}]^{\text{inter}}[\text{Mg}_{2.5}\text{Li}_{0.5}]^{\text{oct}}[\text{Si}_4]^{\text{tet}}\text{O}_{10}\text{F}_2$) was delaminated by immersing it into Millipore water (0.5 wt%). For the synthesis of the small Hec platelets (Hec-S), a 0.5 wt% suspension of Hec-L was sonicated in an ice bath with the ultrasonic device UIP 1000hd. GO-syn, based on the Hummers–Offeman method, was synthesized according to an established procedure.^[28] GO-com was provided by Hangzhou Gaoxi Technology Co. Ltd. (China). The self-supporting films and the thinner films sprayed on a glass substrate were prepared with a fully automatic spray coating system. Every spraying cycle was followed by a drying cycle of 90 s at a temperature of 55 °C. The films were characterized by

X-ray diffraction, transmission electron microscopy, scanning electron microscopy, X-ray photoelectron, infrared, and Raman spectroscopy. Additional information about the sample preparation and characterization methods can be found in Section 11.7.1 (Supporting Information).

11.5.2 Thermal Conductivity Measurements

In-Plane Thermal Conductivity Measurements

Lock-in thermography measures the temperature spreading within thin, freestanding samples upon thermal excitation by an intensity-modulated, focused laser beam. Measurements were conducted in vacuum to prevent heat losses due to conduction and convection. The amplitude and phase data were obtained from the temperature oscillations. The slope method for thermally thin films was used to calculate the in-plane thermal diffusivity from the linear profiles of the radial phase and amplitude profiles.^[41] In combination with the density, determined by helium pycnometry, and the specific heat capacity, determined by differential scanning calorimetry, the in-plane thermal conductivity can be calculated. More details are provided in Section 11.7.2 (Supporting Information).

Cross-plane Thermal Conductivity Measurements

The photoacoustic method exploits the photoacoustic effect to determine the thermal properties of a sample.^{[42],[43]} The sample was fixed to a gas-tight glass cell filled with 20 psi helium. A modulated laser beam was run through the cell volume and periodically heated the transducer layer on the top of the sample. The induced pressure change on the surface of the sample led to an acoustic wave propagating into the gas. A microphone, coupled to a lock-in amplifier, detected the phase shift between the acoustic signal and the modulated laser dependent on the frequency. By comparing the data to a multilayer model describing the temperature distribution in the sample, the total layer resistance of the sample was obtained. Together with the film thickness determined by atomic force microscopy, the effective thermal conductivity was calculated. Details about the photoacoustic characterization can be found in Section 11.7.2 (Supporting Information).

Acknowledgements

The Volkswagen Foundation funded this project through a Lichtenberg professorship. Additional support was provided by the German Research Foundation through DFG RE3550/2-1. Kai Herrmann is acknowledged for discussions on the PA method.

11.6 References

- [1] M. T. Barako, V. Gambin, and J. Tice, „Integrated nanomaterials for extreme thermal management: A perspective for aerospace applications“, *Nanotechnology*, vol. 29, no. 15, p. 154003, Feb. 2018.
- [2] H. Song, J. Liu, B. Liu, *et al.*, „Two-dimensional materials for thermal management applications“, *Joule*, vol. 2, no. 3, pp. 442–463, Mar. 2018.
- [3] J. Xiang and L. T. Drzal, „Thermal conductivity of exfoliated graphite nanoplatelet paper“, *Carbon*, vol. 49, no. 3, pp. 773–778, Mar. 2011.
- [4] Y. Zhang, M. Edwards, M. K. Samani, *et al.*, „Characterization and simulation of liquid phase exfoliated graphene-based films for heat spreading applications“, *Carbon*, vol. 106, pp. 195–201, Sep. 2016.
- [5] K. M. Razeeb, E. Dalton, G. L. W. Cross, and A. J. Robinson, „Present and future thermal interface materials for electronic devices“, *International Materials Reviews*, vol. 63, no. 1, pp. 1–21, Mar. 2017.
- [6] M. C. K. Swamy and Satyanarayan, „A review of the performance and characterization of conventional and promising thermal interface materials for electronic package applications“, *Journal of Electronic Materials*, vol. 48, no. 12, pp. 7623–7634, Sep. 2019.
- [7] R. Prasher, „Thermal interface materials: Historical perspective, status, and future directions“, *Proceedings of the IEEE*, vol. 94, no. 8, pp. 1571–1586, Aug. 2006.
- [8] A. J. McNamara, Y. Joshi, and Z. M. Zhang, „Characterization of nanostructured thermal interface materials – a review“, *International Journal of Thermal Sciences*, vol. 62, pp. 2–11, Dec. 2012.
- [9] Q.-L. Meng, H. Liu, Z. Huang, *et al.*, „Tailoring thermal conductivity of bulk graphene oxide by tuning the oxidation degree“, *Chinese Chemical Letters*, vol. 29, no. 5, pp. 711–715, May 2018.
- [10] J. D. Renteria, S. Ramirez, H. Malekpour, *et al.*, „Strongly anisotropic thermal conductivity of free-standing reduced graphene oxide films annealed at high temperature“, *Advanced Functional Materials*, vol. 25, no. 29, pp. 4664–4672, Jun. 2015.

- [11] N. Song, D. Jiao, P. Ding, *et al.*, „Anisotropic thermally conductive flexible films based on nanofibrillated cellulose and aligned graphene nanosheets“, *Journal of Materials Chemistry C*, vol. 4, no. 2, pp. 305–314, 2016.
- [12] N. Song, D. Jiao, S. Cui, *et al.*, „Highly anisotropic thermal conductivity of layer-by-layer assembled nanofibrillated cellulose/graphene nanosheets hybrid films for thermal management“, *ACS Applied Materials & Interfaces*, vol. 9, no. 3, pp. 2924–2932, Jan. 2017.
- [13] L. Peng, Z. Xu, Z. Liu, *et al.*, „Ultrahigh thermal conductive yet superflexible graphene films“, *Advanced Materials*, vol. 29, no. 27, p. 1700589, May 2017.
- [14] P. Jiang, X. Qian, R. Yang, and L. Lindsay, „Anisotropic thermal transport in bulk hexagonal boron nitride“, *Physical Review Materials*, vol. 2, no. 6, Jun. 2018.
- [15] Y. Lin, T. V. Williams, T.-B. Xu, *et al.*, „Aqueous dispersions of few-layered and monolayered hexagonal boron nitride nanosheets from sonication-assisted hydrolysis: Critical role of water“, *The Journal of Physical Chemistry C*, vol. 115, no. 6, pp. 2679–2685, Jan. 2011.
- [16] B.-H. Xie, X. Huang, and G.-J. Zhang, „High thermal conductive polyvinyl alcohol composites with hexagonal boron nitride microplatelets as fillers“, *Composites Science and Technology*, vol. 85, pp. 98–103, Aug. 2013.
- [17] X. Zeng, L. Ye, S. Yu, *et al.*, „Artificial nacre-like papers based on noncovalent functionalized boron nitride nanosheets with excellent mechanical and thermally conductive properties“, *Nanoscale*, vol. 7, no. 15, pp. 6774–6781, 2015.
- [18] Y.-F. Huang, Z.-G. Wang, H.-M. Yin, *et al.*, „Highly anisotropic, thermally conductive, and mechanically strong polymer composites with nacre-like structure for thermal management applications“, *ACS Applied Nano Materials*, vol. 1, no. 7, pp. 3312–3320, Jul. 2018.
- [19] O. H. Kwon, T. Ha, D.-G. Kim, *et al.*, „Anisotropy-driven high thermal conductivity in stretchable poly(vinyl alcohol)/hexagonal boron nitride nanohybrid films“, *ACS Applied Materials & Interfaces*, vol. 10, no. 40, pp. 34625–34633, Sep. 2018.
- [20] J. Han, G. Du, W. Gao, and H. Bai, „An anisotropically high thermal conductive boron nitride/epoxy composite based on nacre-mimetic 3d network“, *Advanced Functional Materials*, vol. 29, no. 13, p. 1900412, Feb. 2019.
- [21] B. Fischer, M. Ziadeh, A. Pfaff, J. Breu, and V. Altstädt, „Impact of large aspect ratio, shear-stiff, mica-like clay on mechanical behaviour of PMMA/clay nanocomposites“, *Polymer*, vol. 53, no. 15, pp. 3230–3237, Jul. 2012.

- [22] M. R. Schütz, H. Kalo, T. Lunkenbein, J. Brey, and C. A. Wilkie, „Intumescent-like behavior of polystyrene synthetic clay nanocomposites“, *Polymer*, vol. 52, no. 15, pp. 3288–3294, Jul. 2011.
- [23] M. R. Schütz, H. Kalo, T. Lunkenbein, *et al.*, „Shear stiff, surface modified, mica-like nanoplatelets: A novel filler for polymer nanocomposites“, *Journal of Materials Chemistry*, vol. 21, no. 32, p. 12 110, 2011.
- [24] E. S. Tsurko, P. Feicht, F. Nehm, *et al.*, „Large scale self-assembly of smectic nanocomposite films by doctor blading versus spray coating: Impact of crystal quality on barrier properties“, *Macromolecules*, vol. 50, no. 11, pp. 4344–4350, May 2017.
- [25] E. S. Tsurko, P. Feicht, C. Habel, *et al.*, „Can high oxygen and water vapor barrier nanocomposite coatings be obtained with a waterborne formulation?“, *Journal of Membrane Science*, vol. 540, pp. 212–218, Oct. 2017.
- [26] M. D. Losego, I. P. Blitz, R. A. Vaia, D. G. Cahill, and P. V. Braun, „Ultralow thermal conductivity in organoclay nanolaminates synthesized via simple self-assembly“, *Nano Letters*, vol. 13, no. 5, pp. 2215–2219, Apr. 2013.
- [27] Z. Wang, K. Rolle, T. Schilling, *et al.*, „Tunable thermoelastic anisotropy in hybrid bragg stacks with extreme polymer confinement“, *Angewandte Chemie International Edition*, vol. 59, no. 3, pp. 1286–1294, Jan. 2020.
- [28] P. Feicht, R. Siegel, H. Thurn, *et al.*, „Systematic evaluation of different types of graphene oxide in respect to variations in their in-plane modulus“, *Carbon*, vol. 114, pp. 700–705, Apr. 2017.
- [29] C. Clauser and E. Huenges, „Thermal conductivity of rocks and minerals“, in *AGU Reference Shelf*, American Geophysical Union, Mar. 2013, pp. 105–126.
- [30] A. Tiwari, K. Boussois, B. Nait-Ali, D. S. Smith, and P. Blanchart, „Anisotropic thermal conductivity of thin polycrystalline oxide samples“, *AIP Advances*, vol. 3, no. 11, p. 112 129, Nov. 2013.
- [31] U. Hofmann and E. König, „Untersuchungen über Graphitoxyd“, *Zeitschrift für anorganische und allgemeine Chemie*, vol. 234, no. 4, pp. 311–336, Dec. 1937.
- [32] L.-Q. Dao, P. Delage, A.-M. Tang, *et al.*, „Anisotropic thermal conductivity of natural boom clay“, *Applied Clay Science*, vol. 101, pp. 282–287, Nov. 2014.
- [33] M. Stöter, D. A. Kunz, M. Schmidt, *et al.*, „Nanoplatelets of sodium hectorite showing aspect ratios of ≈ 20000 and superior purity“, *Langmuir*, vol. 29, no. 4, pp. 1280–1285, Jan. 2013.
- [34] S. Rosenfeldt, M. Stöter, M. Schlenk, *et al.*, „In-depth insights into the key steps of delamination of charged 2d nanomaterials“, *Langmuir*, vol. 32, no. 41, pp. 10 582–10 588, Oct. 2016.

- [35] H. A. Prescott, Z.-J. Li, E. Kemnitz, J. Deutsch, and H. Lieske, „New magnesium oxide fluorides with hydroxy groups as catalysts for michael additions“, *Journal of Materials Chemistry*, vol. 15, no. 43, p. 4616, 2005.
- [36] M. Wojciechowska, B. Czajka, M. Pietrowski, and M. Zieliński, *Catalysis Letters*, vol. 66, no. 3, pp. 147–153, 2000.
- [37] A. A. Rywak and J. M. Burlitch, „Sol-gel synthesis of nanocrystalline magnesium fluoride: Its use in the preparation of MgF_2 films and MgF_2 - SiO_2 composites“, *Chemistry of Materials*, vol. 8, no. 1, pp. 60–67, Jan. 1996.
- [38] A. Lerf, H. He, M. Forster, and J. Klinowski, „Structure of graphite oxide revisited“, *The Journal of Physical Chemistry B*, vol. 102, no. 23, pp. 4477–4482, Jun. 1998.
- [39] Z. Xu and C. Gao, „Graphene chiral liquid crystals and macroscopic assembled fibres“, *Nature Communications*, vol. 2, no. 1, Sep. 2011.
- [40] U. Hofmann, A. Frenzel, and E. Csalán, „Die Konstitution der Graphitsäure und ihre Reaktionen“, *Justus Liebigs Annalen der Chemie*, vol. 510, no. 1, pp. 1–41, 1934.
- [41] A. Mendioroz, R. Fuente-Dacal, E. Apiñaniz, and A. Salazar, „Thermal diffusivity measurements of thin plates and filaments using lock-in thermography“, *Review of Scientific Instruments*, vol. 80, no. 7, p. 074 904, Jul. 2009.
- [42] H. Hu, X. Wang, and X. Xu, „Generalized theory of the photoacoustic effect in a multilayer material“, *Journal of Applied Physics*, vol. 86, no. 7, pp. 3953–3958, Oct. 1999.
- [43] X. Wang, H. Hu, and X. Xu, „Photo-acoustic measurement of thermal conductivity of thin films and bulk materials“, *Journal of Heat Transfer*, vol. 123, no. 1, pp. 138–144, Jun. 2000.

11.7 Supporting Information

11.7.1 Sample preparation and characterization

Materials

The synthetic clay sodium fluorohectorite (Hec, $[\text{Na}_{0.5}]^{\text{inter}}[\text{Mg}_{2.5}\text{Li}_{0.5}]^{\text{oct}}[\text{Si}_4]^{\text{tet}}\text{O}_{10}\text{F}_2$) was synthesized with high-purity reagents of SiO_2 , LiF , MgF_2 , MgO and NaF in a gastight molybdenum crucible via melt synthesis according to an already published procedure.^[1] To improve the charge density of the clay platelets and relating thereto the intracrystalline reactivity, the melt synthesis is followed by long-term annealing at 1045°C for 6 weeks.^[2] The material featured a cation exchange capacity of 1.27 mmol/g .^{[1],[2]} This sample is called Hec-L. For the fabrication of the small Hec platelets (Hec-S), a 0.5 wt% suspension of Hec-L was sonicated for 15 minutes in an ice bath with the ultrasonic device UIP 1000hd (Hielscher Ultrasonic GmbH, Germany), equipped with ultrasonic horn BS2d22 and a booster B2-1.2, at 20 kHz with a maximal output power of 1000 W. GO-syn, based on Hummers/Offeman's method, was synthesized according to an established procedure.^[3] GO-com was provided by Hangzhou Gaoxi Technology Co. Ltd. (China).

Film preparation

For the delamination, the synthetic Hec was immersed into Millipore water (0.5 wt%). The complete delamination was studied by small-angle X-ray scattering (SAXS).^[4] The self-supporting films of Hec and GO were prepared by spray coating of 0.5 wt% suspensions of the respective material. The fully automatic spray coating system was equipped with a SATA 4000 LAB HVLP 1.0 mm spray gun (SATA GmbH & Co. KG, Germany). Suspensions were sprayed on a corona-treated polyethylene terephthalate (PET) foil (optimont 501, bleher Folientechnik, Germany). The spraying and nozzle pressure were set constant at values of 2 and 4 bar, respectively. The round per flat fan control was set to 6 with a flow speed of 3 mL/s . The distance between the spraying gun and the substrate was 17 cm. The thickness of the suspension layer applied in one spraying step is about $2\text{ }\mu\text{m}$ which corresponds to about 20 nm dry film thickness. For drying the suspension layer, the sample is stopped under infrared lamps until evaporation of the solvent is complete. After every spraying cycle, a drying cycle of 90 s with a temperature of 55°C took place. The spraying/drying cycle is repeated until the desired barrier film thickness of $50\text{ }\mu\text{m}$ is obtained. Afterward, the film was dried at 100°C for 3 days and peeled off from the PET foil for achieving self-supporting films. For characterization by

photoacoustic analysis thinner films on the order of a few μm were spray-coated onto clean 1 mm microscope glass slides. In total, we prepared four different samples: Hec-L, Hec-S, GO-syn, and GO-com.

Small-angle X-ray Scattering (SAXS)

All SAXS data were measured using the small-angle X-ray system “Double Ganesha AIR” (SAXSLAB, Denmark). The X-ray source of this laboratory-based system is a rotating anode (copper, MicroMax 007HF, Rigaku Corporation, Japan), providing a micro-focused beam. The data were recorded by a position-sensitive detector (PILATUS 300 K, Dectris). To cover the range of scattering vectors different detector positions were used. The measurements of the suspensions were done in 1 mm glass capillaries (Hilgenberg, code 4007610, Germany) at room temperature. To improve the detection limit of the in-house machine, the suspensions were first concentrated by centrifugation at 10.000 rpm for 1 hour. The data were radially averaged and background corrected. As background, a water-filled capillary was used.

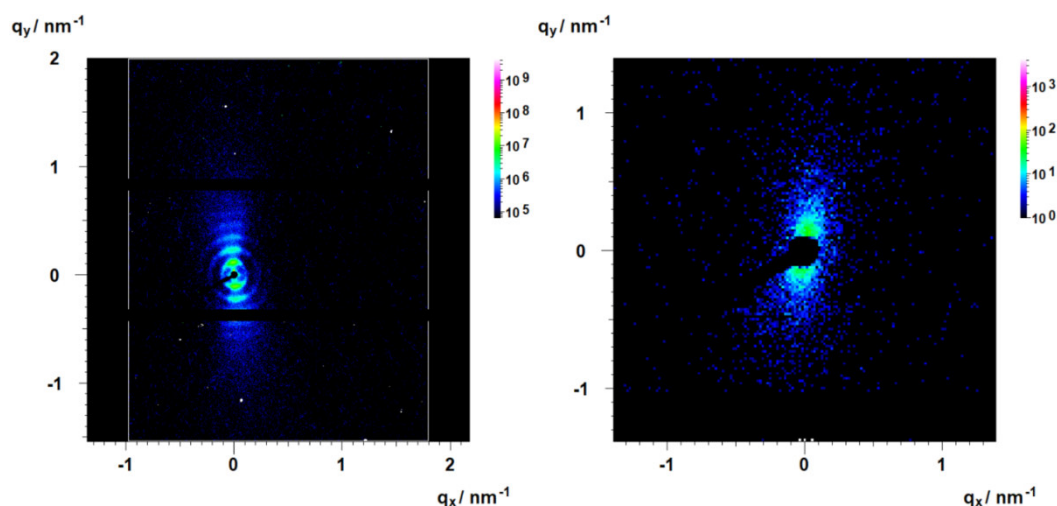


Fig. 11.4: 2D SAXS patterns of an aqueous Hec suspension (left) and an aqueous GO suspension (right).

X-ray diffraction (XRD) analysis

XRD patterns for the films were recorded in Bragg-Brentano-geometry on an Empyrean diffractometer (PANalytical B.V.; the Netherlands) using $\text{Cu K}\alpha$ radiation ($\lambda = 1.54187 \text{ \AA}$). The self-supporting films were placed on glass slides (Menzel-Gläser; Thermo Scientific). Before the measurements, samples were dried at 100°C for one week in a vacuum chamber. As a measure of the quality of the

one-dimensional crystallinity of the films, the coefficient of variation (CV) and the full width at half maximum (FWHM) were determined (Table 11.1). Large CV-values ($\approx 3\%$,^[4]) and large FWHM indicate non-rationality of the diffraction pattern as caused by a random interstratification of different interlayer heights.

Tab. 11.1: Overview of the structural characterization by XRD

Sample	Description	d_{XRD} [Å]	CV [%]	FWHM [$^{\circ}2\theta$]
Hec-L	Large Hec platelets	10.1	1.6	0.7
Hec-S	Small Hec platelets	10.0	1.1	0.6
GO-syn	Synthetic GO	6.2	-	3.1
GO-con	Commercial GO	6.1	-	3.5

Transmission electron microscopy (TEM)

TEM images of the samples Hec-L and Hec-S were taken on a JEOL JEM-2200FS (JEOL GmbH, Germany) at an acceleration voltage of 200 kV. Cross-section pictures of the self-supporting films were prepared with a Cryo Ion Slicer IB-09060CIS (JEOL, Germany).

Scanning electron microscopy (SEM)

SEM images were taken with a Zeiss Ultra plus (Carl Zeiss AG, Germany) at an operating voltage of 3 kV. Samples were prepared by drop coating a 0.001 wt% solution on a plasma-treated silicon wafer. The samples with Hec were sputtered with 10 nm carbon. For analyzing the area of the platelets, ImageJ was used, and at least 100 platelets were evaluated. Figure 11.5 shows the histograms of the platelet areas of Hec (a) and GO (b) samples. Figure 11.6 and 11.7 show exemplary SEM pictures of Hec and GO, respectively.

Cross-sections of the films were prepared by cutting the self-supporting films with a razor blade and sputtering with 10 nm carbon.

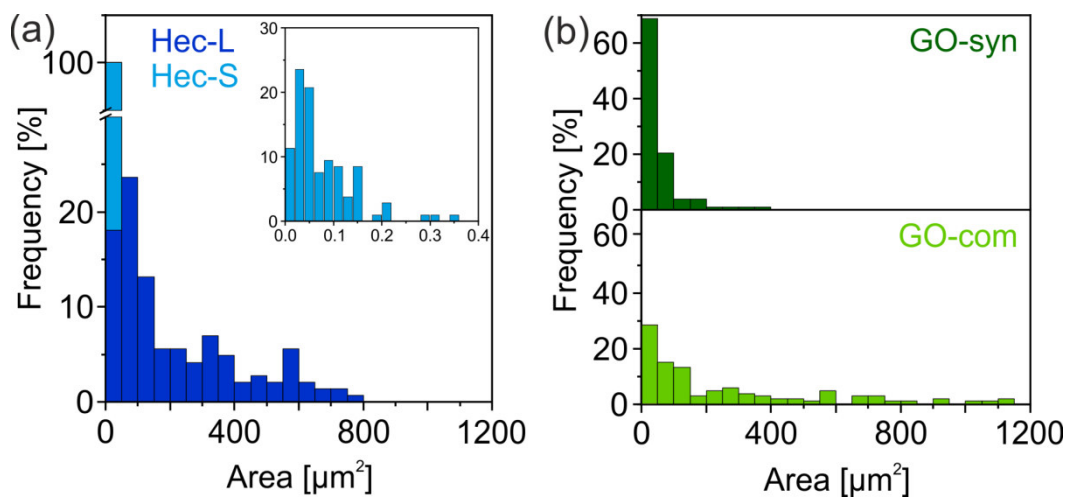


Fig. 11.5: Histograms of platelet areas of Hec (a) and GO (b) samples evaluated from SEM images.

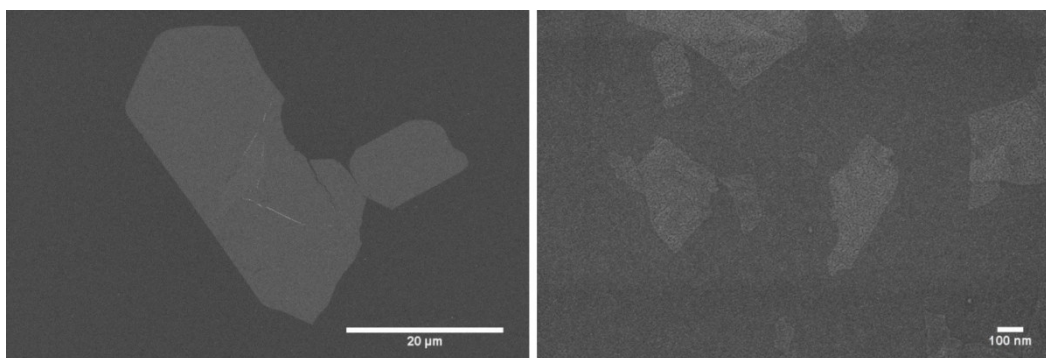


Fig. 11.6: SEM pictures of Hec-L (left) and Hec-S (right).

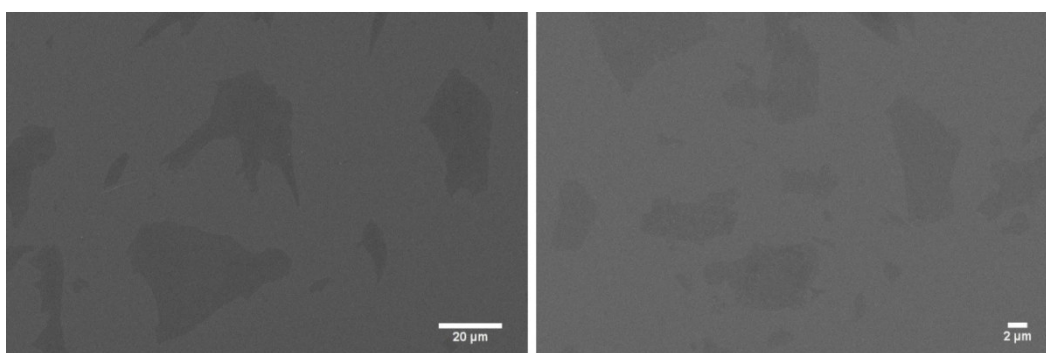


Fig. 11.7: SEM pictures of GO-com (left) and GO-syn (right).

X-ray photoelectron spectroscopy (XPS)

XPS measurements were carried out using a Versa Probe III from Physical electronics. Cu and Au were used for calibration. Shirley-type background-subtracted data is presented. Scotch tape was used to fixate the sample films on the measurement stage. The samples were sputtered with Argon after being introduced into the XPS chamber to remove adsorbed hydrocarbons. To minimize charging effects, a charge neutralization system was used. Figure 11.8 and 11.9 show the XPS spectra of Hec and GO samples. Peaks used for calculation of the elemental composition (Table 11.2 and 11.3) are marked.

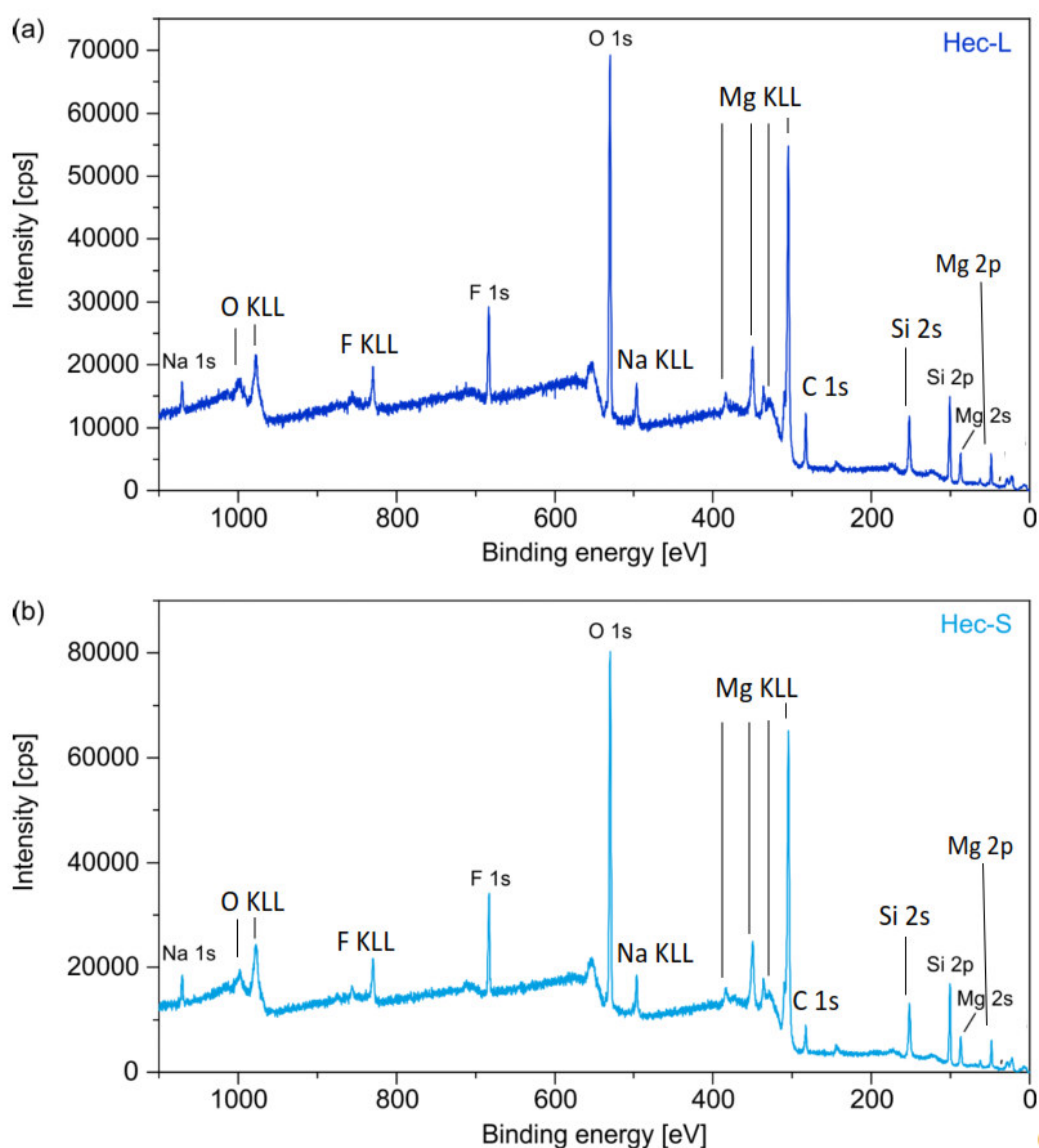


Fig. 11.8: Overview XPS spectra of Hec-L (a) and Hec-S (b). Both spectra show the same chemical composition (see Table 11.2).

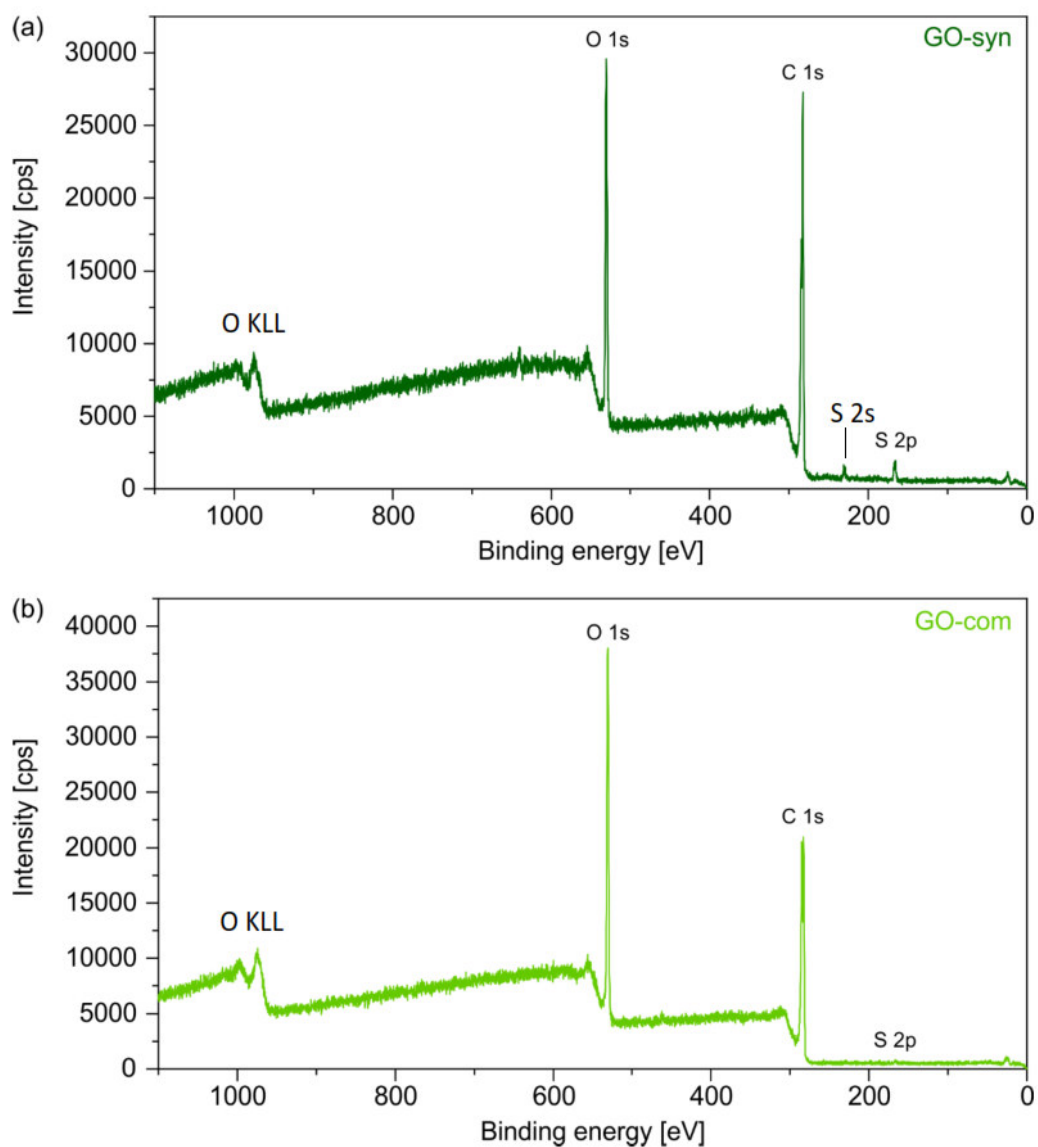


Fig. 11.9: Overview XPS spectra of GO-syn (a) and GO-com (b). Two main differences are visible: GO-com contains more oxygen (O) than GO-syn, and GO-syn contains a little amount of sulfur (S), whereas GO-com contains almost no sulfur (see table 11.3).

Tab. 11.2: Elemental composition of Hec samples extracted from XPS data.

Sample	Na	Mg	Li	Si	O	F
Hec-L	2.95 %	10.67 %	3.79 %	18.26 %	54.06 %	10.27 %
Hec-S	2.58 %	10.72 %	1.89 %	18.90 %	54.33 %	11.57 %

Tab. 11.3: Elemental composition of GO samples extracted from XPS data.

Sample	C	O	S
GO-syn	72.06 %	26.70 %	1.25 %
GO-com	68.74 %	30.94 %	0.31 %

Raman spectroscopy

Raman spectroscopy was performed with a Raman microscope (Horiba Scientific, Olympus Ex41, $\lambda = 635$ nm) equipped with a Synapse CCD camera. The obtained Raman spectra are shown in Figure 11.10. The intensity ratios of the D and G band (I_D/I_G) of both samples are around 1, which is a measure for a high number of defects (functional groups and holes) within the GO structure.

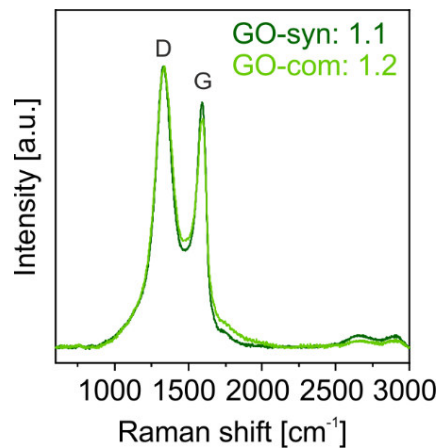


Fig. 11.10: Raman spectra reveal a comparable degree of defects of both samples (I_D/I_G the ratio for both samples is around 1).

Infrared (IR) spectroscopy

For IR spectra, a JASCO FT/IR-6100 Fourier transform IR spectrometer (JASCO Corporation, Japan) with an attenuated total reflectance (ATR) unit was used.

11.7.2 Thermal measurements

Two different methods were used to characterize the thermal transport properties of the Hec and GO samples: lock-in thermography for the in-plane thermal diffusivity and the photoacoustic method for the cross-plane thermal conductivity. For the calculation of the in-plane thermal conductivity and the determination of the cross-plane thermal conductivity, the density and the specific heat capacity are needed. Therefore, Helium pycnometry and differential scanning calorimetry have been used. Before all measurements, the samples have been dried for seven days at 100 °C in a vacuum oven.

Helium pycnometry

The density of the samples was obtained from helium pycnometry using an Ultrapyc 1200e (Quantachrome Instruments). First of all, the volume of the (empty) measurement cell was measured. Then, small pieces of the free-standing films were weighed into the sample cell with a nominal volume of 1.8 cm³. One hundred runs were conducted to measure the volume of the films at room temperature. By knowing the mass (weighed on a fine balance) and the volume, the density of the samples was calculated. The obtained densities are summarized in Table 11.4.

Tab. 11.4: Densities of Hec and GO films (measured at room temperature).

Sample	Density [g/cm ³]
Hec-L	2.73 ± 0.01
Hec-S	2.57 ± 0.02
GO-syn	1.53 ± 0.01
GO-con	1.54 ± 0.01

Differential scanning calorimetry (DSC)

The specific heat capacity was determined by DSC measurements on a TA instruments Discovery DSC 2500, according to the ASTM E1269 standard. All samples were freeze ground for better processability and contact with the DSC pans. Before the measurement, an isothermal step (1 h, 100 °C) was conducted to ensure dry conditions. Subsequently, two heating cycles were performed, whereas only the second cycle was evaluated. The temperature profile ranged in the case of the Hec samples from −40 °C to 250 °C and in case of the GO samples from −40 °C to 100 °C

using a heating rate of 20 K/min with a nitrogen flow of 50 mL/min. Triplicates of each sample were measured (Figure 11.11).

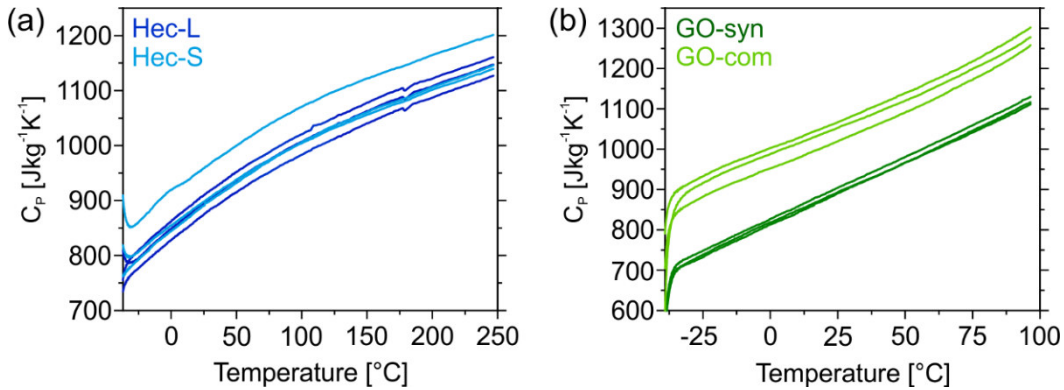


Fig. 11.11: Specific heat capacity C_P versus temperature: (a) Hec-L and Hec-S. (b) GO-syn and GO-com. The C_P at 25 °C was used for the determination of the thermal conductivity.

Lock-in thermography (LIT)

The in-plane thermal diffusivity of free-standing Hec and GO films was obtained by lock-in thermography (LIT). Figure 11.12 shows the self-built LIT set-up. A laser

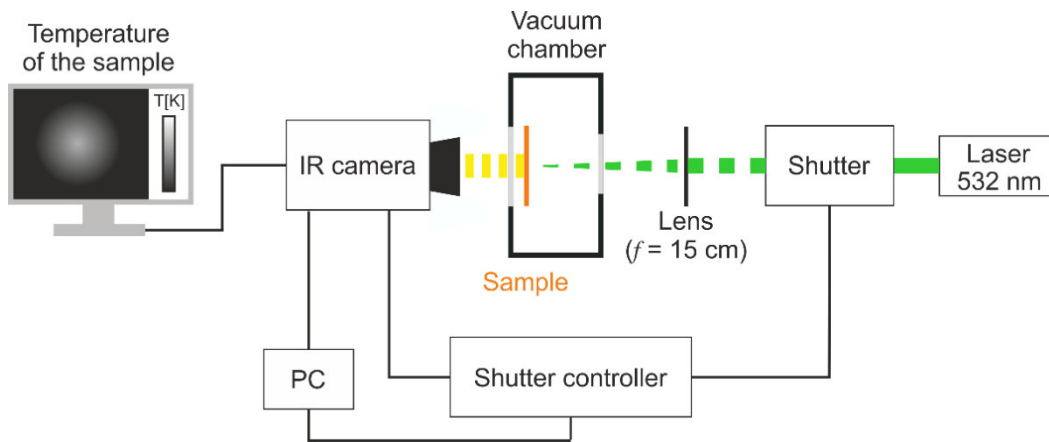


Fig. 11.12: Scheme of the lock-in thermography set-up. The samples were measured in a vacuum chamber to avoid heat losses (convection and conduction) to the environment.

beam periodically heats the free-standing sample (Genesis MX 532-1000 SLM OPS, Coherent, $\lambda = 532$ nm) focused onto the sample surface by a lens of 150 mm focal length. For the modulation of the laser a shutter (SH05/M, Thorlabs) controlled by a shutter controller (SC10, Thorlabs) is used. The emitted infrared (IR) radiation of the sample surface is detected in rear-face configuration (i.e. from the non-illuminated side) by an Infratec VarioCAM HD research IR camera (spectral window: 7.5-14 μm). The IR camera is equipped with a close-up lens which enables a spatial resolution

of around 29 μm . Since heat conduction to the gas and convection lead to an overestimation of the thermal diffusivity^{[5],[6]} all samples were measured in a vacuum ($\sim 3 \times 10^{-3}$ mbar). Furthermore, the Hec samples were coated with a 20 nm carbon layer for enhanced laser absorption. The coating of the sample was facing to the IR camera. Due to the blackish color of GO, the GO samples possess a proper laser absorption, and therefore a coating was not necessary.

LIT measurements were performed using Infratec's IRBISactiveonline software. Measurements were conducted at several lock-in frequencies between 0.309 and 1.765 Hz. Furthermore, each measurement was averaged over several (800-2000) lock-in periods to enhance the signal to noise ratio, with the first 100 periods being discarded. The software calculates the amplitude and phase of the sample's temperature oscillations automatically. Exemplary phase images are depicted in Figure 11.13. The red point marks the focal point of the laser excitation and thus the midpoint of the radial distribution.

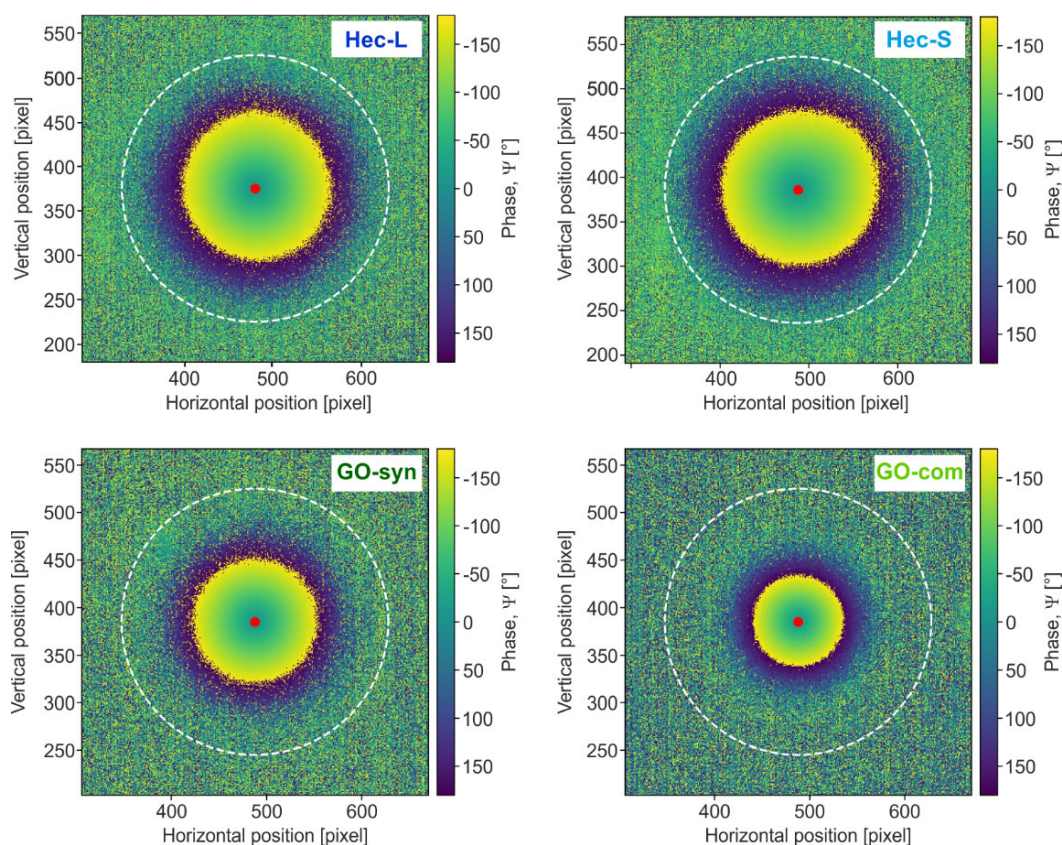


Fig. 11.13: Exemplary two-dimensional phase images measured at a frequency of 1.111 Hz. The penetration depth of the temperature oscillations depends on the material's properties and decreases with decreasing thermal diffusivity. The red point in the center of the phase image marks the focal point of the laser.

Radial profiles for the phase and amplitude images (Figure 11.14) are extracted using a self-written Python script. The in-plane thermal diffusivity is calculated

from the phase and amplitude slopes according to the slope method of a thermally thin film:

$$m_{\Psi} \cdot m_{\ln(T \cdot r^{0.5})} = \frac{\pi \cdot f_{\text{lock-in}}}{\alpha_{\text{in-plane}}} \quad (11.1)$$

Here, m_{Ψ} is the slope of the linear relation of the phase and the radial distance r , $m_{\ln(T \cdot r^{0.5})}$ is the slope of the linear relation of the natural logarithm of the amplitude T multiplied by the square root of the radial distance r , $f_{\text{lock-in}}$ is the lock-in frequency, and $\alpha_{\text{in-plane}}$ is the in-plane thermal diffusivity. Three films have been measured for each sample type. An average in-plane thermal diffusivity value with a standard deviation was calculated from this data (Table 11.5).

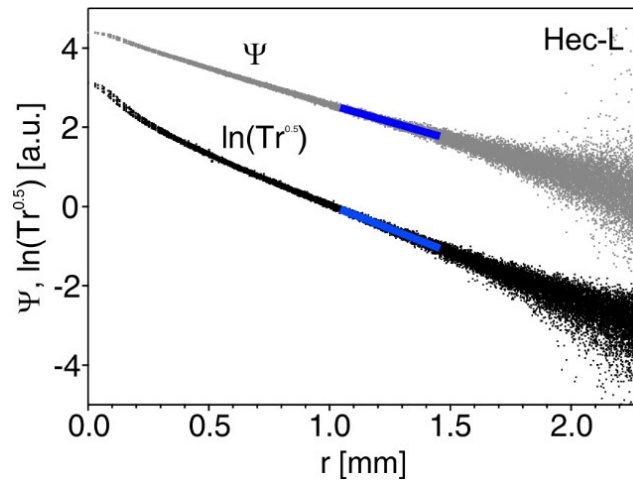


Fig. 11.14: Exemplary phase Φ and amplitude profiles of Hec-L. The blue lines indicate the regions where the linear fit was evaluated. This position is sufficiently far away from the central excitation spot.^[7]

Tab. 11.5: In-plane thermal diffusivity values of Hec and GO films. Three films per sample type were measured, and an average thermal diffusivity with a standard deviation was calculated.

Sample	In-plane thermal diffusivity [mm ² /s]
Hec-L	2.35 ± 0.03
Hec-S	2.36 ± 0.01
GO-syn	1.24 ± 0.02
GO-con	0.63 ± 0.01

Finally, the in-plane thermal conductivity was calculated from the in-plane thermal diffusivity $\alpha_{\text{in-plane}}$, the density ρ , and the specific heat capacity C_P :

$$\kappa_{\text{in-plane}} = \alpha_{\text{in-plane}} \cdot \rho \cdot C_P \quad (11.2)$$

Photoacoustic method

The samples for the cross-plane thermal conductivity characterization were spray-coated on glass substrates. A gold transducer layer (~ 150 nm) was evaporated on top of the samples. In the photoacoustic measurement, a modulated laser beam ($\lambda = 150$ nm) periodically heats the sample. Due to the photoacoustic effect an acoustic response is induced, which relies on the thermal properties of the sample.

The schematic layout of the measurement cell is shown in Figure 11.15a. The gas-tight cell is filled with a helium pressure of 20 psi. The microphone (Bruel& Kjaer, 4398-A-011) connected to the cell detects the acoustic wave, which is induced by the periodic heat conduction from the sample surface to the gas phase. The microphone is linked to a lock-in amplifier with integrated signal generator (Zurich instruments, HF2LI), as shown in Figure 11.15b. The signal generator targets the modulation frequency for the electro-optic modulator (EOM, Conoptics, M25A) and therefore controls the frequency of the laser beam. The lock-in amplifier then transfers the acoustic signal into amplitude and phase shift concerning the modulation of the incident laser beam.

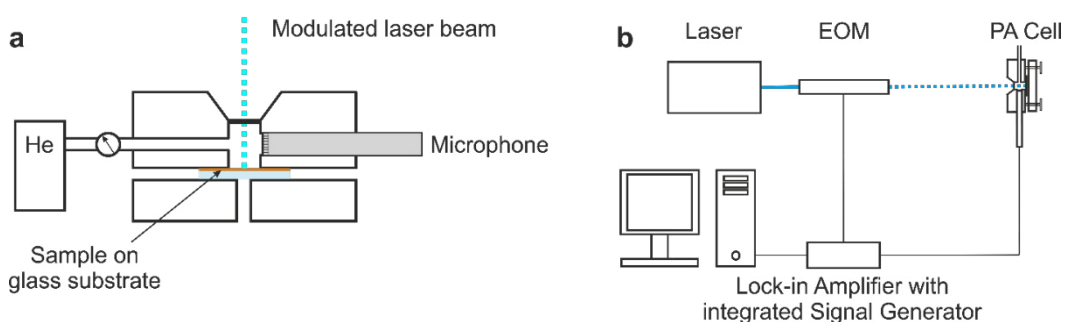


Fig. 11.15: Scheme of (a) the photoacoustic cell and (b) the whole setup.

For measurement, we performed a frequency sweep in a range from 110 Hz to 4000 Hz. The phase shift signal is then normalized with the signal of a thermally thick glass sample (1 mm) of known thermal properties. Figure 11.16 shows a representative measurement curve together with the best fit. The fitting procedure was realized according to Singh *et al.*^[8] Therefore, the generalized multilayer model of Hu *et al.*^[9] is used. The model described the temperature distribution in the sample, assuming a one-dimensional heat transfer. The unknown parameters contact resistance between the gold layer and the sample, the thermal diffusivity of the sample, and the contact resistance between sample and substrate are fitted to match the experimental data. When fitting three parameters at the same time, the results for the individual parameters may not accurately be predicted. However, it was found that the total layer resistance (consisting of all three parameters) can be estimated with high accuracy. The reason is the difference in sensitivity of the model on the individual

parameters.^[10] Hence, we report only the total layer resistance. In addition to that, we calculate the effective thermal conductivity of our samples. We estimated based on literature data^{[11],[12]} that the thermal interface resistance between the gold transducer layer and sample is on the order or less than 10^{-8} Km²/W. We, consequently, do not expect a significant influence of this interface on our calculation of the effective thermal conductivity. The thermal conductivity is obtained by dividing the total layer resistance by the sample thickness. AFM measurements determined the sample thickness. We summarized the values of the total layer resistance, the sample thickness and the resulting effective thermal conductivity in Table 11.6.

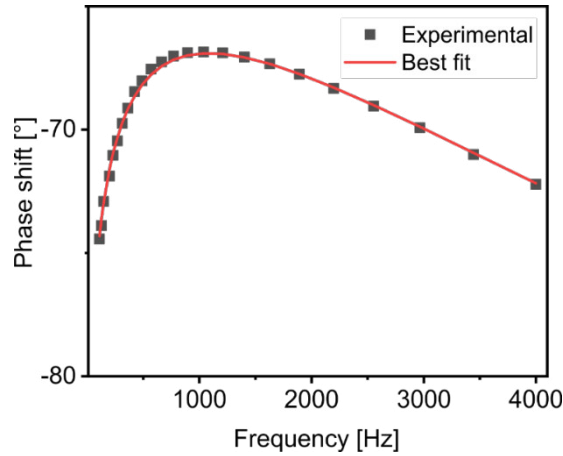


Fig. 11.16: Representative photoacoustic measurement of the GO-syn sample with a thickness of 446 nm. Normalized photoacoustic phase signal is dependent on the frequency. The red line indicates the best fit.

Tab. 11.6: Summary of the photoacoustic measurements. The total layer resistance, the thickness, and the resulting effective cross-plane thermal conductivity are given for each sample.

Sample	Total layer resistance [mm ² K/W]	Thickness [μm]	Effective thermal conductivity [W/mK]
Hec-L	1.58	0.28	0.177
Hec-L	2.55	0.595	0.234
Hec-L	4.34	0.94	0.217
Hec-S	5.39	0.972	0.180
Hec-S	4.62	0.972	0.210
Hec-S	5.86	0.972	0.166
GO-syn	1.92	0.233	0.121
GO-syn	3.99	0.446	0.117
GO-syn	5.52	0.746	0.135
GO-com	1.43	0.179	0.125
GO-com	2.65	0.388	0.128
GO-com	4.50	0.589	0.131

11.7.3 References

- [1] J. Breu, W. Seidl, A. J. Stoll, K. G. Lange, and T. U. Probst, „Charge homogeneity in synthetic fluorohectorite“, *Chemistry of Materials*, vol. 13, no. 11, pp. 4213–4220, Nov. 2001.
- [2] M. Stöter, D. A. Kunz, M. Schmidt, *et al.*, „Nanoplatelets of sodium hectorite showing aspect ratios of ≈ 20000 and superior purity“, *Langmuir*, vol. 29, no. 4, pp. 1280–1285, Jan. 2013.
- [3] P. Feicht, R. Siegel, H. Thurn, *et al.*, „Systematic evaluation of different types of graphene oxide in respect to variations in their in-plane modulus“, *Carbon*, vol. 114, pp. 700–705, Apr. 2017.
- [4] S. Rosenfeldt, M. Stöter, M. Schlenk, *et al.*, „In-depth insights into the key steps of delamination of charged 2d nanomaterials“, *Langmuir*, vol. 32, no. 41, pp. 10 582–10 588, Oct. 2016.
- [5] A. Salazar, A. Mendioroz, and R. Fuente, „The strong influence of heat losses on the accurate measurement of thermal diffusivity using lock-in thermography“, *Applied Physics Letters*, vol. 95, no. 12, p. 121 905, Sep. 2009.
- [6] A. Mendioroz, R. Fuente-Dacal, E. Apiñaniz, and A. Salazar, „Thermal diffusivity measurements of thin plates and filaments using lock-in thermography“, *Review of Scientific Instruments*, vol. 80, no. 7, p. 074 904, Jul. 2009.
- [7] A. Philipp, N. W. Pech-May, B. A. F. Kopera, *et al.*, „Direct measurement of the in-plane thermal diffusivity of semitransparent thin films by lock-in thermography: An extension of the slopes method“, *Analytical Chemistry*, vol. 91, no. 13, pp. 8476–8483, May 2019.
- [8] V. Singh, T. L. Bougher, A. Weathers, *et al.*, „High thermal conductivity of chain-oriented amorphous polythiophene“, *Nature Nanotechnology*, vol. 9, no. 5, pp. 384–390, Mar. 2014.
- [9] H. Hu, X. Wang, and X. Xu, „Generalized theory of the photoacoustic effect in a multilayer material“, *Journal of Applied Physics*, vol. 86, no. 7, pp. 3953–3958, Oct. 1999.
- [10] X. Wang, B. A. Cola, T. L. Bougher, *et al.*, „PHOTOACOUSTIC TECHNIQUE FOR THERMAL CONDUCTIVITY AND THERMAL INTERFACE MEASUREMENTS“, *Annual Review of Heat Transfer*, vol. 16, no. 1, pp. 135–157, 2013.
- [11] M. D. Losego, M. E. Grady, N. R. Sottos, D. G. Cahill, and P. V. Braun, „Effects of chemical bonding on heat transport across interfaces“, *Nature Materials*, vol. 11, no. 6, pp. 502–506, Apr. 2012.

- [12] V. Juvé, M. Scardamaglia, P. Maioli, *et al.*, „Cooling dynamics and thermal interface resistance of glass-embedded metal nanoparticles“, *Physical Review B*, vol. 80, no. 19, Nov. 2009.

Danksagung

Abschließend möchte ich mich bei allen bedanken, die durch ihre fachliche und persönliche Unterstützung zum Gelingen dieser Arbeit beigetragen und mich auf dem Weg begleitet haben.

Mein erster Dank gilt meinem Doktorvater Prof. Dr. Markus Retsch. Er war bereits seit Beginn meines Studiums wie ein Mentor für mich und hat meinen Studienverlauf stark geprägt. Nach Bachelor- und Masterarbeit bot er mir die Möglichkeit, auch meine Doktorarbeit in seiner Gruppe anzufertigen. Von den ersten Handgriffen als studentische Hilfskraft im Labor bis zur finalen Version dieser Arbeit unterstützte er mich und war jederzeit für Fragen erreichbar. Trotzdem ließ er mir genügend Freiraum, meine Ideen umzusetzen. Dieses Betreuungsverhältnis war und ist für mich nicht selbstverständlich. Vielen herzlichen Dank für alles, Markus!

Weiterhin gilt mein Dank allen Kollegen und Kooperationspartnern, die mit ihrem Wissen, ihrem Einsatz und ihrer Zeit zu dieser Arbeit beigetragen haben. Es ist für mich etwas ganz Besonderes, dass ich immer auf die Unterstützung von jedem einzelnen Kollegen zählen konnte. Nur durch das gute Miteinander, die Diskussionen und Denkanstöße, ihre Messungen, Simulationen und Python-Skripte konnte ich diese Arbeit überhaupt beenden. Besonders danken möchte ich auch Martina Heider und Dr. Markus Drechsler von der Elektronenmikroskopie, sowie Dr. Sabine Rosenfeldt für ihre Unterstützung. Außerdem herzlichen Dank an Stefan Rettinger für das ein oder andere DSC-Abenteuer und die vielen LEXT- und STA-Messungen. Danke auch an Elisabeth Dünfelder für die Hilfe bei Verwaltungsfragen und die inspirierenden, kreativen Gespräche im Sekretariat.

Vielen Dank an alle ehemaligen und jetzigen Retschis, die ich während der letzten Jahre kennenlernen durfte. Von und mit ihnen habe ich sehr viel gelernt. Besonders erwähnen möchte ich meine alten Laborkollegen Pia und Fabi, die mir ihr gesamtes Wissen über Partikelsynthese weitergegeben und damit den Grundstein für meine Forschung gelegt haben. Es hat mir immer Spaß gemacht, mit allen zusammenzuarbeiten und auch nach der Arbeit Zeit mit ihnen zu verbringen. Ich

werde die gemeinsamen Kochabende und Freitagnachmittag-Afterworks immer in guter Erinnerung behalten.

Ein großer Dank gilt meiner Familie, meiner Schwester Theresa, meiner Mama Claudia und meinem Papa Detlef, die mich in jeder Lebenslage unterstützt und jede meiner Entscheidungen mitgetragen haben. Danke an dieser Stelle auch an Heidi und Dea, die immer für mich da waren.

Zuletzt geht ein besonderer Dank an meinen Mann Stefan für die Ausdauer, Ruhe und Geduld, mit der er mir jederzeit zur Seite stand. Besonders an das Jahr im gemeinsamen Homeoffice zwischen Frust und Freude und mit der ein oder anderen Kaffeepause werde ich immer gern zurück denken.

Herzlichen Dank !

Eidesstattliche Versicherungen und Erklärungen

§8 Satz 2 Nr. 3 PromO Fakultät

Hiermit versichere ich eidesstattlich, dass ich die Arbeit selbstständig verfasst und keine anderen als die von mir angegebenen Quellen und Hilfsmittel benutzt habe (vgl. Art. 64 Abs 1 Satz 6 BayHSchG).

§8 Satz 2 Nr. 3 PromO Fakultät

Hiermit erkläre ich, dass ich die Dissertation nicht bereits zur Erlangung eines akademischen Grades eingereicht habe und dass ich nicht bereits diese oder eine gleichartige Doktorprüfung endgültig nicht bestanden habe.

§8 Satz 2 Nr. 4 PromO Fakultät

Hiermit erkläre ich, dass ich Hilfe von gewerblichen Promotionsberatern bzw. –vermittlern oder ähnlichen Dienstleistern weder bisher in Anspruch genommen habe noch künftig in Anspruch nehmen werde.

§8 Satz 2 Nr. 7 PromO Fakultät

Hiermit erkläre ich mein Einverständnis, dass die elektronische Fassung der Dissertation unter Wahrung meiner Urheberrechte und des Datenschutzes einer gesonderten Überprüfung unterzogen werden kann.

§8 Satz 2 Nr. 8 PromO Fakultät

Hiermit erkläre ich mein Einverständnis, dass bei Verdacht wissenschaftlichen Fehlverhaltens Ermittlungen durch universitätsinterne Organe der wissenschaftlichen Selbstkontrolle stattfinden können.

Bayreuth, März 2022

Anna Magdalena Neuhöfer

Colophon

This thesis was typeset with $\text{\LaTeX} 2_{\epsilon}$ in the TeXstudio integrated development environment. I used the *Clean Thesis* style developed by Ricardo Langner. The design of the *Clean Thesis* style is inspired by user guide documents from Apple Inc. You can download the *Clean Thesis* style at <http://cleanthesis.der-ric.de/>. I created the vector graphics with Corel Draw X7.

Anna Magdalena Neuhöfer
Thermal Properties of Colloidal Structured Materials
Dissertation, March 2022

University of Bayreuth
Physical Chemistry I (PC I)
Faculty of Biology, Chemistry & Earth Sciences
Universitätsstraße 30
95447 Bayreuth